

Étude de la cristallisation des polymères par simulation numérique

Thomas Vettorel

Thèse soutenue publiquement le 28 juin 2005

Membres du Jury :

- Directeur de thèse* : **J. Baschnagel**
Professeur ULP, ICS, Strasbourg
- Co-encadrant* : **H. Meyer**
Chargé de recherche, ICS, Strasbourg
- Rapporteur interne* : **A. Bieber**
Professeur ULP, ICS, Strasbourg
- Rapporteur externe* : **J.-P. Ryckaert**
Chargé de cours, ULB, Bruxelles
- Rapporteur externe* : **J.-U. Sommer**
Chargé de recherche, ICSI, Mulhouse
- Examineur* : **M. Fuchs**
Professeur, Fachbereich Physik, Konstanz



Contents

Résumé	v
Introduction	v
Méthodes de simulation	vi
Simulations tout-atome	vii
Fusion de cristaux parfaits	ix
Simulation de la cristallisation	x
Simulations coarse-grained	x
Caractérisation de différents modèles	xi
Caractérisation des cristaux	xii
Facteurs de structure	xiii
Facteurs de structure moyens	xiv
Facteurs de structure résolus en monomères	xiv
Facteurs de structure impliquant les centres de masse	xv
Conclusion	xv
Introduction	1
Models of polymer crystallization	2
Computer simulation techniques	4
Molecular simulations of polymer crystallization	5
Motivation of this work	6
Organization of this work	7
1 Simulation methods	9
1.1 Simulation models on different scales	10
1.1.1 Molecular dynamics simulations	10
1.1.1.1 Integration of the equations of motion	10
1.1.1.2 Different ensembles: <i>NVE</i> , <i>NVT</i> , <i>NPT</i>	12
1.1.2 Interaction potentials	18
1.1.2.1 Non-bonded potentials	18
1.1.2.2 Bonded interactions	19
1.2 Simulation methodology	21
1.2.1 Setup of initial configurations	21
1.2.2 Equilibration run	22
1.2.3 Production run	22

1.2.4	Cooling	23
1.2.5	Melting	23
1.3	Definition of observables	24
2	Atomistic simulations	31
2.1	Introduction	31
2.1.1	Experimental facts about <i>n</i> -alkanes	31
2.1.2	Review of simulation studies for <i>n</i> -alkanes	32
2.2	All-atom simulation model	34
2.2.1	Force field	34
2.2.1.1	OPLS-AA	34
2.2.1.2	YASP simulation package	35
2.2.1.3	Special optimization for the torsional potential	36
2.2.2	Model characterization	40
2.2.2.1	General observations	40
2.2.2.2	Influence of the thermostat	40
2.2.3	Discussion	44
2.3	Melting of <i>n</i> -alkane crystals	45
2.3.1	Creation of perfect structures	46
2.3.1.1	Orthorhombic phase	46
2.3.1.2	Triclinic phase	47
2.3.2	Melting experiment	49
2.4	Simulation of crystallization	58
2.4.1	Cooling experiment	58
2.4.2	Isothermal relaxation	62
2.4.3	Discussion	65
2.5	Simulations of polypropylene	66
2.5.1	Introduction	66
2.5.2	Definition of the model	68
2.5.3	Simulation details	68
2.5.4	Preliminary results and outlook	69
2.6	Summary	72
3	Coarse-grained models	75
3.1	Definition of models	75
3.1.1	The CG-PVA model	76
3.1.2	Definition of new models by variation of the angular potential	81
3.1.3	Simulation parameters	84
3.2	Characterization of different models	84
3.2.1	Comparison of different angular potentials	85
3.2.2	Reference values for chain length $N = 100$	97
3.2.3	Further observations	97
3.3	Characterization of the crystal	102
3.3.1	Continuous cooling	102

3.3.1.1	Influence of the cooling rate	102
3.3.1.2	Influence of the chain length	103
3.3.2	Order parameters during the crystallization and melting process	105
3.3.2.1	Global order parameter	105
3.3.2.2	Definition of crystallinity	109
3.3.2.3	Avrami analysis	111
3.3.3	Volkenstein analysis of the influence of the angular potential	117
3.3.4	Isothermal relaxation	121
3.3.5	Structure factors	123
3.3.6	Melting of perfect crystals	126
3.4	Summary	133
4	Structure factors	137
4.1	Definitions	137
4.1.1	Density fluctuations	138
4.1.2	Static structure factors	138
4.1.3	Center-of-mass related structure factors	139
4.1.4	Technical details	140
4.2	Site-averaged structure factors	141
4.2.1	Intra-chain structure factors	141
4.2.2	Inter-chain structure factors	145
4.2.3	Comparison of different models	146
4.3	Site-resolved structure factors	148
4.3.1	Direct correlation functions	148
4.3.2	Intra-chain structure	153
4.3.3	Inter-chain structure	157
4.4	Structure factors involving the center of mass	159
4.5	Summary	164
Conclusion		167
Summary		167
Simulation methods		167
<i>n</i> -alkanes		167
Coarse-grained models		168
Structure factors		170
Outlook		170
List of Tables		175
List of Figures		177
Bibliography		183

Résumé

Introduction

De très nombreux objets que nous utilisons dans la vie de tous les jours sont constitués de matières plastiques ; selon les propriétés (mécaniques en particulier) que l'on souhaite conférer à ces objets, il est possible de choisir un matériau dont la structure à température ambiante sera plus à même de reproduire le comportement désiré. Les matières plastiques constituant de tels objets se composent de polymères qui sont de longues molécules en forme de chaînes dont la structure chimique peut varier dans une large mesure. Un *fundu* de polymères est un mélange *pur* de ces chaînes (on peut également considérer des polymères en solution), qui est un liquide visqueux à haute température et peut prendre plusieurs formes solides de caractéristiques bien distinctes à basse température [62, 100]. Un système de polymères peut devenir soit *vitreux* soit *cristallin* au cours d'un refroidissement ; nous nous sommes intéressés au comportement de ce dernier type de polymères à l'aide de simulations numériques ; la structure de ces systèmes est cependant plus complexes que celle des cristaux de particules plus simples car les chaînes ont tendance à se replier sur elles-mêmes pour former des structures ordonnées à des échelles de longueur très variées (fig. r.1), et sont séparées par des régions dans lesquelles les polymères restent amorphes [120]. On parle alors de systèmes *semi-cristallins*.

L'étude de ces cristaux de polymères donne lieu à quelques controverses du fait du manque d'un modèle permettant de décrire de façon satisfaisante la formation et le développement des structures ordonnées ; récemment la proposition d'un nouveau modèle par Strobl [121] est venue remettre en question les apports de la théorie de Lauritzen et Hoffman [5, 45] qui était bien acceptée et permet de décrire une bonne part des résultats expérimentaux mais ne parvient pas à rendre compte de l'observation de certains phénomènes [87].

Afin de tenter d'apporter un nouvel éclairage sur le phénomène de la cristallisation des polymères qui s'avère suffisamment complexe pour ne pas être — à ce jour — descriptible par un seul modèle simple, plusieurs groupes ont essayé de reproduire des structures semi-cristallines de polymères par simulations numériques afin de pouvoir les étudier plus en détail [73–75, 87, 131, 138, 139]. La cristallisation en solution a été étudiée par Muthukumar, ainsi que le développement d'une structure

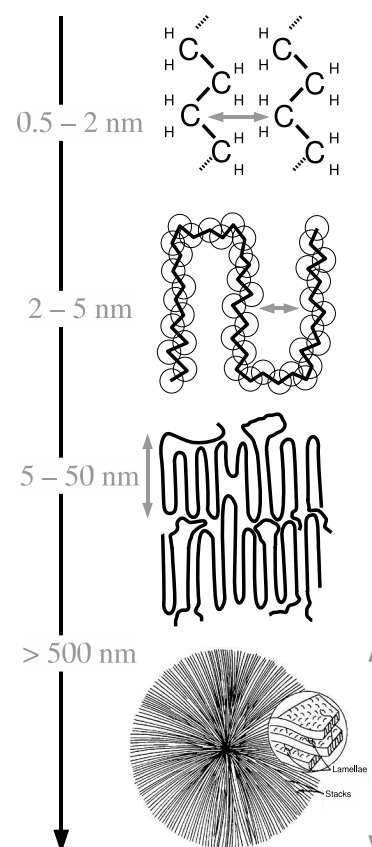


Fig. r.1: Illustration des différentes structures composant un cristal de polymères, depuis l'échelle atomique jusqu'aux sphérolites.



(a) Modèle tout-atome



(b) Modèle atome unifié



(c) Modèle coarse-grained

Fig. r.2: Représentation schématique de différents modèles de simulation numériques des polymères, à différents niveaux de précision.

Equations de Newton :

$$m_i \ddot{\mathbf{r}}_i = \mathbf{f}_i \quad (\text{r.1})$$

(particules de masses m_i aux positions \mathbf{r}_i sur lesquelles s'exercent les forces \mathbf{f}_i)

Algorithme *leap-frog* :

$$\begin{aligned} \mathbf{r}_i(t + \delta t) &= \mathbf{r}_i(t) + \delta t \mathbf{v}_i(t + \frac{\delta t}{2}) \\ \mathbf{v}_i(t + \frac{\delta t}{2}) &= \mathbf{v}_i(t - \frac{\delta t}{2}) + \delta t \frac{\mathbf{f}_i(t)}{m_i} \end{aligned} \quad (\text{r.2})$$

($\mathbf{v}_i(t)$ est la vitesse de la particule i à l'instant t)

Equations de Newton modifiées (thermostat de Berendsen) :

$$m_i \ddot{\mathbf{r}}_i = \mathbf{f}_i + m_i \gamma \left(\frac{T_0}{T} - 1 \right) \mathbf{v}_i \quad (\text{r.3})$$

(γ : coefficient de friction)

semi-cristalline avec des repliements à partir d'un germe [87] ; certains auteurs se sont intéressés à la cristallisation favorisée par la présence de murs [131, 138].

La plupart des études numériques portant sur la cristallisation des polymères est fondée sur des modèles de type « atome unifié » [84] ; il est en effet important de choisir un type de simulation adapté au problème considéré, de manière à retenir suffisamment de détails pour fournir une description précise mais également à ne pas s'encombrer d'informations inutiles. La figure r.2 montre des modèles prenant en compte plus ou moins des détails des molécules, depuis le modèle tout-atome traitant explicitement tous les atomes des polymères jusqu'à un modèle coarse-grained qui permet de représenter un monomère (élément se répétant au sein d'une chaîne de polymère) par une seule particule. Le modèle atome unifié est une étape intermédiaire et consiste à regrouper un carbone et les atomes d'hydrogène y étant rattachés en une seule particule [9].

En utilisant un modèle coarse-grained comme celui présenté sur la figure r.2(c), Hendrik Meyer a pu reproduire des structures semi-cristallines à partir du fondu sans introduction explicite de murs ou d'un germe [73–75, 97] ; dans cette thèse, nous avons approfondi cette étude en nous intéressant plus particulièrement au paramètre le plus important de ce modèle qui est le potentiel angulaire permettant aux chaînes coarse-grained de reproduire de façon réaliste la flexibilité du polymère décrit (voir chap. 3). Nous avons aussi utilisé des simulations tout-atome de chaînes courtes d'alcane de manière à étudier de façon très réaliste des systèmes-modèles pour la cristallisation et la fusion des molécules allongées (chap. 2). Enfin, partant de l'observation d'une corrélation entre les propriétés à haute et basse températures pour les modèles coarse-grained, nous avons procédé à une étude approfondie de la structure à haute température des fondus de polymères (chap. 4). Ce résumé présente brièvement les principales informations développées plus en détails dans la version anglaise de cette thèse.

Méthodes de simulation

Nous avons utilisé des méthodes de simulation classique, faisant appel à des algorithmes de dynamique moléculaire [2, 11, 34]. Que ce soit pour les simulations de modèles tout-atome ou pour les modèles coarse-grained, le principe de la simulation consiste en une résolution numérique des équations du mouvement de Newton [équ. (r.1)], pour toutes les particules du système afin de reproduire son évolution temporelle. Des algorithmes spécifiques permettent de modifier l'ensemble dans lequel la dynamique moléculaire permet de créer des configurations (l'ensemble microcanonique, puisque les équations de Newton conservent l'énergie du système) : un thermostat et un barostat sont utilisés afin de travailler dans l'ensemble isotherme–isobare, à température et pres-

sion constantes.

Les simulations tout-atome ont été effectuées à l'aide du logiciel YASP [82], qui repose sur un algorithme d'intégration des équations de Newton de type leap-frog (éq. (r.2), [44]); les thermostat et barostat appliqués fonctionnent selon la méthode développée par Berendsen (voir éq. (r.3); [10]).

Pour les simulations coarse-grained, le programme utilisé a été développé par H. Meyer spécifiquement pour la simulation des chaînes polymères. Il utilise un intégrateur de type velocity-Verlet (éq. (r.4), [122]), un thermostat de Langevin (voir éq. (r.5); [39, 107]) et un barostat de Berendsen [10].

L'utilisation de ces deux programmes permet d'obtenir des données regroupant les valeurs des positions et vitesses des particules au cours du temps (trajectoires) qui permettent le calcul de toutes les propriétés physiques auxquelles on souhaite accéder.

Les interactions prises en compte pour ces simulations permettent de décrire le comportement des polymères en fondu et, que ce soit dans le cas des simulations détaillées (tout-atome) ou de la méthode coarse-grained plus « grossière », ces interactions consistent en une partie *liée* [connectivité (éq. (r.6) : liaisons entre particules consécutives le long de la chaîne), flexibilité (éqs. (r.7) et (r.8) : angles entre liens et angles de torsions)] et une partie *non-liée* [volume exclu (éq. (r.9) : répulsion entre particules), interaction électrostatique : éq. (r.10)].

Les simulations que nous avons effectuées en utilisant les différents modèles qui nous intéressent ici consistent en une partie d'équilibration de la phase liquide à haute température, puis un refroidissement continu ou une trempe à une température plus basse suivie d'une relaxation isotherme; ces deux méthodes permettent de reproduire les conditions dans lesquelles des cristaux de polymères sont formés. Nous avons également créé des configurations parfaitement cristallines de polymères dont nous avons étudié la fusion.

Simulations tout-atome

Le polymère cristallisable ayant la structure la plus simple est le polyéthylène (PE); il a été supposé pendant très longtemps que les phénomènes de cristallisation des polymères pouvaient se résumer à ce qui est observé dans le cas de ce système en particulier [46]. Si la formation de structures semi-cristallines apparaît maintenant plus complexe et nécessite une description plus détaillée, il n'en reste pas moins que le PE est un système-modèle très intéressant. En particulier, les chaînes courtes de polyéthylène (n -alcane) présentent un comportement très riche qui mérite une étude approfondie : en effet, selon le nombre d'atomes de carbone dans la chaîne, la phase cristalline varie; elle peut être orthorhombique [24, 78–81, 114] (comme c'est le cas pour le PE, qui constitue la limite des chaînes longues de n -alcane) ou tri-

Algorithme *velocity-Verlet* :

$$\begin{aligned} \mathbf{r}_i(t + \delta t) &= \mathbf{r}_i(t) + \delta t \mathbf{v}_i(t) + \frac{1}{2m_i} \mathbf{f}_i(t) \delta t^2 \\ \mathbf{v}_i(t + \delta t) &= \mathbf{v}_i(t) \\ &\quad + \frac{1}{2m_i} \delta t (\mathbf{f}_i(t) + \mathbf{f}_i(t + \delta t)) \end{aligned} \quad (\text{r.4})$$

Equations de Newton modifiées (thermostat de Langevin) :

$$m_i \ddot{\mathbf{r}}_i = \mathbf{f}_i - m_i \gamma_i \mathbf{v}_i + \mathbf{W}_i \quad (\text{r.5})$$

(\mathbf{W}_i : force aléatoire)

Potentiels décrivant les interactions pour une simulation tout-atome :

$$U_{\text{bond}}(b) = \frac{1}{2} k_{\text{bond}} (b - b_0)^2 \quad (\text{r.6})$$

$$U_{\text{ang}}(\theta) = \frac{1}{2} k_{\text{ang}} (\theta - \theta_0)^2 \quad (\text{r.7})$$

$$U_{\text{tors}}(\phi) = \quad (\text{r.8})$$

$$\sum_{n=1}^3 \frac{1}{2} k_n^{\text{tors}} (1 - \cos(n\phi - \phi_n^0))$$

$$U_{\text{mol}}(r) = 4\epsilon \left(\left(\frac{\sigma}{r} \right)^{12} - \left(\frac{\sigma}{r} \right)^6 \right) \quad (\text{r.9})$$

$$U_{\text{ei}}(r) = \frac{q_i q_j}{4\pi\epsilon r_{ij}} \quad (\text{r.10})$$

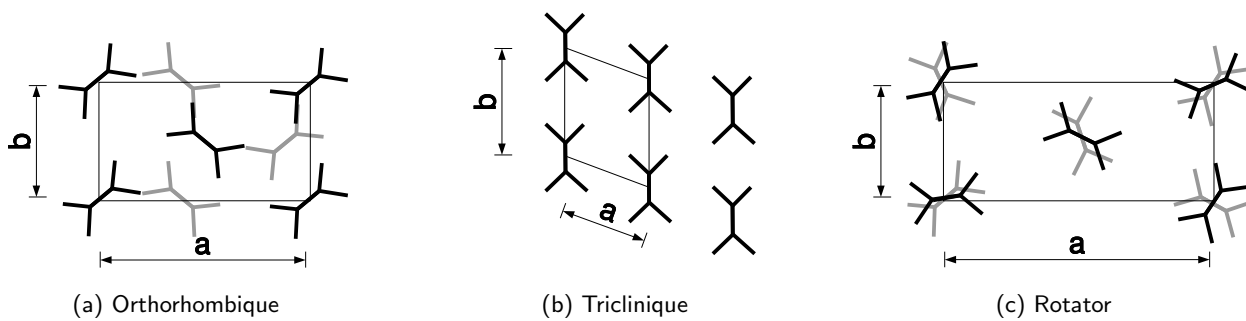


Fig. r.3: Structure des principales phases cristallines observées dans le cas des n -alcanes (les chaînes sont allongées selon leur axe principal perpendiculairement au plan de la figure).

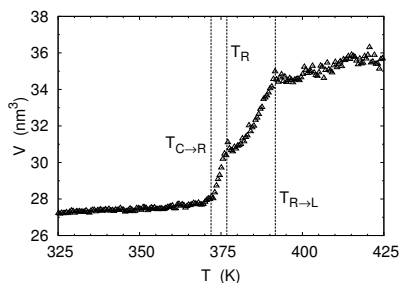


Fig. r.4: Diagramme de phase (volume en fonction de la température) pour $C_{15}H_{32}$ mettant en évidence les différentes transitions de phase : cristal-rotator et rotator-liquide.

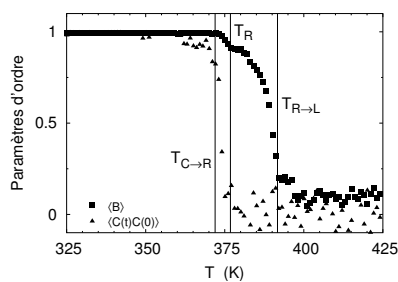


Fig. r.5: Paramètres d'ordre pendant la transition du cristal orthorhombique vers le fondu. $\langle B \rangle$ correspond à la corrélation des vecteurs de l'axe principal d'élongation des chaînes; $\langle C(t)C(0) \rangle$ indique l'auto-corrélation d'orientation d'un plan contenant le squelette d'une chaîne au cours du temps (ici, dans le cas d'un réchauffement continu, le temps et la température sont proportionnels).

clinique pour un nombre de carbones pair [24, 41, 91] (voir fig. r.3; il existe de très nombreux autres cas observés expérimentalement que nous ne mentionnerons pas ici [24]). Il a aussi été découvert par l'expérience l'existence de phases transitoires apparaissant lors du passage du cristal au liquide. Ces phases dites « rotator » (cf. fig. 3(c)) se caractérisent par une symétrie différente de celle du cristal, et un degré d'ordre moindre puisque, dans ce cas, les chaînes sont libres de tourner autour de leur axe principal [20, 25, 26, 43, 56, 67, 112, 113, 115, 116, 127].

Nous avons voulu soumettre à l'expérience numérique ce type de systèmes en utilisant un algorithme détaillé permettant de prendre en compte la structure spécifique des chaînes d'alcanes : en effet, un modèle coarse-grained ne permet pas de reproduire un empilement orthorhombique ou triclinique de molécules. Le modèle atome unifié très couramment employé n'autorise que la formation de structures à symétrie hexagonale. Comme les n -alcanes sont des chaînes relativement courtes, il nous a paru intéressant d'essayer de simuler leur comportement en utilisant un modèle tout-atome très détaillé, même s'il est évident que ce type de simulation ne permet pas d'obtenir des configurations cristallines par refroidissement (à cause du temps de calcul très important nécessaire pour reproduire un protocole suffisamment lent). Nous nous sommes tout d'abord intéressés à la fusion de configurations cristallines parfaites de ces n -alcanes.

Nous avons testé le champ de force OPLS-AA [51] et il nous est apparu nécessaire de modifier les paramètres du potentiel de torsion qui a une influence considérable sur les conformations créées par la simulation : de cette manière, nous avons pu retrouver la distribution des angles obtenues par un autre groupe qui a développé un modèle reproduisant les propriétés du PE avec une bonne précision [140]. À l'aide de ce modèle, il nous a été possible de simuler la fusion et la cristallisation des n -alcanes.

Fusion de cristaux parfaits

Des configurations orthorhombiques et tricliniques de n -alcanes (typiquement $C_{14}H_{30}$, $C_{15}H_{32}, \dots$) ont été créées artificiellement à partir des données cristallographiques [68, 114], puis simulées à très basse température avant d'être réchauffées jusqu'à $T = 500$ K. Le modèle que nous avons optimisé à haute température dans la phase liquide nous a permis de reproduire l'apparition transitoire d'une phase rotator lors de la fusion du cristal (fig. r.4). Même si nos simulations ne montrent pas toute la variété des différentes phases rotator isolées expérimentalement, la transition nette vers une phase à symétrie hexagonale est déjà un résultat très intéressant puisque le modèle utilisé n'est pas suffisamment complexe *a priori* pour reproduire aussi précisément les différentes structures à basse température. On aurait pu s'attendre à ce que les interactions déterminant le comportement du modèle, qui ont été calibrées pour décrire un liquide, ne soient pas suffisamment précises pour autoriser la simulation d'un cristal, et encore moins l'apparition de la phase rotator.

Les caractéristiques indiquant le passage à une phase rotator lors de la fusion des cristaux comprennent la décroissance de plusieurs paramètres d'ordre différents, et le changement de symétrie dans le plan perpendiculaire à l'axe principal des chaînes. Plus particulièrement, on peut observer une décorrélation de l'orientation des plans dans lesquels se situent les chaînes avant la disparition d'une direction privilégiée témoignant de l'allongement des molécules (fig. r.5). Le changement de symétrie est visible sur l'évolution du rapport des paramètres de maille a et b : ce rapport passe de $3/2$ à $\sqrt{3}$ lors de la transition, valeurs qui sont caractéristiques de symétries orthorhombique et hexagonale (fig. r.6).

La transition cristal-rotator a pu être observée également lors de simulations de relaxations isothermes à différentes températures, à partir de configurations obtenues lors du réchauffement continu. De cette manière, la transition a pu être mise en évidence plus clairement, et la phase rotator a pu être isolée pendant 1 ns (fig. r.7), ce qui en permet une caractérisation plus aisée. Cependant, le fait que cette phase reste transitoire et ne puisse être stabilisée comme c'est le cas pour les systèmes étudiés expérimentalement indique les limitations de notre modèle qui ne tient pas compte des particularités de l'état cristallin. Le champ de force optimisé pour des simulations de l'état liquide ne permet pas de reproduire complètement le comportement du système simulé. De plus, les températures de transition obtenues sont bien trop élevées par rapport aux valeurs expérimentales, ce qui est compréhensible puisque les systèmes de départ sont *parfaits*, c'est-à-dire sans défauts favorisant la cristallisation, et *infinis* à cause des conditions aux limites périodiques appliquées. Ces deux différences par rapport aux systèmes expérimentaux combinées aux limites du champ de force utilisé conduisent aux désaccords quantitatifs constatés, cependant que

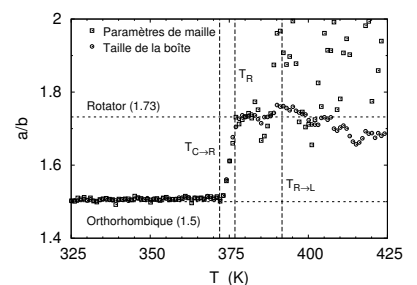


Fig. r.6: Evolution du rapport des paramètres de maille a/b calculé selon deux méthodes différentes pendant un réchauffement continu du cristal orthorhombique de n -alcanes. Cette mesure n'a plus de sens à partir de la fusion complète du système ($T > T_{R \rightarrow L}$).

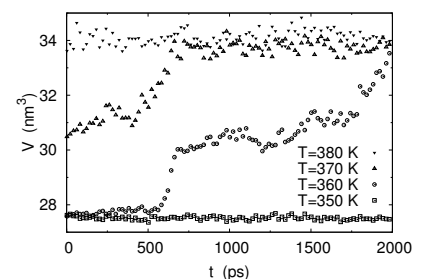


Fig. r.7: Variation de volume lors de relaxations isothermes à différentes températures proches de la température de transition cristal-rotator.

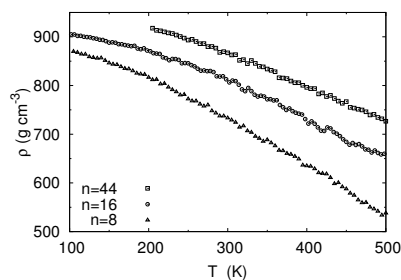


Fig. r.8: Densité en fonction de la température pour des n -alcanes de longueurs différentes.

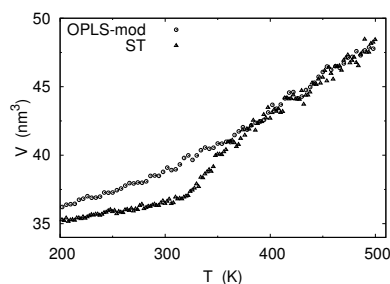


Fig. r.9: Comparaison du diagramme de phase de deux modèles tout-atome : notre modèle OPLS modifié et un modèle dérivé ST ayant un potentiel de torsion exagérément rigide. Ce dernier cristallise lors d'un refroidissement, comme indiqué par le saut observable sur la valeur du volume à basse température ; le modèle OPLS modifié au contraire présente seulement un comportement de type transition vitreuse.

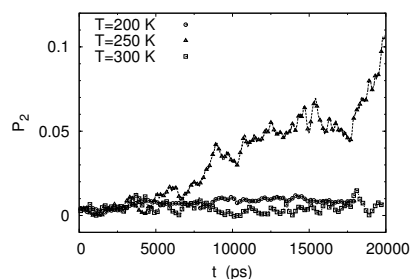


Fig. r.10: Paramètre d'ordre P_2 mesuré au cours du temps à différentes températures pour un système de n -alcanes. Le système est liquide à $T = 300$ K et vitreux à $T = 200$ K, mais on peut voir l'ordre se développer à une température intermédiaire entre ces deux états.

l'accord qualitatif avec les expériences est très bon.

Simulation de la cristallisation

A partir de configurations liquides de n -alcanes équilibrées à haute température, nous avons soumis le modèle à un refroidissement continu. Pour les différentes longueurs de chaîne étudiées et les taux de refroidissements accessibles pour ce type de simulations (typiquement 10^{-3} K ps $^{-1}$), nous n'avons pas pu reproduire de configurations cristallines : la fig. r.8 montre que la densité ne présente pas de saut lors de l'abaissement de la température, mais s'incurve plutôt comme dans le cas d'une transition vitreuse. Cela signifie que l'apparition d'un germe à partir duquel un cristal pourrait croître nécessiterait des temps nettement plus longs, de manière à laisser les chaînes s'organiser en lamelles.

Il est possible également que les paramètres du modèle ne soient pas suffisamment bien ajustés pour conduire les chaînes à s'associer dans des structures semi-cristallines. Il est cependant tout-à-fait possible de reproduire une configuration semi-cristalline à partir d'un modèle tout-atome semblable à celui que nous avons utilisé : nous avons créé un modèle (appelé ST) avec un potentiel de torsion non réaliste qui rend les chaînes très (trop) rigides, et ce modèle soumis à un refroidissement continu dans les mêmes conditions que notre modèle OPLS modifié conduit à la formation d'un cristal (fig. r.9). Le modèle ST ne peut pas être considéré comme un modèle satisfaisant permettant de former des configurations cristallines de n -alcanes ou de PE, car les conformations des chaînes obtenues ne sont pas réalistes, et de plus la température de *cristallisation* observée dans ce cas est supérieure à la température de *fusion* mesurée expérimentalement pour les n -alcanes considérés.

Il semble que le modèle OPLS modifié soit un bon modèle pour les n -alcanes car il permet une bonne description du comportement des cristaux et des propriétés du liquide. On peut aussi montrer que la cristallisation n'est pas observable avec un tel modèle principalement pour des raisons ayant trait au temps de calcul disponible conditionnant les taux de refroidissements accessibles, car des signes précurseurs de la cristallisation ont pu être observés lors de simulations de relaxations isothermes du modèle OPLS modifié à différentes températures : la fig. r.10 présente l'évolution du paramètre d'ordre P_2 (deuxième polynôme de Legendre du produit scalaire des vecteurs représentants les liens entre particules le long des chaînes) au cours du temps à plusieurs températures, et l'on peut distinctement observer le développement d'ordre au cours de la simulation à $T = 250$ K.

Simulations coarse-grained

Le modèle CG-PVA développé par Hendrik Meyer permet de simuler efficacement le comportement de l'alcool polyvinylique à basse température, et la structure semi-cristalline attendue est bien observée sur

les configurations générées après un refroidissement [74, 75, 97]. La formation des lamelles est obtenue grâce à la forme particulière du potentiel gouvernant les états angulaires des chaînes : ce potentiel est déterminé (de même que les paramètres caractérisant les autres interactions) à partir de données mesurées sur des simulations tout-atome ; de cette manière, le modèle coarse-grained peut reproduire les conformations des polymères modélisés de façon précise, sans avoir à prendre en compte tous les détails moins pertinents avec lesquels il faut compter dans une simulation à l'échelle atomique. Le potentiel angulaire ainsi déterminé est représenté sur la fig. r.11 : on peut distinguer trois états favorables pour les états angulaires à l'échelle coarse-grained, qui correspondent aux états *trans-trans* (*tt*), *trans-gauche* (*tg*) et *gauche-gauche* (*gg*) de deux angles de torsion consécutifs sur le squelette de la chaîne originale, à l'échelle atomique.

Ce paramètre du modèle est particulièrement important puisqu'il permet aux chaînes de reproduire des conformations « réalistes », et ainsi de conduire à la formation de structures lamellaires en favorisant l'apparition de plis, tout en permettant leurs déplacements qui autorisent la formation puis la croissance de structures semi-cristallines. Un modèle comportant exactement les mêmes ingrédients mais un potentiel angulaire nul reste complètement amorphe et ne permet pas la formation de cristallites (fig. r.12).

Caractérisation de différents modèles

L'importance de ce potentiel pour la simulation du phénomène de cristallisation nous a conduits à créer de nouveaux modèles dérivés de CG-PVA en modifiant le potentiel angulaire $U(\theta)$; ces modèles peuvent être considérés comme représentant d'autres espèces de polymères de structure chimique différente mais relativement proche de celle de l'alcool polyvinylique et dont les spécificités à l'échelle atomique sont reflétées dans des proportions particulières des occupations des états coarse-grained *tt*, *tg* et *gg*.

Pour chacun des modèles créés ainsi, nous avons étudié les caractéristiques physiques de façon à déterminer l'influence du potentiel angulaire sur le comportement du modèle et en particulier sur la cristallisation. Cette étude nous a permis de mettre en évidence une corrélation entre les propriétés du fondu à haute température et son comportement à basse température : la proportion d'état *tt* à $T = 1$ est liée à la température de cristallisation T_{cryst} (de même qu'à la température de fusion T_{melt} ; voir fig. r.13). Nous avons pu également montrer l'existence d'une corrélation entre la probabilité des états *gg* et la longueur de persistance l_P , qui est donc fortement influencée par la propension des chaînes à se replier sur elles-mêmes.

La corrélation entre P_{trans} (probabilité des états *tt*) et T_{melt} peut être étudiée à l'aide d'un modèle simple développé par Volkenstein [130] ; nous avons pu montrer que cette théorie décrit de façon appropriée

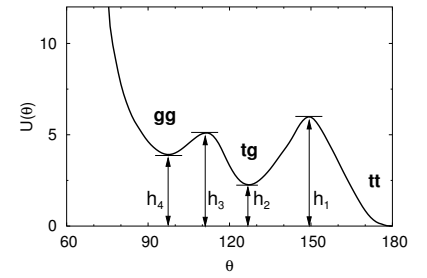


Fig. r.11: Potentiel angulaire du modèle CG-PVA et paramètres permettant de le modifier de façon à créer d'autres modèles coarse-grained.

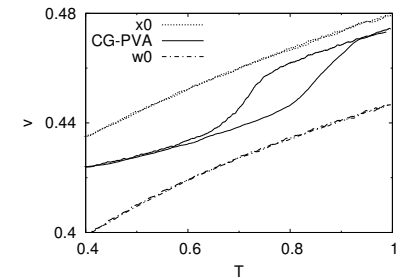


Fig. r.12: Comparaison des diagrammes de phase obtenus avec le modèle CG-PVA et deux de ses variantes sans potentiel angulaire ; w_0 possède exactement les mêmes caractéristiques que CG-PVA, avec un potentiel angulaire $U(\theta) = 0$, et x_0 est un modèle similaire pour lequel les interactions de volume exclu existent aussi pour deux particules situées à deux liens de distances le long d'une même chaîne, ce qui le rend plus rigide.

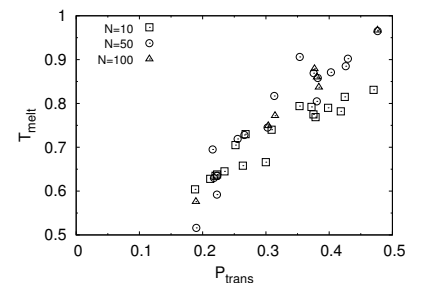


Fig. r.13: Corrélation entre la température de fusion et la probabilité de trouver un état *trans-trans* dans le fondu à haute température ($T = 1$). Chaque point correspond à un modèle différent et à une longueur de chaîne particulière.

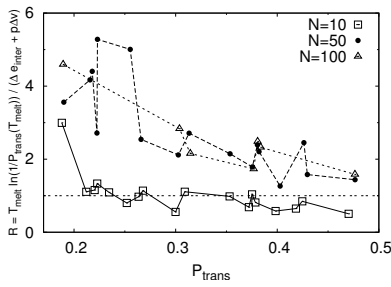


Fig. r.14: Valeur du rapport R en fonction de la probabilité des états tt à haute température pour différents modèles et différentes longueurs de chaînes. La théorie de Volkenstein prédit $R = 1$; les données de simulations permettent de retrouver cette valeur pour les chaînes courtes, et le désaccord dans le cas des chaînes plus longues diminue avec l'augmentation de la rigidité du modèle.

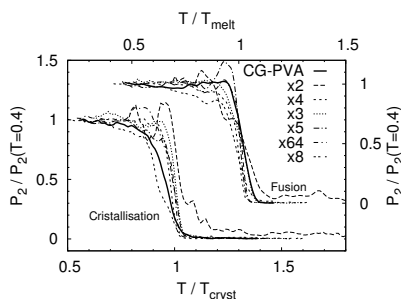


Fig. r.15: Superposition des paramètres d'ordre P_2 obtenus pour différents modèles au cours de refroidissements et réchauffements continus.

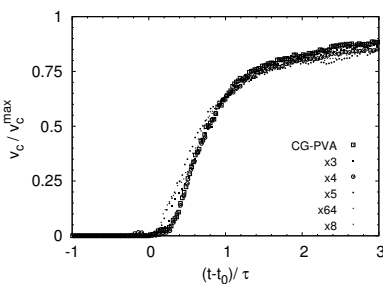


Fig. r.16: Courbe maîtresse présentant l'évolution de la cristallinité au cours d'un refroidissement continu des différents modèles coarse-grained.

la fusion des cristaux de polymères dans le cas où est vérifiée l'hypothèse selon laquelle l'état cristallin est dominé par l'état *trans*. C'est le cas pour des chaînes parfaitement étendues dans des cristaux parfaits, ainsi que pour des cristaux de chaînes très courtes qui parviennent à s'étendre complètement et à s'ordonner en cristaux (ce qui n'est plus vérifié pour des chaînes plus longues, dans le cas desquelles le système devient frustré; cf. fig r.14).

Caractérisation des cristaux

La structure des systèmes semi-cristallins a été caractérisée par différents paramètres d'ordre, et il est possible d'unifier les résultats obtenus pour les modèles étudiés afin de déterminer les caractéristiques principales des phénomènes de cristallisation et fusion des polymères. Le paramètre d'ordre P_2 peut être utilisé pour décrire le développement d'ordre dans le fondu au cours d'une simulation de refroidissement continu. Une fois les valeurs obtenues normalisées par la température de cristallisation et la valeur du paramètre d'ordre à basse température, on peut constater que les courbes correspondant aux différents modèles se superposent relativement bien; il en est de même pour les courbes correspondantes obtenues pour la fusion (fig. r.15). Cela suggère que la cristallisation des modèles coarse-grained se produit selon des mécanismes identiques, même si les configurations finales sont très différentes d'un modèle à l'autre.

Une description plus précise de la formation de la structure cristalline des modèles coarse-grained peut être obtenue à l'aide d'un autre paramètre d'ordre qui permet, sur la base d'un critère local de proximité et de corrélation d'orientation de deux liens, de déterminer des ensembles de particules appartenant à une même structure (cristallite). Couplée à une analyse d'Avrami [135] pour la croissance d'un objet dans un milieu par analogie avec la propagation d'une vague à la surface d'un bassin, la détermination d'un tel paramètre d'ordre — correspondant à une mesure de la cristallinité — permet de décrire de façon unifiée la croissance d'un cristal au sein d'un fondu de polymère à l'aide de deux nouveaux paramètres correspondants à la cristallinité finale extrapolée du matériau et un temps caractéristique associé au développement des cristallites (fig. r.16).

Les modèles coarse-grained que nous avons utilisés permettent de reproduire des résultats observés expérimentalement, comme les lignes de cristallisation et fusion indiquant que les températures T_{cryst} et T_{melt} sont reliées linéairement à l'inverse de l'épaisseur des lamelles dans les cristaux [54, 55, 121]; à l'aide de simulations de relaxation isotherme suivant une trempe à une température située au dessous de la température de fusion, on observe la formation de lamelles d'épaisseur d au sein des zones cristallines du système de polymères. Au cours du réchauffement continu qui suit cette étape, la fusion intervient à une température proportionnelle à $1/d$ (fig. r.17).

Nous avons comparé la structure des configurations semi-cristallines obtenues à la suite d'un refroidissement continu à celles de cristaux « parfaits », c'est-à-dire d'assemblages créés artificiellement de chaînes soit complètement étendues soit régulièrement repliées. Les pics représentatifs d'un réseau cristallin à symétrie hexagonale sont présents, ainsi que d'autres pics dans le cas des configurations créées artificiellement puis équilibrées à basse température : ceux-ci proviennent d'effets de taille finie comme nous pouvons le constater à l'aide de comparaisons avec des facteurs de structures calculés pour des configurations légèrement modifiées afin de mettre en évidence l'effet de la frustration et de la taille finie des chaînes sur la structure d'un cristal de chaînes complètement allongées (fig. r.18).

On peut établir un lien entre le modèle tout-atome pour le polyéthylène présenté plus haut et les simulations coarse-grained en proposant un modèle coarse-grained grossier pour le PE qui consiste à utiliser les paramètres de CG-PVA pour toutes les interactions excepté le potentiel angulaire que l'on peut dériver de la distribution angulaire mesurée à partir des simulations tout-atome de *n*-alcane. Il est a priori nécessaire de procéder à une détermination complète des paramètres des différentes interactions que réclame le coarse-graining, mais on peut justifier cette hypothèse par le fait que les volumes caractéristiques des chaînes de PE et de PVA sont suffisamment proches (faibles différences de structure des deux molécules). On peut considérer en première approximation que les distinctions entre les deux polymères seront prises en compte entièrement au niveau du potentiel angulaire dont nous avons pu constater l'incidence sur le comportement du modèle. Le modèle CG-PE ainsi défini permet de simuler la cristallisation d'un fondu de chaînes courtes de PE, comme on peut le voir sur la fig. r.19 : contrairement à ce que nous avons pu observer dans le cas du modèle tout-atome qui aboutit à une structure amorphe après refroidissement, le modèle CG-PE cristallise de la même manière que le modèle CG-PVA et certaines de ses variantes.

Facteurs de structure

La corrélation observée entre la probabilité de trouver un état angulaire *trans-trans* à haute température et les températures de cristallisation/fusion nous a conduits à calculer des facteurs de structure [40] détaillés correspondants à différents modèles coarse-grained, à haute température ; cela nous a permis de comparer la structure du fondu de polymères avec les résultats attendus pour des liquides simples, et également de tester certaines approximations souvent utilisées pour la description des systèmes de polymères.

Afin d'obtenir des renseignements concernant la structure du fondu plus précis que ce que l'on peut extraire de la quantité globale $S(q)$ (fig. r.20), nous avons distingué les facteurs de structure *inter-* et *intra-*

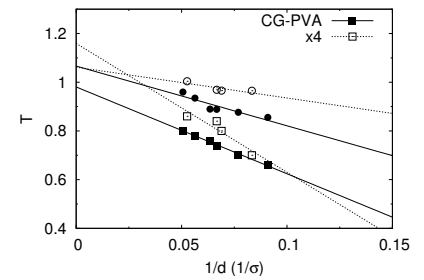


Fig. r.17: Lignes de cristallisation et de fusion pour CG-PVA et le modèle x4. Les symboles carrés représentent la cristallisation et les ronds la fusion du système.

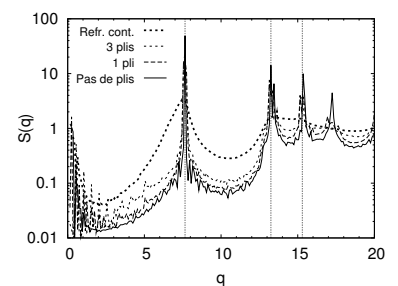


Fig. r.18: Comparaison des facteurs de structure obtenus pour des configurations cristallines à basse température ($T = 0.4$) ayant des cristallinités différentes.

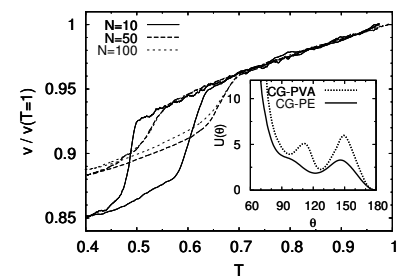


Fig. r.19: Diagrammes de phases obtenus au cours de refroidissements continus du modèle CG-PE dérivé de CG-PVA et des distributions angulaires extraites des simulations tout-atome de *n*-alcane. En encart, les potentiels angulaires des deux modèles coarse-grained sont présentés.

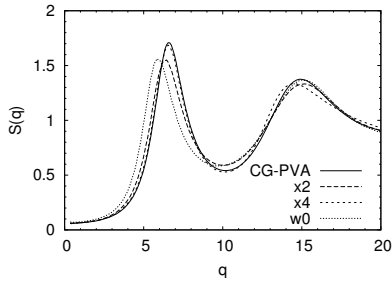


Fig. r.20: Facteurs de structure calculés à haute température ($T = 1$) pour 4 modèles différents : CG-PVA, w_0 (modèle sans potentiel angulaire), x_2 (basse T_{cryst}) et x_4 (haute T_{cryst}).

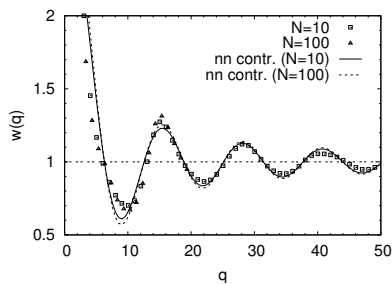


Fig. r.21: Facteur de structure intra-chaîne comparé à l'approximation des plus proches voisins pour deux longueurs de chaînes (modèle CG-PVA).

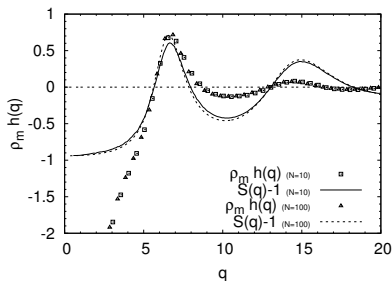


Fig. r.22: Structure inter-chaîne et facteur de structure moyen ($N = 10$ et $N = 100$).

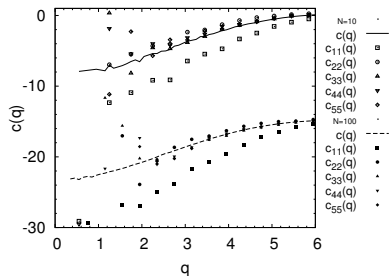


Fig. r.23: Comparaison des premiers éléments $c_{aa}(q)$ avec l'approximation PRISM $c(q)$.

chaîne et calculé des quantités résolues en monomères, c'est-à-dire des fonctions de corrélation de densité dépendant de la position des sites considérés le long des chaînes. La définition de telles quantités se place dans le cadre de la description de Ornstein-Zernike pour un système fluide [40], et nous utilisons plus particulièrement l'extension de ce formalisme aux molécules RISM [13, 14, 16] et son application aux systèmes de polymères, PRISM [108, 109].

Facteurs de structure moyens

La structure observée en comparant ces différents facteurs de structure peut être décrite à l'aide d'approximations permettant de prendre en compte les cas limites. La structure intra-chaîne donnée par $w(q)$ (facteur de forme [22]) est bien reproduite par l'approximation gaussienne à petits vecteurs d'onde q , et par une approximation prenant en compte les effets dus aux plus proches voisins seulement à grands q (fig. r.21). La structure inter-chaîne (fonction $h(q)$) détermine le premier pic du facteur de structure global puisque l'empilement dans le fondu est contrôlé par les interactions chaîne-chaîne, mais n'influence que très peu la structure global pour les vecteurs d'onde plus grands (fig. r.22).

Facteurs de structure résolus en monomères

La structure plus détaillée des fondus de polymères simulés peut être étudiée par le calcul des quantités résolues en sites le long des chaînes : facteurs de structure détaillés global $S_{ab}(q)$, intra-chaîne $w_{ab}(q)$ et inter-chaîne $h_{ab}(q)$. Ces quantités correspondent à des corrélations de densité calculées aux positions des monomères a et b ($a, b = 1, \dots, N$). L'introduction des fonctions de corrélation directe $c_{ab}(q)$ issues du formalisme de Ornstein-Zernike généralisé aux molécules à partir des liquides simples fournit un moyen commode de rendre compte de ces corrélations ; l'approximation Polymer-RISM suggère que pour des chaînes longues la corrélation directe entre monomères a et b ne dépend pas de leur position le long de la chaîne et par conséquent $c_{ab}(q) = c(q)$ [1, 13, 14, 16, 108, 109]. Nous avons pu montrer que ceci est bien vérifié dans le cas des modèles utilisés dans nos simulations, même pour des chaînes relativement courtes ($N \leq 100$), sauf en ce qui concerne les bouts de chaînes dans le pour lesquels il y a une déviation nette de $c_{ab}(q)$ par rapport à la fonction $c(q)$. Ces différences ne dépendent pas de la longueur de la chaîne et les fonctions $c_{ab}(q)$ convergent très rapidement vers $c(q)$ quand a et b augmentent lorsque l'on se rapproche du milieu des chaînes (fig. r.23).

Encore une fois les contributions inter et intra-chaînes peuvent être isolées et étudiées séparément ; nous avons pu montrer que, dans le cas de nos modèles coarse-grained comprenant un potentiel déterminant explicitement la flexibilité des chaînes, l'approximation de Koyama [57,

66] qui prend en compte les aspects non-gaussiens fournit une très bonne description de la structure intra-chaîne résolue en monomères (fig. r.24). La structure inter-chaîne peut être prédite avec une bonne précision (à l'exception des éléments de matrice correspondant aux bouts de chaînes, comme on peut s'y attendre) par une approximation de type PRISM (fig. r.25).

Facteurs de structure impliquant les centres de masse

On peut calculer à partir des données de simulation des facteurs de structure faisant intervenir les centres de masse des chaînes, ainsi que des fonctions de corrélation de densité entre un monomère situé à la position a au sein d'une chaîne et le centre de masse (CM) de cette même chaîne, ou d'une autre. L'approximation calculée dans le cadre de la théorie PRISM est en bon accord avec les mesures effectuées pour le facteur de structure CM–CM (fig. r.26) [59]. Pour les facteurs de structure monomère–CM, nous avons montré que l'approximation gaussienne permet de reproduire les données de simulation de façon d'autant plus satisfaisante que les chaînes considérées sont longues (fig. r.27).

Conclusion

Au cours de nos études des fondus de polymères, nous avons développé plusieurs approches distinctes permettant de caractériser et mieux comprendre l'apparition de structures cristallines à basse température. Deux méthodes de simulation à des échelles différentes ont été mises en œuvre de manière à mener ces études à bien.

Nous avons cherché à reproduire de façon précise la structure cristalline d'un système de chaînes courtes de polymères, correspondant à du PE de très faible masse moléculaire (n -alcanes), pour lesquelles l'arrangement en un cristal parfait est accessible par des simulations réalistes (méthode tout-atome). Cette approche nous a permis de retrouver les résultats expérimentaux concernant le passage à une phase solide transitoire avant l'apparition du liquide lors d'un réchauffement. Ceci justifie l'emploi d'une technique de simulation détaillée afin de décrire un système réaliste avec précision. Par ailleurs, cette méthode ne nous a pas permis d'accéder à la formation de structures cristallines à partir du fondu au cours d'un refroidissement, et nous avons utilisé une méthode différente, plus appropriée, dans ce cas.

Le modèle CG-PVA a été développé afin de simplifier la description des chaînes de polymères et permet ainsi de concentrer les efforts de simulation sur des échelles de longueur et de temps plus adaptées à l'étude de la cristallisation. Nous avons utilisé ce modèle comme point de départ de notre étude et nous avons développé d'autres modèles en faisant varier le potentiel angulaire qui contraint la flexibilité des chaînes. Nous avons pu de cette manière décrire l'influence de ce paramètre dont les effets sur l'arrangement des molécules à basse tempéra-

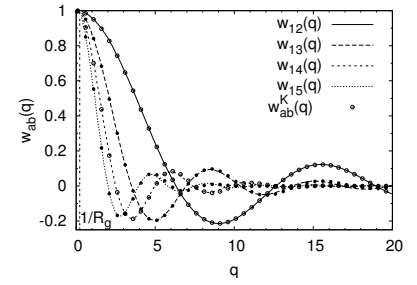


Fig. r.24: Comparaison de la structure intra-chaîne détaillée avec l'approximation de Koyama.

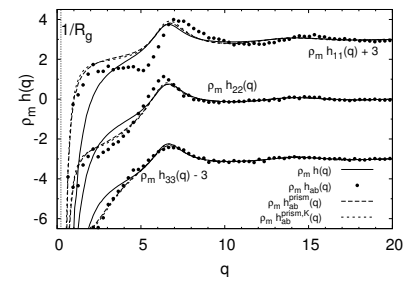


Fig. r.25: Comparaison de la structure inter-chaîne détaillée avec une approximation obtenue dans le cadre de la théorie PRISM.

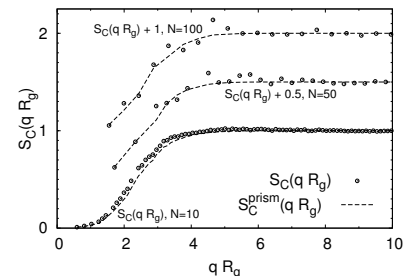


Fig. r.26: Facteur de structure des centres de masse des chaînes comparé à une approximation PRISM.

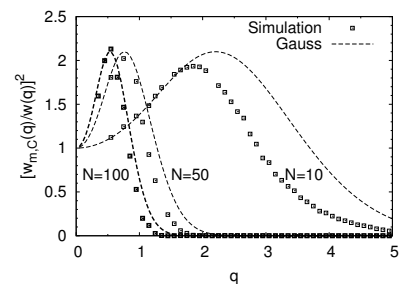


Fig. r.27: Comparaison du facteur de structure monomère–CM avec l'approximation gaussienne.

ture sont très importants. Cela nous a permis notamment de caractériser la croissance de structures cristallines dans le fondu par l'utilisation de divers paramètres d'ordre, et de mettre en évidence une relation entre les propriétés du fondu à haute température et la facilité qu'a le système à cristalliser (ou à fondre). Une approche théorique nous a permis de mieux comprendre cette relation, et nous avons cherché à approfondir l'étude des liens existants entre les propriétés structurales du fondu à haute et basse températures.

A cette fin, nous avons procédé au calcul détaillé de la structure du fondu de polymère à haute température, de manière à comparer avec précision le comportement de modèles ayant une tendance à cristalliser plus ou moins forte. Nous avons utilisé les fonctions de corrélation de densité définies dans le cadre du formalisme de Ornstein-Zernike, adapté au cas des molécules plus complexes et particulièrement aux chaînes de polymères. Cette étude ne permet pas de déterminer des différences qualitatives importantes entre les modèles que nous avons comparés, et les comparaisons avec les différentes approximations et cas limites que nous avons considérés afin de mieux comprendre la structure de fondu s'appliquent indépendamment de la flexibilité des chaînes.

Ces études différentes apportent des éléments utiles à une meilleure compréhension du phénomène de cristallisation des polymères qui n'est encore qu'imparfaitement compris, et suggèrent également des pistes pour des recherches plus approfondies dans certaines directions. Les modèles dérivés de CG-PVA ont permis de décrire la cristallisation des chaînes linéaires avec succès, et de nombreuses caractéristiques de tels systèmes ont pu être reproduites à l'aide de ces modèles à symétrie cylindrique. A présent, il serait intéressant de modéliser des polymères ayant une structure géométrique plus complexe, à l'aide d'un modèle de type coarse-grained plus raffiné construit sur les mêmes bases : il serait possible de définir un modèle permettant de décrire la chiralité d'un polymère comme le polypropylène (PP) en introduisant des groupes latéraux le long de la chaîne de manière à reproduire la structure en hélice caractéristique (cette idée a été étudiée dans la réf. 139). La construction d'un tel modèle devrait s'appuyer sur des simulations tout-atome de PP comme nous en avons étudiées à partir de l'expérience acquise grâce aux simulations de *n*-alcane (cf. partie 2.5). Il deviendrait alors possible de procéder à un test de l'hypothèse selon laquelle la croissance du cristal de PP ne peut se faire selon le scénario impliquant la formation d'une structure à grande échelle, à cause de la nécessaire sélection des chaînes par leur chiralité [63].

L'importance de l'existence des différentes échelles de longueur pour le processus de cristallisation suggère de tirer davantage parti des méthodes de simulations disponibles à des niveaux de détails variables, en combinant les deux techniques de manière à pouvoir bénéficier de l'efficacité de la méthode coarse-grained ainsi que de la précision permise par la méthode tout-atome. Pour ce faire, il est possible de réin-

roduire les détails atomiques dans une configuration obtenue à l'aide d'une simulation simplifiée [125, 126]; ainsi, la méthode coarse-grained peut être employée afin de reproduire la structure des cristaux à grande échelle, et combinée ensuite à une méthode tout-atome dont nous avons pu vérifier qu'elle permet de simuler la structure plus précise du cristal (reproduction de la maille orthorhombique du PE ou des alcanes, alors qu'un modèle coarse-grained n'autorise que la formation de cristaux à symétrie hexagonale de par sa construction). Cette réintroduction des détails atomiques n'est pas une entreprise facile, notamment parce que la correspondance des configurations aux deux échelles différentes n'est plus unique lors du retour à un degré de précision supérieur. Mais les renseignements que l'on pourrait tirer de ce type d'étude sont nombreux, et il serait tout particulièrement intéressant de déterminer si l'introduction des détails dans une configuration semi-cristalline de PE coarse-grained permet de retrouver par la suite la structure orthorhombique caractérisée à l'aide du modèle tout-atome (la transition cristal-rotator que nous avons simulée n'est pas réversible pour nos systèmes).

Afin de compléter et d'approfondir nos travaux, d'autres études complémentaires seraient souhaitables; en particulier les lignes de cristallisation et de fusion observées expérimentalement [54, 55, 121] et qui ont pu être reproduites par la simulation réclament d'être analysées plus en détail pour pouvoir en extraire les propriétés des transitions de phase et des mécanismes sous-jacents. Une comparaison plus poussée avec les résultats théoriques est nécessaire, mais demande la détermination de la tension de surface caractérisant l'interface entre le liquide et le cristal de polymères, ce qui constitue une étude à part entière.

Les résultats obtenus à l'aide des calculs de paramètres d'ordre au cours de la formation du cristal peuvent être affinés de façon à donner de plus amples informations concernant la croissance des cristallites, et en particulier pour des systèmes plus grands. Il est possible également de s'intéresser à l'évolution de la forme de ces cristallites depuis leur apparition en tant que germes jusqu'à leur stabilisation au sein du système semi-cristallin où elles sont contraintes par les régions amorphes environnantes.

Les premières étapes de la formation des cristaux constituent probablement le domaine dans lequel la simulation numérique a les plus grandes chances d'apporter des réponses décisives et pourra peut-être éclairer le débat sur les mécanismes à l'œuvre lors de la création des structures semi-cristallines, grâce à la grande précision dont cette méthode est capable. Des calculs détaillés de structure comme ceux que nous avons utilisé dans notre caractérisation du fondu à haute température seraient sans doute très utiles pour l'étude de l'évolution des systèmes de polymères au cours du refroidissement alors que le cristal se forme.

Enfin, des modèles présentant le niveau de détail approprié pour l'étude de la cristallisation pourraient être utilisés dans des simulations

de systèmes de grandes tailles sur des temps longs afin de reproduire la formation d'un cristal avec un faible taux de surfusion; de cette manière, les conditions optimales seraient réunies pour l'étude d'une éventuelle phase mésomorphe se développant en tant que précurseur du cristal [121].

Introduction

Many objects of everyday life are now plastics. These objects are constituted of polymer molecules in a particular state, in which they are solid and have mechanical properties that make them suitable for a wide range of uses. Depending on the need, different kinds of polymers are used, forming materials with varying properties; however, at high enough temperature, all polymeric systems are found in the state of a viscous liquid (we are considering the case of *pure* polymer melts only, as opposed to polymer *solutions*). Polymers are molecules with a chain-like structure, formed by an assembly of a (possibly very) large number of units called monomers. This nature of the polymer molecules gives rise to their physical properties at high temperature (viscosity arises from the difficulty encountered by the monomers to diffuse, because they are bound to other parts of the chain), and at low temperature [62].

At low temperature, polymeric systems may have distinct behaviors depending on the nature of the interactions between the particles and on the thermal history. All polymers undergo a glass transition after which the system ends up in a glassy state, i.e. its structure remains amorphous as it is in the high temperature melt, but the dynamics of the chains in the glass is considerably slowed down [23]. As a result, the system becomes rigid (and possibly brittle) below the glass transition temperature, whereas it flows above it.

Polymers that are sufficiently regular (little branching, stereo-regularity) can also form crystals at low temperature. This requires that upon freezing the mobility of the monomers is still high enough so that ordering is possible before a glassy state occurs. This mobility strongly depends on temperature, and therefore even crystallizable polymers might end up in a glassy state as a result of fast cooling; the glass transition also occurs below the crystallization temperature, implying that part of the system has evolved to an ordered state. However, crystallization of polymers is still somewhat remote from what is observed in the case of non-polymeric systems, therefore yielding polymer crystals some very specific properties.

We are interested in crystalline polymeric systems, which will be studied using computer simulations. The canonical example of a crystallizable polymer is polyethylene, which has the simplest possible structure (long alkane chain, see fig. i.1(a)); our study addresses polymers

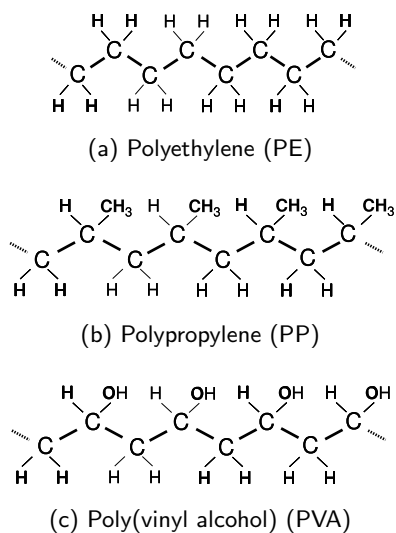


Figure i.1: Chemical formulae of three polymers with simple structure.

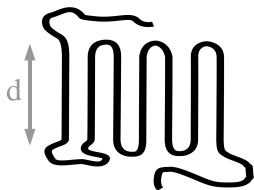


Figure i.2: Sketch of a chain folded to form a lamella. The lamellar thickness is indicated as the length d of one stem composing the lamella.

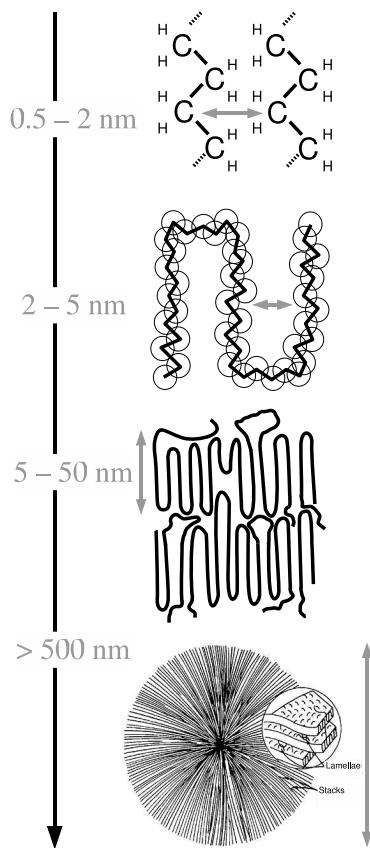


Figure i.3: Illustration of the different length scales relevant to the description of polymer crystals, from the atomistic level to spherulitic structures.

with such a simple structure, as well as slightly more complex molecules like poly(vinyl alcohol) and polypropylene (also presented in fig. i.1).

The polymeric systems that are able to form crystals still do not yield perfectly ordered materials, consisting of fully stretched chains; even if the monomers' mobility is higher than for glass-forming polymers, the connectivity of the chains always hinders the development of order while crystallizing. Thus, the resulting structures are only partially crystalline, and contain a non-negligible amount of amorphous material surrounding the crystalline regions. Hence crystal-forming polymers are referred to as *semi-crystalline* [5, 87, 134]. As perfectly stretched configurations are not accessible for very long chains because of kinetic or entropic effects, the ordered parts of semi-crystalline polymer systems have a typical length which is orders of magnitude smaller than the chain length, as was recognized from scattering experiments which led to the conclusion that polymer chains must be folded back onto themselves [32, 53]; chains thus form lamellae (pictured in fig. i.2), which are stacked and finally form large-scale structures called spherulites.

Polymer crystallization is thus a phenomenon which involves a multitude of different length scales, ranging from the nanoscopic level (atoms constituting the molecule), to intermediate-sized structures (elongated parts of the chains forming stems and the lamellae they enter), to the microscopic spherulites. A schematic representation of these different size objects is given in fig. i.3.

Models of polymer crystallization

The properties of semi-crystalline polymers have been thoroughly studied for several decades, and many morphologies and growth mechanisms have been reported and analyzed [119, 134–136]. A general picture that has been widely used to describe the crystallization process is based on the understanding one has of the formation of crystals of simple particles: There is a nucleation step during which nuclei are formed, and from them the crystal develops in the second, growth step [5, 45, 87]. Actually, one distinguishes *two* nucleation steps: The first step of the process corresponding to the creation of a suitable nucleus (“primary nucleation”) is not addressed in the classical framework of the theory by Hoffman and Lauritzen; their model is based on a description of the “secondary nucleation” process (stems are deposited onto the growth front) which is assumed to be responsible for the formation of large-scale crystals. The theory assumes that some crystal growth front exists. It then describes a path for the development of the crystalline structures according to the classical nucleation-growth theory and predicts values for the growth rate as well as the thickness of the resulting lamellae which can be compared to experimental results. Although initially developed for crystallization from solution, it has been refined and applied to the crystallization in melts [46]. In particular,

the Hoffman-Lauritzen theory allows one to recover the characteristic relation linking the inverse lamellar thickness to the supercooling: As can be determined from simple thermodynamical considerations also (Gibbs-Thomson equation, see eq. (3.56) in section 3.3.4), the melting temperature T_{melt} of a semi-crystalline system is expected to vary linearly with the inverse lamellar thickness $1/d$ [87]. This behavior is observed in many experiments, and together with predictions of growth rates, this made the Hoffman-Lauritzen picture a widely accepted description of semi-crystalline polymers.

However, this understanding of the crystallization process has been challenged several times for its lack of accuracy and its failures at reproducing some experimental results [5]. For example, the lamellar thickness predicted by the model is supposed to be equal to an equilibrium value d , plus a *small* correction; but the large difference in the crystallization and melting temperatures reported in experiments proves that this correction cannot be small. Other models with different basic hypotheses have been proposed. The Sadler-Gilmer model takes entropic effects into account to describe the roughness of the growth front [105]. Recently Strobl has developed a new qualitative model for crystal growth that substantially differs from the classical description [121]. In this new model, the crystalline structures are not formed via adsorption of material *locally* on a growth front but rather emerge from an intermediate assembly of chains that preorders in the amorphous melt: It is conjectured that a so-called “mesomorphic phase” develops in the disordered medium before there is an ordering of the monomers when the mesomorphic phase turns into a lamella (see a sketch in fig. i.4). The proposition of such a model was also supported by the experimental observation of a signal at low wave vectors q before the occurrence of the characteristic peaks at higher q in X-ray scattering [49, 70], which is in favor of a description based on the spinodal decomposition [93]. This suggestion of a completely new route to the formation of polymer crystals has stimulated a lot of new discussions on the polymer crystallization process, and arguments were presented in favor of or against the two competing descriptions [17, 63, 86, 121]. For instance, the analysis of the arrangement of the two chiral species of isotactic polypropylene in the crystalline phase is seen by Lotz as an example where Strobl’s conjecture cannot apply, since the molecules of different kinds need to “probe” the existing growing crystal in order to deposit in the specific location they are found to occupy in the resulting crystal [63]. This is found not to be compatible with the previous arrangement of the chains into a mesomorphic phase that would afterwards evolve toward the final crystalline structure.

In this context, as many experimental facts have been produced and provide arguments in favor of completely different processes, the use of another approach may be useful to shed light on some aspects of the considered phenomenon that are not necessarily accessible to tra-

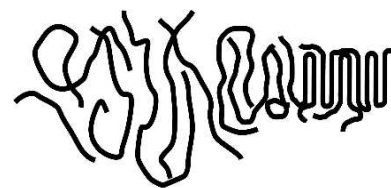


Figure i.4: Sketch of the formation of a lamella from the amorphous melt.

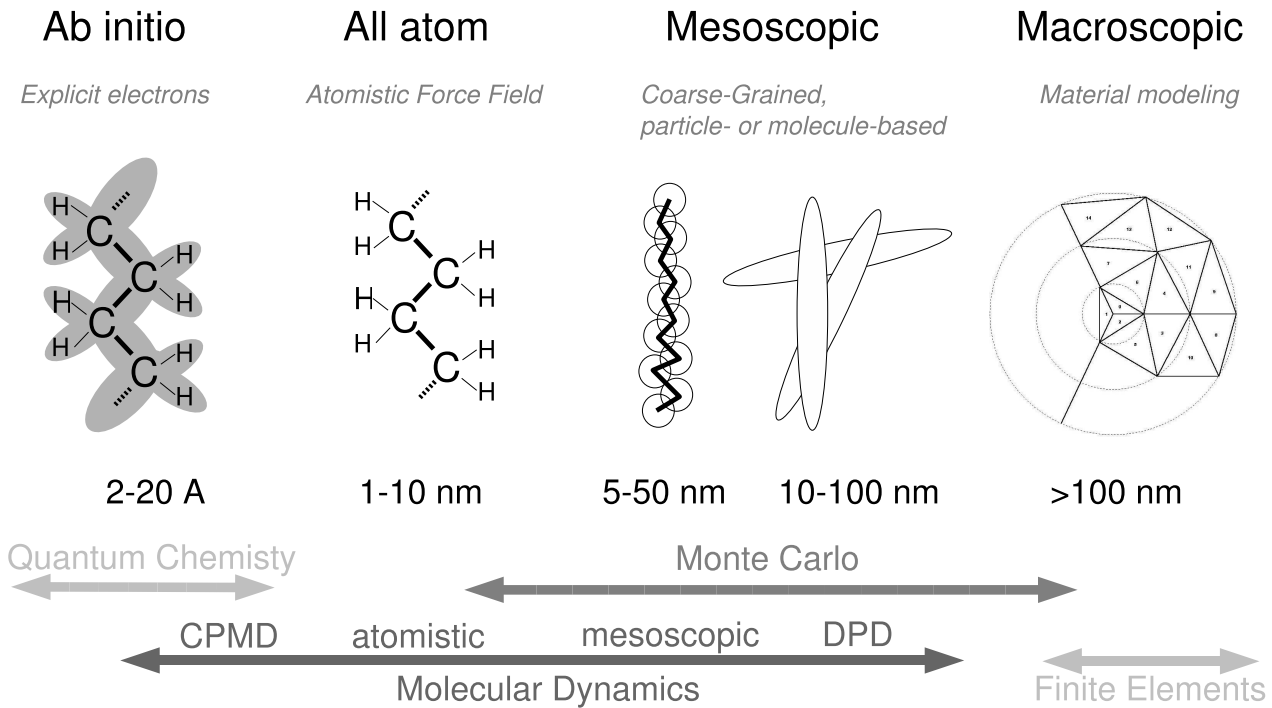


Figure i.5: Schematic representation of the different numerical methods that can be used to model and simulate molecular systems on various scales.

ditional methods: Experiments provide global views, an individual molecules can be visualized only at surfaces or by seriously disturbing the system. Computer simulation is a powerful tool that can be used to investigate a subject in a different manner, and provides insight into the intimate structure of semi-crystalline polymer melts; several contributions have focused on polymer crystallization using different simulation methods, addressing various aspects of the problem.

Computer simulation techniques

The different methods suitable for a study of polymer crystallization are intimately connected to the probed length scale. Figure i.5 shows an overview of the simulation methods and the corresponding resolutions that are accessible to them. As can be expected, the more “accurate” methods require a huge amount of computer time. *Ab-initio* calculations can predict the structure of elementary crystal cells, but they cannot be used to study the process of crystallization, as it is currently possible to simulate a few molecules only. Therefore, one has to forego a realistic description of the monomer–monomer interaction in favor of simpler models. On the other end of scales, *finite-element* simulations are very effective and useful to understand the macroscopic properties

of a material, but they do not permit a resolution of the positions of the different polymer chains since the relevant length scale is too large in this case. Thus, only intermediate solutions between these two schemes are appropriate for the study of polymer crystallization; i.e. the relevant simulation methods are situated on the atomic (all-atom simulations) or molecular level (coarse-grained simulations) [9, 84]. The models simulated using molecular dynamics can retain a varying amount of atomistic details; a widely used scheme is the united-atom model in which the fast motion of hydrogen atoms has already been averaged out. It is possible to achieve greater efficiency by averaging over more degrees of freedom, which is needed in order to be able to simulate large enough time and length scales.

Molecular simulations of polymer crystallization

Computer simulations have been used to address various aspects of polymer crystallization: *Monte-Carlo* simulations on a lattice were applied to model the selection of lamellar thickness in the crystal [4, 27–29, 105], which requires the hypothesis that a growth front preexists between the crystalline and amorphous regions. The Sadler-Gilmer model introduces roughness of this surface and makes the description of crystal growth more realistic [105], but this remains a restricted picture of the general phenomenon since the effects of neighboring lamellae and rearrangement of the chains in the already crystalline material are disregarded. Direct *molecular dynamics* simulations—that mostly use united-atom models of PE—have been applied to short chains in the melt [123], clusters in vacuum [35, 36] or thin films [111].

Muthukumar et al. have investigated several aspects of the crystallization of model polyethylene-like polymer chains [87]. These united-atom simulations introduce single chains that exhibit the typical folds upon cooling; this corresponds to the case of crystallization in solution [61, 88]. A theoretical model is presented to account for the finite size of the lamellae formed in the simulation [85, 87]. Muthukumar et al. also study the kinetics of crystal growth by adding chains in the vicinity of a crystal, and letting them relax [132]. The absorption of the chains into the preexisting crystal is described, showing a deposition of the added monomers onto the folded structure and their rearrangement.

A similar united-atom model was used by Rutledge et al. in order to investigate the crystallization of short alkane chains [131]. The introduction of walls bounding the simulation box allows for a higher probability of crystallization than in the bulk (heterogeneous nucleation), and the simulations are used to study the growth rate of the constrained crystal. An empirical model is used to account for the temperature dependence of this rate, based on an extended Avrami approach (the Avrami description of crystal growth is presented briefly in sec. 3.3.2.3).

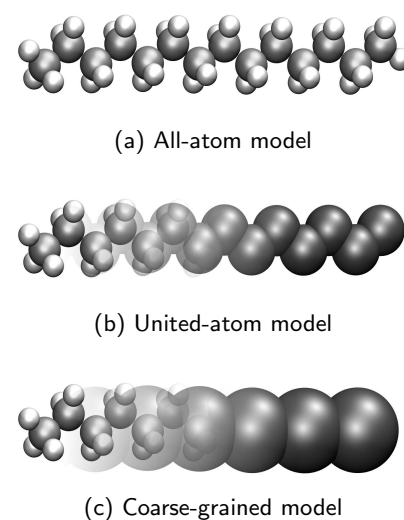


Figure i.6: Schematic representation of different coarse-graining steps in modeling a short alkane chain: The all-atom model explicitly takes into account all the atoms that comprise the molecule individually, whereas the united-atom scheme incorporates the hydrogen atoms together with the corresponding carbon into one single bead. An example of a model coarser such as the one presented in ref. 97 goes one step further and substitutes one particle for two carbons and the relative hydrogens. (Note that the size of the different particles in the representation does not correspond to the parameters used to define the interactions in the simulation code: The excluded-volume potential makes the particles larger than what they seem on the pictures.)

Crystallization from the melt of a constrained system has also been studied by Yamamoto, but with a coarser model than the united-atom scheme used in the abovementioned works [138]. Such a coarse-grained model allows for a higher efficiency, making it possible to simulate larger systems over longer times; the structure and evolution of the growing crystal are monitored, and the fold statistics is investigated. Yamamoto et al. have also recently made first attempts with a coarse-grained model of a more complex structure which allows to describe chiral polymers such as isotactic polypropylene [139].

Another coarse-grained approach that does not require the introduction of walls or explicit nucleus to yield crystallized systems has been developed by Hendrik Meyer [73–75]. A coarse-grained model for poly(vinyl alcohol) is derived on the basis of all-atom calculation (CG-PVA) [97]; effective potentials are determined and provide a realistic description of the melt, in that details from the chemistry of the considered polymer are still accounted for while the unneeded degrees of freedom have been averaged out to yield an efficient simulation scheme. The efficiency of this coarse-grained model allows one to simulate the crystallization of polymer melts in the bulk, since larger time and length scales are accessible compared to simulation schemes with all-atom or united-atom models; it is possible in particular to reproduce crystallization after homogeneous nucleation. Characteristic features of the crystallization of polymers from the melt could be obtained with this model. It was shown that the chain length dependence of homogeneous nucleation of short chains compares very well with droplet experiments on alkanes [58, 73]. In isothermal relaxation experiments, chain-folded lamellar structures were obtained, and the dependence of their thickness on the crystallization temperature as well as the subsequent melting gave well-defined crystallization and melting lines as observed in experiments [74]. Interestingly, the model contains no attractive inter-particle interaction. This means that the conformational statistics and an Onsager-like ordering mechanism which is in competition with the long-chain connectivity are probably dominating the structure formation at large scales. The results have been confirmed with larger systems and longer chains [73].

Motivation of this work

One main conclusion of the latter work was that one needs a better understanding of the influence of the angular potential. This angular potential allows us to keep track of the flexibility of the chain (as determined by the atomistic structure), and therefore contains the relevant information about the polymer. The study of this angular potential in simplified models constitutes an important part of this thesis. However, it appears that these simplified models cannot represent all features of polymer crystallization. We thus undertook a characterization of all-

atom models, and in particular we attempted to determine whether classical force fields can reproduce the complicated phase behavior of *n*-alkanes. This work was started in the longterm perspective of a multi-scale modeling (which will be discussed briefly in the final outlook), but also with the idea to get reference data to construct improved coarse-grained models. Looking for precursors of the crystallization process, we probed the structure of polymer melts with detailed correlation functions, so as to track the reason for high or low propensity to form crystals in the intrinsic properties of several models.

Organization of this work

We start with a brief **description of the technical aspects** of computer simulations. A short presentation of the molecular dynamics method is given, and the basic components of molecular models are described. Last, definitions of the quantities of interest in this study are presented.

The second chapter is dedicated to a **study of *n*-alkanes**, using an *all-atom simulation method*. For a long time this system has been considered a model-system for the study of polyethylene crystallization, since under certain conditions *n*-alkanes form crystals with an orthorhombic structure that resembles the polyethylene crystals [24, 46]. Although the much longer chain length of polyethylene confers it very specific features that are not present in the case of alkanes, and due to the great wealth of phases accessible to these systems, they are still interesting to study; this was also an occasion to set up the parameters of a realistic force field that could afterwards be used to simulate longer polymer chains and to derive a realistic coarse-grained model for PE, as has been done before for PVA (fig. i.1).

The third chapter deals with the **study of CG-PVA and its variants**, and presents a systematic study of the *influence of the angular potential* on the properties of the models, in particular the characteristics of crystallization. A correlation is found between the “flexibility” of the chains (fraction of stretched states of the bond angles measured in equilibrium at high temperature) and the propensity of the melt to crystallize (crystallization temperature). The evolution of the crystalline phase during continuous cooling and after a quench is investigated for different models; order parameters are computed in order to characterize the degree of crystallinity obtained with the different models, and it is shown that using a simple Avrami analysis for the growth of the crystalline regions, crystallization of different models during continuous cooling can be described in a unified manner.

The last chapter is concerned with an extensive **high-temperature study of the structure of the melts** for our different models: Motivation for this analysis is the relation between the high- and the low-temperature states that the study of the influence of angular potential

revealed. We calculated structure factors of the melts and studied the *inter*- and *intra*-chain contributions to these quantities, and applied a more detailed Ornstein-Zernike-like approach to models with different low-temperature behaviors.

Finally, a summary of the most important results and a discussion of perspectives for future simulations conclude this thesis.

1 Simulation methods

There are several methods to simulate the behavior of a system [2, 34, 84, 124]. A choice has to be made according to the length scale to be probed, to capture the relevant phenomenon. In case we are interested in physical properties which involve several polymer chains—which amounts to thousands of atoms at least—the method of choice would definitely not involve explicit electrons, nor should it consider the system as a continuous medium. In the former case one would have to cope with a lot of unnecessary information, while in the latter the relevant degrees of freedom would already be averaged out and therefore not accessible anymore.

Since we are interested in polymer melts and the structures that can form inside, we need to adopt a method that allows to keep track of the behavior of the chains themselves, and therefore retain enough details in the way they are modeled. The possibilities now are still numerous, depending on the degree of accuracy we require in the description of the chains. The more detailed scheme we can use consists in simulating the molecules taking into account all the atoms they contain. It has the advantage that, doing so, we can hope to reproduce precisely the structures that form at low temperatures in the melt: For such phases, the accurate geometry of the molecules (dictated by the interactions) becomes predominant as one heads toward regimes for the description of which a quantum treatment is necessary. It is also possible to run simulations with less details in the structure of the chains, but one has to be careful not to lose too much information to study the considered phenomenon.

Once the adequate model has been chosen, one needs a procedure to actually simulate its behavior, that is to infer from the bare interactions between the different constituents in the system the variation in time of their positions and velocities, from which all other physical quantities can be derived. In the case of molecular dynamics simulations, this is achieved by solving the equations of motion for all the particles in the system.

Contents

1.1 Simulation models on different scales	10
1.1.1 Molecular dynamics simulations	10
1.1.2 Interaction potentials	18
1.2 Simulation methodology	21
1.2.1 Setup of initial configurations	21
1.2.2 Equilibration run	22
1.2.3 Production run	22
1.2.4 Cooling	23
1.2.5 Melting	23
1.3 Definition of observables	24

1.1 Simulation models on different scales

1.1.1 Molecular dynamics simulations

Classical molecular dynamics (MD) simulations [2, 34] consist in solving Newton's equations of motion for a set of particles interacting via effective forces determined either by quantum computation or phenomenologically, i.e. set up so as to reproduce experimental measurements. For systems at relatively high temperature, the replacement of atoms by classical particles is harmless, since quantum specific effects are negligible. Once the different interactions between the MD particles are defined (this is described in sec. 1.1.2), the equations of motion have to be solved:

$$m_i \ddot{\mathbf{r}}_i = \mathbf{f}_i \quad (1.1)$$

where m_i , \mathbf{r}_i and \mathbf{f}_i are respectively the mass, position of particle i and the force exerted on it.¹ This equation has to be solved for all N particles in our system. The force \mathbf{f}_i derives from the potentials describing the interactions:

$$\mathbf{f}_i = - \frac{\partial U_{\text{pot}}(\mathbf{r}_1, \dots, \mathbf{r}_N)}{\partial \mathbf{r}_i}; \quad (1.2)$$

and in the case of pairwise additive interactions,

$$U_{\text{pot}} = \sum_{i=1}^N \sum_{j=i+1}^N U(\mathbf{r}_{ij}), \quad \text{where } \mathbf{r}_{ij} = \mathbf{r}_i - \mathbf{r}_j. \quad (1.3)$$

Using the MD simulation scheme, the positions and velocities of the N particles in the system are calculated at all times, allowing to compute from there all the physical properties. These quantities are time-averaged in the course of the simulation, which corresponds to an ensemble average, if the ergodic principle is to be trusted in that case. An MD simulation originally creates configurations in the microcanonical ensemble since the number of particles N remains unchanged, the volume V of the simulation box does not vary in time, and the equations of motion are known to conserve the energy E . It is possible to add some other degrees of freedom to the system so as to run a simulation in other ensembles than NVE [2, 34]. This is briefly described later.

1.1.1.1 Integration of the equations of motion

The method used to simulate the time evolution of the system consists in solving numerically the equations of motion, and there are several algorithms to do so. All of them rely on the Taylor expansion of the

¹The principles of the simulation method given here apply to any kind of system, and it is not necessary to introduce notations that are specific to polymers yet. Particles are grouped into chains because of the binding interactions described in sec. 1.1.2, and we shall use another convention to distinguish the particles belonging to different chains when introducing the quantities relevant to the system's analysis (sec. 1.3).

expression of the positions at time $t + \delta t$, δt being a short time interval (called “time-step” in the following):

$$\mathbf{r}_i(t + \delta t) = \mathbf{r}_i(t) + \delta t \mathbf{v}_i(t) + \dots \quad (1.4)$$

Combining this to the equivalent expression for $\mathbf{r}_i(t - \delta t)$, one arrives at the Verlet formulation for the resolution of eq. (1.1), which gives an estimate for $\mathbf{r}_i(t + \delta t)$ and $\mathbf{v}_i(t)$ as a function of $\mathbf{r}_i(t)$, $\mathbf{r}_i(t - \delta t)$, δt and the forces $\mathbf{f}_i(t)$ [129]. This result achieves accuracy up to δt^2 for velocities and δt^4 for positions; though, this particular algorithm suffers from several inconveniences ($\mathbf{r}_i(t + \delta t)$ and $\mathbf{v}_i(t + \delta t)$ are not known at the same time, and other problems mentioned, for instance, in [2]). There exist other forms of the algorithm that tackle those problems, such as the so-called *velocity-Verlet* algorithm (this algorithm is implemented in the `md_spherical` program that we used for coarse-grained models). From

$$\mathbf{r}_i(t + \delta t) = \mathbf{r}_i(t) + \delta t \mathbf{v}_i(t) + \frac{1}{2m_i} \mathbf{f}_i(t) \delta t^2 \quad (1.5)$$

$$\text{and } \mathbf{r}_i(t) = \mathbf{r}_i(t + \delta t) - \delta t \mathbf{v}_i(t + \delta t) + \frac{1}{2m_i} \mathbf{f}_i(t + \delta t) \delta t^2 \quad (1.6)$$

one obtains the following expression for the velocities:

$$\mathbf{v}_i(t + \delta t) = \mathbf{v}_i(t) + \frac{1}{2m_i} \delta t (\mathbf{f}_i(t) + \mathbf{f}_i(t + \delta t)) \quad (1.7)$$

and eq. (1.5) is used to advance the positions [122]. Another variant of the original Verlet algorithm is known as *leap-frog*, and uses half time-steps [44]. This algorithm is used by the `cycle` routine of the YASP package we used to simulate all-atom models [82]. It is written:

$$\mathbf{r}_i(t + \delta t) = \mathbf{r}_i(t) + \delta t \mathbf{v}_i(t + \frac{\delta t}{2}) \quad (1.8)$$

$$\mathbf{v}_i(t + \frac{\delta t}{2}) = \mathbf{v}_i(t - \frac{\delta t}{2}) + \delta t \frac{\mathbf{f}_i(t)}{m_i} . \quad (1.9)$$

The velocities at time t can be recovered using:

$$\mathbf{v}_i(t) = \frac{1}{2} \left(\mathbf{v}_i \left(t + \frac{\delta t}{2} \right) + \mathbf{v}_i \left(t - \frac{\delta t}{2} \right) \right) . \quad (1.10)$$

It is also possible to use higher order approximation methods, known as *predictor-corrector* codes. With these schemes, one predicts the value of \mathbf{r}_i at time $t + \delta t$ using a series expansion for positions

$$\mathbf{r}_i^P(t + \delta t) = \mathbf{r}_i(t) + \delta t \mathbf{v}_i(t) + \frac{1}{2} \delta t^2 \frac{\mathbf{f}_i(t)}{m_i} + \frac{1}{6} \delta t^3 \frac{\mathbf{b}_i(t)}{+} \dots \quad (1.11)$$

and similar expressions for velocities, accelerations and higher order time derivatives. These predictions are then corrected using the equations of motion, allowing to calculate $\mathbf{f}_i^C(t + \delta t)$. The final expression reads

$$\mathbf{r}_i^P(t + \delta t) = \mathbf{r}_i^C(t + \delta t) + \alpha_1 \frac{1}{m_i} \Delta \mathbf{f}_i^C(t + \delta t) \quad (1.12)$$

with

$$\Delta \mathbf{f}_i^C(t + \delta t) = \mathbf{f}_i^C(t + \delta t) - \mathbf{f}_i^P(t + \delta t) . \quad (1.13)$$

The coefficients α_k for the positions and their time derivatives need to be optimized for the problem under consideration, and depends on the order of the algorithm [37, 38].

Higher order methods than the Verlet algorithms usually give only little improvement, since they often require several correction iterations which involve costly force evaluation. Moreover, these methods might ensure a better energy conservation at short times, but this is not necessarily the case for long time series. The Verlet algorithms indeed appear to satisfy properties such as time reversibility and phase space volume conservation which lead to a good stability of the method.

1.1.1.2 Different ensembles: *NVE*, *NVT*, *NPT*

As mentioned above, the original MD algorithm allows to perform simulations in the *NVE* ensemble, but it is often desired to switch to canonical (*NVT*) or isothermal-isobaric (*NPT*) ensembles in order to reproduce as closely as possible the conditions of a “real” experiment [11]. The polymer melts we intend to study are obviously experimentally observed under constant pressure, and, whether they are first quenched and left to relax afterwards or continuously cooled down, we need an algorithm capable of imposing a constant temperature, or a variation of temperature in time. These particular conditions can be achieved by the application of specific modifications to the basic, microcanonical, MD algorithms.

Constant temperature. The canonical ensemble is realized by coupling the system to a large heat bath the effect of which is to actually thermostat the particles. This results in maintaining the temperature T constant in the system, T being related to the kinetic energy via the equipartition theorem (we are considering instantaneous values of the different quantities here):

$$E_k = \sum_{i=1}^N \frac{1}{2} m_i \mathbf{v}_i^2 \quad (1.14)$$

$$= \frac{3}{2} N k_B T . \quad (1.15)$$

One way to achieve the coupling is to allow random collisions with (imaginary) particles of the heat bath, which in practice is done by attributing to a particle chosen at random in the system a new velocity taken from the Boltzmann distribution corresponding to the prescribed temperature [3]. The strength of such a coupling is adjusted by changing the frequency of the collisions: In the limit of an infinite time between two collisions, the microcanonical ensemble is recovered, while

for collisions happening with probability one to any particle at all time-steps, the simulation eventually becomes a Monte-Carlo simulation (see also [34, 117]).

Langevin thermostat. Another way of thermostating a simulated system is to switch from the Newtonian to the Langevin formulation of the equations of motion, which is often called *stochastic dynamics* [39, 107]. This is achieved by adding two terms to the original equations, one friction term that damps the dynamics, and a noise term that allows to pump energy to the system. The equations of motion thus become

$$m_i \ddot{\mathbf{r}}_i = \mathbf{f}_i - m_i \gamma_i \mathbf{v}_i + \mathbf{W}_i . \quad (1.16)$$

\mathbf{W}_i is a fluctuating force that acts stochastically on the particles and can transfer some thermal energy to them; it has zero mean ($\langle W_i^\alpha \rangle = 0$ for $i = 1, \dots, N$ and $\alpha = \{x, y, z\}$) and satisfies the following fluctuation-dissipation theorem that links thermal energy and friction so as to keep the temperature at the value T_0 :

$$\langle W_i^\alpha(t) W_i^\beta(t') \rangle = 2m_i \gamma_i k_B T_0 \delta_{ij} \delta_{\alpha\beta} \delta(t - t') . \quad (1.17)$$

The second term on the RHS of eq. (1.16) corresponds to the damping force that takes away energy from the parts of the system that are “too hot”. The friction coefficient γ_i is usually taken with the same value γ for all particles, and is an adjustable parameter to specify whether the thermostat couples strongly or weakly to the particles (this algorithm is implemented in `md_spherical`).

Berendsen thermostat. Following Berendsen [10], one can calculate the rate of change of the temperature when using the Langevin thermostat described above. Using eq. (1.16) integrated over time, we obtain an expression for the velocity

$$\mathbf{v}_i(t + \Delta t) = \mathbf{v}_i(t) + \frac{1}{m_i} \int_t^{t+\Delta t} dt' (\mathbf{f}_i(t') - m_i \gamma_i \mathbf{v}_i(t') + \mathbf{W}_i(t')) \quad (1.18)$$

that is used to express the change in kinetic energy:

$$\frac{dE_k}{dt} = \lim_{\Delta t \rightarrow 0} \left(\frac{E_k(t + \Delta t) - E_k(t)}{\Delta t} \right) . \quad (1.19)$$

Using $\Delta v_i^\alpha = v_i^\alpha(t + \Delta t) - v_i^\alpha(t)$, the previous equation can be written as

$$\frac{dE_k}{dt} = \lim_{\Delta t \rightarrow 0} \left[\frac{1}{2} \sum_{\alpha} \sum_{i=1}^{N_{\text{tot}}} m_i (\Delta v_i^{\alpha 2} + 2v_i^\alpha(t) \Delta v_i^\alpha) / \Delta t \right] , \quad (1.20)$$

which yields, after use of eq. (1.17) (and assuming that $\gamma_i = \gamma$),

$$\frac{dE_k}{dt} = \sum_{\alpha} \sum_{i=1}^{N_{\text{tot}}} v_i^\alpha f_i^\alpha + 2\gamma \left(\frac{3N_{\text{tot}}}{2} k_B T_0 - E_k \right) . \quad (1.21)$$

The second term on the right-hand side would be zero in the case of a microcanonical simulation (conservation of energy), and corresponds to the rate at which energy is transferred from/to the heat bath. Using the equipartition theorem, one arrives at the following relation for temperature change in time (second term in eq. (1.21) RHS):

$$\left. \frac{dT}{dt} \right|_{\text{therm}} = 2\gamma(T_0 - T). \quad (1.22)$$

T is the actual temperature of the system, while T_0 is imposed by the thermostat. The coupling between the two is made with a time constant $\tau_T = \frac{1}{2\gamma}$. One can then propose a modified version of eq. (1.16), accomplishing the same kind of coupling to an external bath without any random force:

$$m_i \ddot{\mathbf{r}}_i = \mathbf{f}_i + m_i \gamma \left(\frac{T_0}{T} - 1 \right) \mathbf{v}_i. \quad (1.23)$$

This corresponds, after resolution of the first-order differential equation for $\mathbf{v}_i = \dot{\mathbf{r}}_i$, to an overall change in the scale of velocities, by a factor λ . Treating the coupling to the heat bath separately, one has [putting aside the influence of interactions that is explicitly taken into account in eq. (1.7)]:

$$v_i^{\alpha'}(t + \delta t) \sim v_i^\alpha(t) e^{\gamma \left(\frac{T_0}{T} - 1 \right) \delta t} \quad (1.24)$$

$$\sim v_i^\alpha(t) \left(1 + \gamma \left(\frac{T_0}{T} - 1 \right) \delta t + \dots \right) \quad (1.25)$$

Thus the mapping $v_i^\alpha(t + \delta t) \mapsto v_i^{\alpha'}(t + \delta t) = \lambda v_i^\alpha(t)$ results in applying the coupling, with

$$\lambda \simeq 1 + \gamma \left(\frac{T_0}{T} - 1 \right) \delta t \quad (1.26)$$

to first order in δt . The latter expression is also equivalent (still to first order in δt) to

$$\lambda = \sqrt{1 + \frac{\delta t}{\tau_T} \left(\frac{T_0}{T} - 1 \right)}, \quad (1.27)$$

which has the advantage to lead to the simple temperature change of $(T_0 - T)\delta t/\tau_T$ per time-step. It is possible to obtain a more precise expression for the time constant τ_T , considering the energy variation associated to the scaling of the velocities [83]:

$$\Delta E = \sum_\alpha \sum_{i=1}^N \left(\frac{1}{2} m_i v_i^{\alpha'2} - \frac{1}{2} m_i v_i^{\alpha2} \right) \quad (1.28)$$

$$= \sum_\alpha \sum_{i=1}^N (\lambda^2 - 1) E_k = \frac{3}{2} N k_B T (\lambda^2 - 1). \quad (1.29)$$

Recalling the definition of the heat capacity

$$C_V = \left(\frac{\partial E}{\partial T} \right)_V \simeq \frac{\Delta E}{\Delta T}, \quad (1.30)$$

one arrives at

$$\lambda = \sqrt{1 + \frac{2C_V}{3Nk_B} \frac{T_0 - T}{T}}, \quad (1.31)$$

which corresponds to $\tau_T = \frac{3Nk_B}{2C_V} \delta t$; however, the value of τ_T does not need to be adjusted with a high accuracy.²

Nosé-Hoover thermostat. Another way of thermostating the system is to use the *Nosé-Hoover* scheme, which derives from a modified Lagrangian formalism that introduces a new degree of freedom governed by its own equation of motion. The equations of motion are then

$$\dot{\mathbf{r}}_i = \frac{\dot{\mathbf{p}}_i}{m_i} \quad (1.32)$$

$$\dot{\mathbf{p}}_i = \mathbf{f}_i - \xi \mathbf{p}_i \quad (1.33)$$

$$\dot{\xi} = \frac{1}{Q} \left[\sum_{i=1}^{N_{\text{tot}}} \frac{(\mathbf{p}_i)^2}{m_i} - 3N_{\text{tot}}k_B T_0 \right]. \quad (1.34)$$

Q is a parameter defining thermal inertia in the system. The difference between this thermostat and the previous one lies in the way the temperature difference $T_0 - T$ is related to the effective friction ξ : In the case of the Berendsen thermostat, the two quantities are simply proportional, while the Nosé-Hoover approach involves a first-order differential equation, meaning that the time-derivative of ξ is determined by the temperature mismatch. Thus the Nosé-Hoover thermostat drives the system temperature more softly than the Berendsen method: If the parameter Q is not chosen carefully, unwanted oscillations may occur [128].

Discussion. The different techniques mentioned above have all been applied successfully to MD simulations in order to prescribe the temperature, and sample configurations at constant NVT . Nevertheless, it has been shown [34, 48] that only the Nosé-Hoover thermostat truly reproduces this particular ensemble in a rigorous manner using one single friction parameter. The other techniques are still useful and even if they are in fact sampling ensembles other than the canonical one, the static properties of fluids simulated this way are not expected to vary. Small changes may occur in the dynamics though, even if a comprehensive study of such effects is still missing. The Nosé-Hoover thermostat also has its specific drawbacks when compared to the other possibilities: The coupling constant between system particles and heat bath has to be chosen arbitrarily but carefully, and does not have a generic value for any system; furthermore, it has been reported that anomalous temperature fluctuations can be observed while at low temperature [47]. The Nosé-Hoover and Berendsen thermostat are applying global temperature scaling as a function of the average kinetic energy in the system,

²This method is used in YASP.

while the Langevin approach is strictly local and allows to relax large heat variations on a local scale very efficiently. The Langevin thermostat ensures great stability since the possible instabilities cannot propagate. This allows to choose a larger time-step, which makes its use more efficient in terms of computational time. On the other hand, the method destroys heat transfer. The Berendsen scheme also allows to get rid of instabilities quite rapidly since the coupling to the heat bath is effective in a relatively strong manner. These two particular techniques have another inconvenience since they violate Galilean invariance [117] which leads to the non-conservation of the overall momentum in the system. In order to circumvent this problem, the momentum has to be reset to zero periodically (round off errors in the numerical integration of the equations of motion could also create such troubles anyway). For more detailed discussion about this topic, see for instance [124].

Constant pressure. Using the same techniques as for the thermostat, one can prescribe the pressure in order to simulate in NPT -constant conditions. In this case, the volume has to fluctuate, allowing the pressure to remain constant. In most molecular simulations, the volume has a particular definition since it cannot approach the dimensions of any real system and is in fact restricted to a small box (typically of the order of 5–20 nanometers in our polymer simulations). In order to limit the influence of finite-size effects, periodic-boundary conditions are applied, meaning that a particle exiting the box on one side will immediately re-enter on the opposite side. This mimics an infinite system to some extent. In the case of constant- NVT simulations, this box size is kept constant, while for constant NPT it varies in time.

In a simulation, pressure can be defined as

$$P = \frac{2}{3V}(E_k - \Xi) \quad \text{with} \quad \Xi = -\frac{1}{2} \sum_{i=1}^N \sum_{\substack{j=1 \\ j < i}}^N \mathbf{r}_{ij} \cdot \mathbf{f}_{ij}; \quad (1.35)$$

$\mathbf{r}_{ij} = \mathbf{r}_i - \mathbf{r}_j$, and \mathbf{f}_{ij} is the force exerted by particle j on i . With the Berendsen method, one defines a time constant τ_P which couples the system to an external piston through

$$\left. \frac{dP}{dt} \right|_{\text{bar}} = \frac{P_0 - P}{\tau_P}, \quad (1.36)$$

where P_0 is the target pressure; to satisfy such a requirement, it is then necessary to impose a new form for the equations of motion, and to modify the volume accordingly:

$$\dot{r}_i^\alpha = v_i^\alpha + \eta r_i^\alpha \quad (1.37)$$

$$\dot{V} = 3\eta V. \quad (1.38)$$

The isothermal compressibility is defined by

$$\beta_T = -\frac{1}{V} \left(\frac{dV}{dP} \right)_T \quad (1.39)$$

and can be used to link η to the coupling constant τ_P [using eqs. (1.36) and (1.38)]:

$$\frac{dP}{dt} = -\frac{1}{\beta_T V} \frac{dV}{dt} \simeq \frac{\Delta P}{\delta t} \quad (1.40)$$

$$\frac{P_0 - P}{\tau_P} = -\frac{1}{\beta_T V} 3\eta V \quad (1.41)$$

$$\Rightarrow \eta = -\frac{\beta_T}{3\tau_P} (P_0 - P) . \quad (1.42)$$

The solution to the differential equation (1.37) for r_i^α can be solved by scaling the positions by a factor

$$\mu = 1 - \frac{\beta_T \delta t}{3\tau_P} (P_0 - P) \quad (1.43)$$

to first order in δt , which is equivalent to

$$\mu = \left(1 - \frac{\beta_T \delta t}{\tau_P} (P_0 - P) \right)^{1/3} \quad (1.44)$$

at the same order. Again, the exact value of β_T needs not be known within great accuracy since it only appears divided by τ_P , and this ratio controls the strength of the coupling to the external piston, which is not critical. This method as it is presented here is valid for an isotropic system; it is possible to extend it to the general case of anisotropic couplings in which the simulation box sizes are allowed to vary independently in each direction. In this case, the pressure tensor is defined by

$$\underline{\underline{\mathbf{P}}} = \frac{1}{V} \left(\sum_i m_i \mathbf{v}_i {}^t \mathbf{v}_i + \sum_{i,j} \mathbf{r}_{ij} {}^t \mathbf{f}_{ij} \right), \quad (1.45)$$

${}^t \mathbf{r}$ being the transpose form of vector \mathbf{r} and $\mathbf{r} {}^t \mathbf{r}$ the tensorial product of the two. The same procedure yields now a scaling tensor

$$\underline{\underline{\boldsymbol{\mu}}} = \underline{\underline{\mathbf{1}}} - \frac{\beta_T \delta t}{3\tau_P} (\underline{\underline{\mathbf{P}}}_0 - \underline{\underline{\mathbf{P}}}) \quad (1.46)$$

which is used to change the particles coordinates via

$$\mathbf{r}_i \mapsto \mathbf{r}'_i = \underline{\underline{\boldsymbol{\mu}}} \mathbf{r}_i, \quad (1.47)$$

as well as the volume:

$$V \mapsto V' = (\det \underline{\underline{\boldsymbol{\mu}}}) V . \quad (1.48)$$

A procedure similar to what led to the Nosé-Hoover implementation of the thermostat can be used to prescribe the pressure, by adding another degree of freedom to the system, and have its evolution governed by a specific equation of motion. Configurations generated this way are known to sample the isothermal-isobaric ensemble satisfactorily, even though in some cases unphysical results have been found [128].

In the simulations we have been using to probe semi-crystalline polymers at different temperatures, either the Berendsen (All-Atom simulations, see sec. 2) or the Langevin thermostat (coarse-grained models, sec. 3) were utilized to control T or impose a steady variation of temperature. In all cases, P was set to the atmospheric pressure and kept constant by means of the Berendsen barostat.

1.1.2 Interaction potentials

The fundamental techniques described above are common to any MD simulation that probes the characteristics of matter at time and length scales comparable to those we address with our polymer melts studies. Perhaps the most important part of the job resides in the way the objects we simulate are actually modeled, i.e. how we define the interactions between the different particles. We will now review the relevant interactions in the case of polymers, and describe how one can translate them into an analytical form.

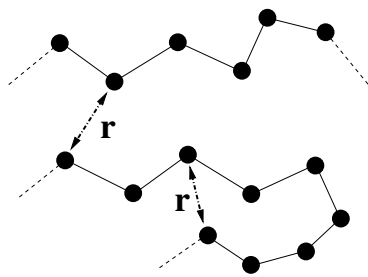
1.1.2.1 Non-bonded potentials

Intermolecular interaction. An important component of any molecular simulation, this interaction originally describes the interaction between two atoms (Argon for instance, which has been the system of choice to study the behavior of liquids in the early days of numerical simulations): Two such particles are impenetrable, which implies a strong repulsive force between them (as a result of quantum state superposition for electrons), and they also attract each other while at larger distances (van der Waals interaction). This results in an overall interaction potential often described in the Lennard-Jones form

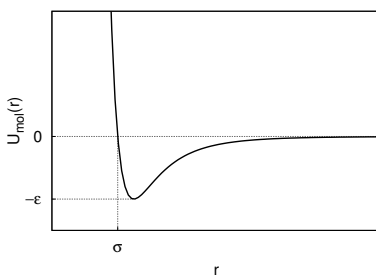
$$U_{\text{mol}}(r) = 4\epsilon^{\text{LJ}} \left(\left(\frac{\sigma^{\text{LJ}}}{r} \right)^{12} - \left(\frac{\sigma^{\text{LJ}}}{r} \right)^6 \right) \quad (1.49)$$

where the r^{-6} is characteristic of the van der Waals attraction, and the r^{-12} part corresponds to a strong repulsion, but has no solid theoretical justification. The parameter σ^{LJ} (van der Waals diameter) and ϵ^{LJ} (attraction energy) are to be adjusted either from experimental data or quantum chemistry calculations, and allows a phenomenological description of the properties of a particular atomic species. Although initially designed to account for interactions between two atoms, such a potential can also be used to model the interaction between groups of atoms, as we shall see later in chapter 3. In this case, softer interaction can be modeled by a lower exponent power law, $\left(\frac{\sigma^{\text{LJ}}}{r} \right)^n$ with $n < 12$. Another form of the repulsive part of the intermolecular potential is also used (Buckingham potential):

$$U_{\text{mol}}(r) = \epsilon^{\text{B}} \left(e^{-\alpha r / \sigma^{\text{B}}} - \left(\frac{\sigma^{\text{B}}}{r} \right)^6 \right). \quad (1.50)$$



(a) Molecular interaction



(b) Lennard-Jones Potential

Figure 1.1: Lennard-Jones potential.

For polymers, it becomes possible that two distinct parts of the same molecules interact as if they actually belonged to different chains. In this case we will describe the interaction as an intermolecular one. The only particularity one has to bear in mind is that one has to define where to suppress the effects of these interactions, since for neighboring particles it does not make sense to consider the attractive and repulsive contributions mentioned above anymore.

The specific interactions (bonds, bond angles, torsions; see below) between particles sitting close to each other inside a molecule are described below. It is thus customary to suppress the intermolecular interactions between particles whose interactions are already explicitly modeled so as to prevent interference.

Electrostatic interaction. For charged or partially charged species in the system, an additional term has to be added to non-bonded interactions; a long-range coulombic potential that is expressed as

$$U_{\text{el}}(r) = \frac{q_i q_j}{4\pi\epsilon r_{ij}} . \quad (1.51)$$

This potential is apparently of the same kind as the previous one, but its long-range character makes it more difficult to implement in a simulation, and requires a specific method (interpolated cutoff, continuum approximation, Ewald summation. . .). Remark: In dense systems, the electrostatic interaction is effectively screened, which justifies the use of a cutoff distance when calculating the forces in the YASP simulation code.

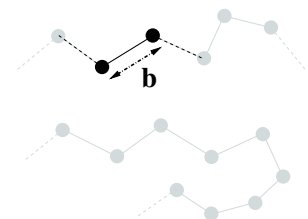
1.1.2.2 Bonded interactions

When dealing with molecules, one needs an appropriate description of the relevant potentials that are keeping the constituent atoms together, and constraining the conformations.

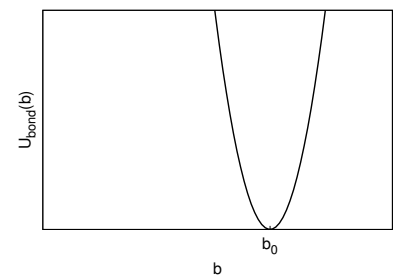
Binding interaction. The covalent bonds in molecules can be modeled by a simple harmonic potential of the form

$$U_{\text{bond}}(b) = \frac{1}{2}k_{\text{bond}}(b - b_0)^2 \quad (1.52)$$

constraining the distance b between two bonded particles to fluctuate around the average value b_0 . This potential is rather stiff, so as to prevent the two neighboring particles to drift apart from each other, and for this reason is associated with the smallest relaxation time in the system (corresponding to a high vibration frequency). This relaxation time, together with the type of algorithm chosen to integrate the equations of motion condition the choice for the time-step in the simulation main loop (the choice of the integrator is less important though).



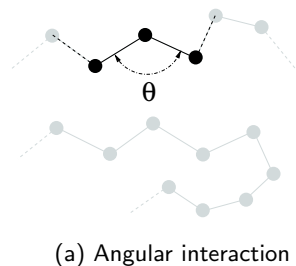
(a) Binding interaction



(b) Harmonic potential

Figure 1.2: Binding potential.

Moreover, this vibrational degree of freedom associated with bonds is mostly irrelevant when attempting to describe the overall chain behavior: The binding potential is so stiff that the bond length distribution is only influenced by this potential (and the temperature), and does not provide any interesting information on the system. That is the reason why several schemes allow to treat the bond vibrations in a different fashion, so as not to spend too much computer time on the evaluation of all the other interactions that do not significantly change on such small time scales. Among these, a constraint algorithm permits to adjust constrained bond lengths at each time-step, thus avoiding the explicit treatment of the bonds with the other interactions. The SHAKE algorithm achieves to constrain bond lengths³ with the following scheme: After each time-step without any binding interaction taken into account, an iterative method allows to progressively satisfy the different constraints in the molecules. The two particles involved in a constrained bond are moved by a certain amount (proportional to their respective masses) in a direction (given by the vector that links the two particles after the last completed time-step) in order to have them separated by the adequate distance. As one atom might be involved in two or more constraints, one needs to apply the procedure iteratively until all the constraints are satisfied within a given tolerance [82, 83, 102].



Bond angle interaction. The angle formed by two consecutive bonds along the backbone of a chain molecule have to be restricted to fluctuate around an average value (given by the arrangement in space of covalent bonds as predicted by quantum chemistry); this can again be modeled by a harmonic potential as in the case of bonds or by a more sophisticated form if the bond angle considered is not a simple C-C-C bond angle and possesses more than one stable or metastable state (see chapter 3 treating of coarse-grained models having a specific angular structure).

$$U_{\text{ang}}(\theta) = \frac{1}{2}k_{\text{ang}}(\theta - \theta_0)^2 \quad (1.53)$$

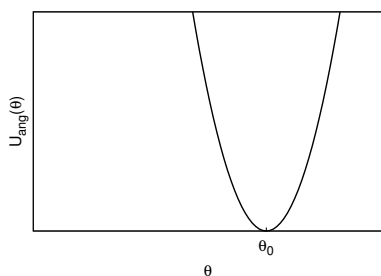


Figure 1.3: Angular potential.

Torsional interaction. The torsion angle defined between two consecutive dihedrals is constrained by a four-particle interaction; it is energetically more favorable for two parts of the same molecule to stay as far as possible from each other. The *trans* conformation is preferred ($\phi = \pi$) over the *cis* one ($\phi = 0$) in which the two parts (part 1 and part 2 in fig. 1.4(a)) overlap. In between these two states, there is usually (depending on the geometry/the chemical structure of the molecule) a

³It is also possible, though less justified and/or interesting, to constrain other degrees of freedom as bond angles and torsion angles.

metastable state named the *gauche* state ($\phi \simeq \pm\frac{\pi}{3}$). This particular degree of freedom is particularly important to describe the behavior of polymers since, for instance, the torsional potential is responsible for the flexibility of the chains (which strongly affects their propensity to crystallize). In order to reproduce the three-state structure of the torsional potential described above, one can use the following form:

$$U_{\text{tors}}(\phi) = \sum_{n=1}^3 \left(\frac{1}{2} k_n^{\text{tors}} (1 - \cos(n\phi - \phi_n^0)) \right). \quad (1.54)$$

The parameters k_n^{tors} and ϕ_n^0 prescribe the heights and positions of the barriers between the favorable states; $n = 1, 2, 3$ allows to reproduce the symmetry of the potential described above (i.e. with three stable/metastable states).

It should be mentioned that even in the case of many-body interactions such as bond angle (involving three particles) and torsional angle (four particles), it is possible to decompose the effects of an interaction so that forces between pairs of particles only are considered, which allows to describe the system as presented in eq. (1.3).

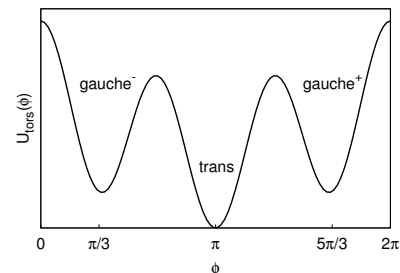
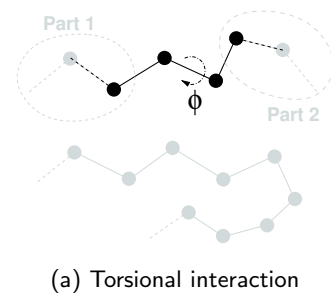


Figure 1.4: Torsional potential.

1.2 Simulation methodology

We described so far the core of MD simulations; we shall now describe some more technical aspects of running simulations.

1.2.1 Setup of initial configurations

The MD scheme takes care of the time evolution of the model used to study a particular system. Still, the first configuration (meaning positions and velocities for all particles) has to be defined.

If one is interested in the crystal structure of a system, the construction of the initial configuration has to take into account the specificity of the experimentally observed crystal parameters, or to be inspired by features determined via a theoretical approach. This has been done for crystals of *n*-alkanes, starting from crystallographic data (sec. 2.3).

If one is interested in the high-temperature liquid state, there are mainly two possibilities to create start configurations. Either the starting point is a regular crystal-like arrangement of the molecules, simply generated by hand, or it already mimics an equilibrium configuration as one expects to observe it later in the course of the simulation. The ordered starting configuration does not have to reproduce accurately any existing crystalline structure, and one only has to prepare an artificial configuration with particles sitting on the knots of a perfect lattice, and to let the MD algorithm “melt” the system till it actually is in a realistic liquid state at high temperature. This procedure is the easiest way to start a simulation involving small molecules, as they would rapidly relax to an equilibrium state. This is not true for long polymer chains; in this case, it is much more appropriate to try to provide a

starting configuration that closely resembles an equilibrated, disordered system. This can be achieved using a Monte-Carlo algorithm that will efficiently decorrelate an artificial configuration so as to let it acquire equilibrium properties. For instance in our coarse-grained simulation program, an algorithm prepares a random-walk-like configuration for each chain, with bond lengths and bond angles distributed according to distributions determined by the potentials constraining them. Then the chains' centers of mass are moved using a Monte-Carlo method to optimize the monomer density [7]. Up to this point, the chains are treated as perfect, meaning that no excluded volume is taken into account. The simulation is then started with an intermolecular potential that is multiplied by a factor increasing steadily in time, from 0 to 1, in order to allow the overlaps of different particles to relax. The initial velocities are picked up at random from a Maxwell-Boltzmann distribution, in order to reproduce the temperature average value and fluctuations as expected in the NVT ensemble.

1.2.2 Equilibration run

Once the initial configuration is created, the system has to relax so that it really is in equilibrium. Our simulations were started under constant temperature and constant volume conditions, and then equilibrated under constant pressure at the same high temperature. When the system has reached equilibrium, the static quantities that one can measure (such as the overall energy, the volume...) fluctuate around their average values. For short chains, this equilibrium situation is obtained after few simulated time-steps. For long polymer chains however, the energy being constant does not necessarily mean that the system is at equilibrium: In this case, one also has to check that the chain's conformation is equilibrated. This is achieved when the end-to-end vector (the vector joining the two ends of a chain, see sec. 1.3) orientation is decorrelated. This can take a very long time when the molar mass increases, and therefore makes it important to use a specific method to generate already-equilibrated configurations.

1.2.3 Production run

The equilibrated polymer melt can be simulated over a longer time at constant temperature and pressure in order to determine its properties with appropriate statistics. This allows to characterize a particular model, and to compare different models. In chap. 2 we compare an all-atom model for n -alkanes to results obtained experimentally, and chap. 3 a study of different coarse-grained models is presented.

The simulation reproduces the time evolution of a system, meaning that the actual positions and velocities of all particles are computed and therefore known at each time-step. However, it is neither convenient nor necessary to store all these data: In practice configurations

are stored in a file at regular time intervals, corresponding to 50τ for coarse-grained simulations, and 2 ps for atomistic simulations. For both kinds of simulation the same file structure was used: a “trajectory” file contains for each saved time-step the list of coordinates and velocity components for all particles. In order to save disk space, these quantities are stored as single-precision real numbers (since a greater accuracy is not needed) and in an unformatted manner, i.e. as a sequence of numbers in their binary representation. A particular formatting operation has to be applied to the data in order to recover the information contained in these files, which has to be done anytime a physical quantity is to be computed. The procedure used to store these trajectory files was defined in the YASP package [82], and is also used in the framework of the `md_spherical` program.

1.2.4 Cooling

Using the algorithms described above to run a simulation with prescribed temperature and pressure, it also becomes possible to simulate the evolution of a system under varying conditions to reproduce the experimental conditions. In this work, we are mainly interested in crystal formation in the melt, induced by a temperature change. This situation is investigated by changing the temperature gradually, or by a rapid quench.

One way of studying the growth of a crystal is to force the temperature to drop continuously at a slow rate and observe the formation of the semi-crystalline structure, using thus an out of equilibrium simulation method (a protocol is sketched in fig. 1.5). The cooling rate used in that case can be taken very low but is still huge compared to what could be imposed for a real experiment, due to computer time limitation. This cooling rate might strongly affect the simulation, if taken too large (see fig. 3.20 in section 3.3.1 for an example).

Another possibility to reproduce a crystalline behavior is to quench the system to a low temperature. This can be done in a simulation by changing discontinuously the value of the target temperature as it is prescribed by the thermostat; the system will then relax to its new equilibrium state at lower temperature. Still it is safer not to use this method which could induce unexpected behavior as a result of the abrupt change in the thermostatting algorithm; it is better to apply a very rapid continuous cooling instead (fig. 1.6). The procedure is followed by an isothermal relaxation simulation during which a crystal can grow under constant NPT conditions.

1.2.5 Melting

A melting run is nothing but the inverse process of a cooling simulation. However, melting is often not simply the reverse of the crystallization phenomenon, as pointed out by the existence of a hysteresis of the

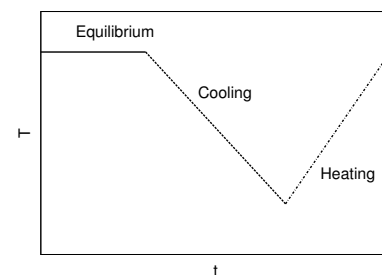


Figure 1.5: Time–temperature protocol for continuous cooling and heating.

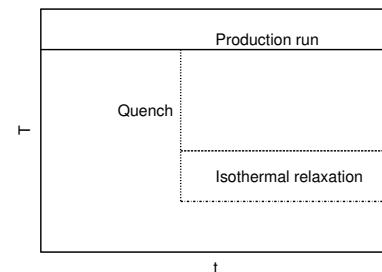


Figure 1.6: Time–temperature protocol for a quench.

transition between the crystallization and the fusion phenomena that does not vanish when decreasing the cooling/heating rates (fig. 3.20). Nevertheless, the melting temperature T_{melt} depends on the heating rate and one wishes to know the limit of slow heating. Once a crystal is formed in the melt, it is also an interesting experiment to reverse the process and increase the temperature again. One can then observe the melting of the low-temperature phase, leading in some cases to the occurrence of transitory phases, as in the case of alkane chains (sec. 2.3).

The procedure used for cooling and heating simulations mimics DSC (Differential Scanning Calorimetry) experiments in which a sample's thermal properties are compared to a reference. This provides a measurement of the specific heat of a particular system, which when plotted against temperature exhibits peaks corresponding to phase transitions. We used a definition for crystallization and melting temperatures a definition in analogy with the experimental data (see fig. 1.7 in sec. 1.3).

1.3 Definition of observables

In order to study polymer melts quantitatively, we have to define the relevant quantities we need to monitor the simulations and to extract the information we are interested in. Some of those quantities are generic thermodynamic variables, and others are polymer-specific. In order to account for these specificities, it is necessary to make a distinction between the different chains and the position of a given particle on one of these chains. We therefore introduce the following notations at this point, that apply directly to the coarse-grained simulations discussed in chapters 3 and 4, where chains consist of identical particles or monomers; they can be generalized to the analysis of the more detailed simulations of alkanes presented in chapter 2, in the case of which the carbon atoms of the backbone are taken as the centers of effective monomers whose conformations are analyzed accordingly. We thus consider a set of n chains of N particles each, whose positions are denoted by

$$\mathbf{r}_i^a, \quad (a = 1, \dots, N; \quad i = 1, \dots, n) \quad (1.55)$$

meaning that the different chains are indexed by i, j, \dots and the particles by a, b, \dots . The velocity of particle a of chain i is then

$$\mathbf{v}_i^a = \dot{\mathbf{r}}_i^a, \quad (1.56)$$

and its mass is m_i^a . The total number of particles in the system is

$$N_{\text{tot}} = n \times N. \quad (1.57)$$

It is also useful to define the bond vector that connect two consecutive particles along the chain (or along the backbone of the chain in case we are dealing with detailed models):

$$\mathbf{b}_i^a = \mathbf{r}_i^{a+1} - \mathbf{r}_i^a. \quad (1.58)$$

The definitions of general quantities given here will be completed later by more specialized order parameters that are introduced where they are discussed.

Energy. Among the first things one has to measure in a simulation, the energy has to be defined. The total energy E , as any other property, is computed from the positions and velocities of the particles at a given time. This global energy can be split up into several parts: The kinetic energy is given by

$$E_k = \frac{1}{2} \sum_{i=1}^n \sum_{a=1}^N m_i^a (\mathbf{v}_i^a)^2. \quad (1.59)$$

As already mentioned, $T = 2E_k/(3N_{\text{tot}}k_B)$. The potential energy is calculated from the coordinates of the particles in the current configuration, using the expressions given for the different interaction potentials of the model. This energy is usually divided into an *intra* and an *inter*-chain contribution. E_{inter} only consists in the intermolecular energy depending on the potential $U_{\text{mol}}(r)$,

$$E_{\text{inter}} = \frac{1}{2} \sum_{\substack{i,j=1 \\ i \neq j}}^n \sum_{a,b=1}^N U_{\text{mol}}(|\mathbf{r}_i^a - \mathbf{r}_j^b|) \quad (1.60)$$

where i and j can be any two different of the n chains, all of them containing N particles. A molecular contribution also exists in E_{intra} , taking into account the occasional overlap between particles of the same chain. The other contributions result from the other potentials that are applied, i.e. $E_{\text{intra}}^{\text{bond}}$, $E_{\text{intra}}^{\text{ang}}$ and $E_{\text{intra}}^{\text{tors}}$. For example, $E_{\text{intra}}^{\text{bond}}$ is computed as

$$E_{\text{intra}}^{\text{bond}} = \sum_{i=1}^n \sum_{\langle a,b \rangle} U_{\text{bond}}(|\mathbf{r}_i^a - \mathbf{r}_i^b|) \quad (1.61)$$

where $\langle a, b \rangle$ means all pairs of nearest neighbor particles in one molecule.

Temperature of transition. Crystallization is a first-order phase transition, which gives rise to discontinuities in first order derivatives of the relevant thermodynamic potentials, such as the volume in this case. This allows to measure a crystallization temperature that will be used to compare several models simulated under the exact same conditions. Still, this temperature is strongly rate-dependent, and does not correspond to the thermodynamic equilibrium T_{cryst} . From a phase diagram as shown on fig. 1.7 there are several ways of defining a crystallization temperature: One could, for instance, use the abrupt slope change that occurs when the volume starts to drop. We found it more accurate to define the crystallization temperature as the point at which the derivative of the volume $\frac{\partial V}{\partial T}$ is maximum. This definition yields an easily reproducible means of computing T_{cryst} as well as the melting temperature T_{melt} .

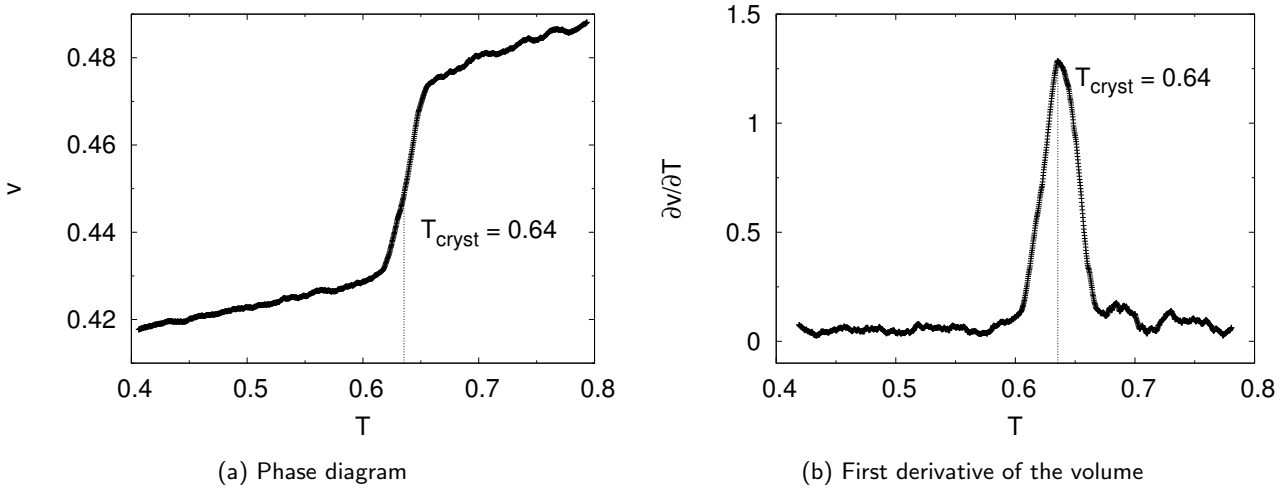


Figure 1.7: Determination of the crystallization temperature (CG-PVA model, chain length $N = 10$).

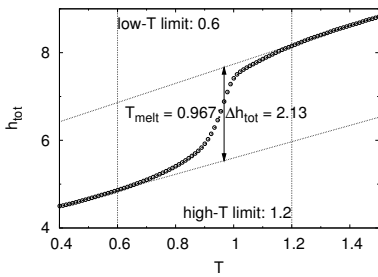


Figure 1.8: Enthalpy variation during melting (x4 model, chain length $N = 100$).

This definition is convenient in the case of our simulations and corresponds to the determination of transition temperatures as measured by DSC experiments. However, this might not be the most appropriate method to characterize a crystallization/fusion process; in sec. 2.3 for instance, as the melting of n -alkanes was found to be a more complicated process than the “simple” fusion observed with coarse-grained models (sec. 3.3.6), other definitions will be introduced.

Latent heat. At some places we are interested in the jump in volume or any other discontinuous quantity during the transition. We adopted a method which relies on linear fits for the two branches that precede and follow the phase transition, and computed the difference between these linearly extrapolated behaviors at the transition, as defined above. Figure 1.8 shows an example of determination of the variation of the total enthalpy per monomer $h_{\text{inter}} + h_{\text{intra}}$ during the melting transition, for a model of polymers with chain length $N = 100$.

Persistence length. Some other quantities we often need to refer to are more polymer-specific: The persistence length l_p is defined by

$$l_p = \frac{1}{b_0} \sum_{k=0}^{\infty} \langle \mathbf{b}^a \cdot \mathbf{b}^{a+k} \rangle_a \quad (1.62)$$

for an infinite chain [100]; b_0 is the average length of one bond, and this quantity is averaged over all sites a on the chain. The persistence length contains information about the “memory” of orientation along the chain. In the simulations, the persistence length is usually measured by using an exponential fit of the bond orientation correlation function (note that this analysis is only justified in the melt for not too large k [133]):

$$P_1(k) = \frac{1}{b_0^2} \langle \mathbf{b}^a \cdot \mathbf{b}^{a+k} \rangle_a \simeq e^{-kb_0/l_p}. \quad (1.63)$$

Note that this exponential approximation is only valid at high T . In the crystal, $P_1(k)$ may develop oscillations which can be used to determine the stem length: Once the chains fold, anticorrelations occur that correspond to two bonds lying antiparallel to each other in hairpins. The measurement of the first minimum of $P_1(k)$ gives an average value for the distance between such hairpins, hence yielding an estimate of the length of the lamellar stems (see secs. 3.3.4 and 3.3.1).

End-to-end distance. In order to characterize the size of one chain, one can use the end-to-end vector R_e that is defined by

$$R_e^2 = \langle \mathbf{R}_e^2 \rangle = \left\langle \left(\sum_{a=1}^{N-1} \mathbf{b}_i^a \right)^2 \right\rangle_i = \sum_{a,b=1}^{N-1} \langle \mathbf{b}_i^a \cdot \mathbf{b}_i^b \rangle_i, \quad (1.64)$$

where $\langle \dots \rangle_i$ denotes an average over all chains i ($= 1, \dots, n$) [22, 100].

Radius of gyration. The radius of gyration R_g is also frequently used:

$$R_g^2 = \frac{1}{N} \sum_{a=1}^N \langle (\mathbf{r}_i^a - \mathbf{R}_i)^2 \rangle_i = \frac{1}{2N^2} \sum_{a,b=1}^N \langle (\mathbf{r}_i^a - \mathbf{r}_i^b)^2 \rangle_i. \quad (1.65)$$

$\mathbf{R}_i = \frac{1}{N} \sum_{a=1}^N \mathbf{r}_i^a$ refers to the position of the center of mass of chain i . For an ideal chain, one expects the following property:

$$R_g^2 = \frac{1}{6} R_e^2 = \frac{1}{6} N \ell^2 \quad (1.66)$$

which defines the statistical segment ℓ .

Oriental order parameter. The crystalline system can be characterized by using the P_2 order parameter for bond vectors. This quantity corresponds to the second Legendre polynomial of a variable, here the scalar product of two vectors.⁴ Taking the sum over all pairs of bond vectors, we get a measure of the degree of orientation correlation in the system:

$$P_2 = \frac{1}{2} \sum_{i,j=1}^n \sum_{a,b=1}^N \left(\frac{3}{2} \langle \mathbf{b}_i^a \cdot \mathbf{b}_j^b \rangle - \frac{1}{2} \right), \quad (1.67)$$

where \mathbf{b}_i^a corresponds to the a th bond of chain i . This quantity can also be divided into intra- and inter-chain contributions.

Relaxation time. The time correlation of the end-to-end vector indicates how long it takes to decorrelate the conformation of one chain.

⁴Note that this order parameter is not equivalent to the one defined for liquid crystalline materials which involves a director.

This is measured practically as the time t_{ocfee} needed for the correlation function

$$\text{OCF}_{\text{ee}}(t) = \left\langle \frac{\mathbf{R}_e(t) \cdot \mathbf{R}_e(0)}{R_e(t)R_e(0)} \right\rangle \quad (1.68)$$

to reach a given value, for instance $1/e$:

$$\text{OCF}_{\text{ee}}(t_{\text{ocfee}}) = \frac{1}{e} . \quad (1.69)$$

Mean-square displacements. The dynamics of particles in a condensed system can be characterized by the square distance over which one of these particles has traveled after time t . This quantity averaged over all monomers of a polymer melt shows several characteristic regimes and allows, at large times, to measure the diffusion coefficient D . g_0 corresponds to the mean-square displacement of one monomer a :

$$g_0(t) = \frac{1}{N} \sum_{a=1}^N \langle (\mathbf{r}_i^a(t) - \mathbf{r}_i^a(0))^2 \rangle_i , \quad (1.70)$$

and g_3 refers to the center of mass of the chains:

$$g_3(t) = \langle (\mathbf{R}_i(t) - \mathbf{R}_i(0))^2 \rangle_i ; \quad (1.71)$$

$\mathbf{R}_i(t)$ is the position of the center of mass of chain i at time t .

Structural characteristics. The structure of a liquid or crystal is usually characterized by means of radial distribution functions or structure factors. The radial distribution (or pair distribution) function measures the probability to find a particle at a distance r of another [40]:

$$g(r) = \frac{V}{N_{\text{tot}}(N_{\text{tot}} - 1)} \left\langle \sum_{a=1}^{N_{\text{tot}}} \sum_{b \neq a}^{N_{\text{tot}}} \delta(\mathbf{r} - \mathbf{r}_{ij}^{ab}) \right\rangle_{i,j} \quad (1.72)$$

$$\stackrel{N_{\text{tot}} \gg 1}{\approx} \frac{1}{\rho N_{\text{tot}}} \left\langle \sum_{a=1}^{N_{\text{tot}}} \sum_{b \neq a}^{N_{\text{tot}}} \delta(\mathbf{r} - \mathbf{r}_{ij}^{ab}) \right\rangle_{i,j} , \quad (1.73)$$

with $\mathbf{r}_{ij}^{ab} = \mathbf{r}_j^b - \mathbf{r}_i^a$, $\rho = N_{\text{tot}}/V$, and $N_{\text{tot}} = nN$.

The structure factor S is defined by the following density-fluctuation correlation:

$$S(\mathbf{q}) = \frac{1}{N_{\text{tot}}} \langle \rho_{\text{tot}}(\mathbf{q})^* \rho_{\text{tot}}(\mathbf{q}) \rangle , \quad (1.74)$$

where the density fluctuations are expressed as

$$\rho_{\text{tot}}(\mathbf{q}) = \sum_i i = 1^n \sum_{a=1}^{N_{\text{tot}}} \exp(i\mathbf{q} \cdot \mathbf{r}_i^a) . \quad (1.75)$$

For an isotropic and spatially homogeneous system, $S(\mathbf{q})$ reduces to $S(q)$ [40]. There is a relation between the structure factor $S(q)$ and the

radial distribution function $g(r)$ defined above:

$$S(q) = \frac{1}{N_{\text{tot}}} \left\langle \sum_{a=1}^{N_{\text{tot}}} \sum_{b=1}^{N_{\text{tot}}} \exp \left[-i\mathbf{q} \cdot (\mathbf{r}_i^a - \mathbf{r}_j^b) \right] \right\rangle_{i,j} \quad (1.76)$$

$$= 1 + \frac{1}{N_{\text{tot}}} \left\langle \sum_{a=1}^{N_{\text{tot}}} \sum_{b \neq a}^{N_{\text{tot}}} \exp \left[-i\mathbf{q} \cdot \mathbf{r}_{ij}^{ab} \right] \right\rangle_{i,j} \quad (1.77)$$

$$= 1 + \rho \int d\mathbf{r} \exp \left[-i\mathbf{q} \cdot \mathbf{r} \right] \frac{1}{\rho N_{\text{tot}}} \left\langle \sum_{a=1}^{N_{\text{tot}}} \sum_{b \neq a}^{N_{\text{tot}}} \delta(\mathbf{r} - \mathbf{r}_{ij}^{ab}) \right\rangle_{i,j} \quad (1.78)$$

$$= 1 + \rho \int d\mathbf{r} \exp \left[-i\mathbf{q} \cdot \mathbf{r} \right] g(r) , \quad (1.79)$$

where the last expression includes the Fourier transform of $g(r)$ (definition from eq. (1.73) has been used). It is also possible, and more common, to relate $S(q)$ to $h(r)$ instead of $g(r)$; $h(r)$ is defined by

$$h(r) = g(r) - 1 , \quad (1.80)$$

and introducing its Fourier transform $h(q)$ into eq. (1.79), one obtains

$$S(q) = 1 + \rho h(q) + (2\pi)^3 \rho \delta(q) . \quad (1.81)$$

The last term is usually dropped as it corresponds to the peak corresponding to forward scattering in experiments, and therefore is not relevant.

Chapter 4 deals with the structure of polymer melts at high temperature, and more detailed quantities are defined and discussed then.

2 Atomistic simulations

2.1 Introduction

Polyethylene is the polymer with the simplest structure, and it exists in a crystalline state at low temperature. This makes it a system of choice to investigate crystallization phenomena experimentally as well as numerically (but not a model for any polymer...). Numerous models have been developed to reproduce the behavior of polyethylene in the bulk at high temperature by computer simulations [94, 140]; therefore it is tempting to use these models to address the question of polymer crystallization from the melt, and of whether they yield the characteristic orthorhombic structure experimentally observed. Nevertheless, the study of low-temperature phases of polymers requires huge amount of computer time, and is not tractable for realistic chain lengths with realistic models. To overcome this limitation of detailed numerical simulations, it is possible to consider n -alkanes instead of polyethylene chains: shorter chains can be expected to behave in the same way as high molecular weight polyethylene, insofar as their packing in a crystal structure must also be determined to a large extent by an optimization of the interactions between the different atomic species, which are of the same kind in both cases.

2.1.1 Experimental facts about n -alkanes

n -alkanes are also called “paraffins”; n stands for *normal*, meaning fully linear chains without branches, and the associated chemical formula is C_nH_{2n+2} . As short n -alkane chains (with $n \lesssim 40$) are still accessible to detailed simulations, it is possible to get insight into the properties of polyethylene crystals through their study; moreover they constitute a very interesting system *per se*, since experiments have shown a great wealth of behaviors for the different n -alkanes. Several crystal morphologies exist, depending on the value of n :

- For n odd, the crystals are found to be orthorhombic [81] and in this respect n -alkanes admit polyethylene as a limit for $n \rightarrow \infty$.
- For n even, the situation is slightly more complicated as the primary crystalline structure is not orthorhombic for short chains, and depends on n . For $n \leq 26$, even- n alkanes crystallize in the

Contents

2.1	Introduction	31
2.1.1	Experimental facts about n -alkanes	31
2.1.2	Review of simulation studies for n -alkanes	32
2.2	All-atom simulation model	34
2.2.1	Force field	34
2.2.2	Model characterization	40
2.2.3	Discussion	44
2.3	Melting of n -alkane crystals	45
2.3.1	Creation of perfect structures	46
2.3.2	Melting experiment	49
2.4	Simulation of crystallization	58
2.4.1	Cooling experiment	58
2.4.2	Isothermal relaxation	62
2.4.3	Discussion	65
2.5	Simulations of polypropylene	66
2.5.1	Introduction	66
2.5.2	Definition of the model	68
2.5.3	Simulation details	68
2.5.4	Preliminary results and outlook	69
2.6	Summary	72

triclinic form [41, 91]; for $28 \leq n \lesssim 40$ they form monoclinic phases, and for larger n an orthorhombic crystal is observed. It should also be noted that several variants of the crystalline forms have been characterized, according to n and/or the experimental conditions [24].

This odd-even effect comes from the symmetry of the chains that differ in the case of even- or odd- n ; there is an influence of this symmetry at the interlayer region and this is reflected in the overall crystal structure. The orthorhombic phase was discovered in 1925 by Müller [81], and well characterized later [78–80, 114]. The change in structure for even- n alkanes at $n = 26$ has been explained by the competition between intra- and interlayer energy minimization: At large n the intra-layer energy is dominant, which favors the monoclinic phase [76]. At $n = 26$, the two energies are comparable, and both the triclinic and the monoclinic crystals are found, while for shorter chains the triclinic form prevails. A transient phase between the crystal and the liquid was also discovered by Müller, and observed for all the different crystalline structures; this phase is characterized by hexagonal symmetry, and has been called “rotator” because of the rotational degree of freedom recovered by the chains over the lower temperature phases (chains are free to rotate around their main axis). This description of the different phases accessible to n -alkanes could be greatly extended by considering all the possible sub-phases that have also been discovered [20, 25, 26, 56, 67, 115, 116, 127]. The importance of the rotator phase on the formation of the crystal has been investigated by Sirota et al. [43, 112, 113]. For reviews, see refs. 89 and 24.

2.1.2 Review of simulation studies for n -alkanes

Many numerical studies have been focusing on n -alkanes either to investigate the properties of the liquid [77] or of the crystalline solid: Several groups have studied nucleation in the melt, always with united-atom models and very short chains ($n \leq 20$). Esselink et al. [31] simulated the crystallization process of short chains ($5 \leq n \leq 12$) by continuous (rapid) cooling and found crystalline structures with hexagonal symmetry. They calculated growth rates, which is questionable for such small systems; moreover the conditions under which the crystals are formed are not completely clear because of the very weak coupling to the heat bath that was used. Rigby and Roe [98, 99] observed a glass-transition-like behavior of n -alkanes with $n \leq 50$; then they measured orientational correlations and radial distribution functions in their $C_{10}H_{22}$ and $C_{20}H_{42}$ systems to predict a crystallization temperature by extrapolation, and subsequently found an ordered phase after quenching to this temperature. Fujiwara and Sato also simulated $C_{20}H_{42}$ which crystallizes after a quench to $T = 400$ K (which is rather high, probably due to an exaggerated stiffness of the torsional potential); they monitored the size of the forming cluster and show evidence for a step-by-step

growth of the crystal [35]. Crystallization of $C_{16}H_{34}$ induced by walls has been investigated by Rutledge et al.; they measured the growth rate and interpreted the results by comparing to an empirical equation derived from Avrami's analysis [131]. All these simulations only can reproduce hexagonally symmetric structures, which is not experimentally relevant for n -alkanes with such a small chain length; however, the united-atom models cannot give rise to other kinds of structures, since they lack the appropriate symmetry-breaking elements.

The crystalline phases of n -alkanes have also been studied by different groups using all-atom models. A pioneering work by Ryckaert et al. addresses the comparison of the orthorhombic and rotator phases of $C_{23}H_{48}$ [104]. The solid was simulated at constant volume, below and above the transition temperature which separates the two solid phases. The transition itself is not investigated; the conclusion points out the importance of the interactions between hydrogen atoms and thus on the choice of an all-atom model so that the interfaces between the layers remain stable [104]. The same group had previously focused on the dynamics of the chains when leaving the orthorhombic phase; simulating infinite chains at constant pressure, they could study the diffusion of the chains along the c -axis (the direction of elongation of the chains) and the rotational behavior in the a - b plane (perpendicular to the c -direction). However, a clear transition to the hexagonal rotator phase could not be reported [103]. Mavrantza et al. studied $C_{23}H_{48}$ and infinite polyethylene chains in the orthorhombic phase below the transition temperature, and described the appearance of *gauche* defects in the crystal [71]. The infrared vibrational spectrum of PE is compared with exs. Frenkel and coworkers have studied the melting transition of n -octane [96] and PE [18]. Complete phase diagrams are calculated via thermodynamic integration for C_8H_{18} and $C_{198}H_{398}$: Free energies are computed for both the liquid and solid systems, and extrapolated to deduce the melting points; but this method does not provide any information on the kinetics of the transition which we are interested in.

The properties of crystalline polyethylene have been extensively studied by Martoňák et al., either by Monte-Carlo and Path Integral Monte-Carlo simulations. Using detailed interactions to precisely account for the crystalline arrangement of the chains, properties like the lattice parameters, thermal expansion and elastic coefficients were determined [68, 69]. The different simulation techniques are compared in [101].

Differences in mechanical properties between even- n and odd- n alkane crystals are discussed in [72, 90], where the effect of external stress on perfect crystalline structures (infinite PE and n -alkanes) is investigated. These works are based on a more complex force field which takes into account cross-terms (bond-angle and angle-angle terms), developed for the computation of the properties of polyethylene crystals [52].

We were interested in using a detailed MD simulation technique to investigate the transition between the liquid and crystalline state of

n-alkanes, inasmuch as these systems correspond to an approximation of polyethylene chains and therefore are easier to simulate. The objective was not to develop the most accurate force field for this kind of molecules, as this deserves an entire study—and has already been addressed often—but rather to check whether a reasonable model could account for at least part of the experimentally determined (and very rich) behavior of such systems.

2.2 All-atom simulation model

2.2.1 Force field

2.2.1.1 OPLS-AA

We used the OPLS-AA force field [51] as a starting point for our atomistic simulations. This force field was developed on the basis of preexisting force fields in order to simulate organic compounds accurately. The set of parameters for OPLS (Optimized Potentials for Liquid Simulations) was obtained partly from AMBER (Assisted Model Building with Energy Refinement [95]) and CHARMM/22 (Chemistry at Harvard Macromolecular Mechanics [12]) parameters for bond stretching and angle bending interactions, and developed using ab initio molecular orbital calculations for torsions and Monte Carlo simulations giving thermodynamic and structural properties for non-bonded interactions.

We give now a summary of the parameters of OPLS-AA for carbon and hydrogen atoms only as we are interested in alkyl chains. The model used for each interaction is recalled, and the corresponding parameters are tabulated.

$a - b$	b_0^{ab}	k_{bond}^{ab}
C – C	0.109	22404.8
C – H	0.153	28424

Binding interaction (b_0^{ab} in nm, k_{bond} in kJ/nm²):

$$U_{\text{bond}}(b_{ab}) = \frac{1}{2} k_{\text{bond}}^{ab} (b_{ab} - b_0^{ab})^2. \quad (2.1)$$

$a - b - c$	θ_0^{abc}	k_{ang}^{abc}
C – C – C	112	334.4
H – C – C	109.5	292.6
H – C – H	107	292.6

Bond angle interaction (θ_0^{abc} in deg, k_{ang}^{abc} in kJ/deg²):

$$U_{\text{ang}}(\theta_{abc}) = \frac{1}{2} k_{\text{ang}}^{abc} (\theta_{abc} - \theta_0^{abc})^2. \quad (2.2)$$

Torsional angle interaction ($^{abcd}\phi_n^0$ in deg, $^{abcd}k_n^{\text{tors}}$ in kJ; in our convention, $\phi = 180^\circ$ corresponds to the *trans* state):

$$U_{\text{tors}}(\phi_{abcd}) = \sum_{n=1}^3 \left(\frac{1}{2} {}^{abcd}k_n^{\text{tors}} (1 - \cos(n\phi_{abcd} - {}^{abcd}\phi_n^0)) \right). \quad (2.3)$$

$a - b - c - d$	$^{abcd}\phi_1^0$	$^{abcd}\phi_2^0$	$^{abcd}\phi_3^0$	$^{abcd}k_1^{\text{tors}}$	$^{abcd}k_2^{\text{tors}}$	$^{abcd}k_3^{\text{tors}}$
C – C – C – C	180	0	180	7.273	6.617	1.166
H – C – C – C	180	0	180	0	0	1.530
H – C – C – H	180	0	180	0	0	1.329

Molecular interaction (σ_{ab} in nm and ε_{ab} in kJ):

$$U_{\text{mol}}(r_{ab}) = 4\varepsilon_{ab} \left(\left(\frac{\sigma_{ab}}{r_{ab}} \right)^{12} - \left(\frac{\sigma_{ab}}{r_{ab}} \right)^6 \right). \quad (2.4)$$

The Lennard-Jones parameters $\sigma^{\text{LJ}} = \sigma_{ab}$ and $\varepsilon^{\text{LJ}} = \varepsilon_{ab}$ are the same for all carbon atoms, whether they belong to a CH_3 , CH_2 or CH group. For an interaction between particles a and b of different kinds, the arithmetic average is used to find the appropriate value of σ^{LJ} , whereas a geometric average is used for ε^{LJ} , according to the Lorentz-Berthelot rules

$$\sigma_{ab} = \frac{\sigma_{aa} + \sigma_{bb}}{2}; \quad \varepsilon_{ab} = \sqrt{\varepsilon_{aa}\varepsilon_{bb}}. \quad (2.5)$$

Electrostatic interaction (q_a indicates the partial charge carried by particle a , as a fraction of the fundamental charge of an electron, $|e|$):¹

$$U_{\text{el}}(r_{ab}) = \frac{q_a q_b}{4\pi\epsilon r_{ab}}. \quad (2.6)$$

$a - a$	σ_{aa}	ε_{aa}
C – C (CH ₃ –)	0.35	0.276
C – C (–CH ₂ –)	0.35	0.276
C – C (–CH–)	0.35	0.276
H – H	0.25	0.125

$a - a$	q_a
C (CH ₃ –)	–0.18
C (–CH ₂ –)	–0.12
C (–CH–)	–0.06
H	0.06

2.2.1.2 YASP simulation package

This model for n -alkanes has been simulated using the YASP simulation package [82], that allows to take all the previously presented interactions into account. This simulation program uses a Berendsen thermostat and barostat (see sec. 1.1.1.2), which permits to run simulations at constant NPT . This program also allows to use the SHAKE algorithm to impose constraints (sec. 1.1.2.2): We have used such constraints to prescribe the distances b_0^{ab} between any two particles a and b linked by a covalent bond instead of a harmonic interaction potential. This makes it possible to enlarge the time-step used in the integration of the equations of motion (here with a Leap-Frog algorithm). The time-step used here was 2 fs.

The YASP simulation program uses “topology” files to describe the geometrical properties of the considered molecules, and to set up the different interactions between all particles in the system. The interactions presented above are summarized in such a file, with the values corresponding to the material that is actually simulated. Moreover, one supplementary part in this file allows us to modify some of the interactions already defined by the preceding general rules. This is particularly important as it enables us to specify which interactions have to be excluded. The non-bonded interactions have to be suppressed for nearest neighbors, as it would not make sense to superimpose the harmonic spring describing a C–C covalent bond with the Lennard-Jones

¹ ϵ is the permittivity of the medium.

potential that is only relevant for two particles separated along the chain. Thus, one has to list explicitly all the interactions that should not be taken into account. The OPLS-AA force field definitions prescribe to switch off the non-bonded interactions for couples of particles that are separated by less than three bonds, and to apply half of the forces when exactly three bonds are involved. In our simulations this procedure would not work since we are using constraints to enforce the distance between two bonded particles. Imposing non-bonded forces between particles that are too close to one another results in preventing the SHAKE algorithm to converge and find a satisfactory conformation with respect to bond lengths. For this reason we had to find the appropriate cutoff distances for the non-bonded interactions. The tests led to the following set up, which correspond to the less restrictive choice:

- C–C interaction: Excluded if the two carbon atoms are separated by less than four bonds
- H–H interaction: Excluded if the two hydrogen atoms are separated by less than six bonds
- C–H interaction: Excluded if the two atoms are separated by less than five bonds.

Using a detailed simulation method one has the great advantage with respect to coarser methods that the physical input and output quantities of the simulation code can be expressed in “real” units and can therefore be directly compared with experimental values. The use of phenomenological force fields allows such a correspondence between the positions and velocities of the particles simulated using a model and physical properties (density, radius of gyration,...). It is thus possible to use SI units for all the physical quantities manipulated by the program, but this might not be the most sensible choice as a result of the particular length and time scales we are to probe with molecular dynamics. Using the YASP package, the relevant units are defined as presented in table 2.1.

2.2.1.3 Special optimization for the torsional potential

One parameter that has paramount importance in the case of polymer chains in general is the torsional potential. This potential determines the conformations of the chains in an outstanding fashion since the torsional angles inside the chains constitute the most flexible degrees of freedom: The bond angles are constrained by a rather stiff harmonic potential that does not allow large modifications of the conformations. On the other hand, a change in the torsional angles relaxes the structure of the chain. This particular degree of freedom has an influence on both the static and the dynamic properties of the chains in the melt: The statistical mixture of *trans* and *gauche* states (see fig. 2.1) determines quantities such as the radius of gyration of the chains, while the

Table 2.1: List of the relevant units for the quantities input and output of the simulation using the YASP package.

Quantity	Unit
length	nm
angle	rad or degree
time	ps
energy	kJ/mol
force constants	kJ/(mol nm ²), kJ/(mol rad ²)
charge	<i>e</i>
temperature	K
pressure	kPa
mass density	kg/m ³

rate of change between these states has an impact on the mobility of one molecule. In order to study the crystallization of polymers, the torsional degrees of freedom are also very important parameters, since the flexibility of the chains is mostly determined by the torsional potential, and the flexibility is the quantity which has the greatest influence on crystallization. Therefore, special attention has to be paid to torsional angles for our simulations.

The first test for our simulations was a variation of the torsional potential in order to investigate which influence it really has on the probability distribution of the torsional angles.

This distribution is more relevant than the torsional potential itself, since the latter might not be the only parameter acting on the angular states. The behavior of the chains in the melt is strongly influenced by the population of these states, and therefore the probability distribution is the quantity of interest to characterize the conformations. In case the other degrees of freedom do not act significantly upon the torsion angles, the distribution is completely determined by the potential and both of them provide the same information. However, the chains' packing as well as the (intra-chain) non-bonded interactions may contribute to distort the probability distribution prescribed by U_{tors} . To check this out, one has to compare the probability distribution measured in the simulations to the “theoretical” distribution that is expected in case the torsional degree of freedom is independent of any other parameter in the system, which is given by the Boltzmann relation:

$$P(\phi) = \frac{1}{Z} \exp\left(-\frac{U_{\text{tors}}(\phi)}{k_{\text{B}}T}\right), \quad (2.7)$$

where the partition function

$$Z = \int_0^{2\pi} d\phi \exp\left(-\frac{U_{\text{tors}}(\phi)}{k_{\text{B}}T}\right) \quad (2.8)$$

has to be inserted to ensure that the probability is normalized.

Figure 2.1(a) presents the OPLS-AA torsional angle potential, while fig. 2.1(b) compares the corresponding probability distribution to what is actually measured in the simulations. The probability distributions measured in the simulations show a significant mismatch with the expected form obtained by Boltzmann inversion [eq. (2.7)]. This can be quantified by looking at the probability to find a *trans* state, P_{trans} :

$$P_{\text{trans}} = P(120^\circ < \phi < 240^\circ) = \int_{120^\circ}^{240^\circ} d\phi P(\phi). \quad (2.9)$$

For a system of one hundred chains of $\text{C}_{44}\text{H}_{100}$ simulated at $T = 500$ K at atmospheric pressure, this value has been found to be 0.65,² whereas the Boltzmann inversion predicts 0.60. This is a strong evidence that

²This probability of a *trans* state does not depend on the chain length in our simulations of *n*-alkanes.

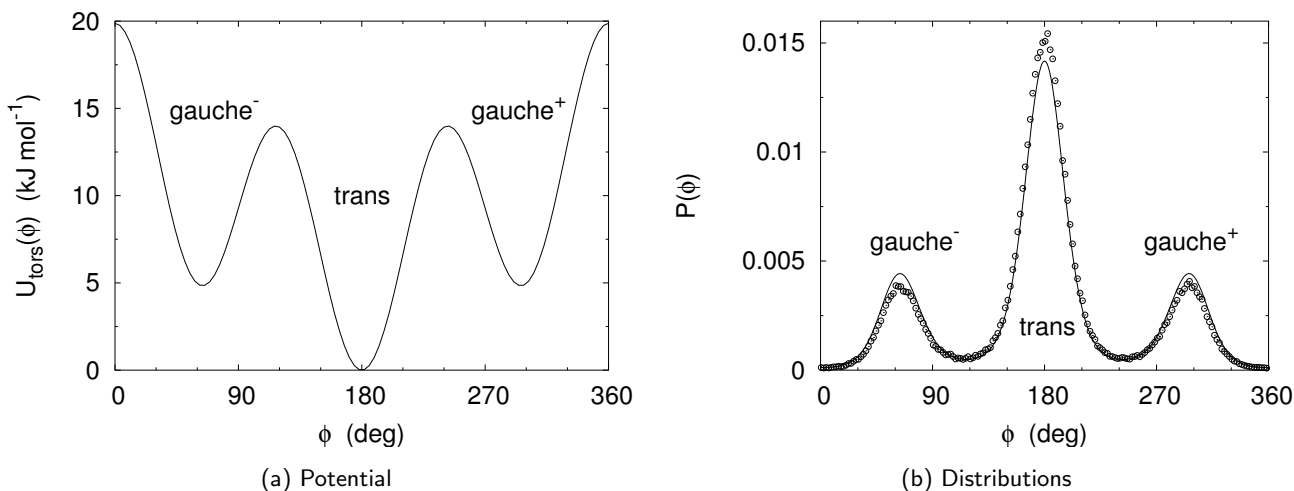


Figure 2.1: Comparison of the measured torsional angular distributions with the prediction from eqs. (2.7) and (2.8) for the OPLS-AA potential. Measurements are taken from a simulation of 100 chains of $C_{44}H_{100}$ at 500 K.

the other degrees of freedom do influence the torsional angles in an appreciable manner. In particular, the role of the non-bonded or molecular interactions is not clear, and it is reasonable to assume that intermolecular interactions could influence the torsional angle distribution, as well as the intra-chain non-bonded interactions which probably have the most significant direct impact on the conformations that the chains can actually take in the melt.

Having noticed this effect of the other interactions on the torsional states, it is interesting to study the effects of a variation of the form of the potential on the probability distribution for torsional angles. First, one should notice that in the case of linear alkyl chains, simplifications are possible for the expression of the torsional potential given in sec. 2.2.1.1. The general expression used by the OPLS-AA description represents the energy associated to torsional states by three terms, corresponding to C–C–C–C, C–C–C–H and H–C–C–H couples of dihedrals (cf. fig. 2.2). As the angles $\phi_{CCCC}(= \phi)$, ϕ_{CCCH} and ϕ_{HCCH} are linearly dependent (there is no influence of the bond angle fluctuation), the three distinct parts of the torsional potential can be merged into one single expression that reads:

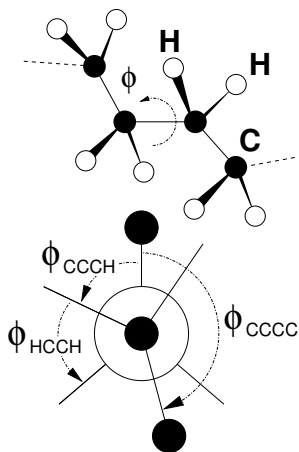


Figure 2.2: Illustration of the three different contributions to the torsional energy.

$$\begin{aligned}
 U_{\text{tors}}^{\text{tot}}(\phi) = & \frac{1}{2} {}^{\text{CCCC}}k_1^{\text{tors}} (1 + \cos(\phi)) + \\
 & \frac{1}{2} {}^{\text{CCCC}}k_2^{\text{tors}} (1 - \cos(2\phi)) + \\
 & \frac{1}{2} \left({}^{\text{CCCC}}k_3^{\text{tors}} + 4 {}^{\text{CCCH}}k_3^{\text{tors}} + 4 {}^{\text{HCCH}}k_3^{\text{tors}} \right) (1 + \cos(3\phi)), \quad (2.10)
 \end{aligned}$$

as there are four C–C–C–H and four H–C–C–H torsional contributions associated with one C–C–C–C angle. This is equivalent to

$$U_{\text{tors}}^{\text{tot}}(\phi) = \frac{1}{2}K_1(1 + \cos(\phi)) + \frac{1}{2}K_2(1 - \cos(2\phi)) + \frac{1}{2}K_3(1 + \cos(3\phi)). \quad (2.11)$$

The three effective force constants K_1 , K_2 and K_3 take the following values:

K_1	K_2	K_3
7.27	-0.66	11.72

In order to study the influence of these parameters on the structure of the simulated melts, we have created several different models with specific torsional potentials derived from the above expression for OPLS (see tables 2.2 and 2.3). The systems created this way were equilibrated at two temperatures ($T = 300$ and $T = 450$ K), and then compared. The relevant parameter here is the probability P_{trans} ; reference values were extracted from simulation results obtained with a different model simulated by Yoon, Smith and Matsuda that has been shown to reproduce quantitatively many features of short polyethylene chains [140]. This model is defined in a different manner and its parameters should not be directly compared to the K_i of OPLS, for instance, as the influence of the non-bonded interaction is responsible for the structure of the effective torsional potential. We were only interested in the effective interaction, reflected in the probability distribution of angle ϕ ; this distribution was measured by Yoon et al. and one variant of the OPLS model reproduces it closely, as indicated by the characteristic integral P_{trans} [eq. (2.9)]. This model is called ‘‘OPLS-mod’’, and has been used for our simulations of n -alkanes, as it is expected to reproduce the static properties in a more accurate fashion.

K_1	K_2	K_3	$P_{\text{trans}}(T = 300)$	$P_{\text{trans}}(T = 450)$	Model
-	-	-	0.649	0.599	YSM
8	-1	12	0.795	0.681	
7	-1	12	0.756	0.656	OPLS
6	-1	12	0.705	0.619	
5	-1	12	0.659	0.592	OPLS-mod
7	0	12	0.825	0.682	
7	-1	12	0.756	0.656	
7	-2	12	0.706	0.622	
7	-1	13	0.745	0.655	
7	-1	12	0.756	0.656	
7	-1	11	0.767	0.651	

Table 2.2: Variation of the parameters K_i defining the torsional interaction, and the resulting proportions of *trans* states at $T = 300$ and $T = 450$ K (84 chains of $\text{C}_{16}\text{H}_{50}$). The target values from Yoon, Smith and Matsuda (YSM) are indicated and compared to the results from the OPLS model and its variants. The model reproducing best the target values is named OPLS-mod, and has been used in the subsequent studies. The parameters corresponding to the YSM model are not indicated since the form of the torsional potential used in this case is different and could not be compared directly to our potentials.

Table 2.2 presents a comparison of the different models and the proportion of *trans* states they yield. It can be observed from the results presented in table 2.2 that the parameter K_1 has a greater influence than the other two; a decrease in K_1 and K_2 produces less favored *trans* states, while P_{trans} increases with a decrease in K_3 , this parame-

Table 2.3: Other variants of the OPLS-model torsional potential, showing the chosen potential compared to other forms. (*): The last column presents the proportion of *trans* states measured on a system of 100 chains of $C_{44}H_{90}$ and not $C_{16}H_{50}$ as for other data. It can be seen that a few models with parameters close to those of OPLS-mod yield similar results, and would probably give very similar simulation results.

K_1	K_2	K_3	$P_{\text{trans}}(T = 300)$	$P_{\text{trans}}(T = 450)$	$P_{\text{trans}}(T = 500)^*$
3	-1	12	-	-	0.536
4	-1	12	-	-	0.560
5	-1	12	0.659	0.592	0.586
6	-1	12	0.705	0.619	0.610
7	-1	12	0.756	0.656	0.636
8	-1	12	0.795	0.681	-
5	-2	12	0.609	0.568	0.557
5	-1	12	0.659	0.592	0.586
5	0	12	0.705	0.621	0.613
5	-1	11	0.658	0.590	0.585
5	-1	12	0.659	0.592	0.586
5	-1	13	0.662	0.595	0.586

ter having the smallest influence on the system. Other variations of the parameters K_i have been tested, for $C_{16}H_{50}$ at $T = 300$ and $T = 450$ K as before, as well as with $C_{44}H_{90}$ at $T = 500$ K (table 2.3). The same trends are observed for the variations of K_1 and K_2 , but the tendency for P_{trans} with K_3 has changed, even though the effect is very small. K_3 is associated with a $\cos(3\phi)$ function, thus a change of K_3 is reflected by both the barriers and minima of U_{tors} , making it difficult to predict its influence on the probability distribution.

2.2.2 Model characterization

2.2.2.1 General observations

Table 2.4 summarizes the different systems we have simulated, showing the duration of the simulation runs for each chain length, and the corresponding characteristic lengths l_p , R_g^2 and R_e^2 .

Table 2.4: Summary of equilibrium simulations of *n*-alkane at $T = 500$ K.

System	Chains	Atoms	Length (ps)	l_p/b_0	l_p (nm)	R_e^2 (nm ²)	R_g^2 (nm ²)	R_e^2/R_g^2
C_8H_{18}	256	6656	2000	2.17	0.332	0.550	0.0707	7.78
$C_{10}H_{22}$	100	3200	2000	2.26	0.346	0.797	0.100	7.96
$C_{13}H_{28}$	243	9963	2000	2.30	0.352	1.20	0.150	8.01
$C_{14}H_{30}$	72	3168	20000	2.33	0.356	1.35	0.168	7.99
$C_{15}H_{32}$	72	3384	20000	2.32	0.354	1.49	0.187	7.97
$C_{16}H_{34}$	84	4200	20000	2.33	0.357	1.63	0.205	7.93
$C_{30}H_{62}$	144	13248	2000	2.29	0.351	3.65	0.498	7.33
$C_{44}H_{90}$	100	13400	4000	2.35	0.359	5.80	0.831	6.98

Figure 2.4 gives an overview of the structure of the system at different temperatures. Peaks can be seen to develop as the glassy state is approached at low temperature.

2.2.2.2 Influence of the thermostat

As indicated above, the thermostat used to carry out this study was the Berendsen thermostat. This thermostat has been widely used to prescribe the temperature in molecular dynamics simulations, owing to

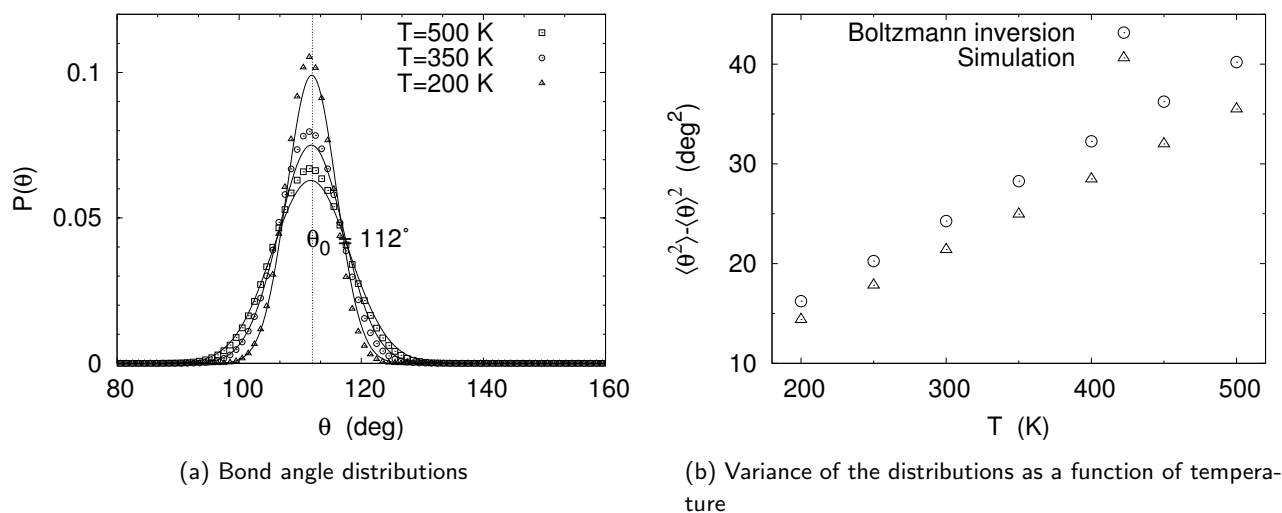


Figure 2.3: Comparison of theoretical expectation and the measured variance for C–C–C bond angle distributions at several temperatures, for a system consisting of 84 chains of $C_{16}H_{34}$. The theoretical and measured distributions do not superimpose as a result of the influence of C–C–H interactions that are not taken into account in the theoretical estimate. The measured variance nevertheless exhibits the same tendency as computed with this approximate model, i.e. a linear increase in the distributions' width with temperature.

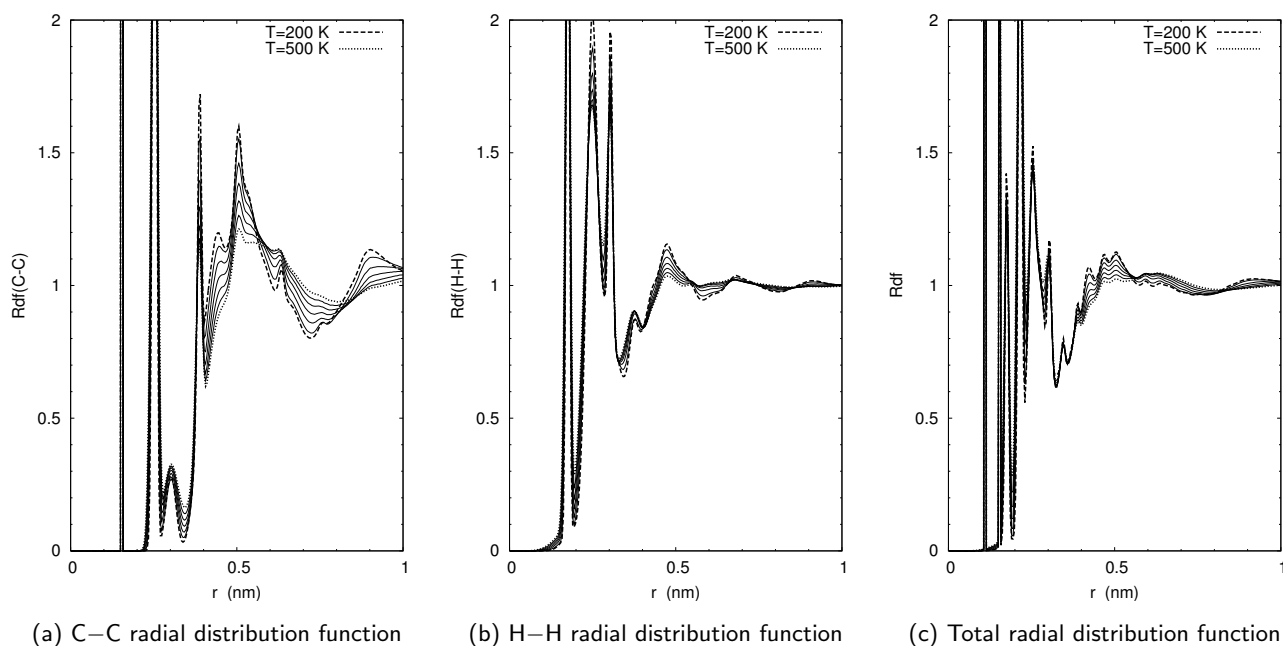


Figure 2.4: Evolution of radial distribution functions with temperature for $C_{16}H_{34}$.

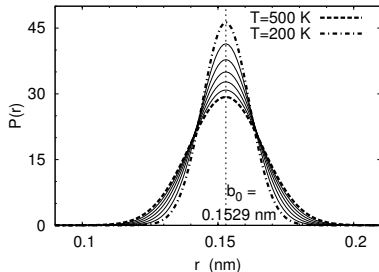


Figure 2.5: Bond length distributions. The narrow gaussians represent the probability distributions for the bond length as prescribed by the OPLS-AA model, centered on the value b_0 that is maintained by the SHAKE constraint algorithm used in our simulations. Curves are plotted for temperatures between 200 and 500 K.

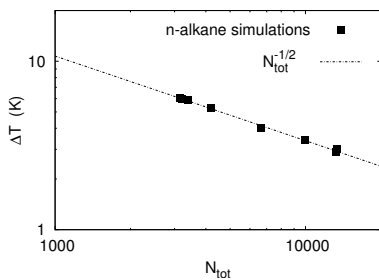


Figure 2.6: Evolution of temperature fluctuations as a function of the total number of particles in the system (Berendsen thermostat). The fluctuations decrease as $N_{\text{tot}}^{-1/2}$, as expected.

its simplicity and great efficiency. Nevertheless, this particular algorithm is known not to sample the canonical ensemble in a satisfactory manner. In order to investigate the influence of such a scheme on our simulation model, we ran tests with another thermostating algorithm (Langevin thermostat), and compared the results obtained in each case with the same system, under the same conditions. For that study, we modified the YASP simulation package so that a Langevin thermostating algorithm is also available. This has been achieved by removing the Berendsen velocity rescaling, and adding two contributions to the force (noise and friction, see sec. 1.1.1.2). The system we used to compare the influence of the thermostat consisted of 84 chains of $\text{C}_{16}\text{H}_{34}$, simulated at different temperatures ($T = 500, \dots, 200$ K, every 50 K) and at constant, atmospheric pressure. A cooling was performed from $T = 500$ K to $T = 200$ K (cooling rate -10^{-3} K ps^{-1}) in order to generate suitable initial configurations at each temperature for the equilibrium runs. We will now compare the average values, and the corresponding standard deviations, for several quantities that characterize the system under consideration. Thus we should be able to stress some differences in the way the two algorithms act upon the system.

The average temperature, enthalpy, volume and radius of gyration are plotted for the two systems and each temperature in figures 2.7 and 2.8. Each point on the plots presents the average value of one quantity at a particular temperature. The error bars are used to indicate the corresponding fluctuations, more precisely the standard deviation

$$\Delta X = \sqrt{\langle X^2 \rangle - \langle X \rangle^2} \quad (2.12)$$

of the quantity X . ΔX is measured from the distribution of X as a fluctuating quantity. It can be observed that the average values are the same when measured from simulation using the two different thermostats, or at least very close, within the error bars. The temperature itself, presented on fig. 2.7(a), is a fluctuating quantity in an constant- NPT simulation, and only equals the *prescribed* temperature on average. The fluctuations of the temperature are supposed to be connected with the system size, as one expects the fluctuations to vanish in the thermodynamic limit of an infinite system; this is verified by our models as indicated in fig. 2.6 which shows a plot of the standard deviation ΔT as a function of the total number of particles N_{tot} (carbon and hydrogen atoms). The scaling as a power law with exponent $-1/2$ predicted by statistical mechanics is observed.

The fluctuations of the different observables that have been measured for this study are also predicted by thermodynamics which provides relations between the standard deviations of various quantities and physical properties. An example of this consists in the relation that links the specific heat with the fluctuations of the enthalpy in an isothermal-isobaric ensemble (see ref. 21 for instance):

$$\Delta H = \Delta(E + PV) = \sqrt{k_B T^2 C_P}. \quad (2.13)$$

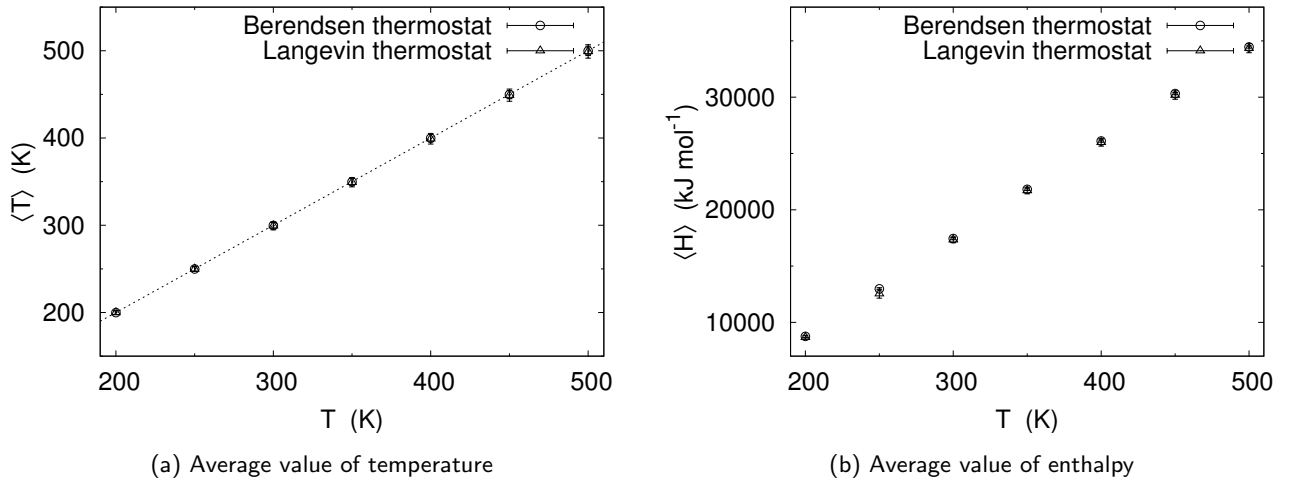


Figure 2.7: Comparison of Berendsen and Langevin thermostats for temperature and enthalpy. The error bars correspond to the fluctuations of each quantity, characterized by the standard deviation of the probability distributions. The average values coincide for both thermostats, while the fluctuations are larger in the case of the Langevin thermostat.

In our case, it has been observed that the two thermostats yield different results for the fluctuations of the physical quantities, but this does not imply that we are actually simulating different systems when using one thermostat or the other. As a matter of fact, the variation of enthalpy with temperature is exactly the same (either from equilibrium values as in fig. 2.7(b) or when looking at the instantaneous values computed during the continuous cooling), which confirms that C_P is the same in both simulations. The conclusion is that the fluctuations generated by a simulation program do depend on the thermostat used, and they are not in agreement with what is expected in the case of a canonical ensemble for constant- NVT simulations (or isothermal-isobaric for constant- NPT). These fluctuations have been proven correct when using a Nosé-Hoover thermostating scheme with the adequate parameters, but this is not the case for the thermostats we used. This makes eq. (2.13) not applicable here.

Another known side-effect of thermostats is an influence on the dynamics. This might be the reason for the differences that can be observed between the two simulations for the average value of R_g^2 : For high and low temperatures, the results are very similar for averages and fluctuations obtained with the two thermostats, but there is a difference around $T = 250$ K. At this intermediate temperature (at lower T , the system is frozen), a peak develops for $\langle R_g^2 \rangle$ and it is much more pronounced for the results obtained with the Langevin thermostat. As we shall see later (sec. 2.2.3), this peak corresponds to the development of order in the system, as a precursor of crystallization. We shall come back to the differences observed for the two thermostats when crystalline order occurs; the fact that R_g^2 is larger and has more important fluctuations in the simulation involving the Langevin thermostat might indicate that the latter accelerates the dynamics.

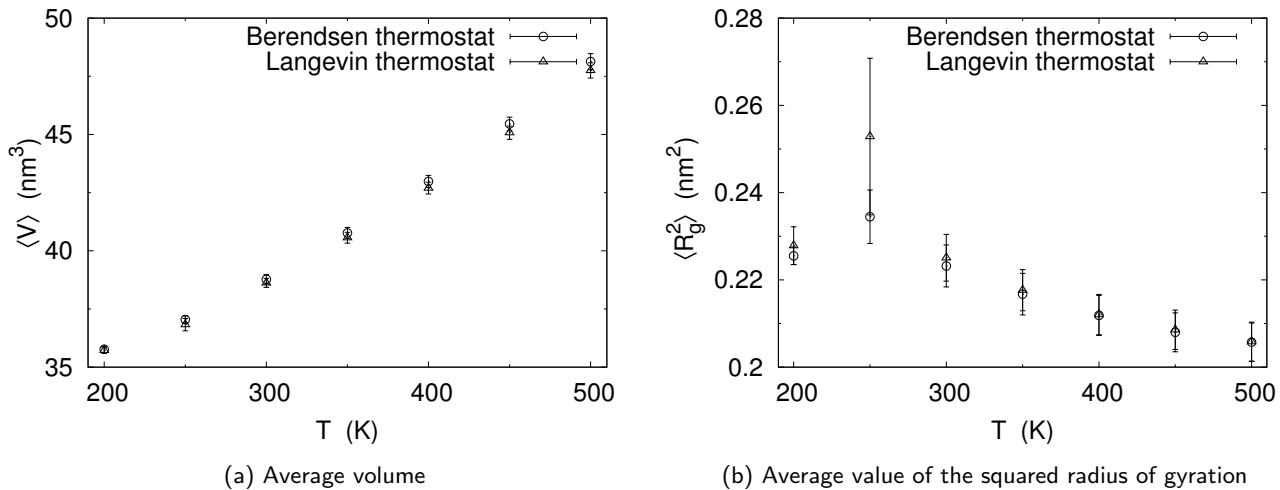


Figure 2.8: Comparison of Berendsen and Langevin thermostats for the volume and squared radius of gyration. Fluctuations are indicated by the error bars. The volume of the sample is slightly larger when the Berendsen thermostat is used. A characteristic property like R_g^2 exhibits very similar values in both cases, showing that the choice of the thermostat does not influence the statics in a significant manner (the deviation for the lowest temperatures is discussed in the text).

2.2.3 Discussion

All-atom simulations have been used in many contexts as a replacement for experiments, and have proven that numerical studies are able to quantitatively reproduce the physical properties observed in many systems. However, there are always discrepancies between computer models and the “real world”, either caused by limitations of the simulation method or by a lack of precision in the parameters of the model. In the case of the model we have been using to simulate *n*-alkane melts, it is possible to identify problems belonging to these two categories.

One possible source of inaccuracy in our simulations is connected to the algorithms that are employed for prescribing temperature and pressure. The Berendsen method chosen for both the thermostat and barostat does not allow to sample the isothermal-isobaric ensemble as it should, and this may lead to contradiction when looking at fluctuations of the physical quantities of interest. For this reason it would have been worthwhile testing a Nosé-Hoover approach that is supposed to give more satisfactory results. However, a comparison with the Langevin thermostat showed that thermostats influence the simulation results probably in an unimportant manner only; the mean values of physical quantities remain unchanged to a good precision under the switch of thermostat. Moreover, as it has already been pointed out in sec. 1.1.1.2, even the Nosé-Hoover thermostat can lead to unphysical results.

Apart from this technical issue, problems arise from the model itself that is used for the study. All-atom simulations are mostly based on empirical results, since the parameters of a force field are usually derived from several experimental sources, and possibly adjusted so as to reproduce accurately some target quantities. The method already

bears limitations in itself, and details of the implementation can make the situation worse. We decided to use constraints instead of the harmonic bonds prescribed in the original OPLS-AA force field, in order to save some computer time by averaging over the unimportant degrees of freedom of the bond fluctuations; in doing so we altered to some extent the consistency of the original model, since the force field parameters had been optimized for the specific design of this form of the potential. It is not clear whether this modification of the simulation model can have noticeable consequences on the observable properties or not, and this would have deserved a specific study. Nevertheless, we do not expect much effect, since bond vibrations are much faster than the other degrees of freedom and thus not likely to be coupled (strongly) to them.

For the same reason it is questionable whether it was justified or not to modify one of the potentials of the OPLS force field. We have argued that this was necessary since we could check that the torsion angles supposedly governed by an explicit potential parametrized in the force field do not necessarily only depend on this potential, and is also influenced by the other degrees of freedom. As the torsional potential is an ingredient of the force field with predominant importance, we decided to adjust it so as to constrain the *observable* quantity, the torsional distribution, to a reference value taken from simulation results that showed a good agreement with experimental data. This tuning of the *effective* torsional interaction allowed us to enforce a sensible prescription for the statics of the chains, but only as an ad-hoc modification of the force field. Instead of that, an optimization of all the different parameters would have been desirable. Furthermore, as we are interested in the crystallization and therefore need a reasonable description of both the liquid and the crystalline states, it is legitimate to ask whether such a *simple* force field as OPLS-AA is suitable to simulate the solid phase; much more complex functional forms exist for crystal simulations. In the end, one has to compromise and find a tractable model that is at the same time efficient and accurate enough.

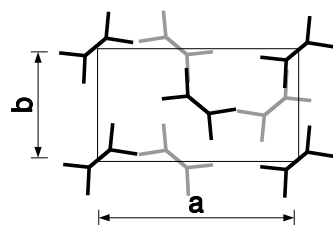
We shall present the results obtained with our model in the next section, and see whether it can be used to reproduce the behavior of short n -alkane chains at low temperatures.

2.3 Melting of n -alkane crystals

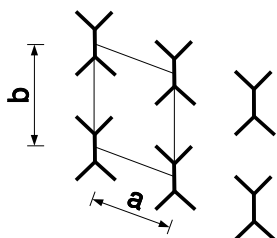
One way of studying alkane crystals consists in creating these structures by hand. It is not obvious *a priori* that the crystalline structure should be stable when simulated with our all-atom model: The force field parameters are determined at high temperature, and there is a large uncertainty on their validity anyway, as we discussed above. Therefore, it is not clear that a model based on such a force field is able to reproduce the correct behavior of n -alkanes at low temperatures, and yields a sensible description of the crystalline phase. The first point to be

checked is whether a crystal created by hand is stable in the simulation or not.

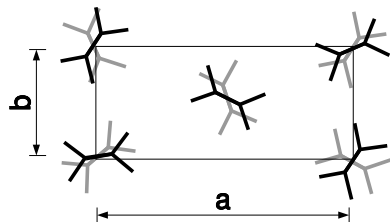
Depending on n being odd or even, the crystalline lattice can be different (sec. 2.1). Odd carbon-number chains are supposed to crystallize in the orthorhombic phase, while for even n a triclinic phase is observed experimentally. A monoclinic phase also exists. The crystalline phase we were mostly interested in is the orthorhombic one, as it is also the structure which polyethylene crystallizes in. Another question of interest is whether there is actually a preference for the triclinic phase in the case of even- n alkanes. We therefore created perfect orthorhombic and triclinic structures and simulated them, using the modified OPLS model.



(a) Orthorhombic



(b) Triclinic



(c) Rotator

Figure 2.9: Sketches of the packing of the chains in the different crystal structures, viewed along the c -axis. The chains' main axes are parallel to this c -axis, the schematic representation of a chain corresponds to the projection of C–C and C–H bonds in the c direction. In the case of the orthorhombic crystal, the elementary pattern consists of two layers, the second of which is represented in gray. When the system shifts to the rotator phase, the two layers sit exactly on top of each other, as it is also the case for the triclinic crystal (for the triclinic arrangement, a and b correspond to the projection of the actual cell constants into the plane orthogonal to the c -axis).

2.3.1 Creation of perfect structures

2.3.1.1 Orthorhombic phase

Odd numbered n -alkanes are mainly found in the orthorhombic phase, which has a structure indicated schematically in fig. 2.9(a); the orthorhombic unit cell contains two chains elongated along the c -axis. The first chain's plane (the first chain is represented at the intersection of cell vectors a and b in fig. 2.9(a); a chain plane contains all C–C bonds of an all *trans* molecule) makes an angle $\psi = 43^\circ$ with the a -direction, and the second chain (in the middle of the figure) lies in a plane perpendicular to the first one's. Chains are packed this way into layers, which are stacked to form the actual crystal. The arrangement of chains in a layer is deduced from the positions of the chains of the previous layer, by a reflection through the a - b plane, and a translation in the a -direction [114]. This two-layer structure allows to minimize the overlap of hydrogen atoms at the interface.

In order to test the quality of the force field, we calculated the coordinates of all atoms of a perfect crystal from the geometrical characteristics described above, and used them as a starting configuration for a simulation at atmospheric pressure and very low temperature ($T = 10$ K). The lattice parameters a , b and c were taken from an extrapolation of their values toward $T = 0$ for polyethylene crystal, calculated by path-integral Monte-Carlo simulations [68] rather than from experimental measurements at room temperature, because using such values might cause the orientation of the chains to be lost as a result of a quick readjustment of the box size due to pressure and the small thermal energy. The cell parameters are summarized in the following table :

a	b	c
0.72 nm	0.49 nm	0.253 nm

The c -axis length actually corresponds to the distance between every second carbon atom, and therefore has to be scaled accordingly to yield the appropriate box size along the z axis, according to the chain length under consideration. Once the configuration created, it is used

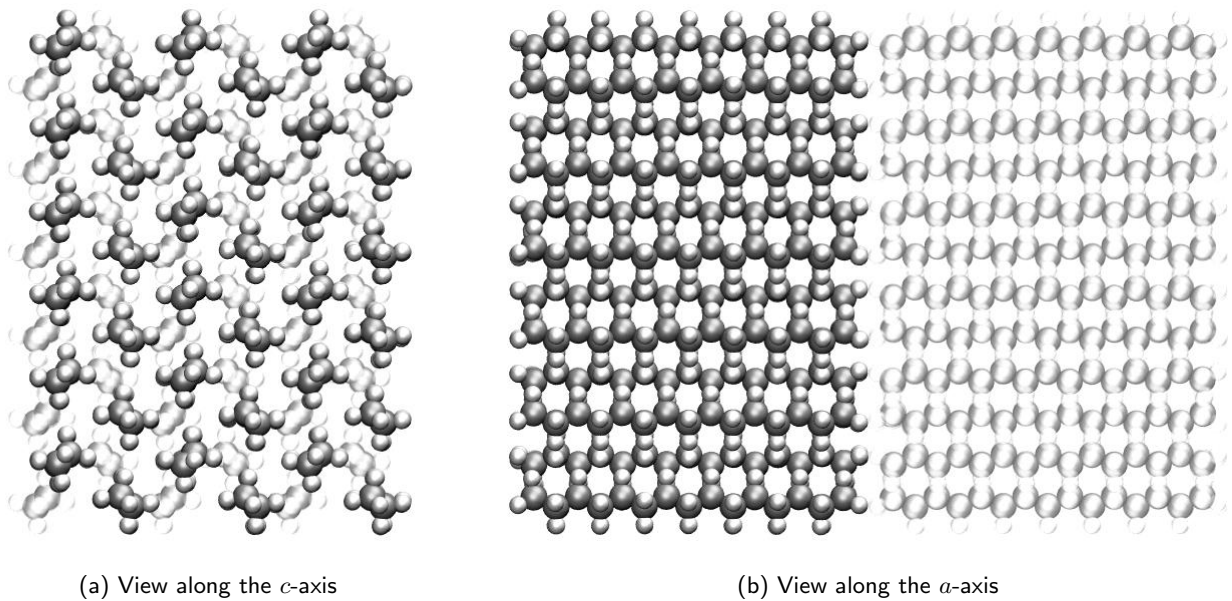


Figure 2.10: Orthorhombic $C_{15}H_{32}$. The two layers are represented, and the second one has been gray-shaded for clarity.

as input for the simulation code and the system is left to relax at 10 K and atmospheric pressure for 400 ps. A representation of the simulated system after this short relaxation simulation is given in fig. 2.10. It is possible to distinguish the two different layers.

2.3.1.2 Triclinic phase

For even n values, n -alkanes are found in the triclinic phase (this changes for $n > 26$, see sec. 2.1). The triclinic phase is characterized by the three cell lengths a , b and c , and the three angles α , β and γ which are no longer equal to 90° (See the sketch in fig. 2.11 and the schematic representation of fig. 2.9(b)). Contrary to the case of the orthorhombic crystal, all the chains are placed in parallel planes; furthermore, there is no differences between layers along the c -axis for the triclinic crystal. Nevertheless, in order to allow a direct comparison of the orthorhombic and triclinic crystals, simulations of the latter were run using two stacks of chains. The parameters used for perfect triclinic crystal are summarized below [89, 110]:

a	b	c	α	β	γ
0.43 nm	0.48 nm	0.253 nm	98°	72°	107°

Snapshots from the simulations (after a short equilibration at 10 K) are shown in figure 2.12; the pictures allow to visualize the γ and α angles that strongly deviate from 90° . It is also noticeable that, even after relaxation at very low temperature, defects are present in the structure of the crystal, indicating that there has been a readjustment of the chains right after the beginning of the simulation. Figure 2.13 shows the evolution of lattice parameters during the first part of the equilibration run at $T = 10$ K; in the case of triclinic $C_{14}H_{30}$, it can

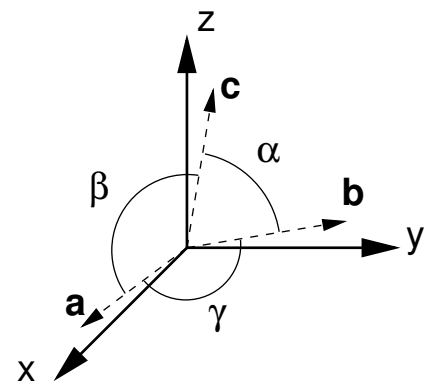


Figure 2.11: Schematic drawing showing the base vectors for the triclinic lattice.

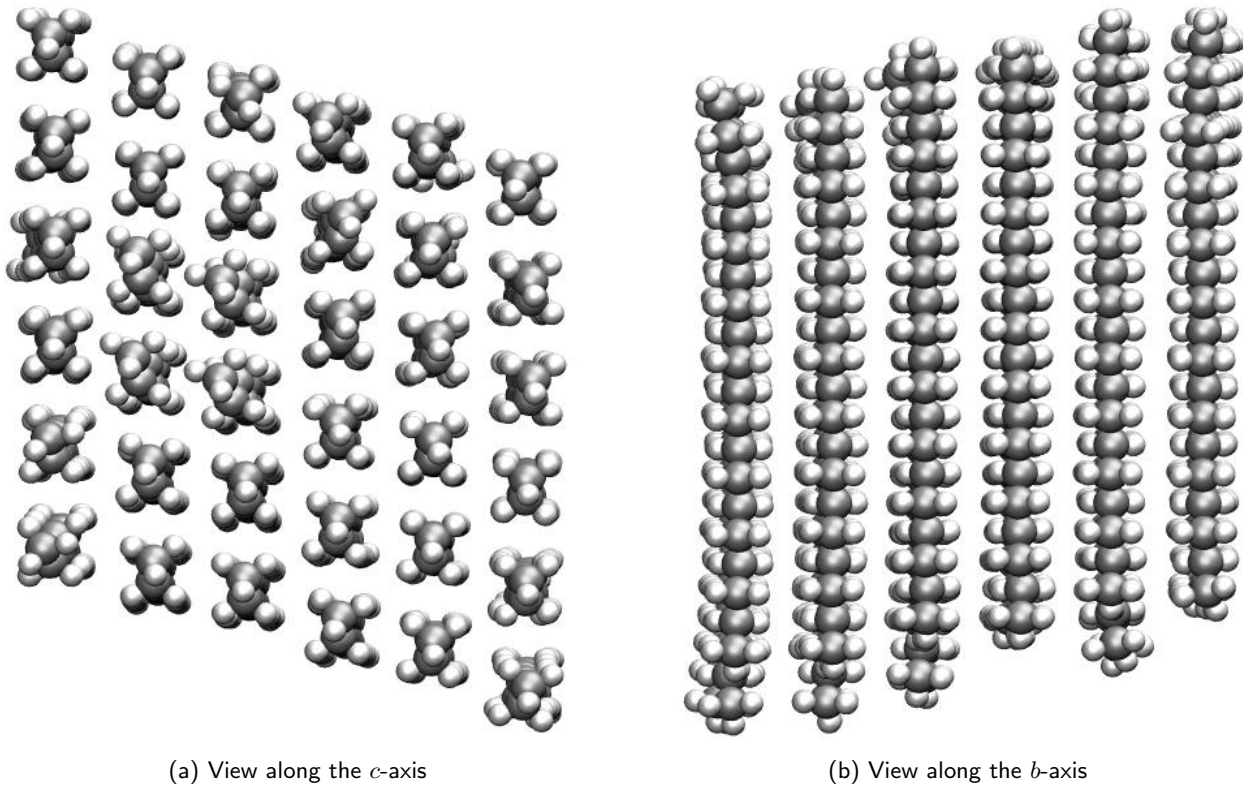
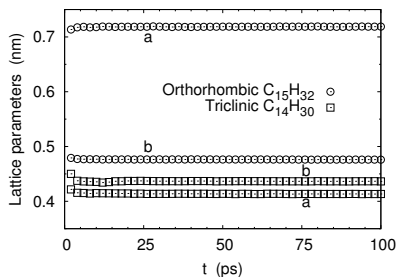
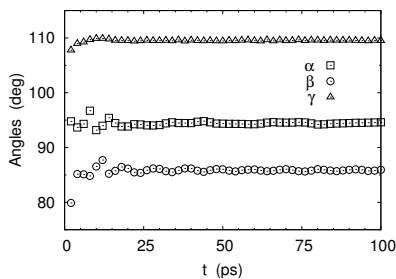


Figure 2.12: Triclinic crystal ($C_{20}H_{42}$). The two pictures present projections onto the a - b and a - c planes, respectively on the left and on the right, emphasizing the γ and α angles. Only one of the two layers is shown.



(a) Initial values of the cell parameters a and b



(b) Initialization of angles α , β , γ for the triclinic crystal

Figure 2.13: Evolution of lattice parameters during startup simulation for orthorhombic $C_{15}H_{32}$ and triclinic $C_{14}H_{30}$.

be seen in fig. 2.13(a) that the lattice constants a and b are relaxing to their equilibrium values very rapidly, causing the chains to rearrange and creating defects. For the orthorhombic crystal, a and b change only slightly to reach equilibrium. Figure 2.13(b) gives an overview of the evolution of angles during initialization; β is larger than the value used to construct the crystal, and γ is slightly larger than expected. All angles fluctuate before reaching a stable value. For the orthorhombic crystal, all angles have the regular value 90° and do not significantly vary.

The values of a , b and c can be obtained by a simple measurement of the box size in the case of the orthorhombic lattice since the lattice vectors are collinear to the sides of the simulation box. This is no longer the case for triclinic crystals, and the values of the angles α , β and γ that differ from 90° also need to be computed in a specific manner. To this end, we used an algorithm that averages the values of the vectors \mathbf{a} , \mathbf{b} and \mathbf{c} over all their realizations in the crystalline system. Of course, this method is only valid for a perfect crystal in which one knows how the chains and atoms are organized.

The equilibrated crystals are found to be very close to the initial perfect structures. Only small changes in the values of the lattice parameters are observed. This means that the force field we are using is not inconsistent with the experimentally observed crystalline struc-

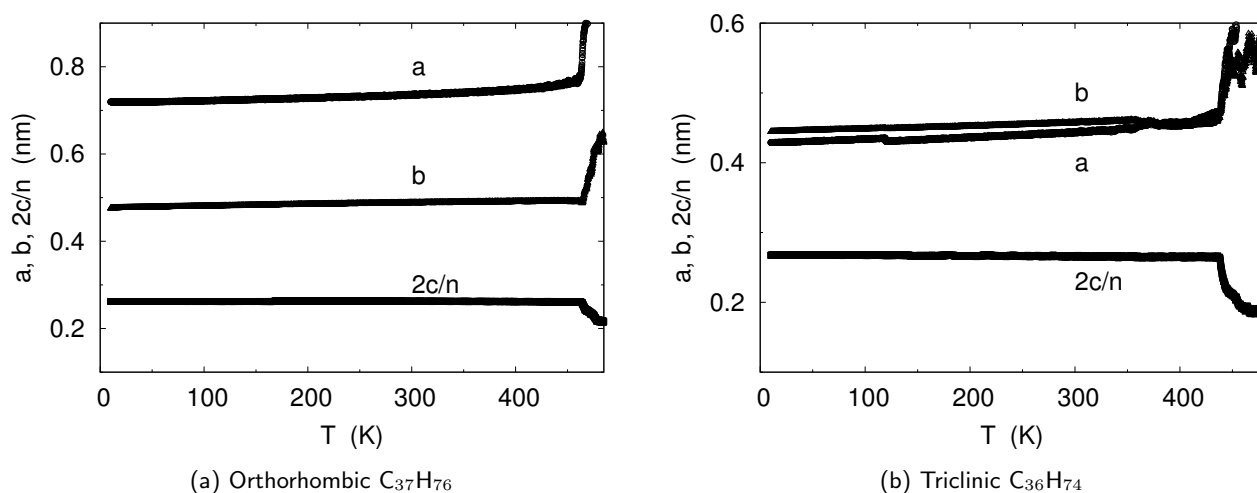


Figure 2.14: Lattice parameters measured for orthorhombic and triclinic crystals as a function of temperature. The different cell lengths increase as a result of thermal dilatation until the crystals eventually melt (Heating rate: 10^{-4} K ps $^{-1}$). The lattice constant along the z -axis is presented in the graphs divided by $\frac{n}{2}$ so that it has a value comparable with a and b . This corresponds roughly to the distance between every second carbon along one chain.

tures; at least the non-bonded interactions are compatible with dense orthorhombic and triclinic packings, and the other interactions do not forbid the stretched conformation of alkane chains—but this is not surprising.

2.3.2 Melting experiment

In order to check whether the force field parameters allow for an accurate enough description of n -alkane crystals, we should now have a look at the evolution of these structures at higher temperature. This is achieved via continuous heating—the opposite of the procedure through which we attempt to produce crystals from the liquid melt in sec. 2.4, and in chapter 3 using coarse-grained models. It is necessary to make sure that our model does not melt at an unrealistic temperature, whether too low or too high, as a result of an incapacity of the force field to reproduce the behavior of the experimental system or of other limitations in the simulation method.

Upon heating, the values of the lattice parameters steadily increase as thermal energy becomes more important. This evolution is displayed in fig. 2.14, for both kinds of crystals. Thermal dilatation is mostly reflected on the values of a and b , while c does not vary much; this indicates that thermal energy is mostly dissipated via vibrations of the chains in the a - b plane. Another test of the stability of the crystals consists in studying the orientation of the chains in time. The orthorhombic and triclinic crystals are too dense to allow chains to migrate from one layer to the next, in the z -direction (unless several chains in a row move cooperatively, which is unlikely because of non-bonded interactions causing repulsion at low temperature), but it is interesting

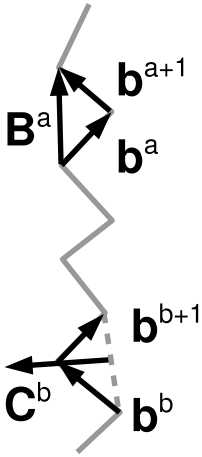


Figure 2.15: Definition of the \mathbf{B} and \mathbf{C} vectors for one n -alkane chain (the subscript i is omitted). $\mathbf{B}^a = \mathbf{b}^a + \mathbf{b}^{a+1}$; $\mathbf{C}^a = \mathbf{b}^{a+1} - \mathbf{b}^a$. Alternating direction of \mathbf{C}^a with a odd or even is taken into account in the average $\mathbf{C} = \langle \mathbf{C}^a \rangle_a$.

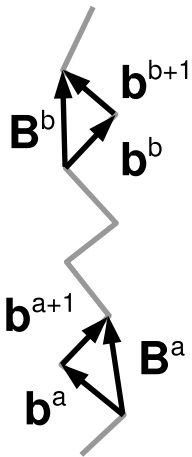


Figure 2.16: Schematic representation showing how the order parameter P_2 is computed: $P_2 = \langle \mathbf{B}_i^a \cdot \mathbf{B}_j^b \rangle$ (\mathbf{B} vectors are represented for chain i only here).

to check whether a chain is allowed to change its plane orientation, meaning the orientation of the plane which contains the carbon-carbon bonds, and which is supposed to be fixed for all molecules in the crystals.

Defining the vector $\mathbf{C}(t)$ as representative of the orientation of the plane of a chain at time t (see fig. 2.15), one can evaluate the correlation function $\langle \mathbf{C}(t) \cdot \mathbf{C}(0) \rangle$ which indicates whether the chains (or at least part of them) have modified their orientation after a period of time. This quantity can be evaluated during continuous heating, the function of time becoming then also a function of temperature as there is a linear relation between T and t during this kind of simulation. This is what is plotted on fig. 2.17(a). It can be observed that, either for orthorhombic or triclinic crystals, this orientational order parameter only decorrelates at high temperature, at the moment the system actually melts. This is an evidence of the stability of the crystals until melting sets in. It can be checked that another order parameter like P_2 also exhibit a good stability in the crystalline phase before melting; this order parameter is computed as explained in sec. 1.3, except that in the case of an atomistic model one has to use the \mathbf{B} vectors instead of the regular bond vectors \mathbf{b} . This is illustrated in fig. 2.16.

As a comparison, fig. 2.17(b) shows the same quantity measured in a simulation of $\text{C}_{20}\text{H}_{42}$ at constant low temperature ($T = 250$ K), for a system equilibrated in a conformation that does not correspond to a crystalline structure. This simulation was started putting the chains on a square lattice with a much lower density than in the case of the crystals described above, and letting the system relax at $T = 250$ K. After a very short time (less than 200 ps), the system is equilibrated with a denser packing (due to the pressure), and it becomes possible to characterize it. In this case, even under constant temperature conditions, $\langle \mathbf{C}(t) \cdot \mathbf{C}(0) \rangle$ is found to decrease with time, even though the thermodynamic quantities are constant: This is typical of the rotator phase, in which the chains are constrained in a layer but still free to “rotate” along their individual axes. Because of this permanent change of orientation, the correlation function $\langle \mathbf{C}(t) \cdot \mathbf{C}(0) \rangle$ decays. An illustration of this rotator phase is shown on fig. 2.18.

The evolution of the volume of a crystalline sample reveals phase transitions; we used the volume as an order parameter to monitor the state of the system of n -alkane chains during heating. Melting of a crystal is signaled by a jump in the volume indicating the occurrence of the less dense liquid phase. This phase transition is strongly dependent on the heating rate, as illustrated in fig. 2.19: For a system consisting of 72 chains of $\text{C}_{15}\text{H}_{32}$, melting is observed almost 50 degrees lower for a heating rate of 10^{-4} K ps $^{-1}$ than in case we are heating one hundred times faster. At the lowest heating rate, on can notice the slope of the volume is very large, corresponding to an abrupt phase transition; contrary to that, for faster heating, a much smaller slope indicates a

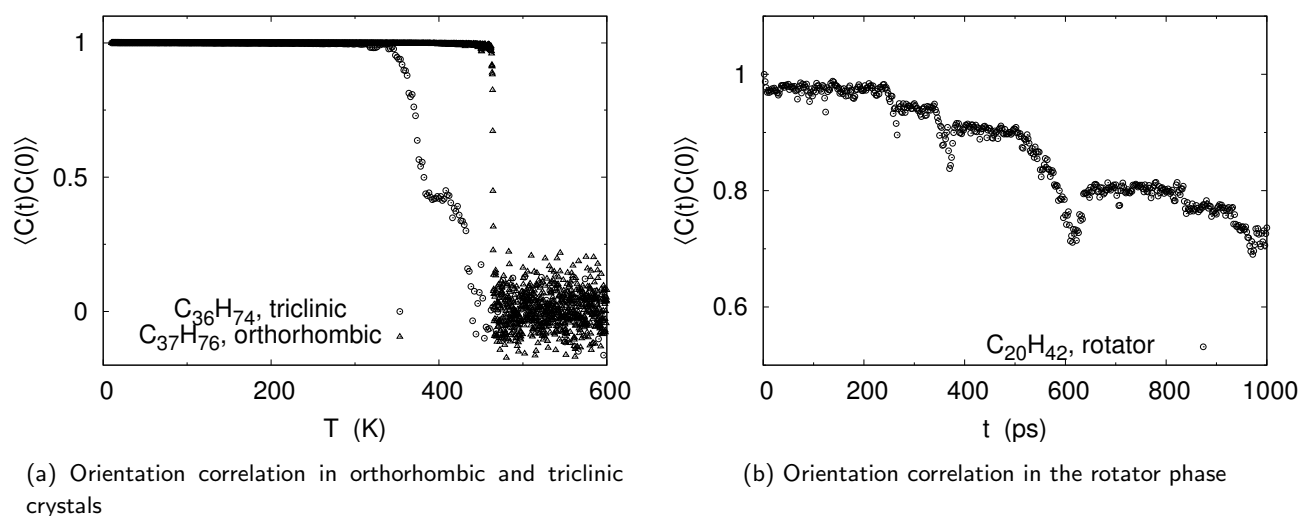


Figure 2.17: Orientation correlation of vectors perpendicular to the elongated chains' planes. In the case of dense crystalline packings, these vectors decorrelate only at the moment of melting. In the case of a “perfect” rotator phase well below the melting point ($C_{20}H_{42}$ at $T = 250$ K here), the correlations decay in time even without a phase change in the system, indicating there is no stable orientation of the chains in this rotator phase.

more gradual transition. Another qualitative effect of the heating rate on the system's configuration is seen from the small jump in the volume that occurs above 150 K for the lowest heating rate, around 200 K for 10^{-3} K ps $^{-1}$, and does not appear for the fastest rate. This small jump takes place when the thermal fluctuations enable the two layers to separate in order to lower the overlap of hydrogen atoms at the interface; this arises from finite-size effects in the simulation, since this change would not be possible anymore in the case of a larger or less symmetric system (several crystalline domains surrounded by amorphous material). The main transition that occurs above 350 K in this case (with the slowest rate) is in fact decomposed into two steps, which is indicated by a slight slowing down halfway between the crystal and the liquid, which is characterized by a higher thermal dilatation coefficient. This break in the volume increase corresponds to a transient rotator phase that forms before the system melts completely. The same observation can be made for systems with different chain lengths for which the same temperature protocol was applied; for triclinic crystals as well as for orthorhombic systems, a rotator phase occurs prior to complete melting, which is in agreement with experiments. Figure 2.20 compares the phase diagrams for the orthorhombic and triclinic structures of odd and even numbered *n*-alkanes, $C_{36}H_{74}$ and $C_{37}H_{76}$.

Some more insight into the solid-solid orthorhombic-rotator phase transition is provided by fig. 2.21 which presents different order parameters measured throughout the melting simulation of an orthorhombic crystal of $C_{15}H_{32}$. As explained above, the quantity $\langle C(t) \cdot C(0) \rangle$ accounts for orientation correlations in time—or equivalently presented as a function of temperature here—and exhibits a quick decay as the

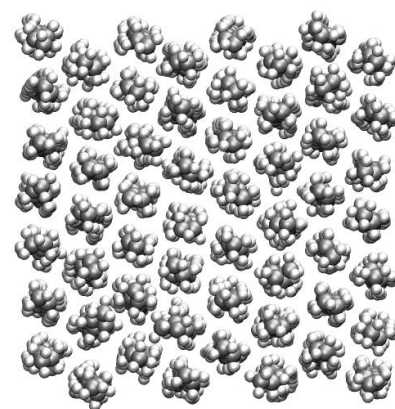
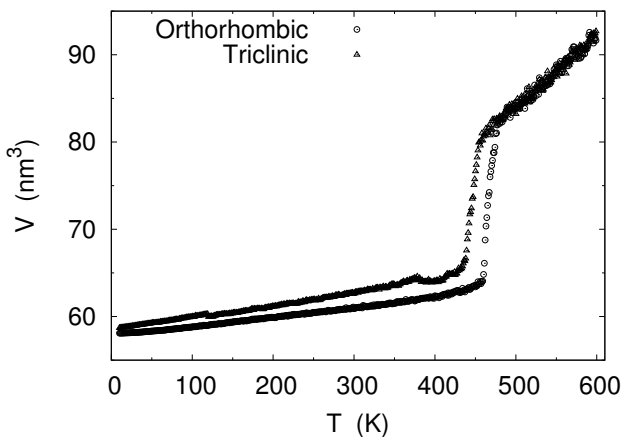
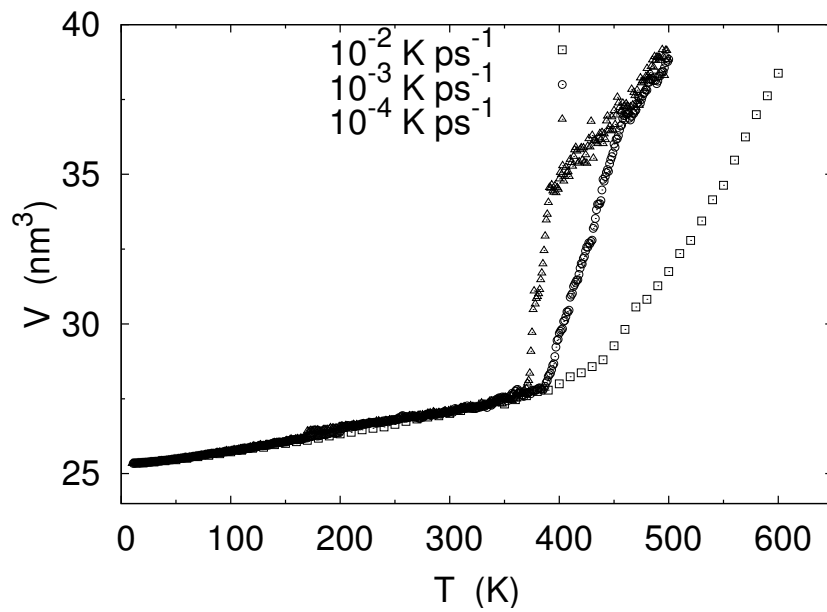
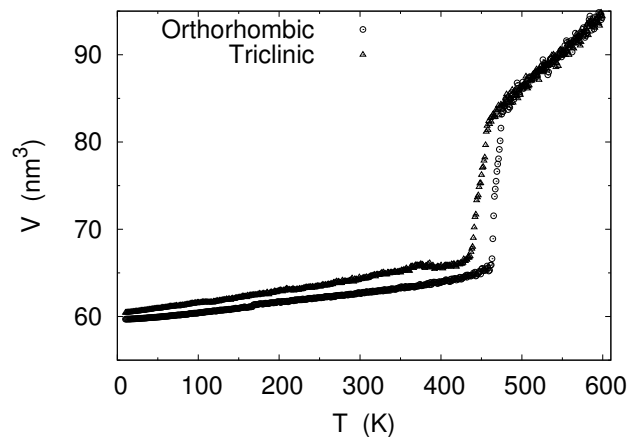


Figure 2.18: Snapshot of the rotator phase for $C_{20}H_{42}$ at $T = 250$ K. Note the hexagonal symmetry and the random orientation of the chains.

Figure 2.19: Comparison of phase diagrams (volume as a function of the prescribed temperature) for different heating rates (orthorhombic $C_{15}H_{32}$). For the lowest rate, the system clearly exhibits a first jump above 150 K when the thermal energy is high enough to overcome the pressure and separate the layers, and during melting a “pause” halfway between the orthorhombic crystal and the liquid state that corresponds to the occurrence of the rotator phase.

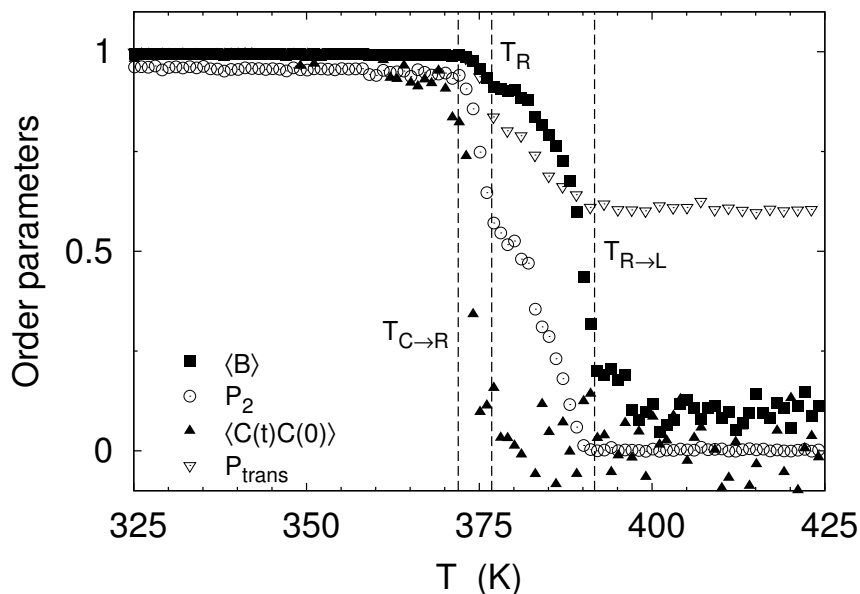


(a) $C_{36}H_{74}$



(b) $C_{37}H_{76}$

Figure 2.20: Comparison of phase diagrams for orthorhombic and triclinic crystals of $C_{36}H_{74}$ and $C_{37}H_{76}$. In each case, the orthorhombic form seems to be more stable, as it melts at higher temperature. The bump one can notice prior to melting for triclinic crystals corresponds to an inversion of the a and b lattice parameters.



orthorhombic phase is left. The degree of ordering in the system measured by P_2 decreases rapidly immediately afterwards and then slows down since the rotator phase is still ordered, with one strongly favored direction for the chains' overall elongation. The decrease in this order parameter is caused by the occurrence with the rotator phase of *gauche* defects, as shown by the drop of P_{trans} to a value different from 1, which was not possible as long as the chains were trapped in the all-trans conformations imposed in the crystal. The last degree of order that remains after the chains have relaxed to the amorphous liquid state is the orientational order measured by $\langle \mathbf{B} \rangle$, which takes longer to relax. After the rotator phase disappears in favor of the liquid state, P_2 quickly falls to zero, while P_{trans} takes its average value and $\langle \mathbf{B} \rangle$ slowly tends to zero, meaning that there is a signature of the previous existence of an ordered phase for a longer time.

The transient phase that appears while the system turns into a liquid is characterized by a change in the overall symmetry of the system: In the orthorhombic phase, the ratio of the cell lengths a and b is approximately 1.5, and jumps to $\sqrt{3}$ at the transition (fig. 2.24). This is the signature of a hexagonal phase and corroborates the fact that the rotational symmetry of the chains is recovered, which was already implied by the decay of $\langle \mathbf{C}(t) \cdot \mathbf{C}(0) \rangle$. It should be noted that the all-*trans* conformation of the chains in the crystal is progressively perturbed by the occurrence of *gauche defects* whose number increases exponentially as the rotator phase is approached; figure 2.22 shows the evolution of the probability for *gauche* states (both *gauche*⁺ and *gauche*⁻) in the vicinity of the transition.

The phase diagram of *n*-alkanes (fig. 2.20) exhibits a large jump that can be decomposed into two parts, a crystal-rotator transition first and then a rotator-liquid transition. It is thus possible to identify several

Figure 2.21: Different order parameters indicating the transition from the orthorhombic crystal to the melt, for $\text{C}_{15}\text{H}_{32}$. The first quantity that decorrelates is the orientation of chains' planes, as the system undergoes first an orthorhombic-rotator phase transition; then the overall order decays (P_2) and the general symmetry is restored (loss of a favored direction) while the probability of *gauche* states tends to its melt-characteristic non-zero value. The different temperatures associated with the transitions are indicated (cf. fig. 2.23).

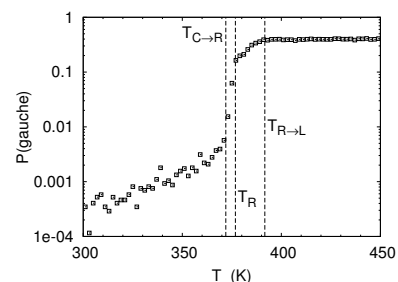


Figure 2.22: Evolution of P_{gauche} with temperature close to the transition, for $\text{C}_{15}\text{H}_{32}$. The number of *gauche defects* increases exponentially (logarithmic scale) before the transition to the rotator phase, indicated by a jump. The transition temperatures are defined in fig. 2.23

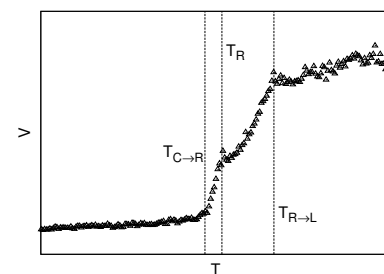
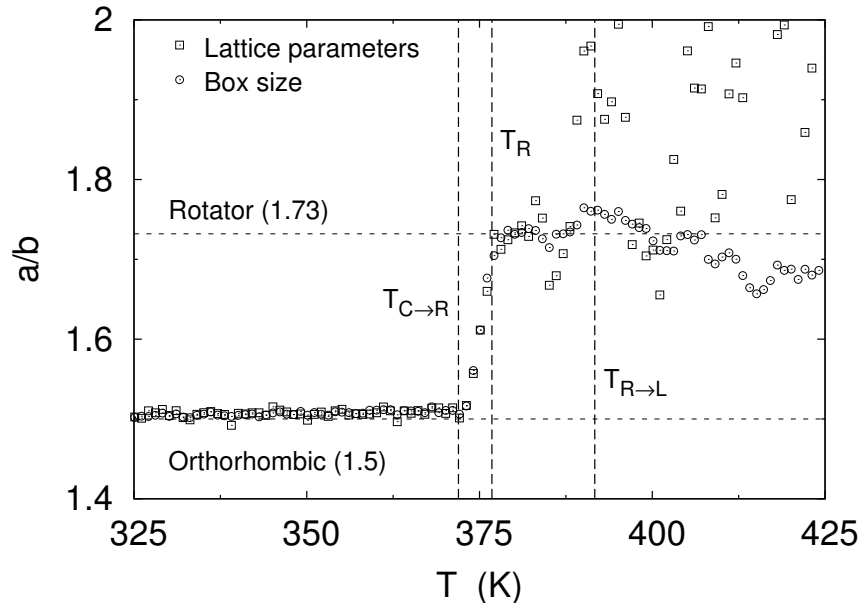


Figure 2.23: Definition of the temperatures associated with the observed phase transitions (for $\text{C}_{15}\text{H}_{32}$: Magnification of the third curve in fig. 2.19; symbols Δ , corresponding to heating rate $10^{-4} \text{ K ps}^{-1}$).

Figure 2.24: Ratio of the cell parameters a and b for orthorhombic $C_{15}H_{32}$ during continuous heating. This ratio is measured with two methods, using either the box size or a more local calculation taking into account the positions of the atoms in the original perfect lattice. The value at low temperatures characterizes the orthorhombic packing and does not significantly change below 350 K, indicating that the crystal thermally expands identically in both the x and y directions. At the transition, a/b shifts to $\sqrt{3} \approx 1.73$, which is typical of hexagonal packing, and therefore the sign of the rotator phase. The measurement based on the second method fails earlier as it is not valid anymore when crystalline order is lost. Temperatures from fig. 2.23 are indicated.



transition temperatures (fig. 2.23 gives an illustration): The first melting temperature $T_{C \rightarrow R}$ corresponds to the point at which the system leaves the regular crystalline (orthorhombic or triclinic) state and enters a transient phase. The system completely loses its long-range order and enters the liquid state after the second transition, at $T_{R \rightarrow L}$. In between these two temperatures, a hexagonal rotator phase appears, which is only a transient phase since at the high heating rates used for our studies, it cannot become stable. It is still possible to associate a temperature T_R with the occurrence of this phase, considering the change in symmetry it implies. The solid-solid phase transition involved here is characterized by a change in the ratio of the lattice parameters a and b as indicated in fig. 2.24. This can be used as a criterion to spot the rotator phase, and the third temperature characterizing the crystal-liquid transition of n -alkanes is defined as the point at which the ratio a/b exceeds a particular value: $\sqrt{3}$ in the case of orthorhombic crystal and 1 for triclinic structures (the difference in this ratio's value in the case of orthorhombic and triclinic crystals come from the preexisting lattice vectors a and b that are different and that evolve differently in each case).

The transition temperatures are presented in figs. 2.25(a) and 2.25(b); for odd- n systems, it can be seen that the experimental tendency for T_m is found qualitatively, with a sublinear increase of the melting point with chain length. It is also observed that the three measured temperatures follow the expected order, i.e. $T_{C \rightarrow R} < T_R < T_{R \rightarrow L}$. The rotator phase with hexagonal symmetry is found to appear shortly after the system has left its first crystalline order, and persists for a longer time before complete melting.

The situation is different in the case of even- n chains: The melting

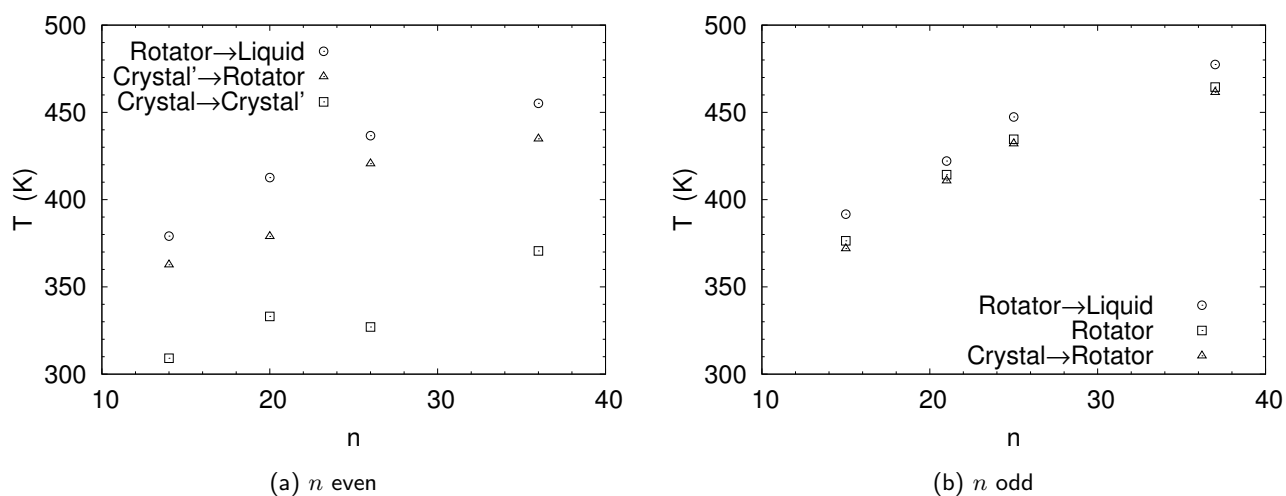


Figure 2.25: Melting temperature as a function of n for even- and odd- n chains. Three points are indicated for each chain length, corresponding to the temperatures at which the crystal is left (\triangle), the symmetry change associated with the rotator phase in the case of orthorhombic odd- n systems (\square), and the beginning of the liquid phase (\circ). In the case of even- n systems, the geometrical change occurs before the first melting point, which is inconsistent and in fact related to the instability of the crystal.

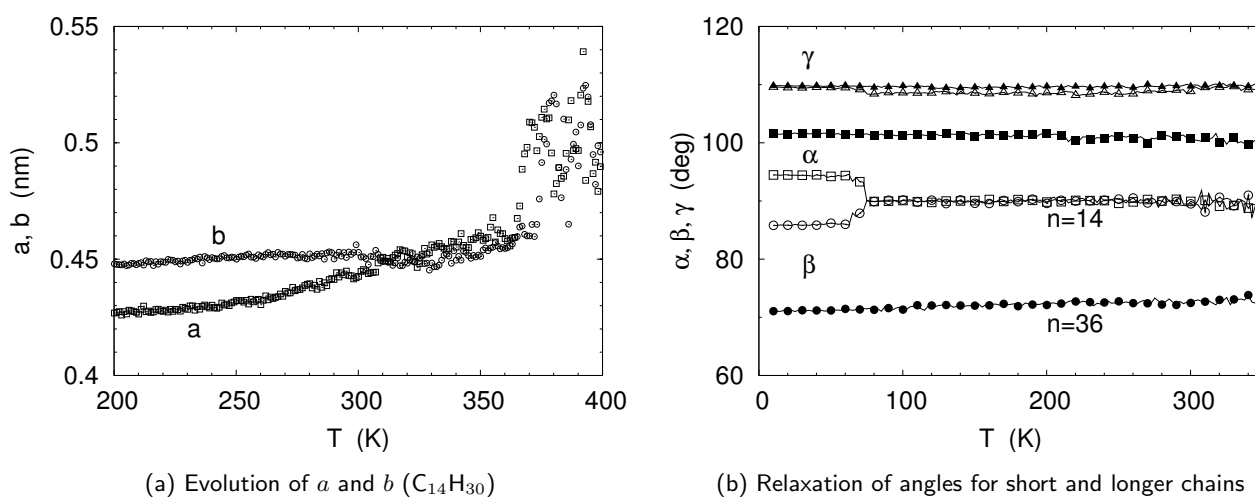


Figure 2.26: The instability of the triclinic crystal is illustrated by a change of the arrangement of the chains at around 310 K for short $C_{14}H_{30}$ chains (left); for such short chains, the tilted structure is already unstable at low temperature, since the angles α and β relax to 90° below 80 K. For longer chains ($C_{36}H_{74}$) the structure is stable (right). (α : \square ; β : \circ ; γ : \triangle . Open symbols: $C_{14}H_{30}$, closed symbols: $C_{36}H_{74}$)

temperatures $T_{C \rightarrow R}$ and $T_{R \rightarrow L}$ again agree with the experimental trend, but the rotator temperature lies outside of the interval $[T_{C \rightarrow R}, T_{R \rightarrow L}]$, which is inconsistent. This can be explained by looking at the evolution of the box size on approaching the transition: Figure 2.26 shows the lattice parameters as functions of temperature for triclinic crystals, exhibiting an inversion of the two lengths a and b more than 50 K before the transition. This change occurs because the system finds a more favorable packing by tilting the chains in another direction: The chains' planes are effectively rotated by an angle $\pi/2$, allowing to optimize the packing. This fact shows clearly that the triclinic structure is not a stable configuration for our n -alkane model; another evidence of that is given in fig. 2.26(b), which compares the angles α , β and γ for two triclinic crystals of different chain lengths. One can notice that for short chains ($n = 14$), the triclinic structure is not stable since even at low temperature α and β relax to 90° , whereas for longer n -alkanes ($n = 36$ here), the initial values of the three angles are conserved until melting occurs. The short-chain triclinic crystal has α and β angles that depart from the (experimentally found) prescribed values even at the very beginning of the simulation, as a result of a first relaxation right after startup; at $T \approx 75$ K, the system eventually turns into a monoclinic crystal—which is supposed to be less stable than the triclinic form for such short chains.

Figure 2.28 shows the relation between the inversion of a and b and the signal in the different quantities that usually indicates the occurrence of a hexagonal phase, in the case of $C_{36}H_{74}$: It can be seen that the ratio a/b exceeds 1 at the moment of the inversion, and then remains constant before increasing again to signal either a rotator phase or regular melting. The re-arranging of the chains prior to melting observed in the case of the triclinic crystals also accounts for the two-step relaxation of the chains' plane orientation correlation function shown in fig. 2.17.

Another possibility to study the crystal-rotator transition is to allow the system to relax at different temperatures during heating, as indicated in fig. 2.27. This way it becomes possible to observe the rotator phase that arises from the crystal configuration under constant temperature conditions. Figure 2.29(a) shows a first series of calculations at $T = 350, 360, 370, 380$ K: At $T = 350$ K, the system remains crystalline, and for $T = 380$ K it is already molten. At $T = 350$ K, one observes the transition to the rotator phase after 500 ps, and in this case the system remains in that state for approximately 1 ns before it melts completely. Another series of isothermal relaxations is presented in fig. 2.29(b), between $T = 350$ and $T = 360$ K, with steps of one degree. This does not permit to establish a transition temperature with such an accuracy however, since the 2 ns runs are too short to make sure that a system will not melt at a particular temperature. As a result of thermal fluctuations which may or may not help overcome the

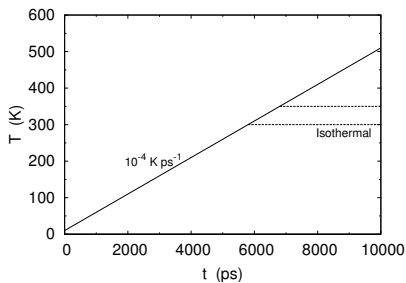


Figure 2.27: Schematic drawing of the temperature protocol used for simulations of n -alkanes: Isothermal runs are started at several points during a continuous heating.

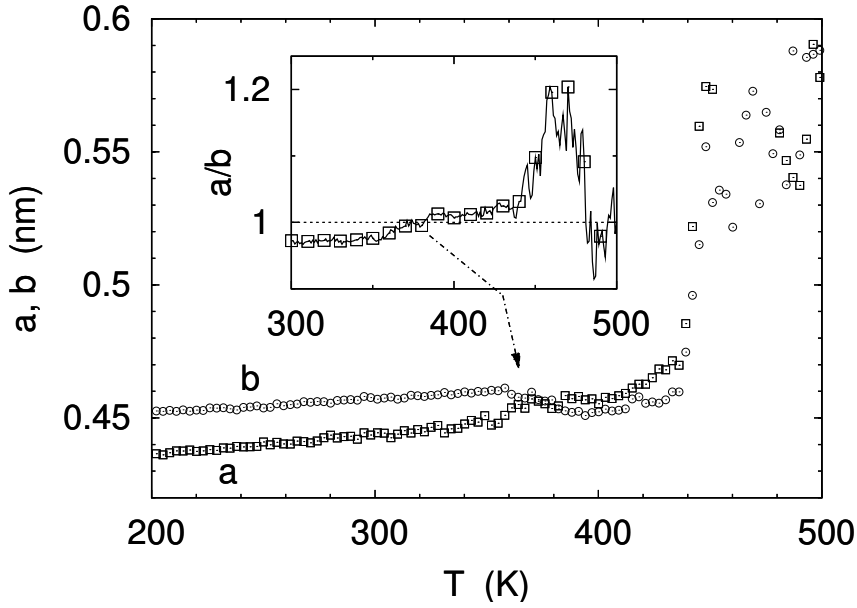


Figure 2.28: Evolution of the lattice parameters a and b with temperature during continuous heating: Above 360 K, a and b clearly switch, as a result of a recombination of the chains in the crystal. This phenomenon is reflected by an increase of the ratio a/b , which is plotted in the inset: The sudden change in the overall conformation of the crystal causes a/b to become greater than 1, which is supposed to indicate the transition to the rotator phase (symmetry change). This signal is present at $T \approx 450$ K, where the ratio increases quickly before the crystalline order is lost (making the measurements meaningless above $T_m = 455$ K).

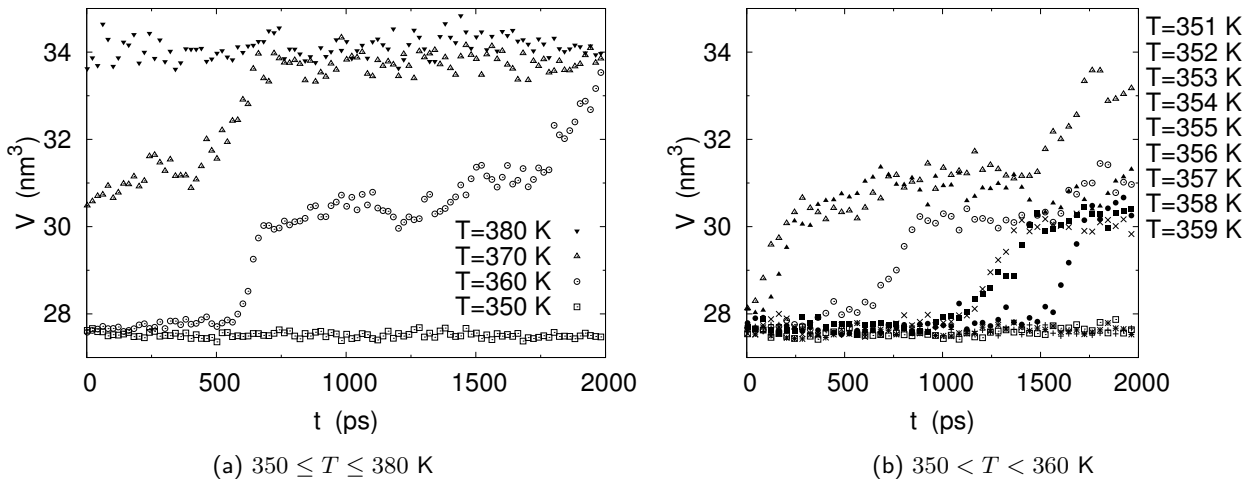


Figure 2.29: Evolution of the volume of the sample as a function of time for isothermal relaxations at various temperatures ($C_{15}H_{32}$). The crystal melts above $T = 350$ K; it becomes difficult to determine whether the systems melt for runs at $T = 351, 352, \dots$ K, since melting might occur after a much longer time than 2 ns. The system is observed to melt at $T \geq 352$ K, except for $T = 354$ K.

energy barrier, the system melts erratically at temperature T_1 and not at $T_2 > T_1$.

For isothermal relaxation as well as for the continuous heating above, an analysis of the different order parameters is possible during the phase transitions. This is the object of figure 2.30. As observed before, the orientation correlation for the chains' planes vanishes quickly as the rotator phase appears; there is even a precursor sign of this phase that shows up in $\langle \mathbf{C}(t) \cdot \mathbf{C}(0) \rangle$ since the beginning of the isothermal run, which means that defects (single “rotating” chains in the otherwise unperturbed crystal structure) can form as the transition temperature is approached. While in the rotator phase, the other order parameters

Figure 2.30: Order parameters indicating the transition from the orthorhombic crystal to the melt during an isothermal simulation at $T = 360$ K, for $C_{15}H_{32}$, as presented in fig. 2.29(a) (curve with \circ symbols). As was observed for the same quantities in a continuous heating, the orientation correlation in the plane perpendicular to the c -axis decays first, as the rotator phase sets in. The transition is less abrupt for the other order parameters, and the rotator phase is more stable under such conditions. It can be observed that in this case, the occurrence of *gauche* states precedes the loss of overall orientation that characterizes the complete melting of the solid system.

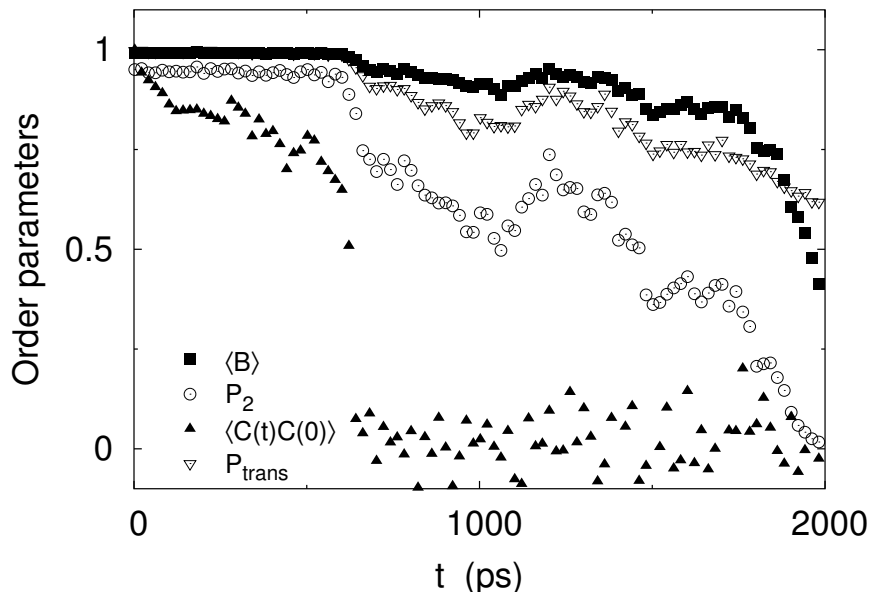


exhibit correlated fluctuations and finally decay.

2.4 Simulation of crystallization

2.4.1 Cooling experiment

A crystalline structure is obtained from a liquid either by cooling below its melting point, or by quenching it to a low temperature and let it relax so that a new equilibrium crystalline state is reached. We performed both kinds of experiments with systems consisting of several chains of alkanes with different chain lengths.

A summary of the simulations that were run as an attempt to reproduce homogeneous crystallization is presented in table 2.5. The number of chains and the total number of particles for each studied chain length are shown, as well as the range of temperatures for the cooling and the associated rate. Systems of n -alkanes with n ranging between 8 and 44 were studied, with total number of particles between 3000 and 13000 (many systems were created to study the melting of perfect structures in the first place, as discussed in sec. 2.3. Bigger systems with longer chains were especially designed for crystallization experiments upon continuous cooling). The cooling rates applied vary between -10^{-4} and -10^{-3} K ps $^{-1}$.³

For all experiments, the systems were prepared at high temperature (fully elongated chains ordered on an artificial lattice, allowed to relax (and thus to melt immediately) at $T = 500$ K), before starting the cooling. Figure 2.33 shows the evolution of $R_e^2(t)$ during this equilibration phase, showing that chains longer than $C_{16}H_{34}$ do not relax instantaneously. An equilibrium run has been performed at $T = 500$ K so as to

³Cooling rate -10^{-4} K ps $^{-1}$ corresponds to -10^8 K s $^{-1}$.

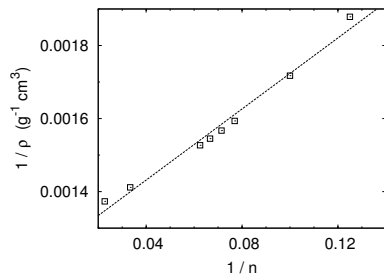


Figure 2.31: Inverse of the density at $T = 500$ K as a function of $1/n$. This shows that the volume can be expressed as $v = v_\infty + \Delta v_e/n$.

System	Chains	Nb. of atoms	T_i	T_f	rate
C_8H_{18}	256	6656	500	100	-10^{-4}
$C_{10}H_{22}$	100	3200	500	200	-10^{-4}
$C_{13}H_{28}$	243	9963	500	300	-10^{-4}
$C_{14}H_{30}$	72	3168	500	0	-10^{-3}
	72	3168	500	0	-2×10^{-4}
$C_{15}H_{32}$	72	3384	500	0	-10^{-3}
	72	3384	500	0	-2×10^{-4}
$C_{16}H_{34}$	84	4200	500	0	-10^{-3}
$C_{30}H_{62}$	144	13248	500	300	-10^{-4}
$C_{44}H_{90}$	100	13400	500	200	-10^{-4}

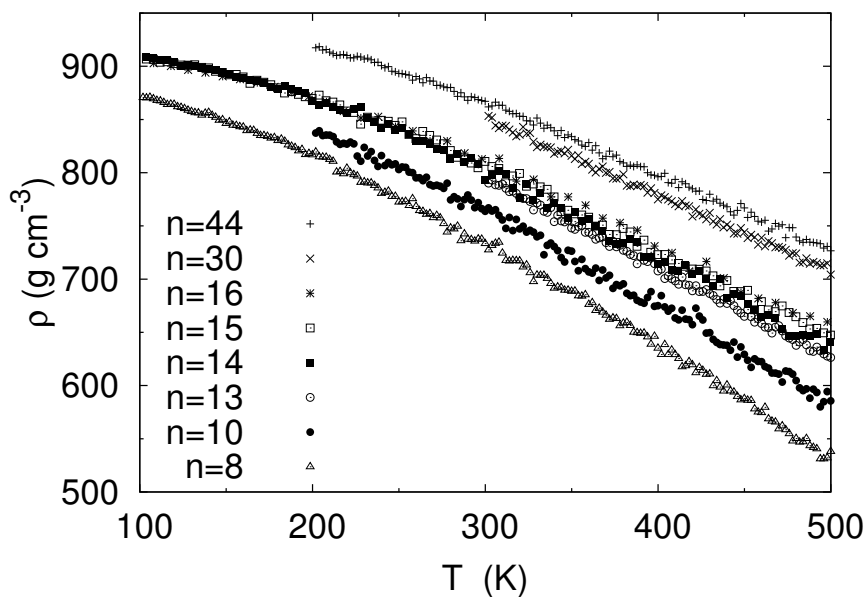


Table 2.5: Summary of the cooling experiments carried out for different chain lengths. For each value of n , the initial and final temperatures T_i and T_f are indicated, as well as the cooling rates used (respectively in K and $K \text{ ps}^{-1}$, see table 2.1).

Figure 2.32: Evolution of the density as a function of temperature while cooling down the systems. All curves exhibit the same trend, showing no abrupt transition as one would expect in the case of crystallization. However, there is a noticeable reduction of the slope as the systems freeze at low temperature.

make sure that the initial “crystalline” configuration does not influence the simulation. As is observed in fig. 2.32, the evolution of the density of the samples is qualitatively the same for all chain lengths, and there is no apparent phase transition. The influence of the cooling rate on these experiments is shown in fig. 2.34(a), which presents volume vs. temperature for a system consisting of 72 chains of $C_{14}H_{30}$, cooled down at -10^{-3} and $-2 \times 10^{-4} \text{ K ps}^{-1}$. There is no significant change for a cooling rate five times smaller, and one would probably have to use cooling rates orders of magnitude smaller in order to observe crystallization using such a model.

Looking at the configurations created while cooling down the alkane melts, it is still possible to find precursors of a growing ordered phase in a particular range of temperatures. For some systems in our studies ($C_{16}H_{34}$ and $C_{44}H_{90}$), the observation of a quantity such as the mean-square radius of gyration R_g^2 that accounts for the extension of chains reveals a (slight) tendency of the chains to organize as the temperature is lowered. This is related to an ordering of the chains that try to stretch and form a crystal. However, this trend quickly disappears as the temperature is lowered further; the cooling is too quick to let the

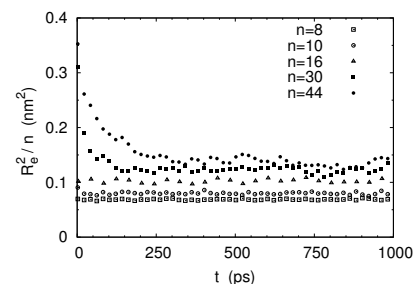


Figure 2.33: Relaxation of the end-to-end vector during the initialization part of the simulation. Very short chains do not display a particular change, indicating that they instantly melt. Longer chains take more time to relax.

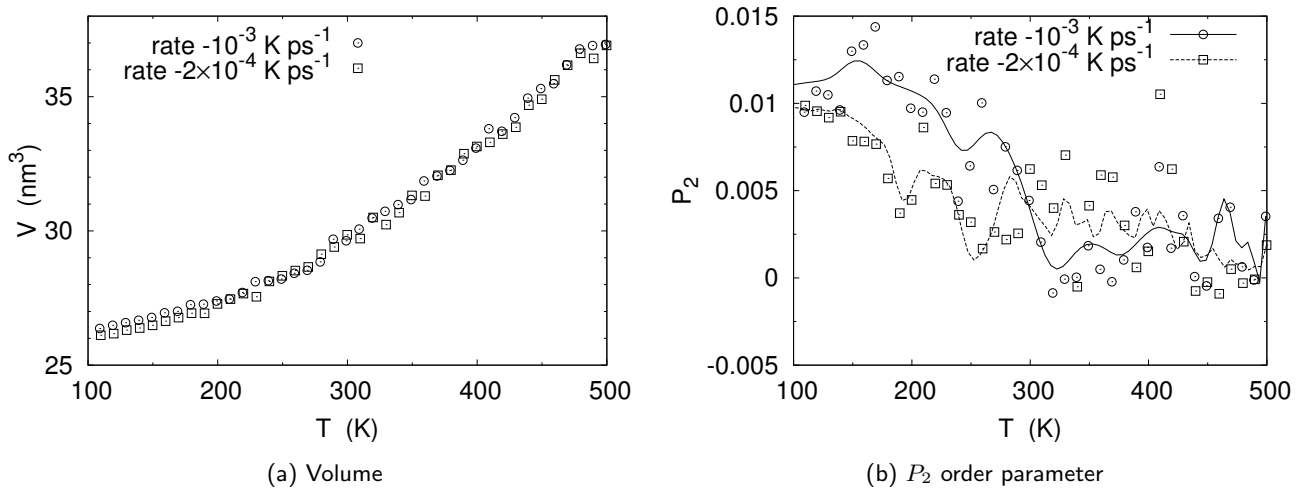
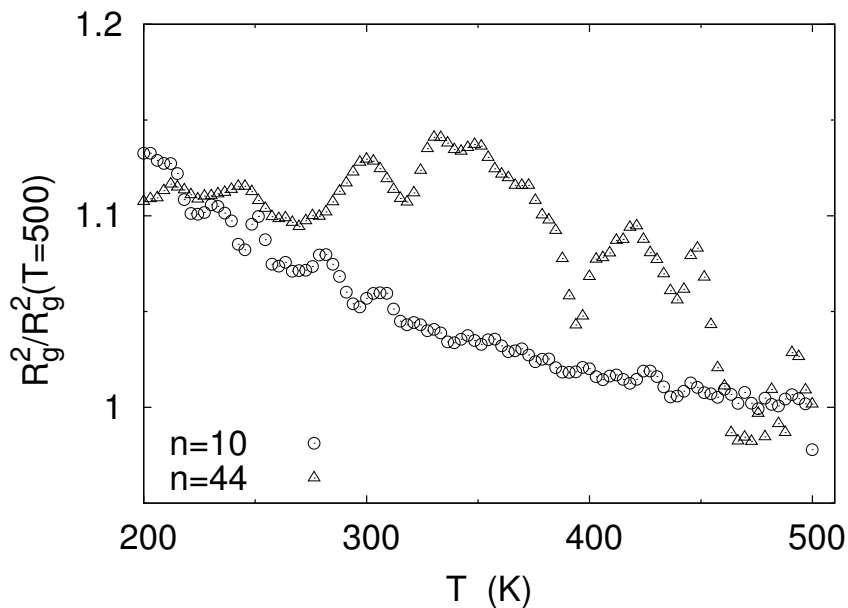


Figure 2.34: Volume and order parameter as a function of temperature while cooling down a system consisting of 72 chains of $C_{14}H_{30}$. The two curves correspond to two different cooling rates, -10^{-3} and -2×10^{-4} K ps $^{-1}$. The behavior of the volume does not significantly vary under the decrease of the cooling rate by a factor 5, still leading to a frozen state at low temperature; the order parameter either does not exhibit a big difference for the two rates. (Smoothed lines are drawn to guide the eye in the second plot.)

Figure 2.35: Variation of the mean-square radius of gyration with temperature, for two chain lengths ($n = 10$ and $n = 44$). In the case of short chains (this is also observed for $n = 8$), there is a steady increase of the radius of gyration during the cooling. For $n = 44$, on the other hand, a more complex behavior of R_g^2 shows that there is a slight tendency for the chains to stretch as the temperature is lowered, which is later hindered as the lowest temperatures are reached. The same fact is observed for other (smaller) chain lengths, but not for $n = 30$ (i.e. this is not related to larger chain lengths). The mean-square radii are divided by their average value at temperature $T = 500$ K, to allow for an easier comparison.



chains relax and organize; they rather start to freeze. Then R_g^2 drops and takes values comparable with those measured in cases for which no particular signal is observed during cooling—the chains simply get stiffer and stiffer until they eventually freeze ($n = 8$, $n = 10$, $n = 30$). This effect is probably not connected to chain length but rather to configurations that are favorable or not to the appearance of a seed for the growth of ordered structure. This emphasizes the small probability for a melt to crystallize under such high cooling rates.

For our model OPLS-mod with an optimized torsional potential that yields a reasonable proportion of *trans* and *gauche* states in the liquid

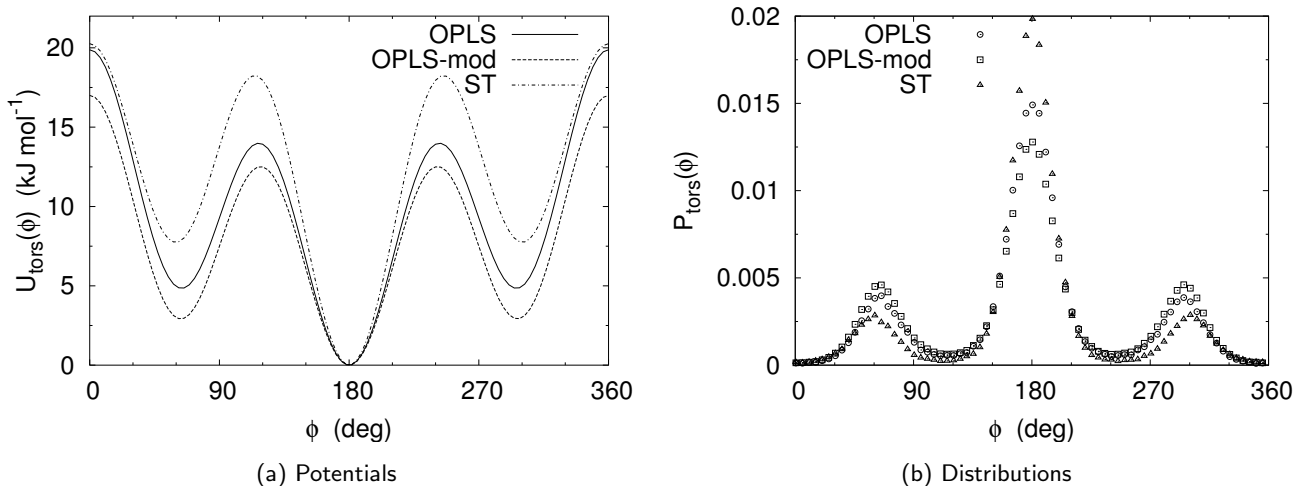


Figure 2.36: Comparison of the original and modified OPLS-AA torsional potential (sec. 2.2.1.3) with the ST potential. This last potential is much stiffer than the other two, as indicated by the corresponding P_{trans} at $T = 500$ K: $P_{\text{trans}}(\text{OPLS}) = 0.65$, $P_{\text{trans}}(\text{OPLS-mod}) = 0.58$, $P_{\text{trans}}(\text{ST}) = 0.75$.

state, it is actually difficult to reproduce a crystalline structure, since the *trans* state is favorable enough at very low temperatures only. A high proportion of *trans* states is necessary to form elongated chain conformations, but still a high enough thermal energy is needed so that the different rigid chains can assemble into an ordered structure. In order to get a comparison and check whether our cooling simulations can actually produce crystalline structures or not, we used a variation of the force field with a very unrealistic torsional potential that favors strongly the *trans* state. This model, which we will call “ST” in the following, has a probability P_{trans} of 0.75 at $T = 500$ K, whereas OPLS-mod yields $P_{\text{trans}} = 0.58$ under the same conditions. This arises from unrealistically high barriers between *trans* and *gauche* states. The point here is to compare our model to an extreme case in which the probability to form the stable all-*trans* conformations is very high. The different torsional potentials are shown in fig. 2.36, together with the corresponding distributions taken from equilibrium simulations.

The phase diagram obtained for this ST model is compared to the volume vs. temperature plot for $\text{C}_{16}\text{H}_{34}$ in fig. 2.38(a). It can be seen that a phase transition occurs around $T = 350$ K for that very stiff model, which contrasts with the behavior of OPLS-mod that does not exhibit any jump in the volume. There is a noticeable change in the slope at the transition, but there is still a big difference with the ideal, sharp phase transition for which an infinite slope is expected; this is a sign that the cooling rate we used here is much too large. The cooling rate in the case of this simulation of ST was -10^{-4} K ps^{-1} , which is smaller than the rate used in the simulation for the modified OPLS model to which it is compared in fig. 2.38; but we expect this difference not to be relevant, since fig. 2.34(a) shows there is no appreciable change in this range of cooling rates for OPLS-mod.

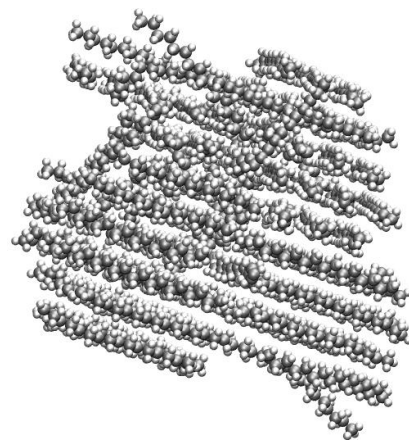


Figure 2.37: Snapshot of the final structure obtained by cooling of the ST model with very rigid torsional potential. The crystal exhibits two stacks of elongated chains, and additional ordered parts.

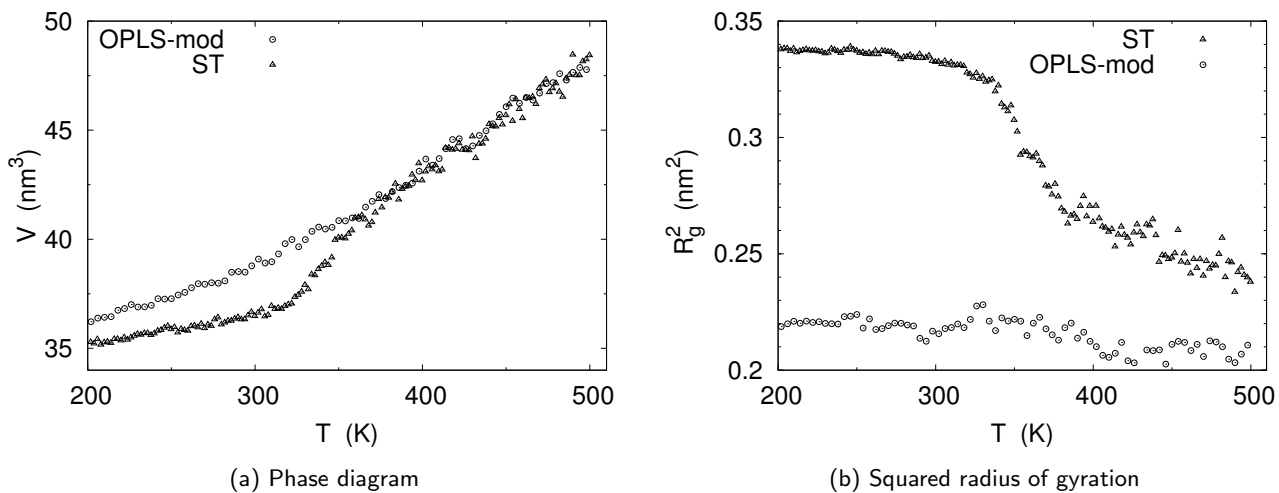


Figure 2.38: Volume and R_g^2 as functions of temperature for $C_{16}H_{34}$ simulated with the usual OPLS-mod model as well as with the ST torsional potential. In this case, a phase transition does appear, leading to the formation of a crystalline phase at around 350 K. This however is not consistent with experimental measurements that locate the *melting* point just below 300 K for this chain length (from ref. 118, see fig. 2.39).

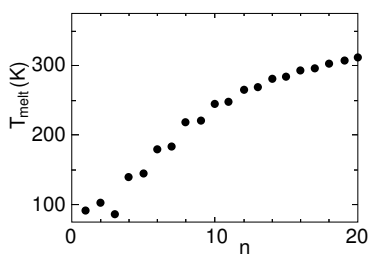


Figure 2.39: Experimental melting temperature for n -alkanes as a function of n .

The final crystalline structure obtained with ST is represented in fig. 2.37. One can observe the arrangement of almost perfectly elongated chains in two consecutive layers plus some other perpendicular, smaller structures. This crystal thus has features of a realistic alkane crystal and proves that our molecular dynamics simulations are capable of producing crystalline configurations via homogeneous nucleation from the melt; however, the ST torsional potential is much too stiff and its use leads to the unrealistic formation of a crystal, moreover at a very high cooling rate, at a temperature $T_{\text{cryst}} \approx 350$ K that is very large compared to the experimental *melting* temperature for $C_{16}H_{34}$, $T_{\text{melt}} \approx 300$ K.

2.4.2 Isothermal relaxation

As the cooling rates we could afford for all-atom n -alkanes models are too high to allow the crystalline structures to grow during continuous cooling, we completed this study by isothermal relaxations starting from the configurations saved during cooling to several temperatures. This way the simulation mimics the experimental situation corresponding to a quench to a temperature below the melting point, at which the crystal can then develop. The time-temperature protocol is depicted on fig. 2.40. This procedure was applied to a system of very short chains, C_8H_{18} , at temperatures ranging from 230 to 180 K, in steps of 10 degrees. The experimental melting point is about 220 K; so one expects the crystal to form when the system is supercooled at temperatures below T_{melt} . Figure 2.41 presents several properties measured from these simulations, showing that there is no sign of ordering at temperatures lower than the experimental T_{melt} : The volume never

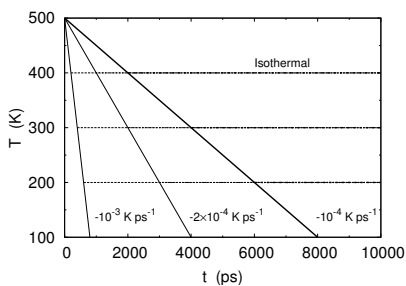


Figure 2.40: Schematic drawing of the temperature protocol used for simulations of n -alkanes: Isothermal runs are started at several points during a continuous cooling.

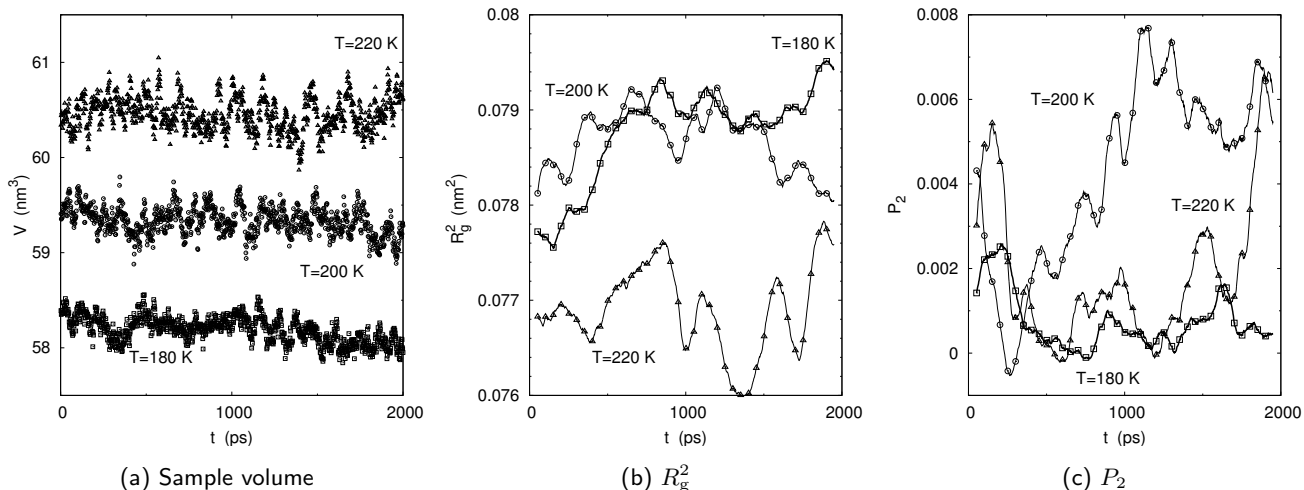


Figure 2.41: Characteristics of the C_8H_{18} liquid at different temperatures around and below the experimental melting point ($T_{\text{melt}} \approx 220$ K): $T = 230, \dots, 180$ K, every 10 degrees. The volume exhibits no abrupt change during these runs at constant temperature and pressure, and even though the system is not yet in equilibrium after 2 ns, as the volume decreases and the radius of gyration still increases, there is no sign of ordering in the order parameter P_2 , only somewhat larger fluctuations in the case of the lowest temperatures. Gliding averages (over 50 points) have been applied to the data for R_g^2 and P_2 , in order to reduce the noise. The indicated times are in ps, as indicated in table 2.1

exhibits a characteristic jump, nor does the radius of gyration of the chains increase in a significant manner. There is a somewhat larger increase in R_g^2 at the lowest temperature, but the P_2 order parameter tells us that this is not connected with an appreciable change of the structure of the melt.

It is possible that for such small chains the mobility does not decrease quickly enough for an ordered structure to develop; combined with the small stiffness of our model, this could explain that no crystalline phase arises. It may be necessary to probe the system at an exaggeratedly large supercooling in order to observe crystal formation, contrary to what one would expect for the small chains studied here.

The same procedure (cooling and isothermal relaxation) has been applied to the longer $C_{16}H_{34}$ chains, as part of the more systematic study of this particular chain length. In this case, isothermal runs were produced between 200 and 500 K, with steps of 50 K. The volume and mean-square radius of gyration are shown on fig. 2.42(a) and 2.42(b), and while there is no noticeable trend in the volume for any temperature, the radius of gyration displays an unusual increase at $T = 250$ K. For other temperatures, this quantity gradually increases on average with decreasing temperature, as expected; only its fluctuations become larger for smaller temperatures, except for the last two we probed, $T = 200$ and 250 K. At the lowest temperature, the fluctuations are much smaller, indicating that the system is starting to freeze. On the other hand, at $T = 250$ K, there is an interesting continuous increase in R_g^2 which shows that equilibrium is not reached during the 20 ns of this isothermal run. The fact that this tendency is not observed

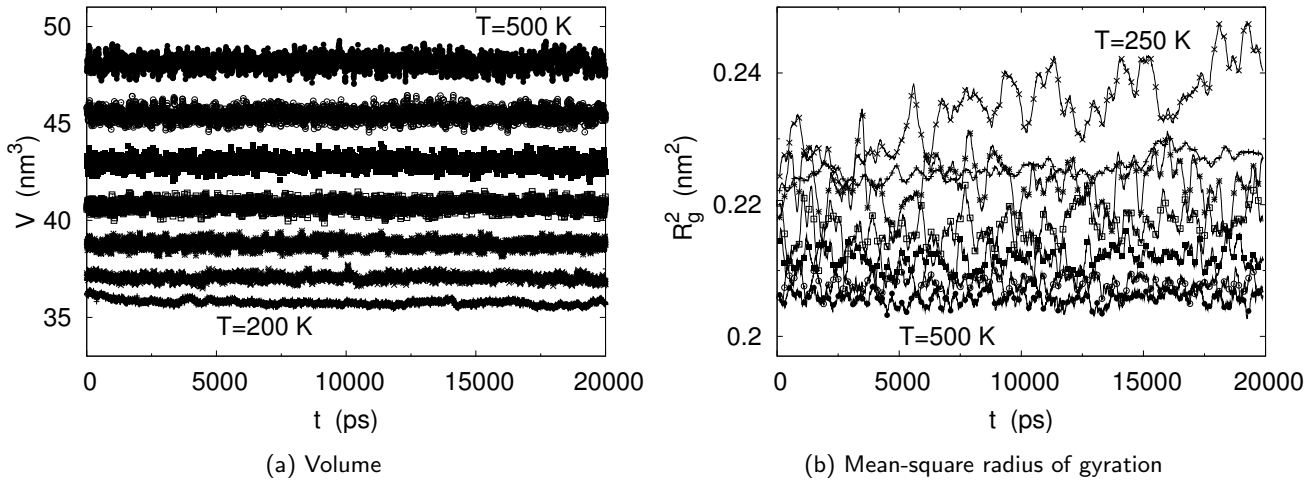


Figure 2.42: Volume and mean-square radius of gyration as functions of time for a system of 84 chains of $C_{16}H_{34}$, at $T = 500, \dots, 200$ K, every 50 degrees. The density increases in a natural fashion with decreasing temperature, and the volume does not show any jump characteristic of a phase transition. However, a significant increase of the mean-square radius of gyration can be observed at $T = 250$ K, and not at higher or lower temperatures. This is the sign for a change in the structure of the melt, even though there is no crystallization yet. A gliding average has been applied to the data for R_g^2 .

for higher or lower temperatures is an indication that there might be a phase transition occurring in the vicinity of this temperature. The increasingly large fluctuations of R_g^2 at temperatures higher than 250 K which then settle at 200 K also support this hypothesis, as fluctuations diverge at the critical point.

In order to investigate further what happens at $T = 250$ K, we calculated the P_2 order parameter for all temperatures, and the results are plotted in figs. 2.43(a) and 2.43(b). For the sake of clarity, only the three lowest temperatures are presented in the graphs, as there is no particularity for higher T : As observed for R_g^2 , the amplitude of the fluctuations of the order parameter increase as the temperature is lowered, except for $T = 200$ K where they are much smaller, and for $T = 250$ K where something different happens. It can be seen clearly that order is developing in the system at this particular temperature, after a latency time.

The two graphs of fig. 2.43 display the same quantity for two simulations with identical parameters except for the thermostating method, using Berendsen's algorithm (2.43(a)) in one case and the Langevin thermostat in the other (2.43(b)); see also sec. 2.2.2.2. In the simulation realized with the Langevin thermostat, order develops earlier and to a larger extent than with the other thermostating method. This could be due to a higher responsiveness of the Langevin thermostat that accelerates the dynamics. On the other hand, this is not clear since the two simulations at $T = 250$ K were started from different start configurations, which makes the comparison of the effect of thermostat difficult in this case.

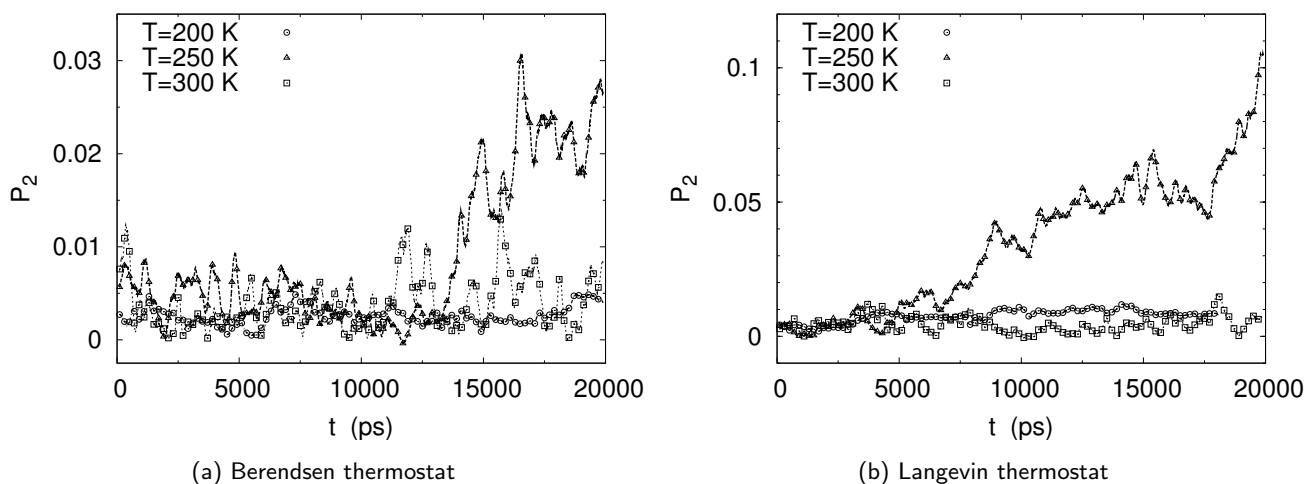


Figure 2.43: Order parameter P_2 vs. time for $C_{16}H_{34}$ at temperatures $T = 200, 250, 300$ K. Both graphs show the same quantity under the same conditions, except that in the first case the Berendsen thermostatting method was used, whereas the Langevin thermostat was applied in the second. Qualitatively the results are identical in each simulation: P_2 fluctuates more and more as the temperature is lowered, until T reaches 300 K, where the fluctuations are much smaller (The results for $T > 300$ K are not shown for clarity). At $T = 250$ K, an increase is noticeable in the average value of P_2 , suggesting that a phase transition may occur at a temperature between 200 and 300 K; if the Langevin thermostat is used, the increase in the value of P_2 is larger, and develops faster (note the difference in vertical scales). Gliding averages were applied to the data to reduce the noise.

2.4.3 Discussion

The study of crystallization of short n -alkane chains with an all-atom model is a time-consuming task, even for small systems. This is the reason why we could not access the crystal via homogeneous nucleation with continuous cooling experiments, since the affordable cooling rates are still orders of magnitude too large.

It is still possible to force the system to crystallize under these conditions using an unrealistically stiff torsional interaction which causes the chains to stretch very early during the cooling. This allows for the formation of a crystalline structure whose features are consistent with what is expected for such small chains. Nevertheless, the phase transition for this model takes place at a much too high temperature, even above the experimental melting point; this is a strong drawback of this model, and it is to be expected that the use of such a force field for crystallization experiments with much longer chains (as PE can be considered as the limit of alkanes for large n) would not yield sensible results. In particular, the too low proportion of *gauche* states would prevent the chains to fold and form lamellae, which is an important feature of polymer crystals.

The modified OPLS model we have been using for this study has a more reasonable proportion of *gauche* states at high temperatures as it was shown in sec. 2.2.1.3, but this also makes it less stiff and thus does not favor the fully stretched conformation of the chains that would enter the crystal. For this reason, crystallization could not be observed while cooling down at a high rate, and precursors of a phase transition could

only be observed after several nanoseconds of an isothermal run at $T = 250$ K (little less than 50 degrees of undercooling with respect to the experimental melting point). Fluctuations in the mean-square radius of gyration and the P_2 order parameter indicate that a phase transition should be observable between $T = 300$ and 200 K, but other isothermal runs and continuous cooling would be necessary to characterize the transition more precisely.

2.5 Simulations of polypropylene

2.5.1 Introduction

Motivation for studying polypropylene. Another polymer of key importance for industrial purposes is polypropylene (PP). In addition to being a component of many everyday-life objects, this material also has many interesting physical properties. Some of these arise directly from its crystalline structure at ambient temperature, making it widely used for plastic products. This polymer shows a very good resistance to chemical solvents, bases and acids. Its main industrial application comes from its ability to be injection-molded, yielding a semi-crystalline material whose mechanical properties permit many different uses. The structure of the polymer itself influences the arrangement of the molecules in the solid phase. The difference in structure of PP and PE, although small in chemistry terms, may have a great influence on the crystallization of the polymers due to a change in chirality (the monomers of PP are chiral, contrary to those of PE).

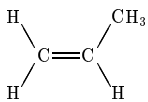


Figure 2.44: Propylene.

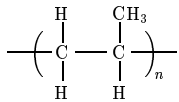


Figure 2.45: Polypropylene.

Some background from chemistry. Polypropylene is produced from propylene (fig. 2.44) through different methods, yielding chains with variable mass distributions, purity and stereoregularity. Polypropylene chains consist of a polyethylene-like backbone, with a methyl group substituting a hydrogen atom on every second carbon atom of this backbone. The overall chemical formula of the pure polymeric material is C_nH_{2n+2} , as for polyethylene. This hides the important difference between PE and PP: The change arises from the methyl groups, giving the polymer stereospecific properties. There are three possible stereoregularities which also correspond to different physical properties:

- Isotactic polypropylene has all methyl groups on the same side of the chain (fig. 2.46(a)).
- syndiotactic polypropylene presents an alternate configuration of methyl groups along the chain (fig. 2.46(b)).
- Atactic polypropylene consists in a random arrangement of both tacticities.

The tacticity of the polypropylene chains is determined by the process through which polymerization of propylene units is achieved. As

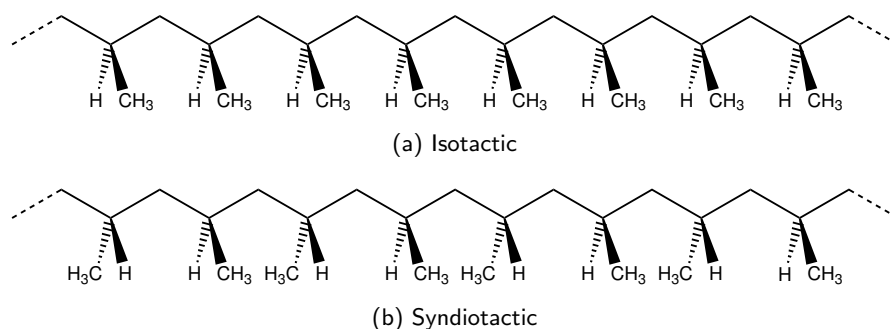


Figure 2.46: Chemical formulae of isotactic and syndiotactic polypropylene. Note that the methyl groups are always on the same side of the chain in the isotactic PP, but alternating in the syndiotactic form.

there are several ways of polymerizing propylene, some methods do not impose any stereoregularity and therefore yield the atactic stereoisomers of polypropylene. By contrast, the Ziegler-Natta polymerization method allows to select a certain stereo-specificity of the resulting macromolecules. The use of a TiCl_3 crystal and AlEt_2Cl as Ziegler-Natta initiators forces the generated polymer to grow with methyl groups all on the same side of the chain, corresponding to the isotactic form of the molecule. The use of other catalysts allows to produce the syndiotactic species by enforcing an alternating orientation of the methyl groups.

Isotactic and syndiotactic polypropylenes (iPP and sPP) have a stereoregular structure that makes the organization of the chains in a crystal easier. In particular, steric effects greatly favor the formation of a helical structure in the case of iPP, which results in a crystalline structure composed of both left- and right-handed helices [92].

Crystalline phases of PP. Stereoregular polypropylene chains exhibit a wealth of different crystalline phases that have been extensively studied [64].

The iPP chains are composed of a mixture of *trans* (*t*) and *gauche* (*g*) torsion angles of the carbon backbone, as is the case for polyethylene. As the temperature is lowered, energy minimization favors the sequence *tgtgtg...*, which leads to the formation of 3_1 helices. The isotactic polypropylene crystals are found in three specific forms, which are:

- The α phase, consisting of left- and right-handed chains in a monoclinic cell (angle $\beta \approx 100^\circ$). The chain axes are parallel, and alternate layers of left- and right-handed chains were identified.
- The β phase, which is a frustrated arrangement of left-handed (or right-handed) chains only, and has a trigonal unit-cell.
- The γ phase, which is similar to the α phase and usually mixed with it in the same crystallites; the difference consists in a tilt of about 80° between the axes of left- and right-handed chains.

Syndiotactic polypropylene has a structure that does not require the formation of helices for energetic reasons, because the all-*trans* configuration does not imply steric overlaps as in the case of iPP. This could therefore be expected to be the ground state for sPP, which would then tend to crystallize as PE chains. However, it has been observed that another structure is actually privileged at low temperatures, as the crystals are formed of helical chains: The helices are not of the 3_1 type as in the case of iPP, but rather consist in a sequence of $g^+ g^+ ttg^- g^- tt \dots$ states. Two crystalline structures are observed experimentally:

- An isochiral phase, composed of left-(or right-)handed helices only, obtained either under shear or at high pressures;
- an antichiral phase with alternating left- and right-handed helices, which is more stable at atmospheric pressure and high temperatures.

2.5.2 Definition of the model

As a first attempt to simulate PP melts, we used the parameters of the force field described above for *n*-alkanes. This certainly represents an over-simplification of the structure of PP, but might already give an idea of the behavior of such a polymer at high temperature and under cooling. This corresponds to a simplification of the model prescribed by the OPLS force-field, but we expect the rotation about the C–C bond that links a methyl group to the backbone to be unimportant for the description of polypropylene melts. The excluded volume due to this side-group on the other hand has high importance for the chains' packing. The parameters are exactly the same as described in sec. 2.2.1, without any specific features taken into account for the methyl groups. This means that the rotation of the methyl group around the C–C bond that links a backbone carbon to a methyl carbon is not constrained by an explicit torsional potential, and that the torsional interaction between consecutive backbone carbons is not explicitly modified to take into account the specificity of PP. This would certainly deserve improvement. Here we take the stance that most of the characteristics of polypropylene chains result from steric effects associated with the presence of the methyl groups.

2.5.3 Simulation details

We simulated both isotactic and syndiotactic PP chains, in systems containing 84 $C_{22}H_{46}$ molecules. The constituent chains consist of 6 repeat units ($-CH_2-CH(CH_3)-$), plus a “head” (one methyl group CH_3-) and a “tail” (one propyl group $-C_3H_7$). Figure 2.50 shows a representation of an iPP chain with its “head” and “tail”. The structure of the head and tail parts was given by looking at the initial and final conditions of the Ziegler-Natta reaction. Figures 2.47 and 2.48 show

snapshots of one chain of iPP and sPP extracted from the simulations at high temperature.

The systems were created at high temperature ($T = 500$ K) and atmospheric pressure as a set of elongated chains positioned at the sites of a perfect (arbitrary) lattice, and then equilibrated after the immediate melting process occurring under these conditions. The all-*trans* configuration is a stable state for sPP, but not for iPP; in this case the steric interactions would yield a much too large energy, and the simulation would break down. Thus for iPP another initial configuration has to be used as input for the simulation program. One possibility would be to create the helical structure by hand, computing the positions of all the atoms in the molecule so that they conform to the ground state of iPP. However, this configuration is much more complicated than the all *trans* conformation that has been used for PE (and sPP with a slight modification to add the extra methyl groups). Therefore we used a trick to create the equilibrium iPP configuration from the simpler sPP-like all *trans* conformation: A method often used in simulation to anneal a system and provide a suitable initial configuration was adopted: The molecular interactions were turned off and gradually switched on during a short one-chain simulation, providing an equilibrated structure that could be duplicated to create an appropriate initial configuration to be simulated as explained above.

The melt equilibrated at high temperature has been cooled down to $T = 200$ K, at two different cooling rates (-10^{-4} and -10^{-5} K ps $^{-1}$).

2.5.4 Preliminary results and outlook

The very small chains used in this preliminary study obviously do not allow to form folded helical structures as observed experimentally. The main goal here was to extrapolate our PE model to a more complex, but still very simple polymer, and to attempt to form crystal precursors via continuous cooling. Crystallization was however not observed, perhaps due to a too crude model and the lack of enough time to let the system relax at low temperatures (it would have been interesting to carry out isothermal relaxations as we did for *n*-alkanes). Still, the few results we obtained present some interest as they provide an insight into the internal structure of polypropylene chains in the melt.

Torsions. As is the case for *n*-alkanes and PE—as well as for any kind of polymer—the torsional degree of freedom is the most important for the relaxation of polypropylene conformations. It is interesting to look at the probability distribution of torsion angles, and compare it for the two stereoregular polypropylene species and for the alkane reference. This is done in fig. 2.49, which shows such a probability distribution at $T = 450$ K, for iPP, sPP and PE. This comparison demonstrates that the simple assumption about the torsional potential we made for this very simple model yields results in agreement with what is expected

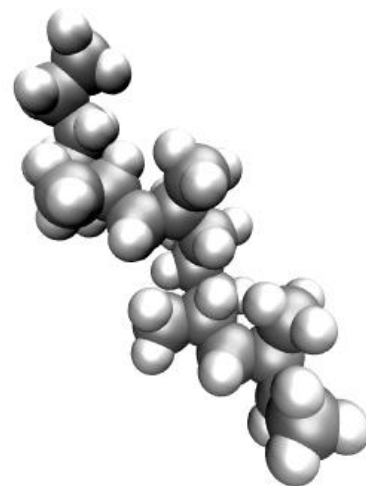


Figure 2.47: Short chain of isotactic polypropylene.

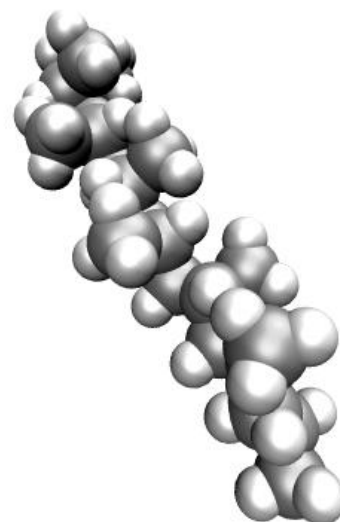


Figure 2.48: Short chain of syndiotactic polypropylene.

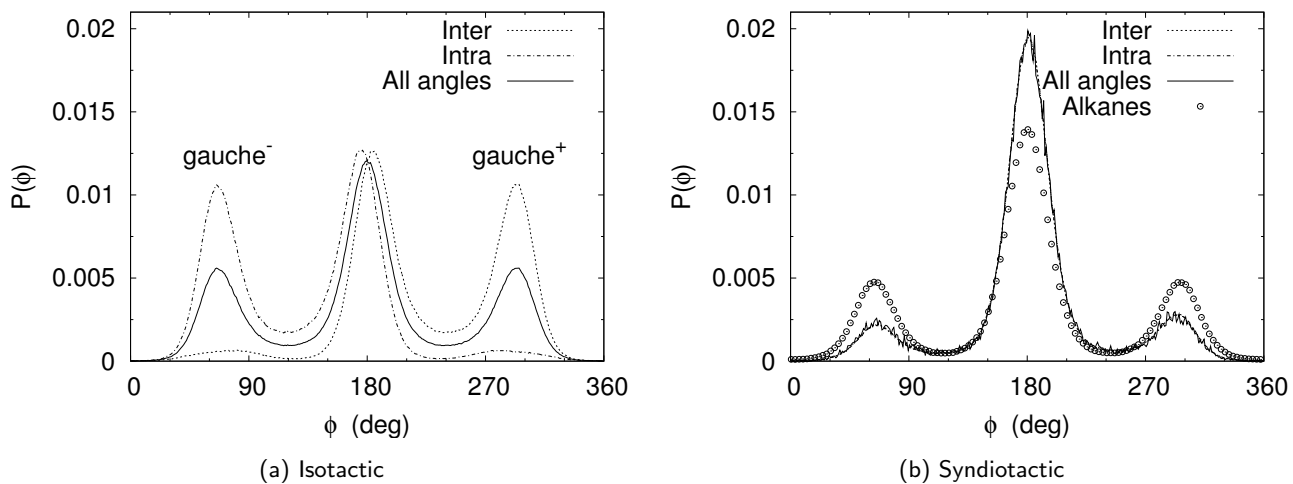
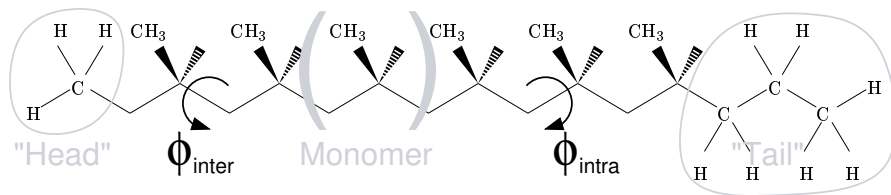


Figure 2.49: Probability distributions of torsion angles for iPP and sPP chains at $T = 450$ K. Full lines correspond to average distributions, taking into account all torsion angles inside the chains; the two other curves present partial distributions for either the “intra-” or “inter-monomer” torsion angles (see text for a definition). In the case of sPP, all torsions exhibit the same behavior, and a comparison with the same distribution obtained for n -alkanes ($C_{16}H_{34}$) at the same temperature shows that the presence of methyl groups make the chains much stiffer. For iPP, the situation is totally different as the chains are slightly less rigid than polyethylene, and depending on their position along the chain, angles are preferably $gauche^+$ or $gauche^-$. These tendencies balance in the average distribution which is symmetric.

Figure 2.50: Schematic representation of the *intra*- and *inter*-monomer torsions; one monomer as we defined them is stressed with brackets. “Head” and “tail” of the iPP short chain are also explicitly indicated.



for polypropylene: It can be seen from fig. 2.49(b) that the presence of methyl groups does not qualitatively change the torsion angle distribution, but strongly favors the *trans* state as this configuration allows to minimize overlaps of the different parts of the molecule. The fact that this distribution still exhibits the same features in the case of iPP is more surprising, as one would expect the chiral structure of the whole molecule to break the symmetry of the distribution. This appears not to be the case however (fig. 2.49(a)), and this is explained by decomposing the torsion angle distribution into two contributions, named *intra*- and *inter*-monomer. Figure 2.50 illustrates the different positions of the so-called *intra*- and *inter*-monomers; note that this distinction is arbitrary and completely connected to our conventions for labeling the different atoms. Figure 2.49(a) points out the fact that the distribution of *intra* and *inter* angles are completely different and compensate to yield the average $P(\phi)$. For each torsion angle, one *gauche* state is unfavorable because of the overlap of $-CH_3$ groups; this is reflected in the population of the other two states. The chain is thus composed of a sequence of *trans* and $gauche^\pm$ states, with alternate preference for $gauche^+$ or $gauche^-$ along the backbone. This result seems reasonable, but still at this point a more rigorous modeling of the torsional in-

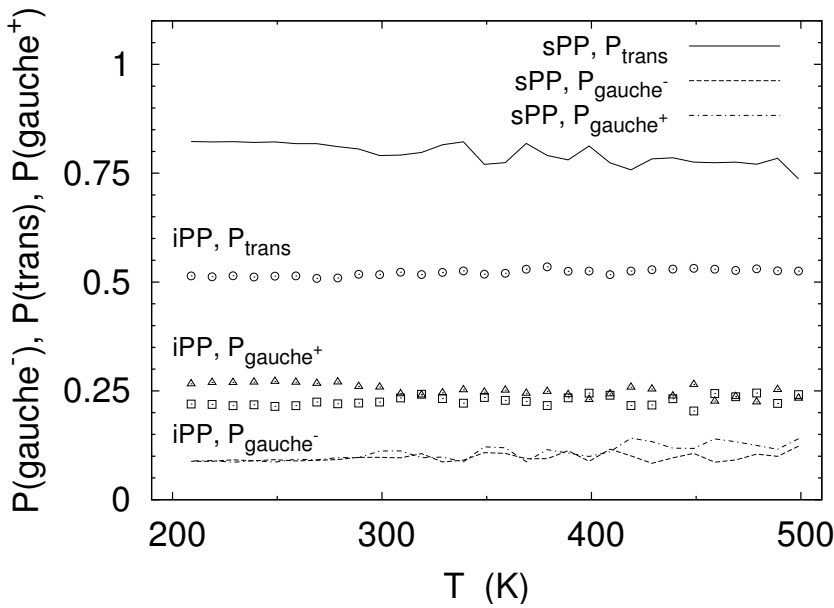


Figure 2.51: Evolution of the probabilities P_{trans} , P_{gauche^+} and P_{gauche^-} for isotactic (symbols) and syndiotactic (lines) polypropylene during cooling (rate 10^{-4} K ps $^{-1}$). For syndiotactic chains, only a slight increase in P_{trans} is noticeable from below $T = 300$ K when the melt begins to freeze. The probability of *gauche* states decreases accordingly, while P_{gauche^+} and P_{gauche^-} remain identical. In the case of isotactic polypropylene, the probability of *trans* states does not vary much, but a selection of *gauche* $^+$ over *gauche* $^-$ states occurs at low temperatures.

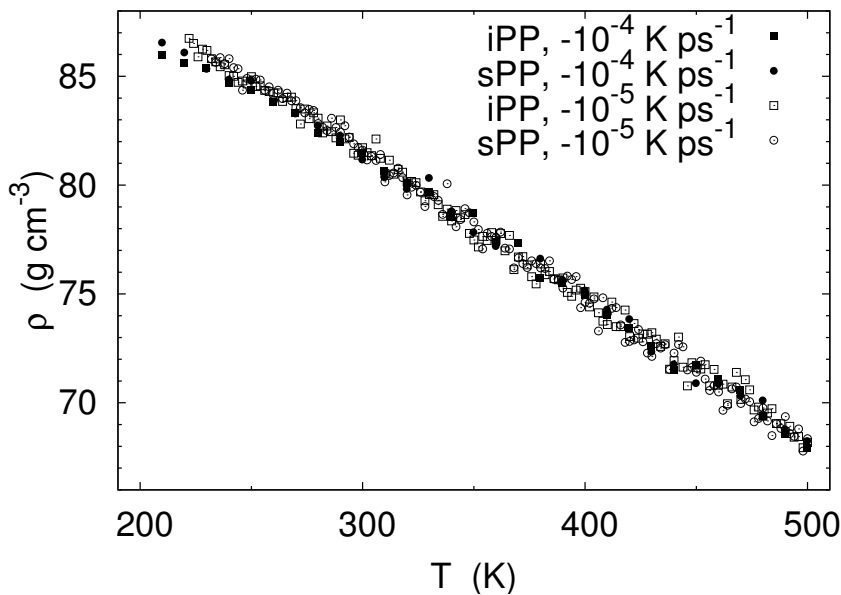


Figure 2.52: Density vs. temperature for isotactic and syndiotactic polypropylene cooled at two different rates. There is no important difference between the two tacticities or for cooling rates. The density does not exhibit any jump, and bends only slightly as the systems tend to freeze.

teractions would be needed to reproduce the correct helical structures accurately.

Another aspect of the evolution of polypropylene melts toward lower temperatures is presented in fig. 2.51: The probability of *trans* and *gauche* $^{\pm}$ states is plotted as a function of temperature during the cooling. In the case of sPP, there is a slight increase in P_{trans} and therefore a small decrease in $P_{\text{gauche}^{\pm}}$. This result is similar to what has been observed in the case of *n*-alkanes, to a smaller extent though. What is observed in the case of iPP is different: The probability of the *trans* state does not vary much, but the probabilities of *gauche* states split, showing a larger population of *gauche* $^+$ at low temperature. Although very small, this effect might be interpreted as the first sign of the formation of stable helical structures in the melt, with one favored *gauche*

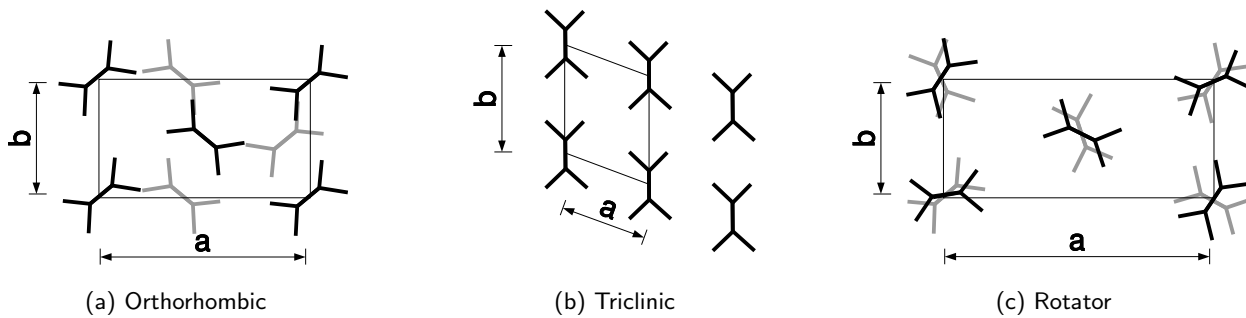


Figure 2.53: Different crystal structures of n -alkanes (fig. 2.9).

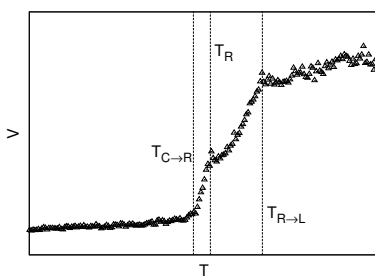


Figure 2.54: Phase diagram showing the different phase transitions (fig. 2.23)

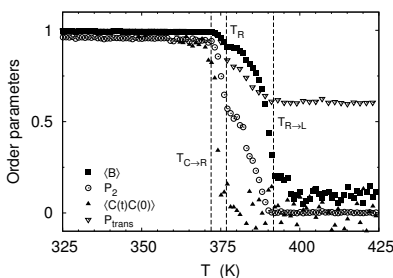


Figure 2.55: Order parameters during the transition from the orthorhombic crystal to the melt (fig. 2.21).

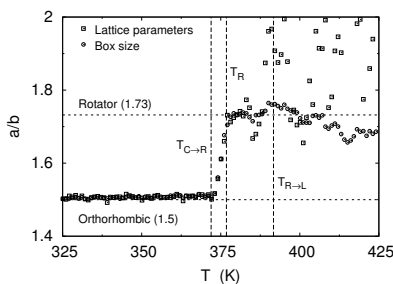


Figure 2.56: Ratio of the cell parameters a and b during continuous heating (fig. 2.24).

state ($gauche^+$ for *inter*-monomer torsions) and one favored *trans* torsion angle (*intra*-monomer).

Density. Continuous cooling has been applied to the melts of iPP and sPP short chains, in the same manner as it was introduced in sec. 2.2.2; the resulting density as a function of temperature is plotted in figure 2.52. Two different cooling rates were employed, -10^{-4} and -10^{-5} K ps $^{-1}$. There is no significant change associated with stereoregularity, i.e. the density appears to be identical for both iPP and sPP, as one can expect. There is no noticeable variation of the density with cooling rate either, except a slight change in the slope for the fastest rate which does not appear for slower cooling; this indicates a glass transition that occurs at higher temperature for larger cooling rate and is consistent with experiments—but the effect is very small.

2.6 Summary

We have been using an all-atom model to simulate short chains of n -alkanes in the melt; these systems are accessible to such detailed simulation scheme and may be considered as a first step in the study of polymer systems. The wealth of structures that are observed experimentally make n -alkanes very interesting systems for numerical studies. We tested the OPLS force field and modified the torsional potential in order to reproduce more closely the torsional angle distribution measured in another detailed study of polyethylene chains; using this new model we could attempt to simulate the melting and crystallization of n -alkanes.

The most common crystalline states for n -alkanes are orthorhombic and triclinic; experiments also revealed the existence of a solid-solid phase transition that led to the formation of an intermediate phase between the solid and the liquid, called the rotator phase (fig. 2.53). Our model was shown to successfully reproduce this phase transition and the occurrence of the rotator phase during continuous heating simulations starting from perfect crystalline configurations generated by

hand (fig. 2.54). Experimentally several rotator phases have been isolated and have slightly different features; our simulations only yield a generic rotator phase with hexagonal symmetry, but this is already an interesting finding since the simple model used is aimed at reproducing liquid state properties and could not be expected to give such an accurate description of solid phases *a priori*.

Evidence for the occurrence of the rotator phase include the decay of several order parameters that show more specifically the decorrelation of the orientation of the chains' planes before the loss of a privileged direction for the molecules (fig. 2.55); and the change from orthorhombic (or triclinic) to hexagonal symmetry before the transition to the molten state, as indicated by the characteristic jump in the ratio of the lattice parameters a and b (fig. 2.56).

The transition is also observed during isothermal relaxation, and in this case the rotator phase could be stabilized for at most 1 ns (fig. 2.57); this is still far from the behavior of n -alkane systems observed experimentally, as the rotator phase is found to be stable over a large range of temperature. This fact points out the limitations of the model: The force field used is not optimized for solid-state simulations, and the perfect, infinite crystalline configurations are not realistic; this leads to a much too high melting temperature observed in the simulations compared to experimental values.

Another study of the n -alkane crystals consists in trying to reproduce crystalline configurations from the melt via a cooling procedure. This approach did not prove very successful as a result of both the probable limitations of the model and the too large CPU time needed for such a detailed simulation scheme; cooling simulations only led to frozen configurations (fig. 2.58). However, it could be shown that a model with an unrealistic, stiffer torsional potential yields a crystallized structure upon cooling (fig. 2.59), and that using the OPLS-mod model a signal is observable in the order parameter characterizing the development of order in a supercooled n -alkane melt at intermediate temperatures between the frozen and the liquid states (fig. 2.60).

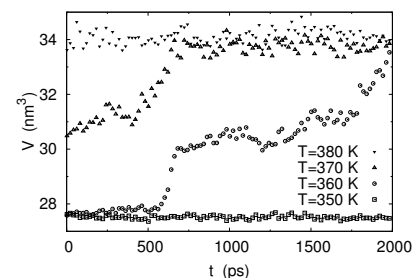


Figure 2.57: Volume during isothermal relaxations at various temperatures (fig. 2.29(a)).

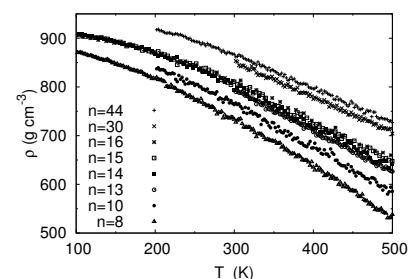


Figure 2.58: Density as a function of temperature (fig. 2.32).

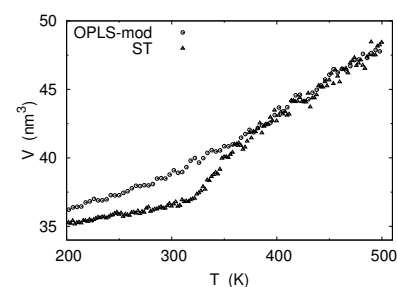


Figure 2.59: Phase diagram for the OPLS-mod and ST models (fig. 2.38(a)).

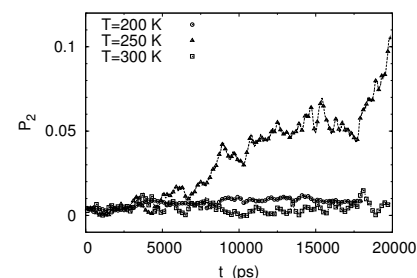


Figure 2.60: Order parameter P_2 as a function of time and temperature (fig. 2.43(b)).

3 Coarse-grained models

3.1 Definition of models

Studying polymer crystallization with computer simulations is a difficult task, since one needs for that purpose huge computational resources: It is necessary to use a large simulation box so as to avoid artifacts of chains interacting with themselves and in order to increase the probability of a nucleation event; also a long simulation time is needed to monitor the crystal growth process. It is a formidable task to simulate that process with a detailed model such as the all-atom model as is presented in chapter 2. Thus the study of polymer crystallization with computer simulation is restricted to a small amount of matter over a rather short period of time (i.e. using a large cooling rate for instance), and is still impossible with a detailed model. That is the reason why we are forced to use a simplified approach: One possible choice to increase the efficiency of the simulation is to use a so-called united-atom model. This scheme assumes that the structure of the molecules on the scale of the hydrogen-carbon bond is unimportant to describe the general behavior of the chains. Thus, several hydrogen atoms are absorbed with the corresponding carbon into one single spherical bead, whose size, position and interaction characteristics are calculated accordingly. This procedure allows to restrict the number of degrees of freedom that one would have had to take into account when looking at the original atomistic model. This simplification allows to reduce the amount of time needed for the simulation since the number of particles has decreased (roughly by a factor of three, in the case of hydrocarbons); but that is not the only reason why a simulation with united-atom chains would be faster: Losing details on the length scale of the bonds (and considering heavier particles), one can safely increase the time-step used for the integration of the equations of motion. Since the smallest relaxation time is associated with the vibration of the atoms around their equilibrium position, and that it is this relaxation time that provides an upper limit for the integration time-step, the latter can be increased while averaging over the fastest degrees of freedom as one does when going from an all-atom simulation to a united-atom scheme.

Coarse graining the particles involved in the simulation thus makes

Contents

3.1	Definition of models	75
3.1.1	The CG-PVA model	76
3.1.2	Definition of new models by variation of the angular potential	81
3.1.3	Simulation parameters	84
3.2	Characterization of different models	84
3.2.1	Comparison of different angular potentials	85
3.2.2	Reference values for chain length $N = 100$	97
3.2.3	Further observations	97
3.3	Characterization of the crystal	102
3.3.1	Continuous cooling	102
3.3.2	Order parameters during the crystallization and melting process	105
3.3.3	Volkenstein analysis of the influence of the angular potential	117
3.3.4	Isothermal relaxation	121
3.3.5	Structure factors	123
3.3.6	Melting of perfect crystals	126
3.4	Summary	133

the code more efficient, at the cost of a lower resolution of the resulting configurations, since information about the atomistic structure is lost. We therefore have to adjust the simulation scheme to the desired precision that is needed for a particular study. Choices for different schemes range from the most detailed quantum mechanical ab-initio calculations to the completely macroscopic finite-element methods. For our purpose, an access to information about the conformations of the different molecules interacting in a polymer melt is needed. The relevant molecular simulation methods consist of the all-atom scheme we already presented, and mesoscopic approaches such as molecule-based Monte-Carlo methods. We have to compromise and choose a tractable simulation method that would allow us to simulate big enough systems over long times while keeping enough accuracy on the molecule configurations to get a clear description of the resulting crystalline structure. One scheme that matches both requirements consists in using a model slightly coarser than the united-atom picture. This kind of model has been successfully applied to several polymers, and offers a high efficiency. We now briefly review the characteristics of such a scheme applied to poly(vinyl alcohol), showing how the needed parameters for such a model can be derived; then we introduce new models designed to understand the influence of the most important parameter of these coarse-grained models, and use them to study crystallization.

3.1.1 The CG-PVA model

The CG-PVA model [97] is a coarse-grained simulation model [84] with parameters similar to these of the abovementioned all-atom scheme. It consists of a set of particles characterized by the way they interact with each other; the different interactions are accounting for connectivity, excluded volume and flexibility of the coarse-grained chains. Connectivity is ensured by a harmonic interaction between two consecutive particles along the chain; excluded volume results from a repulsive potential applied between any two beads, provided they are not close neighbors along the chain, and flexibility arises from the angular interaction that restricts angles between consecutive bonds. The simulation is based on exactly the same ingredients as the atomistic method; only the physical scales are modified. We need to define the interactions between the coarse-grained beads; there is a standard procedure to map the original potentials onto the coarse-grained ones, i.e. to define how two coarse-grained particles interact as a result of the underlying interactions between all the constituents of those beads. One way to do so is to go back to the quantum physics level and derive the form of the interaction taking into account the fine structure of the molecules [125]; it is also possible to use another method that avoids these heavy calculations to rely on the already “quantum-averaged” atomistic force field instead. Using this method, one has first to run simulations for the relevant polymer with an all-atom force-field. The information extracted

from such a simulation is then used in an iterative optimization procedure that adjusts the form of the different coarse-grained interactions.

The first part of the coarse-graining procedure consists in defining a scaling factor and where to put the center of the coarse-grained particle with respect to the original atoms. In the case of the CG-PVA model we use, one monomer was chosen to be replaced by one single particle which sits on the carbon next to the hydroxyl group; one particle replaces then seven atoms in the original molecule. Once this choice is made, one has to define the interactions between the new particles. To achieve this, probability distributions are measured on the atomistic simulations. One probability distribution is related to a potential that governs the behavior of the corresponding variable through the Boltzmann relation:

$$P(x) \sim \exp \left[-\frac{U(x)}{k_B T} \right]. \quad (3.1)$$

In the case of a polymer in a melt, the situation is rather complicated as there are several interactions binding the particles together; there might be a non-negligible influence of one parameter on another. We can still make the assumption that these probability distributions we are interested in (probability for bond length, angle between bonds, distance between two particles) are almost independent of each other, and then use the simple relation (3.1) to derive the potential corresponding to the considered variable. An *a posteriori* verification is then required to check that the coarse-grained potentials used still yield the correct distributions, as they were measured on the original model. Another commonly used approximation consists in assuming that the many-body interactions in the dense system can be reduced to pairwise contributions. The use of pair potentials only reduces the complexity of the simulation algorithm; the interactions taken into account introduce more complex correlations between the different particles.

The interactions taken into account on the atomistic scale can be split into two parts : the *bonded* interactions, and the *non-bonded* ones. The first kind consists in the bonding potential (U_{bond}) which connects two consecutive particles, the angular potential (U_{ang}) which governs the angle between two consecutive bonds, and the torsional potential (U_{tors}) which describes the relative orientation of two consecutive dihedrals. The second sort of interactions regroups the intermolecular potential (U_{mol}) and the electrostatic contribution (U_{el}). U_{mol} is in turn composed of two distinct parts, a repulsive *hard-core* potential which prevents overlapping of two different beads,¹ and an attractive van der Waals interaction. Finally, the electrostatic part U_{el} accounts for the interaction between two partially charged particles.

¹The excluded volume potential is switched off between two particles that are close neighbors along the chain and thus necessarily or occasionally overlap. For our coarse-grained simulations, the excluded volume interaction is off for particles that are separated by less than three bonds, so that the bonded and non-bonded interactions do not have combined effects on some particles.

The interactions described above are used to reproduce the behavior of molecules when simulated with an atomistic resolution. The very same types of interactions are assumed to be suitable for a description of the interactions between two coarse-grained beads, and an automated procedure is applied to adjust the parameters of such interaction potentials. A functional form is defined for the different potentials, and an optimization scheme modifies the values it may involve until a satisfactory agreement is found with an atomistic measurement for a given distribution. One starts the optimization procedure by giving guessed values to the different potential parameters; a series of simulations of the so-defined coarse-grained model is run for each potential, varying the corresponding parameters. The first potential to be adjusted corresponds to the strongest interaction; all potential are then treated until the weakest contribution is determined. Potentials are thus considered in the following order:

- Binding potential,
- Angular potential,
- Excluded-volume potential,
- Torsional potential.

The electrostatic potential should also be taken into account, but depending on the kind of systems under consideration, it might have a very weak or strong influence. In the case of poly(vinyl alcohol) the system is neutral, and the (weak) effects of partial charges born by the different groups are taken into account in the determination of the other interactions (no specific coarse-grained electrostatic interaction needs to be determined explicitly).

In the case of the CG-PVA model [97], for both the binding and the angular potentials, the measured distributions could be inverted according to

$$U_{\text{bond}}(r) = -k_{\text{B}}T \ln [P(r)] \quad (3.2)$$

and

$$U_{\text{ang}}(\theta) = -k_{\text{B}}T \ln \left[\frac{P(\theta)}{\sin(\theta)} \right] \quad (3.3)$$

and used directly in the coarse-grained simulation. The resulting distributions compared well enough with the original ones, so that no further optimization was needed. This is the sign that the associated degrees of freedom are (almost) completely uncorrelated from other parameters in the system.

The situation is more complicated in the case of the excluded volume interaction, since the non-bonded interaction between two particles is necessarily influenced by the structure of the polymer chain as dictated by the strong bonded interactions. For this reason, careful choice of the form of the interaction and an optimization of the involved parameters were needed. The coarse-grained beads are spheres that represent

one whole monomer comprising seven atoms in a relatively large volume; one therefore expects those beads to interact more softly than two atoms as they are described in the original all-atom model. In the latter, the potential used has the usual 6–12 Lennard-Jones form [eq. 2.4]; for CG-PVA, a softer 6–9 form was found to yield a satisfactory agreement while comparing radial distribution functions computed for every second carbon along the atomistic backbone and for the coarse-grained beads:

$$U_{\text{mol}}(r) = \varepsilon_0 \left(\left(\frac{\sigma_0}{r} \right)^9 - \left(\frac{\sigma_0}{r} \right)^6 \right). \quad (3.4)$$

The potential was optimized by running several simulations with different values for the two Lennard-Jones parameters $\varepsilon^{\text{LJ}} = \varepsilon_0$ and $\sigma^{\text{LJ}} = \sigma_0$, and minimizing the difference between the two distributions using a simplex algorithm.

No torsional potential was used on the coarse-grained level, since the corresponding distribution in the atomistic simulation does not show any structure. The electrostatic part of the interaction was also disregarded because the beads are electrically neutral. Any influence of partial charges taken into account in the atomistic model is contained in the angular and non-bonded potentials.

We give now a summary of the different parameters obtained for this CG-PVA model through the procedure described above [97]:

- Connectivity:

$$U_{\text{bond}}(b) = \frac{1}{2} k_{\text{bond}} (b - b_0)^2, \quad (3.5)$$

with an equilibrium distance between the beads $b_0 = 0.26\text{nm} = \sigma/2$, and a spring constant $k_{\text{bond}} = 2704k_{\text{B}}T/\sigma^2$ (fig. 3.1). The equilibrium value of the bond length thus sets up the unit distance σ used in the program.

- Intermolecular interaction:

$$U_{\text{mol}}^0(r) = \varepsilon_0 \left(\left(\frac{\sigma_0}{r} \right)^9 - \left(\frac{\sigma_0}{r} \right)^6 \right), \quad (3.6)$$

with bead diameter $\sigma_0 = 0.46\text{nm} = 0.89\sigma$ and energy well $\varepsilon_0 = 1.511k_{\text{B}}T$ (fig. 3.2). The latter Lennard-Jones potential has been truncated and shifted so that

$$\begin{aligned} U_{\text{mol}}(r) &= U_{\text{mol}}^0(r) + U_{\text{mol}}^{\text{cut}} \\ &= \varepsilon \left(\left(\frac{\sigma_0}{r} \right)^9 - \left(\frac{\sigma_0}{r} \right)^6 \right) + U_{\text{mol}}^{\text{cut}}, \end{aligned} \quad (3.7)$$

where $U_{\text{mol}}^{\text{cut}} = U_{\text{mol}}^0(r_{\text{cutoff}})$ for $r \leq r_{\text{cutoff}}$, and $U_{\text{mol}}^{\text{cut}} = -U_{\text{mol}}^0(r)$ for $r > r_{\text{cutoff}}$. Thus results for r larger than the cutoff distance r_{cutoff} , $U_{\text{mol}}(r) = 0$. In our simulations, $r_{\text{cutoff}} = 1.02\sigma$. We expect that this shift in the potential will not influence the statics or dynamics of the simulation.

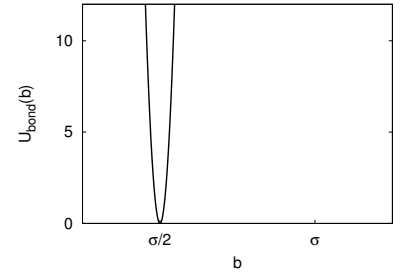


Figure 3.1: Bonded interaction potential.

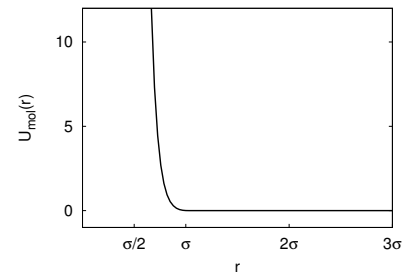


Figure 3.2: Intermolecular interaction potential.

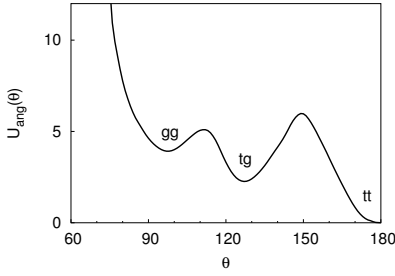


Figure 3.3: Angular potential.

- **Angles:** The shape of the angular potential is shown in fig. 3.3, and will be described in more details later. The measured distribution is Boltzmann inverted and used as a tabulated potential in the simulation program.

When creating a coarse-grained model like the one we just presented, one has to bear in mind that there are multiple possibilities for the coarse-graining procedure. Apart from the different possibilities that arise from the many choices one has for the position of the coarse-grained beads, there are also a lot of possible ways to adjust the potential: It is possible to tune the interactions so as to reproduce the behavior of a polymer as it can be described with the use of atomistic simulations. The most general procedure would involve a systematic minimization of a function with dimensionality corresponding to the number of parameters needed, and could even be much more complicated if more general tabulated potentials are used (i.e. the interaction does not have to be described by a simple analytical form); this method is normally not tractable, and so one has to decompose the parameter optimization into several parts, assuming some interactions are independent from each other. It is also possible to take some other parameters into account in the minimization scheme, such as pressure. This ensures the pressure does not have unreasonable values in the simulation using the optimized interaction parameters.

Table 3.1: List of units for the quantities input and output of the coarse-grained simulations.

Quantity	Unit
length	σ
angle	rad or degree
time	τ
energy	$k_B T$
force	$k_B T / \sigma^2$,
constants	$k_B T / \text{rad}^2$
temperature	$k_B T$
pressure	$k_B T / \sigma^3$

Unlike in the case of detailed simulations on the atomic level, it is not possible to define all physical scales properly: The characteristic quantities phenomenologically established on the atomic scale that are used to yield the all-atom simulation parameters are not available for other arbitrary scales like these relative to a particular coarse-grained scheme. In the case of the CG-PVA simulation scheme, there is a definite mapping for length scales, since the coarse-graining method explicitly specified the length scale σ that corresponds to 0.52 nm (the average distance between monomers). On the other hand, there exists no such mapping for time scales, and it is not easy to determine. Table 3.1 presents a list of the reduced units used in the coarse-grained simulation.

The model presented above has been found to describe the properties of poly(vinyl alcohol) well, and in particular to allow one to simulate its crystallization with high efficiency compared to atomistic or united atom models. We have been using this coarse-grained model as a basis for our studies and varied one of its most important parameter, the angular potential. We therefore created several derived models and tried to describe the influence of that particular parameter upon the general behavior of the system.

3.1.2 Definition of new models by variation of the angular potential

The angular potential is a very important parameter of our simulation model; its presence allows to keep track of underlying physical properties that could have been “lost” in the course of the coarse-graining process². From the original interactions one has to consider when simulating a polymer with an atomistic scheme, we have seen that two were neglected in the definition of our coarse-grained model: The torsional potential turned out to be almost zero in the case of PVA, and therefore was disregarded; and the electrostatic interactions were among the completely averaged degrees of freedom we do not need to describe anymore. Going one step further, we would have used a coarser “bead-spring” model consisting only in beads representing a bigger number of atoms (up to several monomers). In such a case, the interactions could be limited to connectivity and excluded volume, without any parameter determining explicitly the chain stiffness. This stiffness arising from the bare atomic interactions is indeed predominant when attempting to describe crystallization, since without such a parameter, no component of the model would drive the phase transition:³ Upon cooling down, the angular potential provides a driving force that leads the chains to stretch and thus create nuclei from which the crystalline phase can grow. As an illustration of the importance of this particular parameter of our model, one can consider the curves presented in fig. 3.5: This represents the phase diagram obtained for CG-PVA during a continuous cooling simulation (that we shall describe in more details later), and slightly different models which use the very same parameters as CG-PVA, except for the angular potential which is then zero. It is easy to see that, while the first model exhibits a clear first-order like phase transition which is the signature of crystallization, the latter just evolve toward low temperatures without any such transition, until they eventually freeze (for the w0 model, the glass transition occurs around $T \simeq 0.1$; see fig. 3.4). This is a clear evidence that in the case of our model, the angular potential is responsible for ordering the polymers and driving them to a crystalline phase.

The angular potential appears to be an important parameter since it allows to reproduce the phase transition to the crystal in our simulations, and it is a very interesting element of the model: This potential constitutes a simple and general enough means of taking into account several physical properties of the considered polymer. It is then conceivable to simulate different kinds of polymers with chemi-

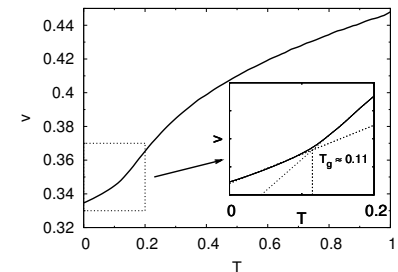
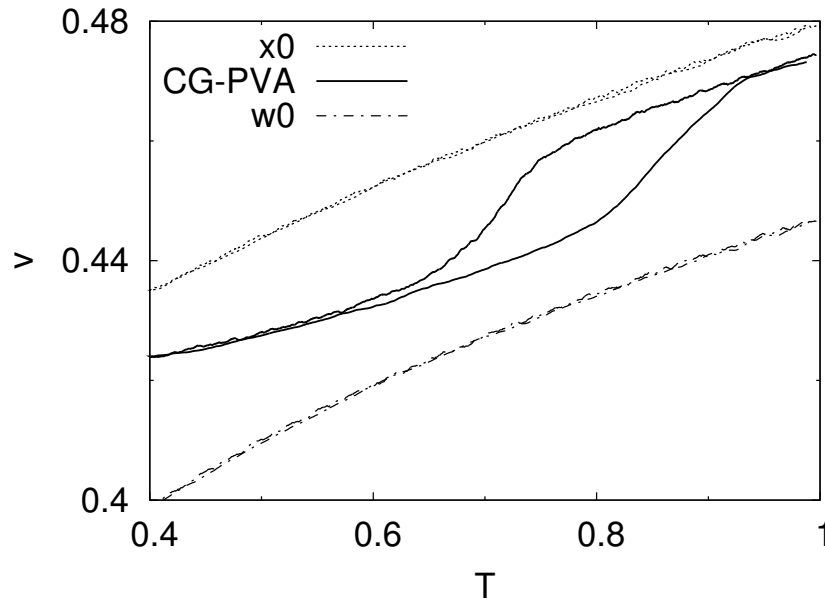


Figure 3.4: Phase diagram for the w0 model, extended to very low temperatures. No abrupt jump in the volume is witnessed, but a clear change in the slope is the sign of the glass transition. Linear fitting of the different branches allows one to determine the glass transition temperature, $T_g \simeq 0.11$.

²as would be the case of a coarser model that could account for the large-scale properties of polymers (gaussian model) but would be too crude to reproduce the detailed behavior on a more local scale.

³Apart from the attractive part in the intermolecular potential; however this contribution is not sufficient to account for the tendency of the chains to stretch and crystallize. The CG-PVA model that succeeds at reproducing semi-crystalline configurations does not include any attractive interaction.

Figure 3.5: Comparison of the phase diagrams for CG-PVA and two other models **without** angular potential: Volume per monomer as a function of temperature (measured during continuous cooling). The $w0$ model has exactly the same parameters as CG-PVA, except for the angular potential; $x0$ has another difference which lies in the settings of the Lennard-Jones potential. For CG-PVA and $w0$, this interaction is turned off for nearest-neighbors and next-nearest-neighbor beads along one chain; whereas for $x0$, the interaction is on for next-nearest-neighbors. The resulting overall *intra*-chain interaction (combination of angular and Lennard-Jones potentials) makes the $w0$ chains more flexible than for the CG-PVA model, and the chains are stiffer in the case of $x0$. For these reasons, $w0$ has a higher density and $x0$ a smaller density than CG-PVA.



cally different structures, that would be mainly reflected in the shape of that potential. Indeed, the other parameters are completely general, and their form does not need to be varied to describe other chemical species: The harmonic potential ensuring connectivity and the soft Lennard-Jones repulsive potential preventing overlaps of the particles could be used for many different kinds of polymers. One could then imagine to reproduce several polymers' characteristics with changing only the angular potential in the coarse-grained model defined above; the energy scales could then be renormalized to account for a smaller or greater influence of excluded volume for instance. This procedure would allow to describe qualitatively many different polymers with little change from the original model; still, it would not be appropriate to use such a scheme to simulate polymers with very different geometries (bigger side-groups, several chemically different groups, ...), neither would it be suitable for polymers with very specific or strong interactions.

In order to investigate more precisely the influence of this angular potential on the behavior of our coarse-grained model, we decided to create several new models inspired from CG-PVA and differing only in this parameter. This is a reverse procedure: Instead of modeling different polymeric systems from the atomic scale, we start with the opposite point of view and create arbitrarily new models that could describe a whole set of somewhat different polymers with varying flexibility. The angular potential derived for poly(vinyl alcohol) is a good starting point for such an undertaking, since it exhibits very clearly the general structure one could expect from a linear polymer: Looking at the shape of the angular potential in fig. 3.3, one can notice three

minima that correspond to the three states we expect from the general properties of polymer chains. The angle θ we are considering here in the coarse-grained model is defined as the angle between two consecutive coarse-grained bonds. This corresponds, in terms of the underlying atomistic geometry, to bonds linking every second carbon; thus one of these angles θ results from the configuration adopted by five consecutive carbon atoms, which is directly related to the torsional states of the backbone. One coarse-grained angle is then defined by two consecutive torsional angles of the backbone (neglecting the variations around the carbon atoms' equilibrium states, arising from bond length and bond angle fluctuations on the atomistic level). The possible states of the backbone result from a statistical mixture of the torsional states, which are, for one quadruplet of carbon atoms: *trans* (torsion angle $\phi = 180^\circ$, all bonds lying in the same plane), *gauche* $^\pm$ ($\phi \simeq 60^\circ$ or 300°) and *cis* ($\phi = 0^\circ$ or 360°), from the most to the least favorable (in the case of simple polymers like polyethylene or PVA, see chapter 2 for more discussion on the torsional states in the case of alkane model; fig. 2.1 presents a typical torsional potential for simple polymer chains). In the case of two consecutive *trans* states, on the coarse-grained scale the angle would be equal to 180° . A quick calculation of the θ values corresponding to other torsion angles combinations gives the following estimate, using polyethylene geometry:

- For *trans–trans* $^\pm$ states, $\theta \approx 180^\circ$.
- For *trans–gauche* $^\pm$ states, $\theta \approx 122.1^\circ$. This corresponds roughly to the second minimum exhibited in fig. 3.3.
- For *gauche* $^\mp$ –*gauche* $^\pm$ states, $\theta \approx 91.9^\circ$. This is close to the value reported for the last minimum of the CG-PVA angular potential.

These estimates are computed using the equilibrium positions of carbon atoms of the backbone with respect to the bond length and bond angle fluctuations. Values observed for the minima in fig. 3.3 are closer to 130° and 95° approximately; this can be understood by considering that bonds can be stretched, and (this is more probable however) that bond angles are slightly above their equilibrium value (which is actually an equilibrium value only in case the other degrees of freedom do not interfere) because of packing and thermal excitation. Moreover, these estimates were obtained using the polyethylene force field specifications, just to get an order of magnitude of the angles we should expect. This could give slightly different results in the case of PVA.

The new models created in order to study which influence the angular potential has on the general behavior of the model were defined this way: The original CG-PVA angular potential has been cut into pieces which are interpolated by cosine functions. The last, repulsive part of the potential that ensures the chain cannot fold onto itself, was extrapolated by a parabola (cf. fig. 3.7). This combination of functions provides a continuously differentiable expression for the potential,

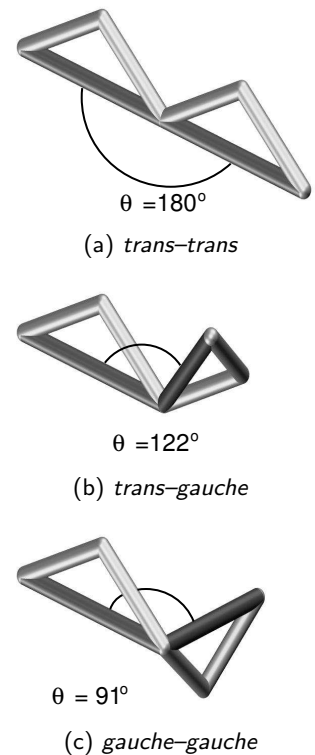


Figure 3.6: Schematic representation of the favorable torsional states on the atomistic level, and the corresponding coarse-grained bond angles. The angular potential corresponding to these states is presented in fig. 3.7. (Original backbone: light color; coarse-grained model bonds: dark color.)

which is necessary since the simulation code computes from there the force exerted by one bead on another. This scheme also has the advantage that it makes it easy to adjust the depth of the minima and the height of the different barriers in between. This parametrizable potential has been used to generate several potentials which we will use as different models in our study; these models could account for differences in the chemical structure of various polymers, having still in common the positions of the minima that are rather general for simple enough polymers (in one case though, we varied slightly the position of the last minimum from 90° to 95°).

3.1.3 Simulation parameters

The simulations we used to investigate the influence of the angular potential involved the different models described above; they have several parameters in common that we shall review now. These simulations were run in the isothermal-isobaric ensemble, through the use of a thermostat and a barostat. The thermostat used is the Langevin thermostat presented earlier (cf. sec. 1.1.1.2), with friction coefficient $\gamma = 0.5 \tau^{-1}$. The simulation always started with a setup followed by an equilibration at high temperature, $T = 1.0$. What we refer to as a *temperature* is actually a thermal energy, setting the energy scale of the simulation - it could actually be expressed in units of $k_B T$. This “high temperature” corresponds to $T = 550$ K, as it was the temperature at which the atomistic simulations were run to determine the coarse-grained potentials’ parameters. This temperature is referred to as “high”, since, in the case of PVA, it is above the melting point.

The pressure is kept constant during all simulations, at a value of $8 k_B T / \sigma^3$. This is achieved using the Berendsen barostat with coupling constant $\beta_T / \tau_P = 10^{-5} \tau^{-1}$. The actual value of the pressure does not matter much here; it has been set to reproduce the conditions of the original atomistic PVA simulations, which were run at atmospheric pressure $P = 101.3$ kPa.

3.2 Characterization of different models

We have used many combinations of the parameters h_1-h_4 (fig. 3.7) with different chain lengths; from these simulations many different quantities were measured, allowing a comparative summary. Since the influence of a general functional form is far more complicated to describe than a single scalar parameter, we were led to group several models together in series in order to attempt a clearer description of separate components of the angular potential. For each series, we have emphasized the differences in the angular potential shapes, and the effects on the corresponding angular distribution which, although giving an almost equivalent information, is usually found to be more telling.

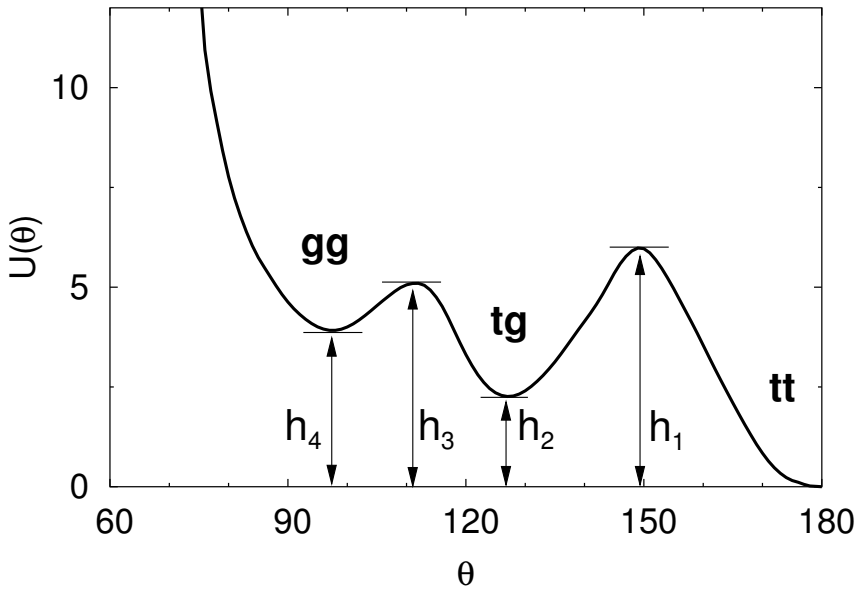


Figure 3.7: Angular potential parameterization. The depths of the wells h_2 , h_4 and the heights of the barriers h_1 , h_3 have been varied to generate new models. The different states corresponding to the angles on the original backbone are indicated (*trans-trans*, *trans-gauche* and *gauche-gauche*). The positions of the different barriers and wells characterized by the quantities h_i are denoted θ_i .

Characteristic quantities measured on the simulation data are used to compare the different models: The persistence length l_p , the squared radius of gyration R_g^2 , the crystallization temperature T_{cryst} , properties of the angular state (probability of the *trans-trans* state, average cosine of the bond angle $\theta \dots$), or the energy $\langle E \rangle$.⁴ These quantities are defined in sec. 1.3.

3.2.1 Comparison of different angular potentials

The first group of models consists of four different models for which the angular potential only differs by the depth of the second minimum, h_2 ; fig. 3.8 presents these potentials and the corresponding angular distributions. As can be seen on the latter, a decrease in the minimum's depth is directly related to a decrease in the population of *trans-gauche* states. The *trans-trans* state becomes increasingly more populated, as it is more favorable than the folded *gauche-gauche* states; this can also be observed through the small increase in the average cosine of the angle between bonds. This quantity is usually correlated with the persistence length which, though, does not seem to follow the same trend in this particular case, showing how small the effect is. A more important effect that we will generally observe in this comparison is the trend of the crystallization temperature measured during continuous cooling, T_{cryst} with the probability of finding an angle θ in a stretched conformation (i.e. greater than 150° , corresponding to the *tt* state). Looking at the different models of this group, one notices that the shallower the second well is, the higher the crystallization temperature. This, as we will see later, is more generally linked to the probability of

⁴The values indicated for the energy are computed for the simulated system as a whole, and thus cannot be directly compared for different chain lengths since the total number of particles is not the same for simulations with different N .

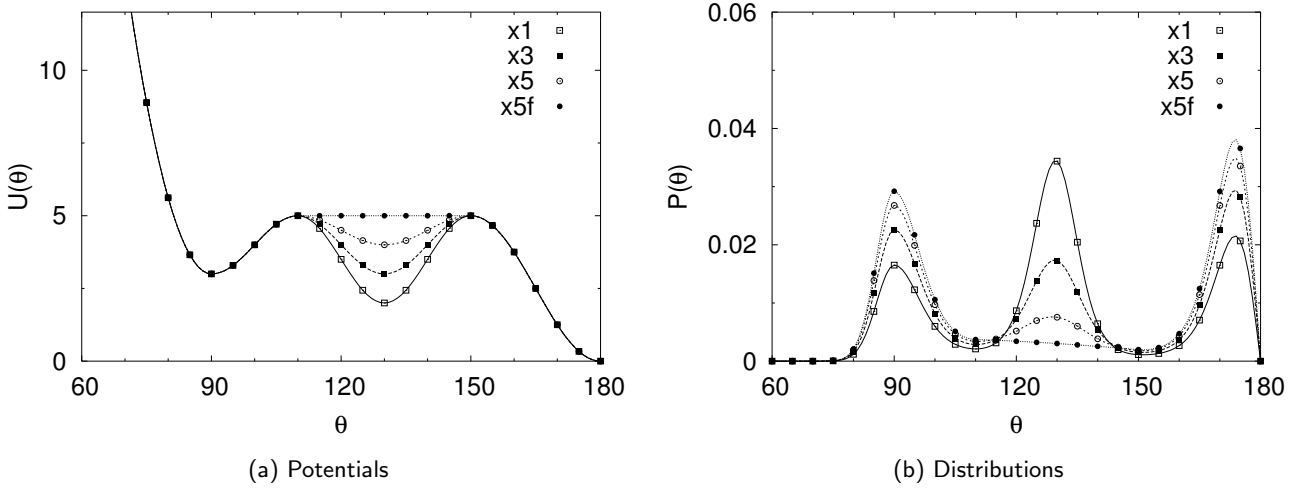


Figure 3.8: First group: Effect of the variation of the depth of the second well, t_g .

trans states. The more flexible the chains, the more difficult it appears to have them crystallize.

Table 3.2: Group 1, $N = 10$.

Potential	h_2	l_p	T_{cryst}	$P(gg)$	$P(tg)$	$P(tt)$	$\langle \cos \theta \rangle$
CG-PVA	2.3	1.32	0.64	0.15	0.47	0.38	-0.68
x1	2	0.94	0.49	0.28	0.50	0.22	-0.55
x3	3	0.93	0.60	0.36	0.33	0.31	-0.53
x5	4	0.88	0.63	0.42	0.21	0.38	-0.52
x5f	5	0.94	0.64	0.45	0.13	0.42	-0.51

Table 3.3: Group 1, $N = 50$.

Potential	h_2	l_p	T_{cryst}	$P(gg)$	$P(tg)$	$P(tt)$	$\langle \cos \theta \rangle$
CG-PVA	2.3	1.40	0.73	0.15	0.47	0.38	-0.68
x1	2	0.97	0.54	0.27	0.51	0.22	-0.56
x3	3	0.95	0.62	0.35	0.33	0.31	-0.54
x5	4	0.96	0.70	0.41	0.21	0.38	-0.53
x5f	5	0.93	0.71	0.44	0.13	0.47	-0.52

The second group contains again a variation of the second minimum. With respect to the models in the first group, the energy of the *gg* state is higher. In addition, two subgroups characterized by a different height of the *tt*-*tg* barrier are summarized here. The first subgroup contains three different models (x9, x8, x6), while the second has two (x64, x4). The height of the barrier between the *trans*-*trans* and *trans*-*gauche* states is higher in the case of this second subgroup (see fig. 3.9).

As already stated before, the decrease in the depth of the potential well causes the probability of finding an angle in the *tg* state to decrease. This is again connected to an increase in the population of *tt* states, which results in higher crystallization temperatures. It should also be noted that the third peak in the angular distribution varies much less than the two others, indicating that the modifications of the

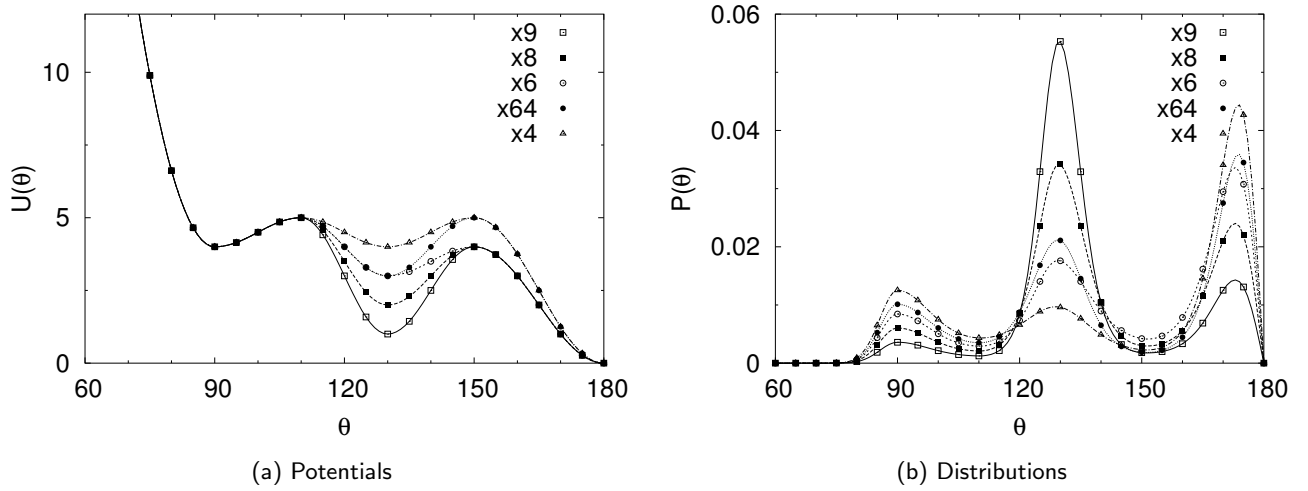


Figure 3.9: Group 2: Another study of the effect of the depth of the second well, t_g .

second energy level mostly affects the population of tt and tg states. The gg state is much less populated, and l_p in this group is much higher than in the first one.

Potential	h_1	h_2	l_p	T_{cryst}	$P(gg)$	$P(tg)$	$P(tt)$	$\langle E \rangle$	$\langle \cos \theta \rangle$
CG-PVA	6	2.3	1.32	0.64	0.15	0.47	0.38	1280.8	-0.68
x9	4	1	1.22	-	0.089	0.73	0.18	1285.4	-0.66
x8	4	2	1.29	0.60	0.14	0.56	0.30	1281.0	-0.67
x6	4	3	1.37	0.70	0.19	0.39	0.42	1280.0	-0.68
x64	5	3	1.19	0.67	0.22	0.41	0.37	1283.3	-0.64
x4	5	4	1.27	0.74	0.27	0.26	0.47	1276.6	-0.65

Table 3.4: Group 2, $N = 10$.

Potential	h_1	h_2	l_p	T_{cryst}	$P(gg)$	$P(tg)$	$P(tt)$	$\langle E \rangle$	$\langle \cos \theta \rangle$
CG-PVA	6	2.3	1.40	0.73	0.15	0.47	0.38	1412.9	-0.68
x9	4	1	1.21	0.47	0.089	0.73	0.18	1421.3	-0.66
x8	4	2	1.30	0.63	0.14	0.56	0.30	1421.0	-0.67
x6	4	3	1.37	0.76	0.19	0.38	0.43	1410.6	-0.69
x64	5	3	1.20	0.73	0.22	0.41	0.38	1425.2	-0.64
x4	5	4	1.34	0.82	0.26	0.26	0.48	1412.5	-0.65

Table 3.5: Group 2, $N = 50$.

In the third group we take the potential x1 from the first group and study the influence of the height of the barrier between the tt and tg states. It is observed from the angular distributions showed in fig. 3.10 that this modification does not lead to a change in the height of the tt state peak, but rather to a decreasing amount of transitory states between tt and tg . In our convention, this is still accounted for as a decrease of $P(tt)$, since the latter probability is defined as $\int_{\theta=150^\circ}^{\theta=180^\circ} P(\theta)d\theta$. The states that disappear between tt and tg are moved so as to increase the population of the two less favorable states, tg and gg . As the height of the barrier is increased, the average value of $\cos \theta$

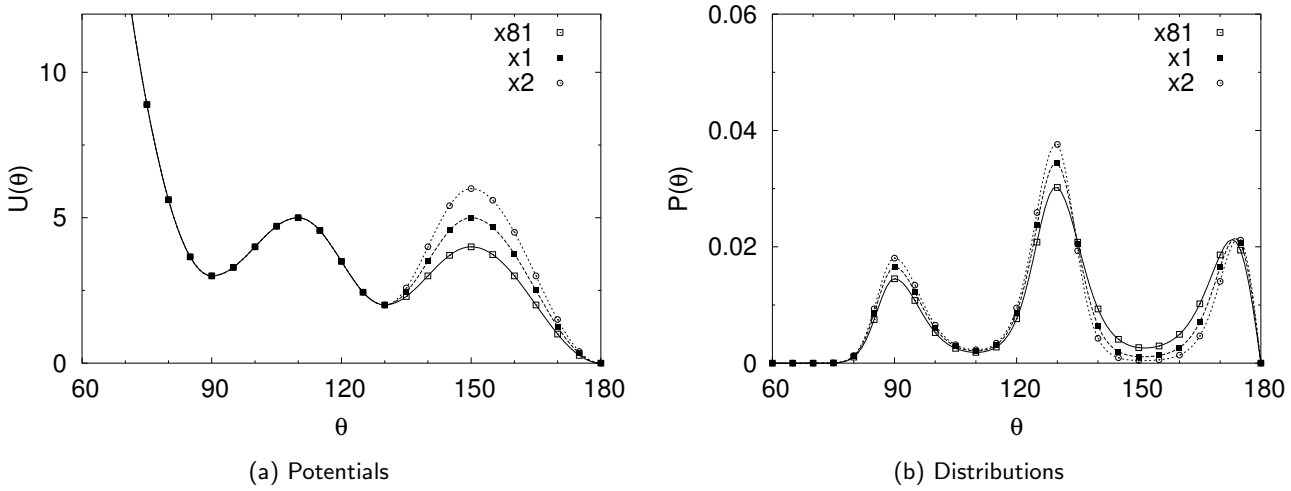


Figure 3.10: Group 3: Effect of the height of the first barrier, tt - gg .

increases, corresponding to less stretched angular conformations, on average. The lower $P(tt)$ values correspond to lower crystallization temperatures; the more folded the chains are, the less easily they could stretch at low temperature and form a crystalline phase.

Table 3.6: Group 3, $N = 10$.

Potential	h_1	l_p	T_{cryst}	$P(gg)$	$P(tg)$	$P(tt)$	$\langle E \rangle$	$\langle \cos \theta \rangle$
CG-PVA	6	1.32	0.64	0.15	0.47	0.38	1280.8	-0.68
x81	4	1.03	0.53	0.25	0.49	0.26	1298.0	-0.59
x1	5	0.94	0.50	0.28	0.50	0.22	1303.7	-0.55
x2	6	0.89	0.46	0.30	0.51	0.19	1312.6	-0.53

Table 3.7: Group 3, $N = 50$.

Potential	h_1	l_p	T_{cryst}	$P(gg)$	$P(tg)$	$P(tt)$	$\langle E \rangle$	$\langle \cos \theta \rangle$
CG-PVA	6	1.40	0.73	0.15	0.47	0.38	1412.9	-0.68
x81	4	1.09	0.56	0.25	0.49	0.27	1444.3	-0.59
x1	5	0.97	0.54	0.27	0.51	0.22	1460.3	-0.56
x2	6	0.91	0.51	0.29	0.52	0.19	1472.0	-0.53

In the fourth group we regroup some models from groups 1 and 2 in two subgroups characterized by a different height of the gg state's energy level. The first three potentials (x8, x64, x4) have increasing second minimum, while the first barrier is also higher for x64 and x4; the second subgroup shows an increasing second minimum as well. The third minimum for the first subgroup is higher than for the second one. Comparison of data for the different models is useful as the trends we have already stressed can be observed in each subset and the *relative* values can be confronted to rationalize the effect of the gg states' energy. From the angular distributions one notices that the last peak [corresponding to $P(gg)$] continuously increases as we go from one model to the next in the group. However, there does not seem to be any quantity following exactly the same behavior (i.e. there is always a breakpoint at the crossover from one subgroup to the next), which

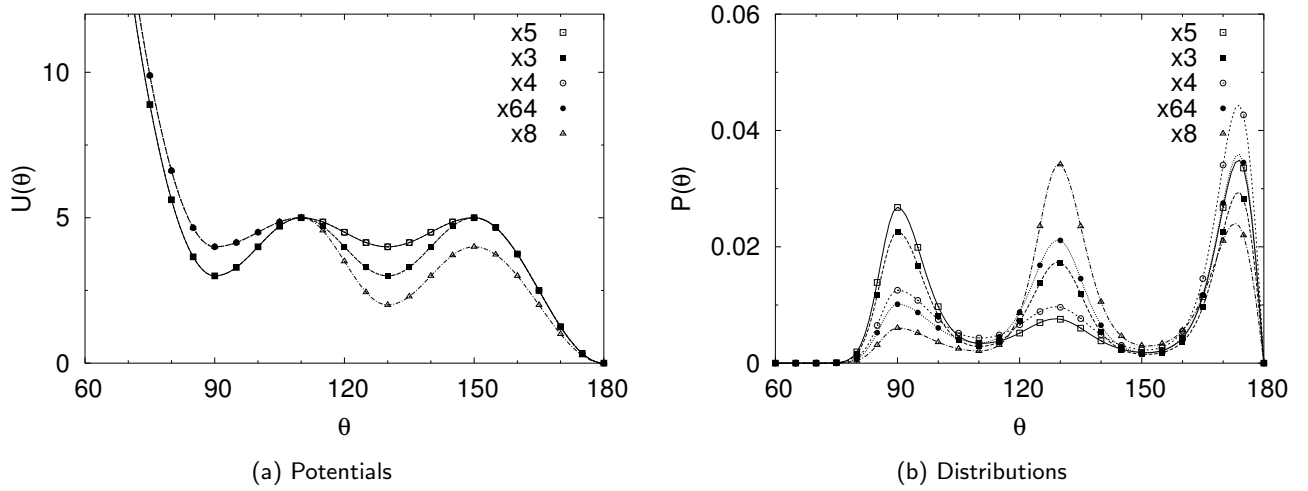


Figure 3.11: Group 4: Effect of the depth of the gg well.

is related to the trends for the other two angular states' populations. This indicates that the proportion of folded configurations in the system does not dictate the behavior of the physical quantities as strongly as $P(tt)$ does. One can still observe that, as usual, the crystallization temperature follows the tendency indicated by $P(tt)$.

Potential	h_1	h_2	h_4	l_p	T_{cryst}	$P(gg)$	$P(tg)$	$P(tt)$	$\langle \cos \theta \rangle$
CG-PVA	6	2.3	3.9	1.32	0.64	0.15	0.47	0.38	-0.68
x8	4	2	4	1.29	0.57	0.14	0.56	0.30	-0.67
x64	5	3	4	1.19	0.67	0.22	0.41	0.38	-0.64
x4	5	4	4	1.27	0.74	0.27	0.26	0.47	-0.65
x3	5	3	3	0.93	0.61	0.36	0.33	0.31	-0.53
x5	5	4	3	0.88	0.63	0.42	0.21	0.38	-0.52

Table 3.8: Group 4, $N = 10$.

Potential	h_1	h_2	h_4	l_p	T_{cryst}	$P(gg)$	$P(tg)$	$P(tt)$	$\langle \cos \theta \rangle$
CG-PVA	6	2.3	3.9	1.40	0.73	0.15	0.47	0.38	-0.68
x8	4	2	4	1.30	0.63	0.14	0.56	0.30	-0.67
x64	5	3	4	1.20	0.73	0.22	0.41	0.38	-0.64
x4	5	4	4	1.34	0.82	0.26	0.26	0.48	-0.65
x3	5	3	3	0.95	0.62	0.35	0.33	0.31	-0.54
x5	5	4	3	0.96	0.70	0.41	0.21	0.38	-0.53

Table 3.9: Group 4, $N = 50$.

The fifth group attempts to focus on the influence of the second barrier of the potential. The different models considered here all have in common the first barrier in the angular potential, and they differ when it comes to the parts describing the tg and gg states. Two of the four potentials are flat, meaning they have no barrier in between tg and gg . In these cases, the angular distributions show a common population for the two states that are not separated anymore. Cycling through the different models, one can notice a decrease in the overall tg - gg population, which results in an increase in the number of stretched states;

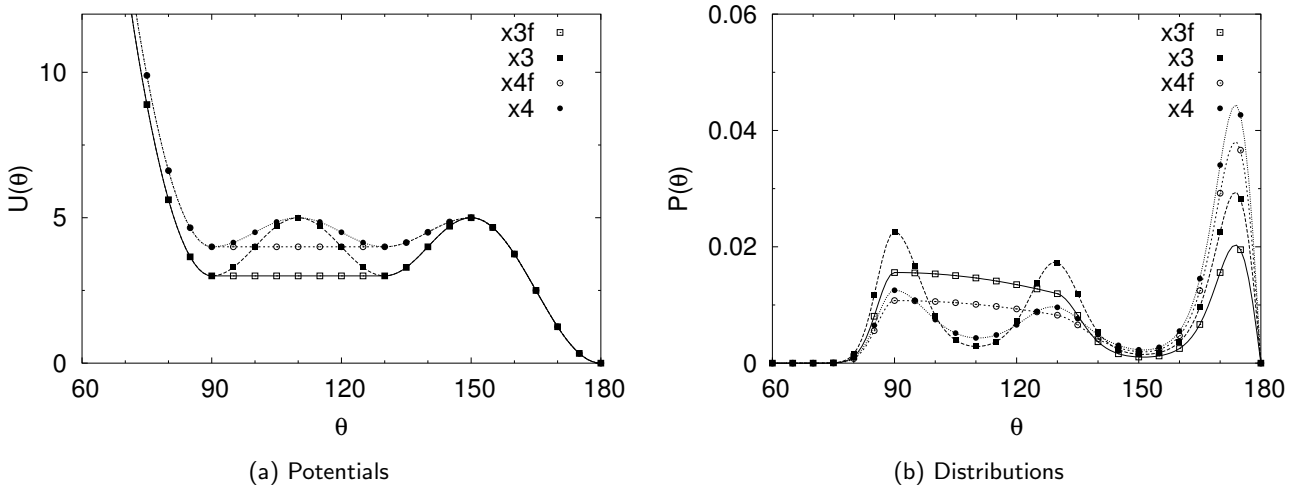


Figure 3.12: Group 5: Effect of the second barrier, $tg-gg$.

this also leads to a more elongated angular configuration on average, as shown by the decrease in $\langle \cos \theta \rangle$. The persistence length, which does not usually exhibit a correlation with $P(tt)$, increases steadily when decreasing the population of both the tg and gg states, and the crystallization temperature presents the usual tendency following the value of $P(tt)$. The conclusion about the influence of the $gg-tg$ barrier is not straightforward with this group of potentials, since other parameters than those directly constraining h_3 are varying as well here.

Table 3.10:
Group 5, $N = 10$.

Potential	h_2	h_3	h_4	l_p	T_{cryst}	$P(gg)$	$P(tg)$	$P(tt)$	$\langle E \rangle$	$\langle \cos \theta \rangle$
CG-PVA	2.3	5.1	3.9	1.32	0.64	0.15	0.47	0.38	1280.79	-0.68
x3f	3	3	3	0.83	0.51	0.39	0.40	0.21	1319.29	-0.48
x3	3	5	3	0.93	0.60	0.36	0.33	0.31	1299.52	-0.53
x4f	4	4	4	1.06	0.69	0.30	0.30	0.40	1290.59	-0.60
x4	4	5	4	1.27	0.74	0.27	0.26	0.47	1276.61	-0.65

Table 3.11:
Group 5, $N = 50$.

Potential	h_2	h_3	h_4	l_p	T_{cryst}	$P(gg)$	$P(tg)$	$P(tt)$	$\langle E \rangle$	$\langle \cos \theta \rangle$
CG-PVA	2.3	5.1	3.9	1.40	0.73	0.15	0.47	0.38	1412.88	-0.68
x3f	3	3	3	0.86	0.55	0.38	0.40	0.22	1484.94	-0.49
x3	3	5	3	0.95	0.62	0.35	0.33	0.31	1451.38	-0.54
x4f	4	4	4	1.09	0.76	0.29	0.31	0.40	1432.57	-0.61
x4	4	5	4	1.34	0.82	0.26	0.26	0.48	1412.53	-0.65

Another comparison of the different parameters for our angular potentials is obtained by considering several models that were created to approach the original CG-PVA model as close as possible using the interpolation form for $U_{\text{ang}}(\theta)$. The x7 model is a crude approximation for the original CG-PVA angular potential. The h_i parameters (well depths and barrier heights) roughly have the same values while the θ_i which correspond to the angular positions of the extrema, are slightly shifted, as a result of the generic values taken for the x models

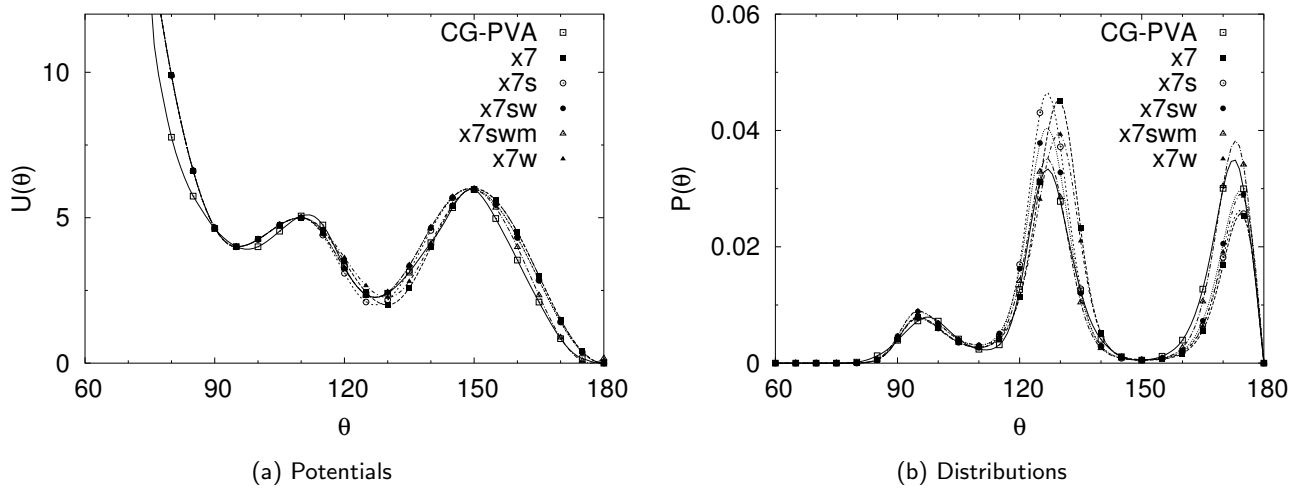


Figure 3.13: Group 6: Effect of the parameterization on models close to CG-PVA.

Potential	θ_0	θ_1	θ_2	θ_3	θ_4	h_1	h_2	h_3	h_4
CG-PVA	180	149	127	112	97	6	2.3	5.1	3.9
x7	180	150	130	110	95	6	2	5	4
x7s	180	149	127	110	95	6	2	5	4
x7w	180	150	130	110	95	6	2.3	5	4
x7sw	180	149	127	110	95	6	2.3	5	4
x7swm	177	149	127	110	95	6	2.3	5	4

Table 3.12: Group 6 — Parameters.

being rounded off. These—relatively small—differences lead to rather large changes in the physical properties, for instance the crystallization temperature is much lower for x7. Indeed, it is observed that for CG-PVA $P(tt)$ is higher, while in the case of the other, “approximate” model, the probability of *trans-gauche* states is high. The x7 and x7s only differ by a small shift in the values of θ_i ; there is no significant difference between the results obtained for these two models, meaning that a small change in the position of the minima and barriers is not essential. On the other hand, the x7w model which was designed to fit more accurately the depth of the second well, exhibits a higher $P(tt)$ which is reflected in a higher propensity for the system to crystallize. The x7sw shows no significant change when compared to x7w (the same modification leads to the definition of x7s from x7 and of x7sw from x7w). Last, the x7swm model is the one that mimics CG-PVA the more accurately. Their properties are quite similar, which arises from a better match of the two values of $P(tt)$: In order to reproduce more precisely the shape of the last part of the potential corresponding to the *trans-trans* state, and which appears to be steeper in the case of CG-PVA than for a cosine interpolation, the minimum for x7swm has been shifted toward smaller θ angles. This change results in a greater difficulty for a system in the tt state to escape, which is observable in the population of that particular state. This observation is another evidence of the prominence of $P(tt)$ on the physical properties of the

Table 3.13: Group 6, $N = 10$.

Potential	l_p	T_{cryst}	$P(gg)$	$P(tg)$	$P(tt)$	$\langle E \rangle$	R_g^2	$\langle \cos \theta \rangle$
CG-PVA	2.6	0.64	0.15	0.47	0.38	1280.8	1.2	-0.68
x7	2.2	0.50	0.15	0.63	0.22	1286.4	1.1	-0.64
x7s	2.2	0.50	0.15	0.62	0.23	1285.6	1.1	-0.63
x7w	2.3	0.56	0.17	0.58	0.25	1286.7	1.1	-0.64
x7sw	2.3	0.56	0.16	0.57	0.27	1288.0	1.1	-0.63
x7swm	2.6	0.64	0.14	0.50	0.35	1281.3	1.1	-0.67

Table 3.14: Group 6, $N = 50$.

Potential	l_p	T_{cryst}	$P(gg)$	$P(tg)$	$P(tt)$	$\langle E \rangle$	R_g^2	$\langle \cos \theta \rangle$
CG-PVA	2.8	0.73	0.15	0.47	0.38	1412.9	9.7	-0.68
x7	2.2	0.58	0.15	0.63	0.22	1421.9	8.3	-0.64
x7swm	2.6	0.70	0.14	0.50	0.35	1414.3	9.2	-0.67

system, in particular on the formation of the crystalline phase. The data for $N = 50$ support the conclusions drawn from the behavior of the models at $N = 10$; for the longer chain lengths, only two of the models discussed above were actually simulated.

The gg well. In order to obtain an insight into the influence of the last parameter in our angular potential, the depth of the gg well, we can again try an indirect observation: We proceed by comparing groups 1 and 2, as well as the two subgroups of group 4. Group 1 (x1, x3, x5, x5f) and group 2 (x9, x8, x6, x64, x4) are constituted of models with varying second minimum. The two series are distinguished by a different value of the third minimum: The third potential well is deeper in the case of group 1. Equivalently, subgroups (x3, x5) and (x64, x4) of group 4 have exactly the same structure except for the last minimum, which is deeper in the case of the first subgroup. Looking at the measured quantities for these series, some correlations appear between the depth of the last minimum and the persistence length for instance: The deeper the minimum, the lower the persistence length. This means that the persistence length is strongly affected by the probability of forming folds along the chains, more clearly than by $P(tt)$. A higher $P(gg)$ is observed from the compared distributions in the case of a deep third minimum. This is also correlated with a much smaller average angle. The number of self-contacts corresponds to the probability of finding two particles of the same chain closer than a cutoff distance. This quantity can be seen to raise with the increase of $P(gg)$, which is interpreted as the propensity of the chains to fold back onto themselves as the small-bond-angle states are favored.

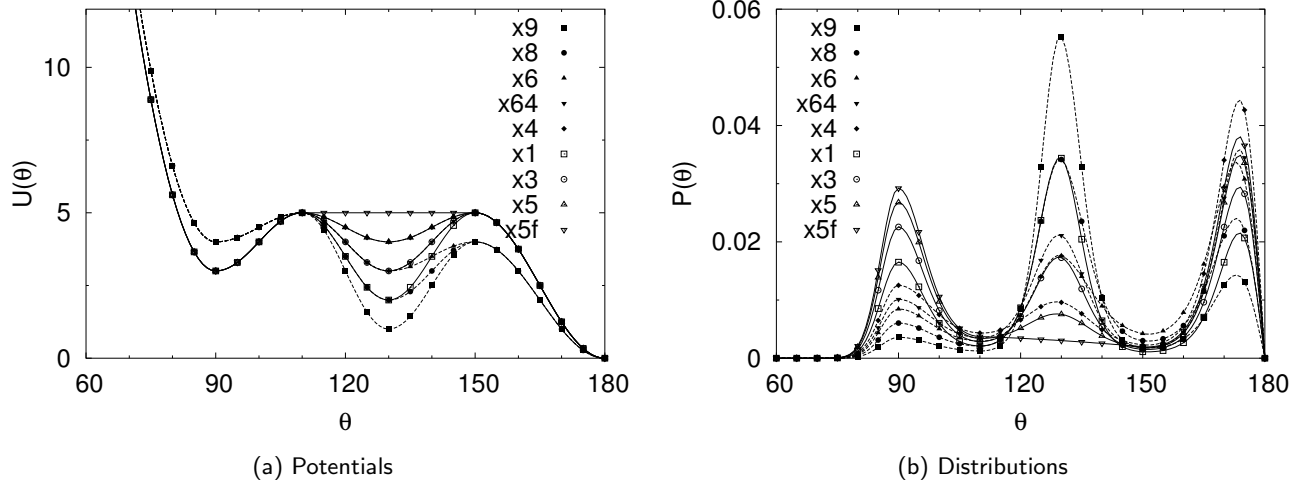


Figure 3.14: Group 1–2: Another study of the effect of the depth of the gg well.

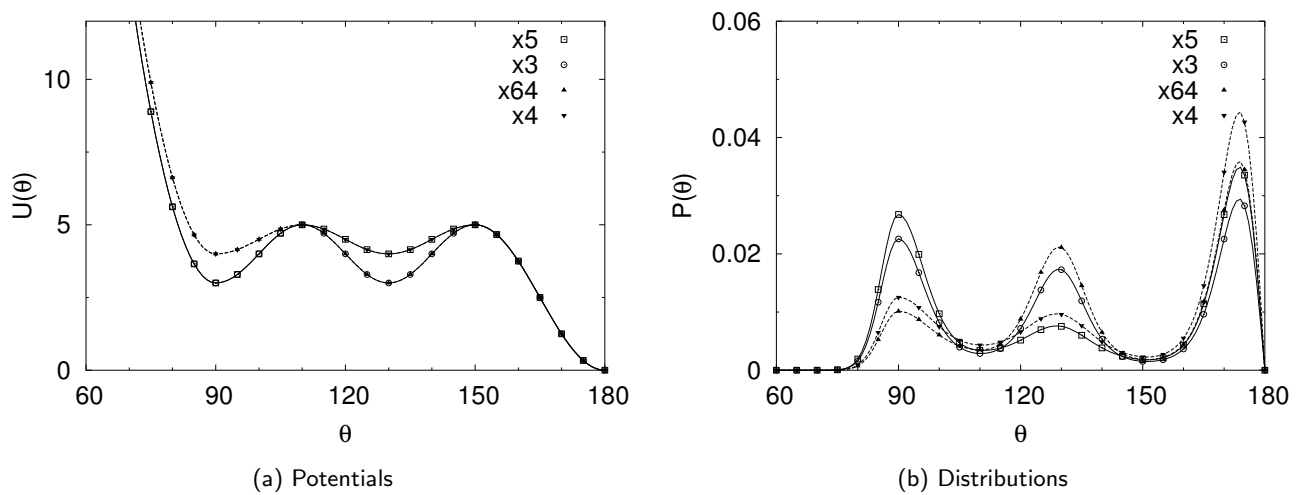


Figure 3.15: Group 4–2: Another study of the effect of the depth of the gg well.

Table 3.15: Group 1–2, $N = 10$.

Potential	l_p	T_{cryst}	$P(tt)$	Self-contacts	$\langle E \rangle$	$\langle \cos \theta \rangle$
CG-PVA	1.32	0.641	0.378	27.10	1280.79	-0.679
x1	0.94	0.495	0.220	29.81	1303.73	-0.554
x3	0.93	0.602	0.309	29.86	1299.52	-0.534
x5	0.88	0.629	0.375	29.91	1290.94	-0.520
x5f	0.94	0.638	0.418	29.60	1285.94	-0.514
x9	1.22	-	0.180	27.56	1285.39	-0.661
x8	1.29	0.569	0.300	27.38	1280.94	-0.669
x6	1.37	0.699	0.425	27.03	1279.96	-0.681
x64	1.19	0.667	0.372	28.13	1283.26	-0.640
x4	1.27	0.737	0.470	27.62	1276.61	-0.646

Table 3.16: Group 4–2, $N = 10$.

Potential	l_p	T_{cryst}	$P(tt)$	Self-contacts	$\langle E \rangle$	$\langle \cos \theta \rangle$
CG-PVA	1.32	0.641	0.378	27.10	1280.79	-0.679
x5	0.88	0.629	0.375	29.91	1290.94	-0.520
x3	0.93	0.602	0.309	29.86	1299.52	-0.534
x64	1.19	0.667	0.372	28.13	1283.26	-0.640
x4	1.27	0.737	0.470	27.62	1276.61	-0.646

Table 3.17: Group 1–2, $N = 50$.

Potential	l_p	T_{cryst}	$P(tt)$	Self-contacts	$\langle E \rangle$	$\langle \cos \theta \rangle$
CG-PVA	1.40	0.727	0.380	191.54	1412.88	-0.681
x1	0.97	0.543	0.223	223.12	1460.29	-0.559
x3	0.95	0.625	0.313	221.67	1451.38	-0.540
x5	0.96	0.699	0.382	220.06	1438.91	-0.528
x5f	0.93	0.715	0.426	221.89	1428.81	-0.523
x9	1.21	0.472	0.181	195.74	1421.32	-0.661
x8	1.30	0.630	0.303	195.53	1420.95	-0.671
x6	1.37	0.756	0.430	188.03	1410.64	-0.686
x64	1.20	0.727	0.375	199.97	1425.20	-0.644
x4	1.34	0.819	0.477	195.13	1412.53	-0.652

Table 3.18: Group 4–2, $N = 50$.

Potential	l_p	T_{cryst}	$P(tt)$	Self-contacts	$\langle E \rangle$	$\langle \cos \theta \rangle$
CG-PVA	1.40	0.727	0.380	191.54	1412.88	-0.681
x5	0.96	0.699	0.382	220.06	1438.91	-0.528
x3	0.95	0.625	0.313	221.67	1451.38	-0.540
x64	1.20	0.727	0.375	199.97	1425.20	-0.644
x4	1.34	0.819	0.477	195.13	1412.53	-0.652

Concluding remarks. This study of the influence of the angular potential on the properties of different models allows to stress a few characteristic features of polymers in the melt. The CG-PVA model has as a very important ingredient an angular potential that reproduces the generic angular states *trans–trans*, *trans–gauche* and *gauche–gauche* (on the coarse-grained level one bond angle corresponds to two consecutive torsional angles of the atomistic backbone); starting from there the energy levels of these states have been varied as well as the energy barriers between them. It was pointed out that the *tg* state influences the propensity of the model to crystallize: The deeper the minimum associated to it, the lower the crystallization temperature T_{cryst} . This is related to the more general observation that T_{cryst} (as well as T_{melt}) is proportional to the probability of *tt* states (see fig. 3.16(d)). The *gg* state energy level was shown to influence the persistence length; the probability of the folded state is also noticeable on the average cosine of angle θ as it has a more drastic effect on the chain’s conformation than the *tg* state that is just intermediate between stretched and folded (see fig. 3.16(a)). The effect of the level of the *gg* state is also observable on other characteristic lengths like R_g and R_e . The heights of the barriers between the different states have effects on both the persistence length and the crystallization temperature since they determine the probability of intermediate states and their modification causes a redistribution of the angular states into *tt*, *tg* and *gg* states. An increase in the *tg–tt* energy barrier leads to a decrease in both l_p and T_{cryst} , whereas an increase in the *gg–tg* barrier has the opposite effects. The change in T_{cryst} is always related to a variation of $P(tt)$.

Figure 3.16 summarizes the correlations found with this study of the influence of the parameters of the angular potential on the properties of the model; it is shown that the crystallization (or melting) temperature is strongly influenced by the probability of *trans–trans* states $P(tt)$, and that the persistence length is related to the probability of *gauche–gauche* states $P(gg)$. Figures 3.16(b) and 3.16(c) also show that there is no cross correlation between these quantities. Section 3.3.3 is devoted to the analysis of the correlation between $P(tt)$ and T_{melt} , and presents a theoretical explanation for this finding.

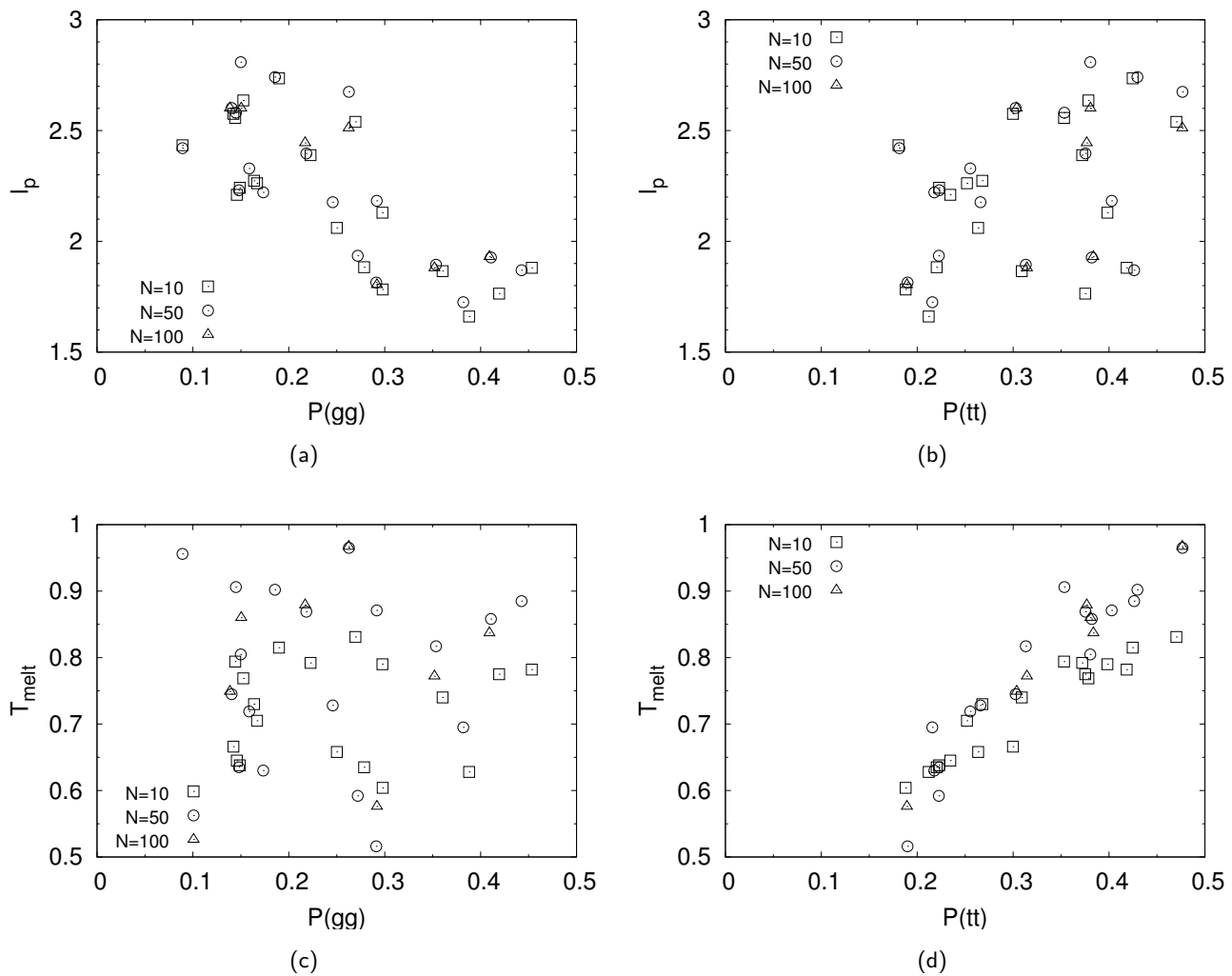


Figure 3.16: Correlations between the persistence length/the melting temperature and the probabilities of *trans-trans/gauche-gauche* states. All points are for different models and different chain lengths; it can be observed that there is a correlation between l_p and $P(gg)$, and that $P(tt) = P_{\text{trans}}$ influences the melting temperature strongly. On the other hand, l_p seems independent of the probability of *trans*-states, as well as $P(gg)$ does not influence the crystallization/melting significantly. The results for *crystallization* temperature are similar to what is observed for the *melting* process.

3.2.2 Reference values for chain length $N = 100$

A list of values measured for the models simulated with chain length $N = 100$ follows (192 chains):

Potential	l_p	T_{cryst}	T_{melt}	t_{ocfee}	$P(gg)$	$P(tg)$	$P(tt)$	$\langle E \rangle$	$\langle R_g^2 \rangle$	$\langle \cos \theta \rangle$
CG-PVA	1.30	0.721	0.860	9062.09	0.150	0.469	0.381	7408.85	19.59	-0.680
x2	0.90	0.518	0.576	4645.58	0.292	0.519	0.189	7728.21	14.98	-0.532
x3	0.94	0.650	0.772	5011.19	0.352	0.334	0.314	7623.31	15.89	-0.541
x4	1.26	0.825	0.967	7095.90	0.262	0.261	0.476	7406.64	19.64	-0.652
x5	0.97	0.701	0.837	5235.17	0.409	0.207	0.384	7554.14	15.55	-0.530
x64	1.22	0.746	0.879	5373.31	0.217	0.406	0.377	7463.04	19.16	-0.645
x8	1.30	0.626	0.749	6237.33	0.139	0.558	0.304	7449.56	20.60	-0.672

Table 3.19: Values for $N = 100$.

3.2.3 Further observations

The results gathered for the different polymer models presented above can be used as a means of testing general polymer physics properties.

Dynamic properties. One can check that the mean-square displacements of the monomers reproduce the expected behavior, i.e. that the subdiffusive regime predicted by the Rouse model can be observed for intermediate times. The quantity

$$g_0(t) = \left\langle \frac{1}{nN} \sum_{a=1}^N \sum_{i=1}^n (\mathbf{r}_i^a(t) - \mathbf{r}_i^a(0))^2 \right\rangle \quad (3.8)$$

describes the mean-square displacement of the monomers (the average is to be taken over all monomers a of the different chains $i = 1, \dots, n$). At very short times, the behavior $g_0(t) \sim t^2$ corresponds to the ballistic regime in which the motion of the particles is free since no interaction has been exerted yet; in this case the displacement is just proportional to time. $g_0(t)$ is expected to vary like t for long times (normal diffusion), and to undergo a slowing down with a $t^{1/2}$ -like variation at intermediate times. This is due to the connectivity of the chains: One monomer can then be viewed as a moving particle whose mass increases with distance, since it has to “pull” the other parts of the chain [22, 100]. Figure 3.17(a) presents the evolution of $g_0(t)$ for two chain lengths, and the different regimes can be observed. For the longest chains we used in the high-temperature equilibrium simulations ($N = 100$), it is also possible to observe a tendency to the $t^{1/4}$ regime as predicted by the reptation theory, but the chains are still not long enough to show a completely clear evidence of the influence of entanglements on the dynamics [22, 100].

Another simple quantity that allows to measure the dynamics of the polymer melt is the orientation correlation function of the end-to-end vector, as defined in eq. (1.68); it is shown in fig. 3.17(b) that this correlation function decays very rapidly for short chains ($N = 10$), and much slower as the chain length increases. This function can

Potential	h_1	h_2	h_3	h_4
CG-PVA	6	2.3	5.1	3.9
x2	6	2	5	3
x3	5	3	5	3
x4	5	4	5	4
x5	5	4	5	3
x64	5	3	5	4
x8	4	2	5	4

Table 3.20: $N = 100$ — Parameters.

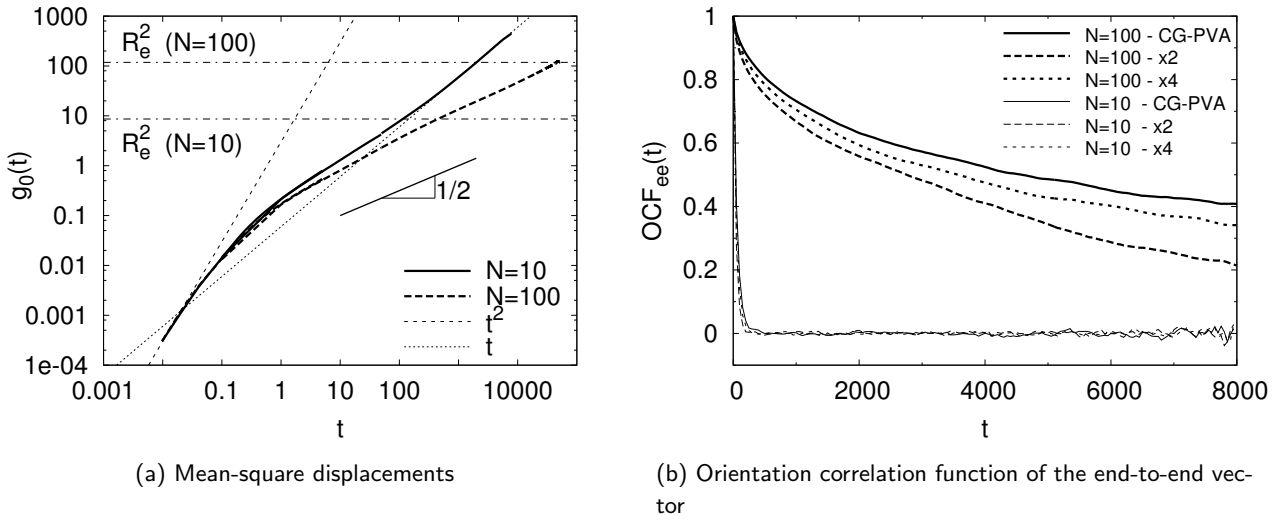


Figure 3.17: Dynamical quantities for the coarse-grained models: Mean-square displacements $g_0(t)$ and orientation correlation function of the end-to-end vector $OCF_{ee}(t)$. The difference in behavior for short ($N = 10$) and longer ($N = 100$) chains is shown for the CG-PVA model, and $OCF_{ee}(t)$ is also compared for three different models.

also be used to compare the dynamical behavior of different models: $OCF_{ee}(t)$ is presented here for CG-PVA and two other models (x4 and x2) that are opposed in the following because of their high and low propensity to crystallize. It is observed that the decay of the orientation correlation function is faster for x2 than for CG-PVA, but the results are qualitatively similar and vary only slightly from one model to the next, as is the case for dynamical quantities in general with our models.

Static properties. For the static properties of the chains, it is sensible to compare our simulation results with a simple model such as the freely rotating chain model (FRCM): This model describes a polymer as a collection of N bonds of fixed length, joined at fixed bond angles [33]. One bond is free to rotate about the axis of the previous bond, meaning that there is no preferred rotational state. This model is a refinement of the simplistic freely jointed chain model, in which there is no correlation between two consecutive bonds. The freely rotating chain model is appropriate to account for the properties of our coarse-grained models for the following reasons:

- The bonds in the CG-PVA model are constrained by a very stiff harmonic potential, such that the probability of finding a bond length 10% above or below its average value b_0 at $T = 1.0$ is less than 1.5%. They could thus be considered to have a constant length in a (good) first approximation.
- The angles between consecutive bonds are not constrained to one single value, but can vary according to the angular potential governing the corresponding interactions. One thus has to use the

average value of the bond angle to compare with the freely rotating chain model.

- There is no torsional potential in our models that could force the chains to prefer one torsional state over any other; the torsional angle distribution is then flat [or almost, cf. fig. 3.19(a)], and the bonds are therefore free to rotate about the axes defined by the neighboring bonds.

It is obvious from the simulation data obtained for the different models and varying chain lengths that there is a correlation between the persistence length l_p and $\langle \cos \theta \rangle$, the average value of the cosine of the bond angle.⁵ This can be understood by looking at the relations one can derive in the framework of the freely rotating chain model. The angle between two consecutive bonds is θ , so the projection of one bond \mathbf{b}^a on the next is

$$\mathbf{b}^a \cdot \mathbf{b}^{a+1} = b_0^2 \cos \theta . \quad (3.9)$$

This can be generalized as:

$$\langle \mathbf{b}^a \cdot \mathbf{b}^{a+k} \rangle = b_0^2 c_\theta^k , \quad (3.10)$$

where $c_\theta = \langle \cos \theta \rangle$ is the averaged value of $\cos \theta$ which is related to the angular potential. One can then calculate the squared end-to-end distance for one such chain (eq. 1.64):

$$R_e^2 = \langle \mathbf{R}_e^2 \rangle = \sum_{a=1}^n \mathbf{b}^a , \quad (3.11)$$

with $n = N - 1$ being the number of bonds in a chain. Evaluation of this quantity gives:

$$R_e^2 = nb_0^2 \left(\frac{1 - c_\theta}{1 + c_\theta} + \frac{2}{n} c_\theta \frac{1 - (-c_\theta)^n}{(1 + c_\theta)^2} \right) \quad (3.12)$$

$$= nb_0^2 C_n . \quad (3.13)$$

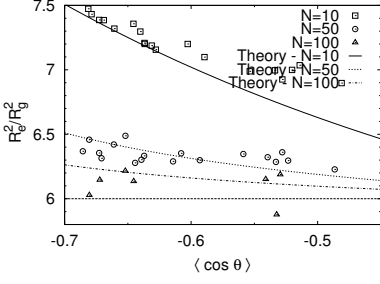
The latter expression is often used in the form of its limit as the chain length tends to infinity, C_∞ (in this limit, the number of repeat units N and the number of bonds n become equivalent):

$$R_e^2 \xrightarrow{N \rightarrow \infty} Nb_0^2 C_\infty = Nb_0^2 \left(\frac{1 - c_\theta}{1 + c_\theta} \right) \quad (3.14)$$

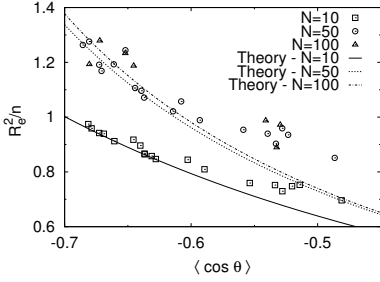
The radius of gyration is computed according to eq. (1.65) and has the following expression within the FRCM:

$$R_g^2 = nb_0^2 \left(\frac{(2+n)(1-c_\theta)}{6(1+n)(1+c_\theta)} + \frac{c_\theta}{(1+n)(1+c_\theta)^2} + \frac{2 \cos^2 \theta}{(1+n)^2(1+c_\theta)^3} + \frac{2 \cos^3 \theta (1 - (-c_\theta)^n)}{n(1+n)^2(1+c_\theta)^4} \right) , \quad (3.15)$$

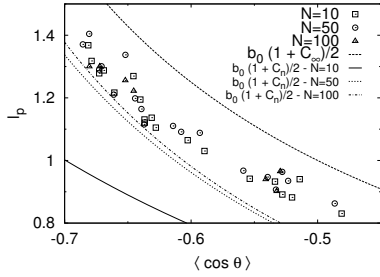
⁵It should be emphasized that the angle θ used throughout this work is related to the angle θ_F defined by Flory by the following: $\theta = \pi - \theta_F$. This introduces some changes in the expressions we refer to, as $\cos \theta = -\cos \theta_F$.



(a) Ratio of the mean-square end-to-end distance and radius of gyration



(b) Mean-square end-to-end distance over the number of bonds $n = N - 1$



(c) Persistence length

Figure 3.18: Characteristic lengths R_e , R_g and l_p as functions of the average cosine of the bond angle θ . Theoretical expectations for the FRC model are compared to the simulation data.

which has again a simplified form in the limit $N \rightarrow \infty$:

$$R_g^2 \xrightarrow{N \rightarrow \infty} N b_0^2 \frac{(1 - c_\theta)}{6(1 + c_\theta)} = \frac{1}{6} R_e^2(N \rightarrow \infty). \quad (3.16)$$

The end-to-end distance is related to the persistence length [eq. (1.62)],

$$l_p = \frac{1}{b_0} \sum_{k=0}^{\infty} \langle \mathbf{b}^a \cdot \mathbf{b}^{a+k} \rangle, \quad (3.17)$$

by the following relation [100]:

$$\begin{aligned} R_e^2 &= \left\langle \left(\sum_{a=1}^n \mathbf{b}^a \right)^2 \right\rangle = \sum_{a,b=1}^n \langle \mathbf{b}^a \cdot \mathbf{b}^b \rangle \\ &= 2 \sum_{a=1}^n \sum_{b=a}^n \langle \mathbf{b}^a \cdot \mathbf{b}^b \rangle - n b_0^2 \\ &= 2 \sum_{a=1}^n \sum_{k=0}^{n-a} \langle \mathbf{b}^a \cdot \mathbf{b}^{a+k} \rangle - n b_0^2 \\ &\simeq 2N b_0 l_p - N b_0^2 \quad (N \gg 1), \end{aligned} \quad (3.18)$$

where the last line is valid if the correlation between the bonds \mathbf{b}^a and \mathbf{b}^{a+k} decays so rapidly that the upper bound of the sum ($N - a$) may be replaced by ∞ .

Figure 3.18 shows a comparison of these theoretical estimates from the FRCM and the corresponding quantities as measured in the simulation. The ratio of the mean-square end-to-end distance and radius of gyration [eqs. (3.12) and (3.15)] is well reproduced, and it can be seen that its value tends to 6 as the chain length increases, as expected. The data for end-to-end distance show a good agreement with the theoretical expression from eq. (3.12), which improves for longer chains and higher average angle (the higher the average value of the angle θ , the more its cosine approaches -1 and in this case the data are observed to be fitted more accurately by the FRCM). The FRCM estimate for the persistence length is not very successful; for our models l_p is observed not to vary significantly with the chain length, and this is not in agreement with the theoretical expectation. The approximation used for the sum in eq. (3.18) is probably not valid in this case.

The torsional angle distribution can be measured as well as the bond angle probability distribution. If the physical meaning of the latter is still clear as one bond angle of the coarse grained models is related to torsional angles of the original backbone, it is far less simple to establish a connection between the atomistic degrees of freedom and the coarse grained torsional angle. As stated above, there is no explicit torsional potential in the model (i.e. the applied potential is zero), and therefore one expects a flat distribution of those torsional angles,

$$\int_0^{2\pi} d\phi P(\phi) = P \int_0^{2\pi} d\phi = 1 \quad (3.19)$$

$$P = \frac{1}{2\pi}. \quad (3.20)$$

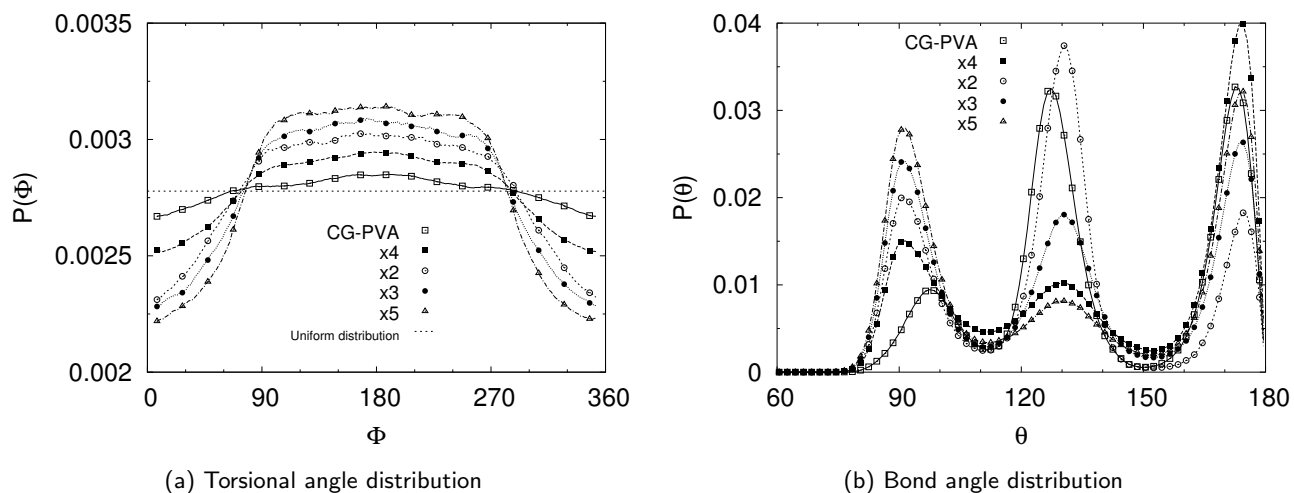
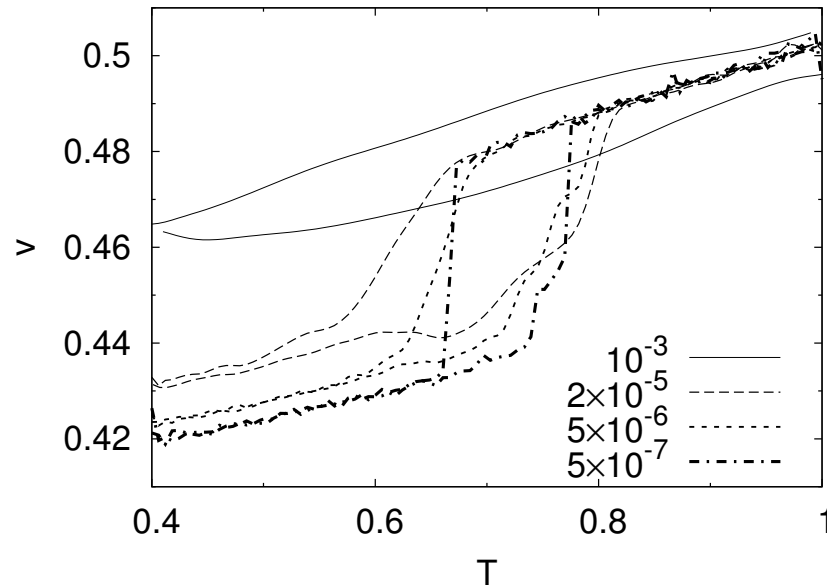


Figure 3.19: Torsional angle and corresponding bond angle distributions for several coarse-grained models, $N = 100$. The deviation from the uniform distribution is worse for x5 than for CG-PVA.

What we observe from the simulations is nevertheless slightly different, as the distributions show minor deviations from the constant value computed for the case of a completely free variable, as is shown in fig. 3.19(a). The reason for such differences between the models becomes clear when one looks at the corresponding bond angle distributions: It can be seen that the model for which the torsional angle distribution differs the most from the flat distribution is x5, which exhibits the largest probability for the *gauche-gauche* state (fig. 3.19(b)). This relation between $P(cis)$ and $P(gg)$ [*cis* denotes the *cis*-state for torsional angles (i.e. $\phi = 0$ in our convention)] holds for the other examples shown here, so that the higher $P(gg)$, the worse the agreement between the flat torsional angle distribution and the actual measurement. The more probable the *gg* state is, the most folded the chains are. In such folded configurations, other torsional states than the *trans* configuration would lead to some overlap between neighboring parts of the chains. Thus, the *cis* state is more unlikely.

Figure 3.20: Comparison of phase diagrams (volume per monomer as a function of the prescribed temperature) for different cooling/heating rates. For high rates ($> 10^{-4}\tau^{-1}$), the system freezes before crystallization is complete, whereas for low rates ($< 10^{-5}\tau^{-1}$) the transition resembles more a first order phase transition. In this study, the cooling and heating rates were taken identical for the different curves. The system consists in 288 chains, $N = 10$. Note the steps in the melting curves indicating the progressive fusion of distinct crystallites. (According to the rate, running averages with different window lengths have been applied to the data.)



3.3 Characterization of the crystal

3.3.1 Continuous cooling

3.3.1.1 Influence of the cooling rate

The simulation protocol we used to reproduce cooling experiments consists in a continuous cooling of the polymer melts at a definite rate. The cooling rate should be taken as small as possible in order to address the phase transition at equilibrium; here we are approaching that ideal phenomenon with non-equilibrium simulations. The applied cooling rate has a significant influence on the phase transition we are addressing, insofar as a too fast cooling would lead to a glassy or at least poorly crystalline configuration even in the case of a crystallizable model. The cooling process thus needs to be as slow as possible, but is severely limited by the amount of computer time available. We therefore investigated the dependence of the cooling rate with a system consisting of 288 chains of $N = 10$ monomers, which is small enough so that low rates can be probed. Once the final crystalline configuration is formed at low temperature, melting is provoked by increasing the temperature in an inverse protocol, which is also expected to be rate-dependent. Nevertheless, in the case of melting there is no need for the chains to order and thus apart from some overheating we do not expect a strong effect of a change in the heating rate. Four different phase diagrams corresponding to decreasing cooling and heating rates are shown in fig. 3.20, pointing out that a very fast cooling ($10^{-3} \tau^{-1}$) leads to a completely flat diagram exhibiting no jump characteristic of a first-order phase transition. This jump develops as the rate decreases, and finally is really abrupt as is expected (for rate $5 \times 10^{-3} \tau^{-1}$). This is only possible for very short chains as otherwise kinetic effects arise as we shall see

later on. Even though crystallization sets in very rapidly, in the case of the slowest cooling, it is very clear that a hysteresis still exists as melting only occurs at a significantly higher temperature (here cooling and heating rates are equal for each crystallization-melting cycle); this indicates that this feature is characteristic of polymer crystallization and would not disappear even for infinitely slow rates. The different heating curves show evidence for a step-wise melting process: The crystalline material starts melting partially and a higher temperature is needed to provide enough energy for the rest of the system to return to the liquid state. This suggests a multi-structure nature of the crystalline system.

For continuous cooling and heating simulations described in the following, we used the cooling rate $5 \times 10^{-6} \tau^{-1}$ and heating rate $2 \times 10^{-5} \tau^{-1}$.

3.3.1.2 Influence of the chain length

The crystallization of polymers produces folded structures of intermediate size, which is not observable with simulations of too short chains like in the case of the small systems mentioned above. Simulations of the CG-PVA model for longer chain lengths allow to reproduce the characteristic folded structures, which is indicated by the simple observation of the evolution of the volume during a continuous cooling. Figure 3.22 presents the results for chain lengths $N = 10, 50, 100$ and 1000 , allowing to compare the drop in volume associated with the transition; all curves are normalized by the value at $T = 1$. The volume of the sample at high temperature varies like $1/N$, which can be understood if the following form is assumed to take chain-end effects into account:

$$v = v_{\infty} + \frac{1}{N} \Delta v, \quad (3.21)$$

where v is the volume per monomer that tends to v_{∞} in case of infinitely long chains, and Δv is the correction for chain ends. As can be seen on the figure, the drop in volume is more pronounced for the shortest chains in the case of which fully stretched configurations are still possible and lead to an almost perfect crystal: Several lamellae consisting of aligned chains. At a larger chain length like $N = 50$, the chains cannot reach such an energetically favorable state anymore, and frustration arises. The chains then fold and the semi-crystalline states at low temperature show well-ordered lamellae surrounded by amorphous zones. There is no qualitative difference between the phase diagrams for $N = 50$ and $N = 100$; this has to do with the two chain length not being really different, but still shows that the crystallization process has the same features for intermediately long polymers, which differ from what is observed in the case of oligomers ($N = 10$). There is again a noticeable difference between the phase diagrams for $N = 50$ and $N = 100$ and the longest chain length we investigated, $N = 1000$. In this case, it is to be expected that entanglements have a much stronger impact on crystallization than for shorter chains, and

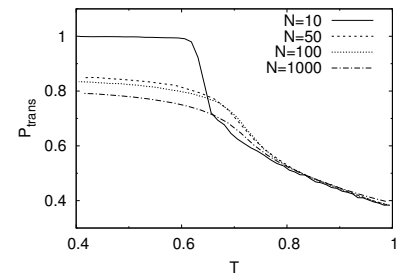


Figure 3.21: Evolution of P_{trans} during continuous cooling for various chain lengths.

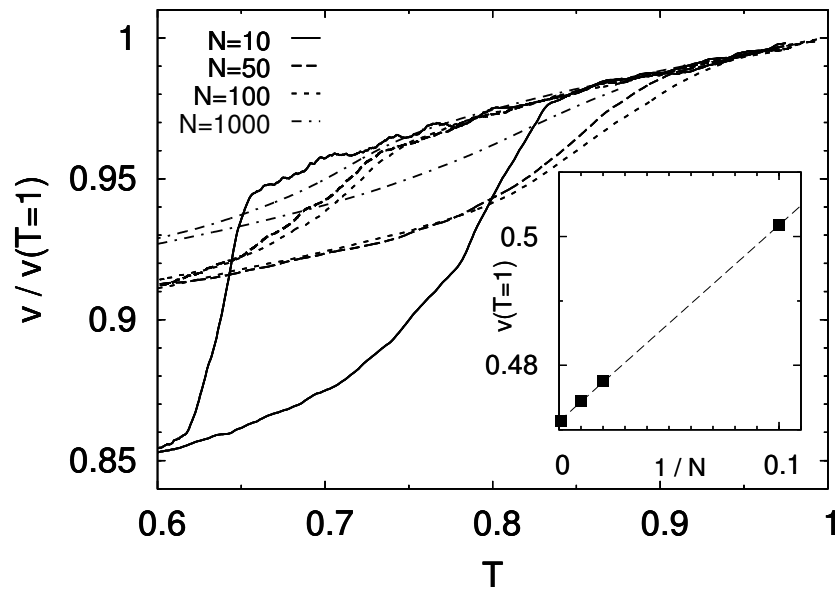


Figure 3.22: Phase diagrams (volume per monomer v as a function of temperature) obtained for the CG-PVA model, for different chain lengths; v has been rescaled by its value at $T = 1$. The linear variation of the volume at high temperature with the inverse chain length $1/N$ is shown in the inset.

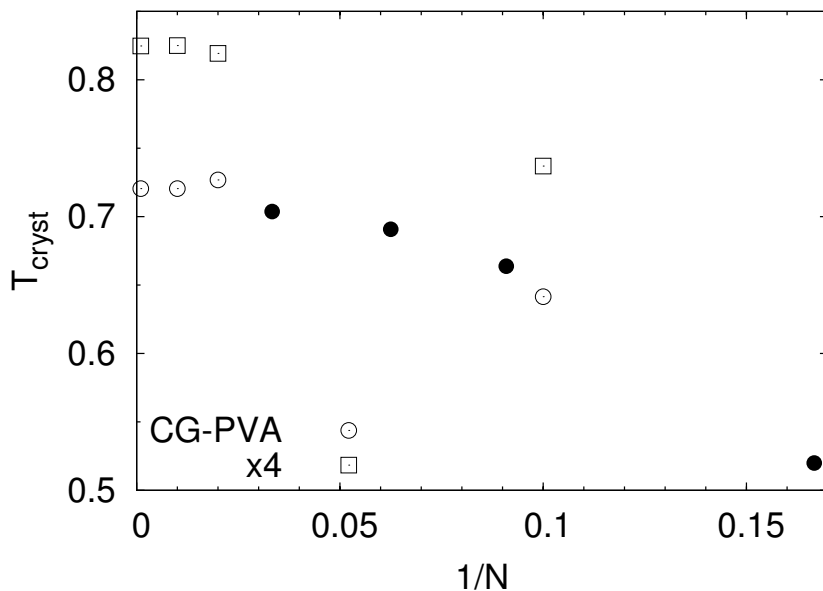


Figure 3.23: Evolution of the crystallization temperature as a function of the chain length, for CG-PVA (\circ and \bullet) and x4 (\square). T_{cryst} rapidly saturates, showing only a small difference for chain length $N = 50, 100$ and 1000 . The crossover to polymer-like behavior for our models thus appears to be located in between $N = 10$, for which crystallization occurs much later, and $N = 50$. For small chains, the melt remains in a metastable liquid state for a longer time, because of the higher mobility of oligomers; for longer molecules the supercooling leads to structure formation surrounded by material trapped in a frustrated configuration. (Points \bullet are data from H. Meyer.)

the process is hindered because of the smaller overall mobility of the monomers. The amount of amorphous material in the final configurations for each chain length can be related (in a first approximation) to the fraction of *trans* states in the crystal. Figure 3.21 shows the evolution with temperature of this quantity for the different chain lengths, and it can be seen that in the case of very short chains this fraction ends up being 1, which corresponds to all-*trans* configurations of the chains. This is not the case for longer chains, and there is a slightly lower fraction of *trans* states in the case of $N = 1000$.

The crystallization temperatures for the different chain lengths are indicated in fig. 3.23 for CG-PVA and the x4 model. It can be seen that there is a large difference between $T_{\text{cryst}}(N = 10)$ and $T_{\text{cryst}}(N = 50)$, but only small variations for the longer chain lengths. This is related as

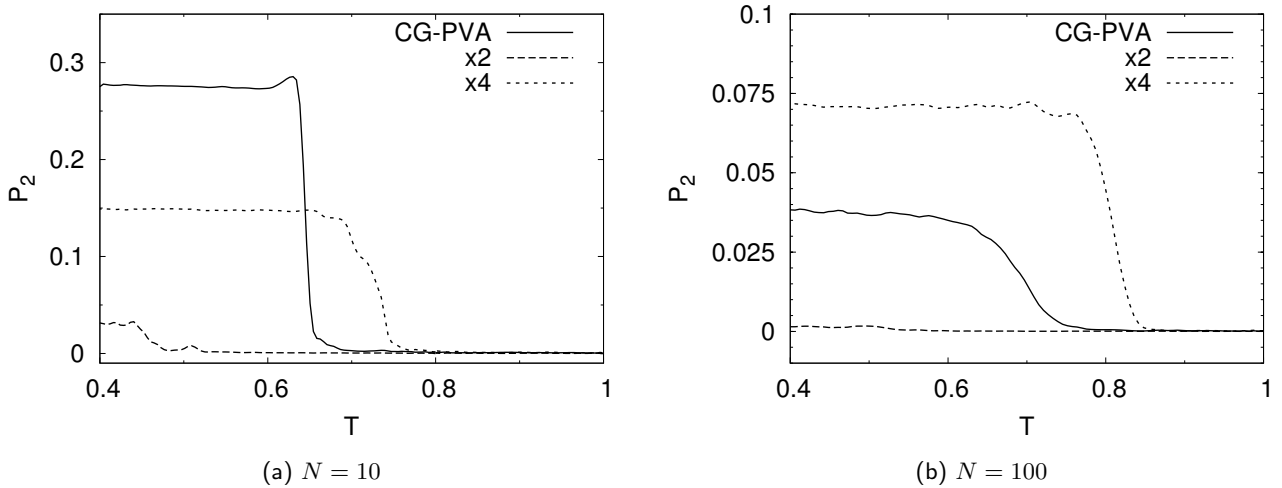


Figure 3.24: Evolution of the P_2 order parameter during continuous cooling, for short and long chains. The x4 model always crystallizes earlier, and in the case of short chains this leads to a poisoning of the crystalline configuration (worse order parameter than in the CG-PVA model which crystallizes later and has lower crystallinity for $N = 100$; see also figs. 3.27 and 3.29). Note the difference in vertical scales for the two plots (much higher crystallinity in the case of short chains).

stated above to the difference in mechanism for oligomers and polymers; for long polymer chains crystallization occurs at a supercooling that is representative of the nature of the chains rather than their length.

3.3.2 Order parameters during the crystallization and melting process

3.3.2.1 Global order parameter

P_2 order parameter. In order to characterize the crystalline state and the crystal formation in the polymer melts we have simulated, it is necessary to introduce order parameters. One simple measurement of the order in the system is provided by the computation of the P_2 order parameter as defined in 1.3 which quantifies the *global* correlation of orientation of the bonds in the system. When averaged over individual chains, this parameter gives an information on the degree of orientational order at the level of one chain, and allows to determine whether the chains are stretched or not. These parameters can be used to describe the crystallization of our polymer melts, and become especially useful to compare the different models and chain lengths. The evolution of the global order parameter is represented on fig. 3.24: The formation of crystalline structures for the CG-PVA model is compared with crystal growth for two other models, x2 and x4. The x2 model crystallizes rather poorly, at a very low temperature (below $T = 0.6$), while x4 crystallizes at high temperature. In the case of long polymer chains ($N = 100$), this model which shows a larger tendency to crystallize also forms a better ordered structure, as indicated by a higher value of P_2 than for CG-PVA. This is however different from what happens for shorter chains: In this case, the low flexibility of the model favors the

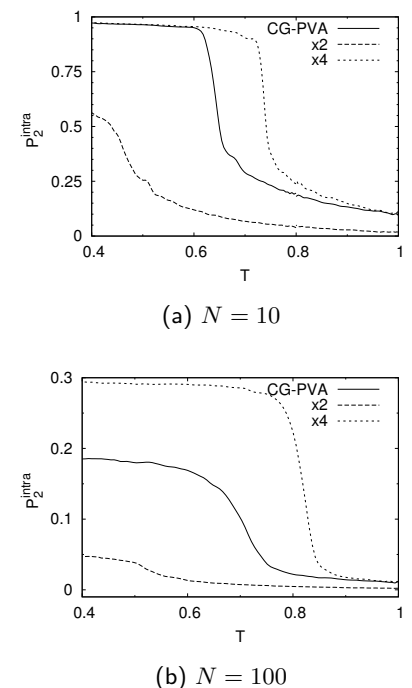


Figure 3.25: Intra-chain P_2^{intra} order parameter as a function of temperature during cooling, for $N = 10$ and $N = 100$.

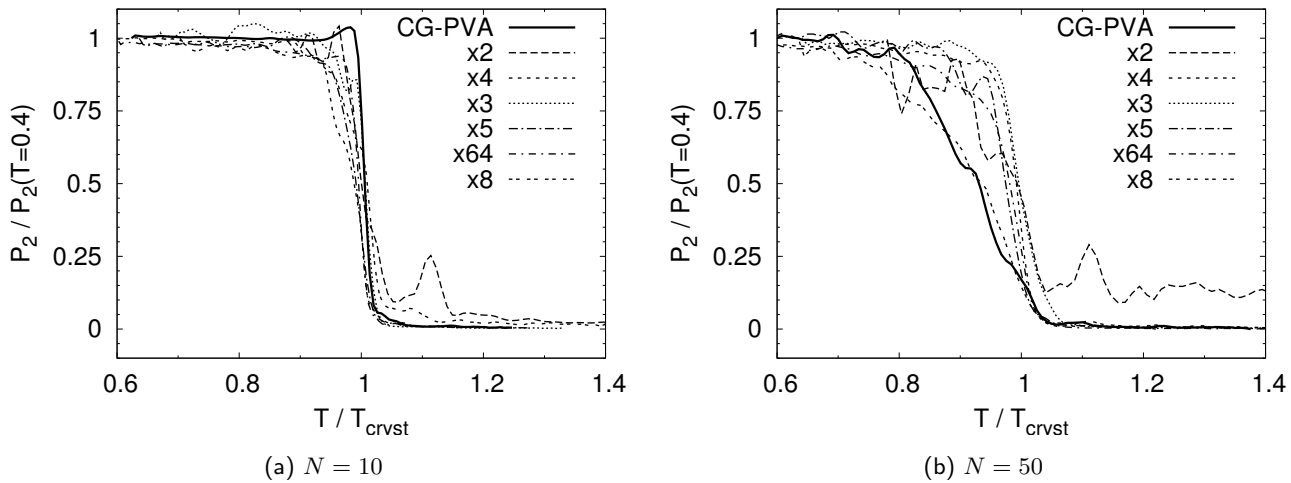
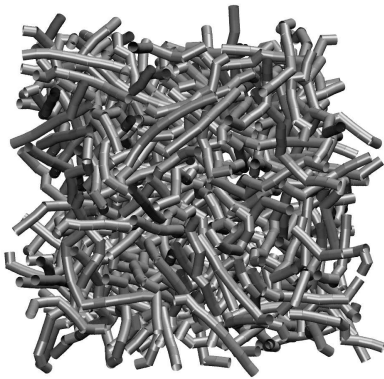
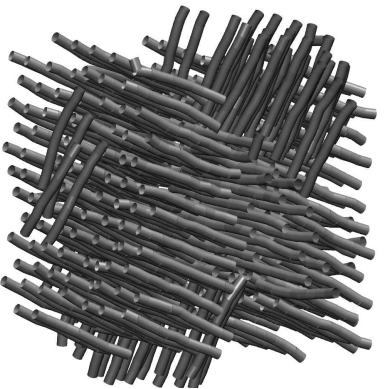


Figure 3.26: P_2 order parameter evolution during continuous cooling. Curves for the different models superimpose, indicating a common crystallization mechanism.



(a) $T = 1$



(b) $T = 0.4$

Figure 3.27: Snapshots of a continuous cooling simulation: Initial and final configurations, CG-PVA model for $N = 10$ chains. One can observe that the lower rigidity of the model led to the formation of less stable nuclei than in the case of x4 (fig. 3.29).

occurrence of all-*trans* conformations of the chains *too fast*, which hinders the *inter*-chain ordering. This self-poisoning of the crystallization process is reflected in the low P_2 value observed for x4 (fig. 3.24(a)).

Decomposition of the order parameter into *inter*- and *intra*-chain contributions allows to verify that there is no difference in the final state for the CG-PVA and x4 models at the level of the chain for $N = 10$: Both models yield all-*trans* conformations at low- T (fig. 3.25(a)). Thus the difference observed in fig. 3.24(a) arises from the packing of the rigid chains into many small structures instead of one large lamella (or several parallel lamellae).

The evolution of the order parameter during a cooling experiment indicates that the different models crystallize at different temperatures, and yield semi-crystalline structures with varying degrees of ordering. This triggers the question of whether crystallization occurs as a result of the same mechanism for each model, or if there are significant model-specific features for this process. Figure 3.26 shows that it is possible to superimpose the variation of P_2 for the different models using an appropriate normalization: The order parameters have been normalized to their values at low temperature ($T = 0.4$) for every model, and the horizontal axis corresponds to the ratio T/T_{cryst} . It would have been more satisfactory to use $P_2(T = 0)$ (or an extrapolation to that point) to normalize the vertical axis, but it can be seen that the order parameter has already saturated at this temperature, so we do not expect a significant change due to that. It is observed that all curves superimpose nicely for $N = 10$, indicating that the process of crystallization is identical for each model and does not depend on the crystallization temperature (fig. 3.26(a)). The curves corresponding to models that do not crystallize easily (i.e. at low temperature and not yielding a strongly ordered crystal), like x2 and x8, exhibit more noise after nor-

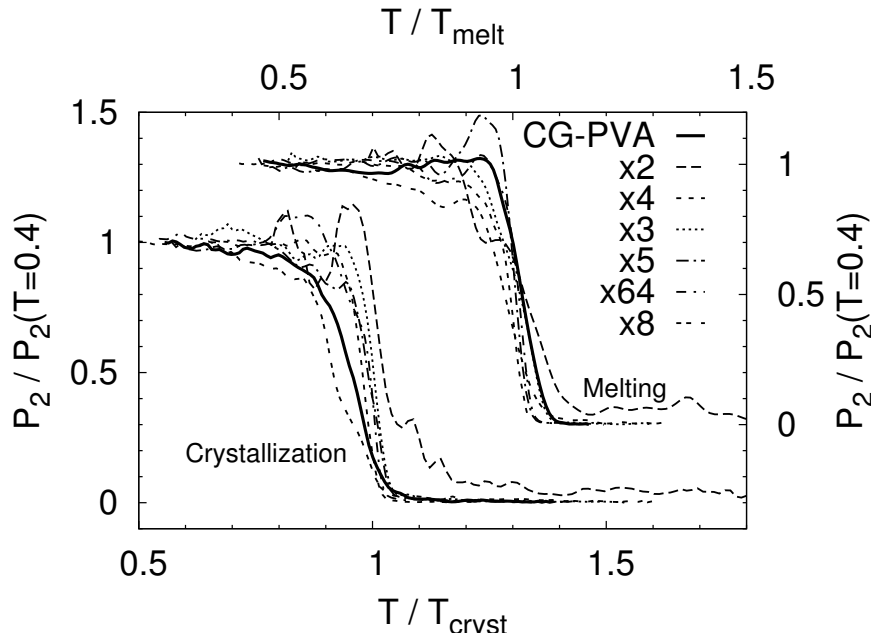


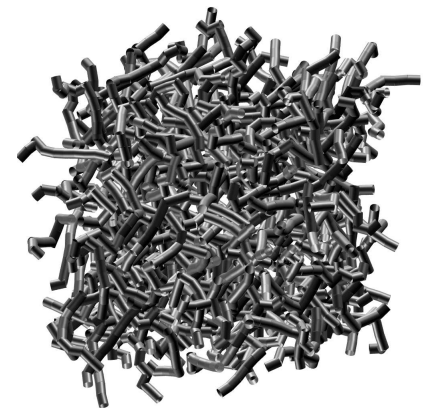
Figure 3.28: P_2 order parameter evolution during continuous cooling and heating, for $N = 100$. The different curves corresponding to various models exhibit the same features which suggests a common mechanism for crystallization (and for melting). The left and bottom axes correspond to the crystallization curves, and the top and right axes to the melting simulation results.

malizing, and even show a signal prior to the transition. In the case of x2, there is a peak above T_{cryst} corresponding to a first attempt to form an ordered structure that does not become stable and vanishes. One can also notice oscillations right after the transition, when the crystalline structure has to relax to its final form.

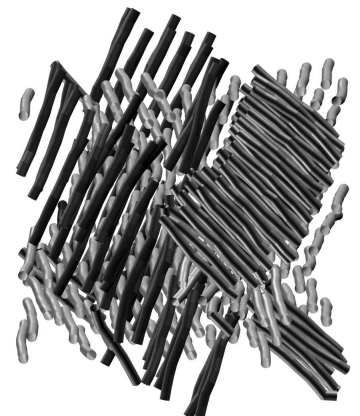
For systems with longer chains ($N = 50$) the crystallization curves do not superimpose as nicely as for $N = 10$, but all of them show the same features (fig. 3.26(b)). The specificity of long polymer chains shows up in that the transition is less abrupt than for short chains. The x2 model shows a very high level of noise as for $N = 50$ already the final crystalline state is poorly ordered (and the corresponding value of P_2 very small).

Figure 3.28 presents the equivalent information for longer chains, $N = 100$. As crystallinity decreases with increasing chain length, in this case the data are more strongly affected by noise and averaging over decorrelated configurations would be useful (though time-consuming). Nevertheless it appears that again all models follow the same trends and seem to crystallize according to the same process. Pre-ordering signals are again noticeable in the case of the x2 model, as well as the oscillations after the transition. The crystallization process seems a bit slower in the case of the CG-PVA model, when compared to the other models. The same plot also shows the corresponding data for the heating simulations that followed the crystallization experiments. Also in this case it appears that all models behave in a similar fashion, with minor distinctions though. The melting and crystallization curves do not exactly match, but the comparison is not obvious because rates were not the same for cooling and melting.

It is possible to establish a correlation between the crystallization temperature and the order in the low-temperature phase, at least for



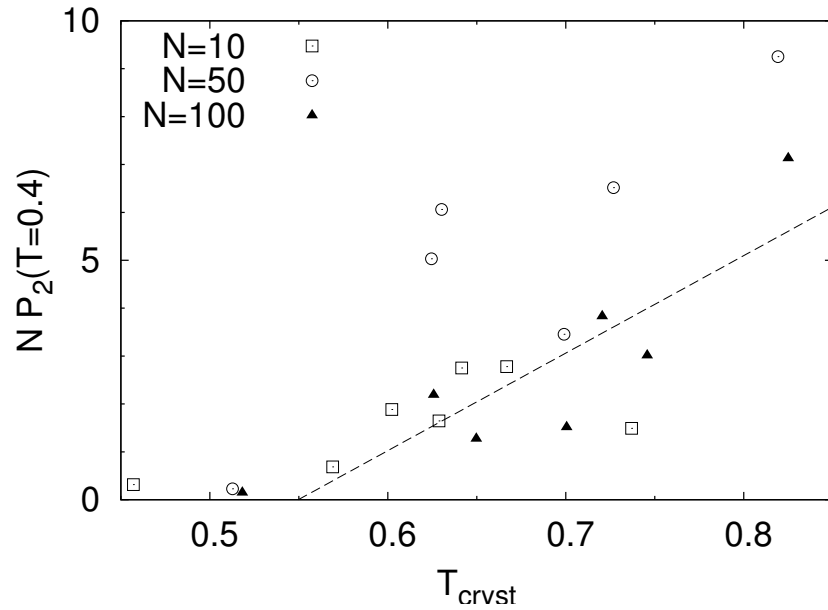
(a) $T = 1$



(b) $T = 0.4$

Figure 3.29: Snapshots of a continuous cooling simulation: Initial and final configurations, x4 model for $N = 10$ chains. The lamellae impinge and give rise to a multi-domain configuration, which explains the relatively small value of the order parameter P_2 (cf. fig. 3.24(a)).

Figure 3.30: Correlation between the order parameter of the final crystalline structure [$P_2(T = 0.4)$] and the temperature of crystallization. The order parameter has been multiplied by the chain length so that the scale fits for all points. A fit line for $N = 100$ is shown, to point out that the lower T_{cryst} , the worse the order in the final semi-crystalline structure. For $N = 10$ the evolution of $P_2(T = 0.4)$ does not show a monotonic behavior as a result of the self-poisoning effect mentioned above; for $N = 50$ the data do not match these for other chain lengths, probably due to the simulation boxes being too small in that case.



long enough chains. Figure 3.30 shows that the value of P_2 increases when the system crystallizes at higher temperature.

This indicates that the more mobile the monomers are, the better the crystalline structure. In case the temperature has to be greatly lowered in order to allow for rigid enough conformations that could favor the occurrence of crystallization, the system approaches its frozen state and thermal energy is not high enough to help the chains organize on a large scale. There is thus a competition between the two effects (mobility/flexibility). However, this is not true for short chains as we pointed out in the preceding, since models that crystallize too rapidly prevent themselves to find an optimized *inter*-chain structure. This can be observed here again, as the point corresponding to the x4 model has lower crystallinity than other models for $N = 10$, even though its crystallization temperature is higher. It should also be noted that the evolution of P_2^{inter} and P_2^{intra} with N is monotonic for all models, whereas for x4 and two other models, the overall P_2 parameter is smaller for $N = 10$ than for $N = 50$. This indicates that the relation between *intra*- and *inter*-chain effects is not simple, and that the P_2 order parameter cannot precisely account for the packing of chains in the crystals.

The simple order parameter P_2 provides an efficient way of characterizing the order in a polymer melt during continuous cooling or heating simulations. However, such a global parameter does not yield precise information about the local structure of the semi-crystalline systems and thus it is difficult to define a *crystallinity* accurately. The decomposition into *inter*- and *intra*-chain contributions does not allow to access information about the intimate organization of the chains inside the partially crystalline system since there is still no distinction between particles belonging to the crystal and the amorphous medium. It is

necessary to define another order parameter using more local criteria in order to distinguish the crystallites.

Tensor order parameter. Another order parameter is also indicated in order to study the development of the crystalline phase from the melt: The tensorial order parameter defined for liquid crystals can be applied to crystalline polymers as well [50]. This order parameter is based on the definition of the orientational tensor Q , given by:

$$Q_{\alpha\beta} = \sum_i \left(\tilde{b}_i^\alpha \tilde{b}_i^\beta - \frac{1}{3} \delta_{\alpha\beta} \right). \quad (3.22)$$

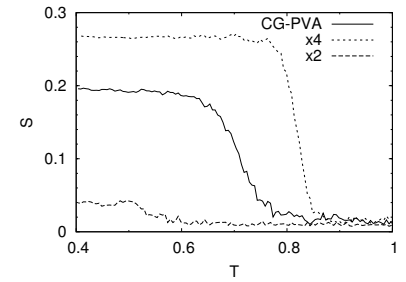
Here \tilde{b}_i^α denotes the α -coordinate of the unit vector along the direction of bond i which joins the monomers i and $i+1$. The sum is to be taken over all bonds in the system. One scalar order parameter that can be defined using eq. (3.22) is the following:

$$S = \sqrt{\frac{3}{2} \text{Tr } Q^2}. \quad (3.23)$$

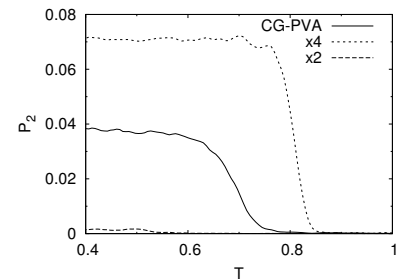
This order parameter S has been computed from the simulation data for the different coarse-grained models with $N = 100$, yielding results qualitatively similar to those obtained with P_2 . As can be seen in fig. 3.31, the absolute value of the order parameter S is significantly higher than the result of P_2 . The order parameter S built on the orientational tensor S is better suited to distinguish the contributions of the ordered and amorphous regions, whereas P_2 tends to couple them, which results in a loss of signal. However, the most relevant information being the relative value of the parameters for the different models we intend to compare, both order parameters can be considered as equivalent in our case.

3.3.2.2 Definition of crystallinity

To provide an effective definition of crystallinity for our semi-crystalline samples, we used an order parameter that takes into account orientational order of the bond vectors like P_2 but that is restricted in space, so that correlations between different regions of the simulation box are left aside. For a given configuration, a set of “neighbors” are defined for each bond. Two bonds are tagged neighbors if their centers of mass are closer to each other than the distance r_{cut} , and if the cosine of the angle between them is greater than another parameter c_{cut} (see fig. 3.32). Once this list of neighbors is created, the information is sorted and sets of neighboring bonds are determined. The so-defined crystallites are then analyzed as this procedure allows to monitor their evolution during the simulation, showing the growth of structures during cooling. Crystallites that are smaller than a given size N_b^{min} are not taken into account as they might only arise accidentally; a distinction is made between regular crystallites larger than N_b^{min} and larger structures with



(a) Order parameter S



(b) Order parameter P_2

Figure 3.31: Comparison of two order parameters: P_2 and S . The results are qualitatively similar, even though the absolute values are different: The result given by S is closer to 1 for all models. Still, the relative measurement of ordering in the system is the same for both parameters, as illustrated here (for clarity, the results for three models only are shown).

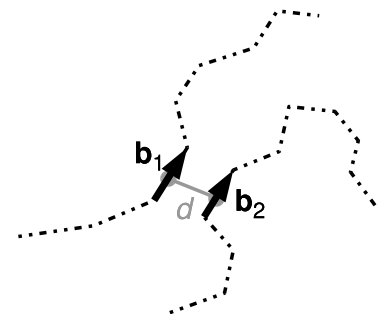
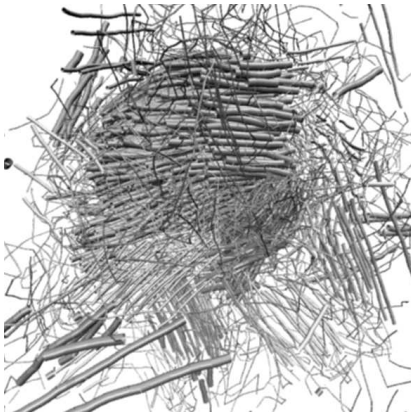


Figure 3.32: Schematic representation of the definition of the local order parameter: Two bonds are tagged “neighbors” if they are separated by a distance d smaller than r_{cut} and if the angle between \mathbf{b}_1 and \mathbf{b}_2 is such that $|\mathbf{b}_1 \cdot \mathbf{b}_2| > c_{\text{cut}}$.



(a) CG-PVA



(b) x4

Figure 3.33: Snapshots of semi-crystalline configurations ($T = 0.4$); the crystallites detected using our analysis program are represented using larger diameter bonds, so that they are more easily distinguishable from the amorphous zones (plotted here as simple lines). It can be seen that crystallinity is higher in the case of the x4 model.

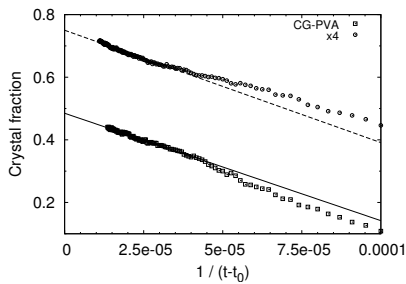


Figure 3.34: Extrapolation giving the value of v_c as $t \rightarrow \infty$: The value v_c^{\max} obtained this way is an approximation to $v_c(T = 0)$.

more than N_b^{big} bonds. These large crystallites have been analyzed in more details. Crystallinity is defined as the ratio of the number of bonds that belong to crystallites to the total number of bonds in the system. This is equivalent to the volume fraction v_c of the crystalline material.

We applied this analysis method mostly to the systems of chains with chain length $N = 100$; in this case, the values used as parameters were the following:

- $r_{\text{cut}} = \sigma$,
- $c_{\text{cut}} = 0.99$ (i.e. the maximum angle between two neighboring bonds is approx. 8°),
- $N_b^{\text{min}} = N/10 = 10$,
- $N_b^{\text{big}} = N = 100$.

These values necessarily affect the resulting quantities such as the crystallinity; we studied the effects of the variation of these parameters and made sure that around the chosen values this would not lead to an important qualitative change. What we are mostly interested in anyway is the evolution of crystallinity as a function of time or temperature, and a comparison between our different models rather than an absolute measurement.

The different models with different angular potentials we have been studying become semi-crystalline upon cooling and as we have already seen using the order parameter P_2 , the degree of order and thus the crystallinity varies from one model to another. For instance it has been observed that the x4 model has a high crystallization temperature and is well-ordered in the low-temperature phase while the x2 model seems to crystallize poorly at a low temperature (fig. 3.33). A comparison of the crystallinities for these models and CG-PVA is presented in fig. 3.35, showing that the crystallinity is indeed much higher for x4 and very low in the case of x2.

Figure 3.36 shows an attempt to plot the crystallinity as a function of temperature for several models on a master curve, in order to isolate the relevant characteristics of the processes. However, the different curves do not completely superimpose, which indicates that the parameters used to normalize the data may not contain the relevant information that describes the crystallization process accurately.

One reason why the curves do not superimpose well is that the value of the crystal fraction at $T = 0.4$ taken as a reference is not relevant for this order parameter as it was for P_2 : If P_2 had already almost saturated for all models at $T = 0.4$, this is no longer the case for v_c . One way of getting a more satisfactory normalization would be to use $v_c(T = 0)$ instead. An approximation of this quantity is obtained by linear extrapolation of $v_c(1/t)$ as $t \rightarrow \infty$, since time and temperature are connected in a continuous cooling simulation. The values determined

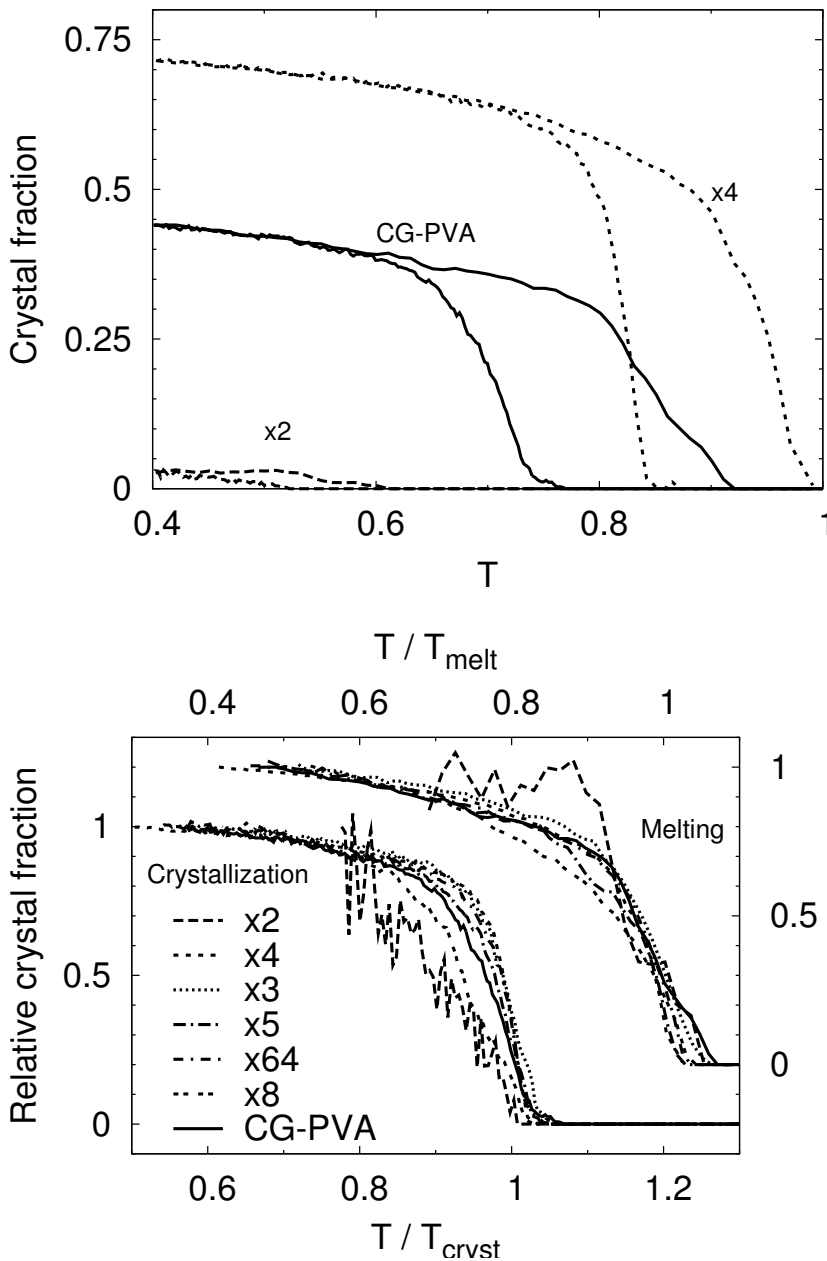


Figure 3.35: Crystal fraction as a function of temperature for three different models ($N = 100$). The crystal fraction is computed using the definition of crystallites given in the text; each point is the result of an average over 10 consecutive configurations stored during the simulation. The crystallinity does not reach a plateau as T approaches 0.4 but rather increases as the decreasing temperature favors ordering of the amorphous domains left around the main crystallites.

Figure 3.36: Evolution of the crystal volume fraction during crystallization and melting, for different models. Temperature has been normalized either by the crystallization temperature or the melting temperature. The relative crystal fraction corresponds to the crystal fraction measured during the simulation which has been divided by the value at $T = 0.4$. The curves superimpose but there are deviations, particularly for the x2 model that crystallizes badly.

this way (see fig. 3.34) are slightly overestimated because the variation of v_c with $1/t$ is not necessarily linear. But this already provides a better-defined quantity to compare the different models, as it does not depend anymore on the crystallinity at $T = 0.4$, which is arbitrary.

3.3.2.3 Avrami analysis

In order to describe the growth of the crystallites, it is useful to adapt a simple analysis that has been applied a long time ago by Avrami to the growth of crystalline structure [135]. This analysis in the case of polymer crystals has been used to interpret the growth of spherulites, which are orders of magnitude larger than the crystallites we are to observe in our simulations; yet, it seems reasonable to model the growth

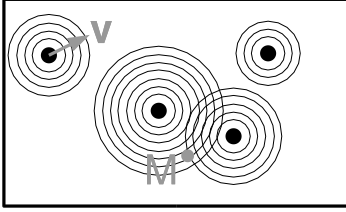


Figure 3.37: Expanding waves on a pond surface. The wave fronts are moving away from the centers with velocity v ; the interesting quantity is the probability that no wave has passed a particular point M at time t .

of these crystalline regions in the same way, since we are also dealing with growing objects in an amorphous medium. Avrami's description of crystal growth can be presented by analogy with the problem of expanding waves created by the fall of raindrops on the surface of a pond; each drop is the starting point of a wave that grows circularly, and after several waves have been initiated and expanded, they finally impinge. A similar model allows to account for the growth of three-dimensional objects in a polymer melt, which has to be fast in the first steps when the different crystallites cannot see each other, and should slow down as they come into contact. As shown schematically in fig. 3.37, waves are expanding and possibly meet each other; the probability that k waves have passed at point M during time t can be expressed as a Poisson law, since the different events can be considered independent:

$$P_k(t) = \frac{E^k}{k!} e^{-E} . \quad (3.24)$$

E is the expected number of waves at time t , and contains the information about the propagation of the waves. In the case of circular waves on a water surface, E can be estimated in the following way: The number of waves having reached point M from a distance r after time t is

$$dE = I \left(t - \frac{r}{v} \right) 2\pi r dr , \quad (3.25)$$

if there the rate of droplets is I per unit time and area. In order to account for all possible waves, eq. (3.25) has to be integrated over all values of r , i.e. between 0 and $r_{\max} = vt$:

$$E = 2\pi I \int_0^{vt} dr \left(t - \frac{r}{v} \right) r = \pi I v^2 \frac{t^3}{3} . \quad (3.26)$$

The same reasoning can be applied to the growing crystal situation, using an appropriate expression for E and changing the dimensionality (we are considering three-dimensional objects). Then, this simple theory provides an expression for the crystallinity of the semi-crystalline system: The probability that no structure has passed point M at time t represents the fraction of amorphous material still existing in the sample, and this is simply $P_0(t)$; thus the crystal fraction is

$$v_c = 1 - P_0(t) \quad (3.27)$$

$$= 1 - e^{-E} . \quad (3.28)$$

In three dimensions, the growth of a crystallite can be described using a similar expression for E as for the propagating waves on a pond: For crystallites that are created through thermally activated nucleation, the result is just the same as in eq. (3.26):

$$E = 4\pi I \int_0^{vt} dr \left(t - \frac{r}{v} \right) r^2 = \pi I v^3 \frac{t^4}{3} . \quad (3.29)$$

In case the crystallites are only created at $t = 0$ (athermal nucleation), E becomes:

$$E = 4\pi I \int_0^{vt} dr r^2 = 4\pi I v^3 \frac{t^3}{3}. \quad (3.30)$$

Using other models to predict E , several expressions can be found for v_c , having the general form

$$v_c = 1 - \exp\left(-\left(\frac{t}{\tau}\right)^n\right). \quad (3.31)$$

Experimental results have been found to match this simple rule, and many interpretations have been given to account for the different values of n that allowed to fit eq. (3.31). It has been proposed that according to the shape of the growing objects, crystal growth could be modeled using Avrami equations with different n . There were also many discussions on whether this method is relevant, since this interpretation might be misleading. We will not try to use Avrami equations to describe the spatial characteristics of the growing structures; we are only interested in the convenient way this simple model provides to compare the results for our different models.

We have presented in fig. 3.38 the evolution of the measured crystallinity for two models, in such a way that a direct comparison with Avrami equation is possible. It can be seen that if the first points are left aside, both models show a behavior that can be described using an Avrami equation with $n = 3$. In order to allow for the comparison with eq. (3.31), the measured v_c has been divided by the extrapolated v_c^{\max} (since the Avrami equation considers the final configuration as perfectly crystalline). Time also has to be modified so that the comparison of the different models becomes possible: Therefore the time scale has been shifted by an amount t_0 corresponding to the time at which the system starts to crystallize (occurrence of non-zero values in the crystallinity). A comparison of the original data for v_c and the Avrami estimation is plotted in fig. 3.39; it can be observed that the Avrami function reproduces well the behavior shown by the simulation data, for the early stages of crystallization. It is possible to propose such a description of the development of crystallinity for all the different models, which allows to define a characteristic time τ in each case; this makes it possible to draw the crystallinity as a function of time on a new master curve, which shows a better superposition than in fig. 3.36; the relative crystal fraction for CG-PVA and x4 in particular superimpose quite well, indicating that in both cases the crystallization process has the same features during the first stages of crystallization, which was not obvious from the shape of the original curves as presented in fig. 3.35.

The physical signification of the characteristic time τ is not obvious; still we could find that it corresponds to the time that is needed for several quantities characterizing the evolution of the crystallites to decay. Figure 3.41 shows the evolution of the crystalline domains during the cooling. The total number of crystallites (structures containing at

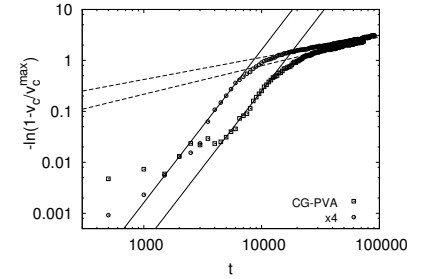


Figure 3.38: Avrami plots for the CG-PVA and x4 models: The relative crystal fraction v_c/v_c^{\max} behaves as $1 - \exp\left(-\left(\frac{t}{\tau}\right)^3\right)$ during the early stages of crystallization. Later on, another regime shows a slowing down in the crystallization process. Fits allowing to define the characteristic time τ are indicated for the $n = 3$ regime (as well as for the slow second phase).

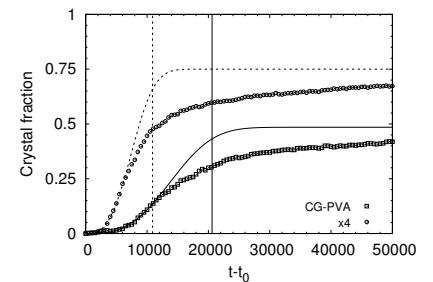


Figure 3.39: Comparison of the simulation data for the crystallinity and the fitted Avrami expression. There is a good agreement for short times; the characteristic times τ are indicated for the two models.

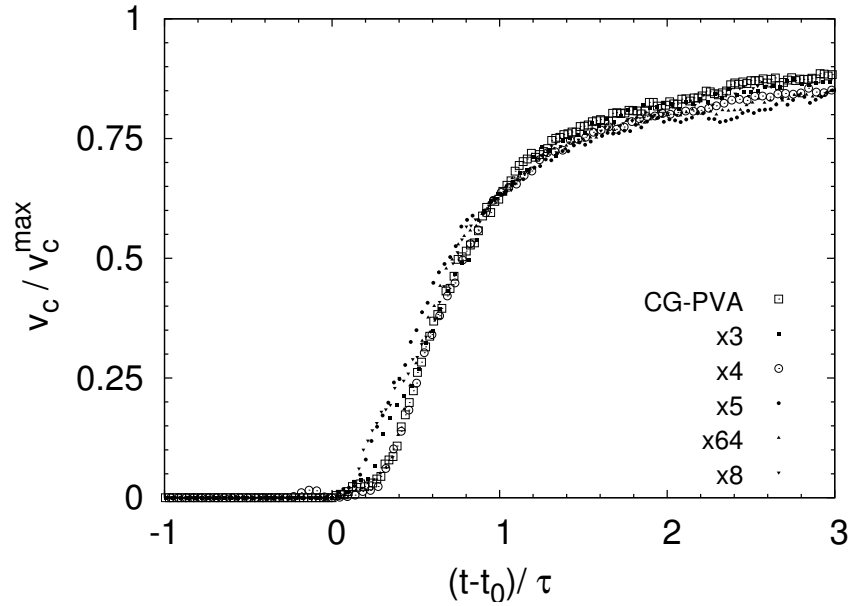


Figure 3.40: Master curve presenting the increase in crystallinity as a function of the reduced time t/τ . v_c has been normalized using the values v_c^{\max} determined as shown in fig. 3.34 and τ was obtained through a fit using the expression given in eq. (3.31) (with $n = 3$).

least $N_b^{\min} = 10$ bonds) first increases in a linear fashion with time (and thus with the supercooling since temperature is proportional to time in a continuous cooling), then drops down as the formation of larger crystallites occurs: Small ordered domains are absorbed into the larger crystallites, and these growing objects leave less and less material that can in turn give rise to new seeds (fig. 3.41(a)). After $t = \tau$ there is a slowing down in the decrease of crystallite number, but this value does not saturate yet. The evolution of the larger crystallites ($N_b^{\text{big}} > 100$) is also interesting (fig. 3.41(b)): For all models there is a clear saturation that occurs at $t = \tau$ (or slightly later in the case of models that formed a larger number of these big structures). This is the sign that after $t = \tau$, the development of new large ordered domains has become impossible. The fact that the total number of crystallites does not reach a limit immediately after τ suggests that reordering still occurs in the small crystallites embedded in the amorphous zones surrounding the major crystallites. More detailed information is available for the larger crystalline domains (fig. 3.42): The number of bonds involved in the largest crystallites is displayed in fig. 3.42(a), and shows that these numbers increase much more slowly or saturate after the characteristic time τ . The size of these crystallites is presented in fig. 3.42(b); this “size” is computed as a radius of gyration from the distance of all bonds belonging to a crystallite and its center of mass:

$$S^2 = \frac{1}{N_{\text{cryst}}} \sum_{i=1}^{N_{\text{cryst}}} (\mathbf{r}_i - \mathbf{r}_i^{\text{cm}})^2 . \quad (3.32)$$

This size reaches a plateau after $t = \tau$, giving another indication that the system’s crystallinity does not evolve significantly after the characteristic time determined from the Avrami analysis. An exception though to this observation is the behavior of the second largest crys-

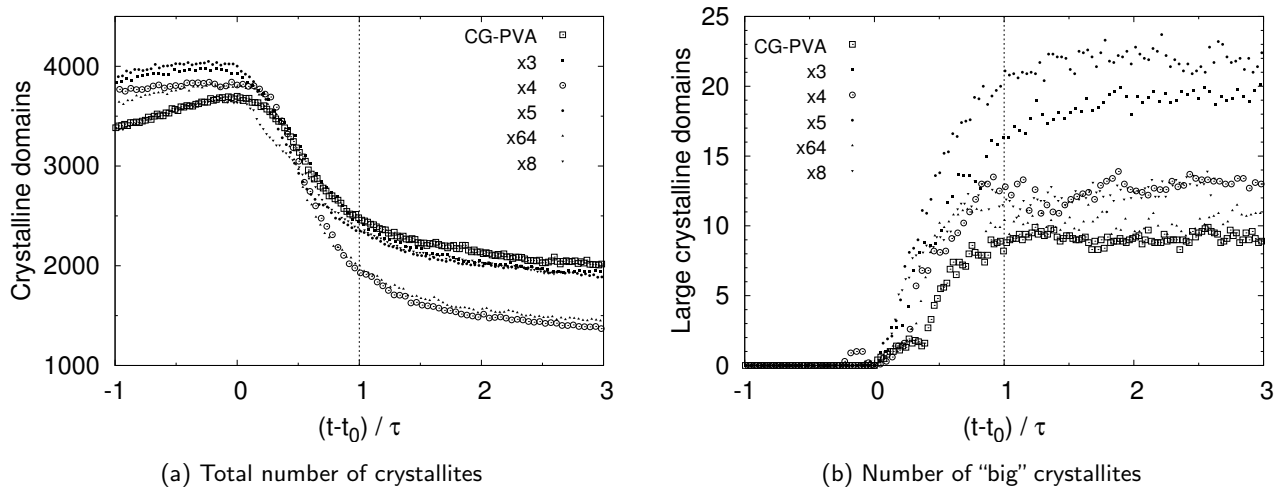


Figure 3.41: Evolution of the number of crystallites ("big" crystallites contain at least $N_b^{\text{big}} = 100$ bonds). The total number of crystalline domains does not completely saturate after τ ; on the other hand, the number of bonds in the larger crystalline structures reaches a plateau after time τ . This indicates that the major part of the crystallites have formed after τ , but there is still some recombination of the smallest crystallites occurring in the amorphous regions.

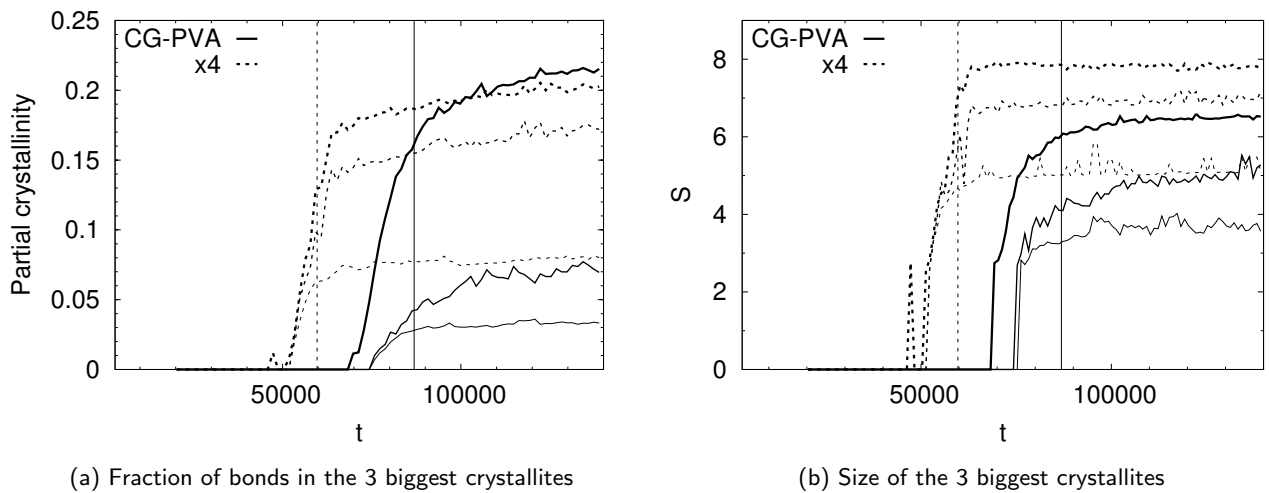


Figure 3.42: Evolution in time of the number of bonds and sizes of the three biggest crystalline domains for two models. It clearly appears that there is a saturation that takes place after $t = \tau$ (indicated for the two models by vertical lines). The second biggest crystallite continues to grow slowly in the case of the CG-PVA model, indicating that the structure of the system is not totally frozen and can still evolve after crystallization.

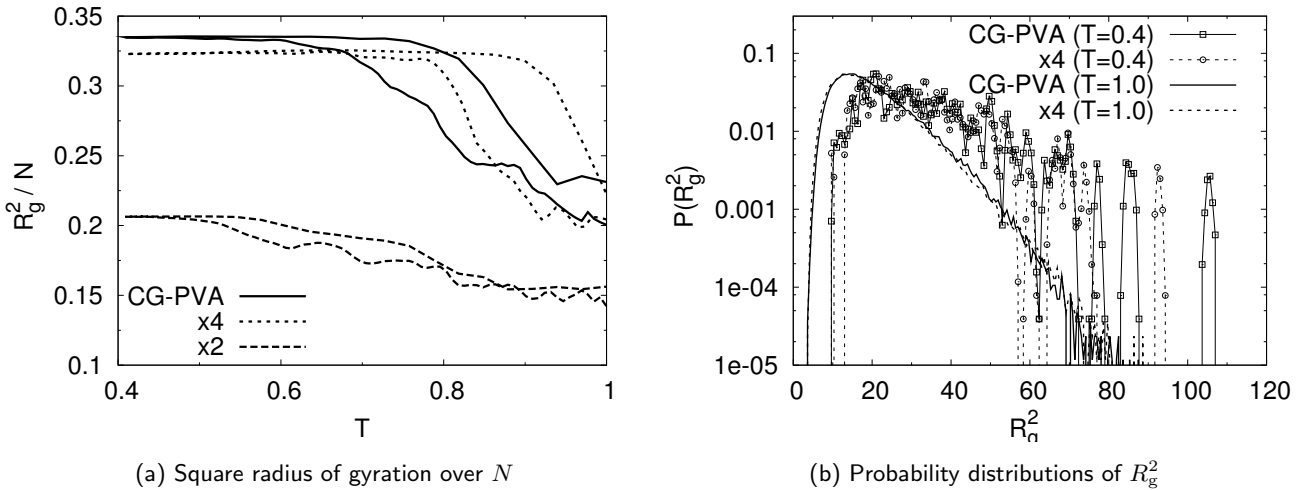


Figure 3.43: Comparison of the radii of gyration for three models; R_g^2 increases as the transition is approached, and then saturates. The final value is slightly larger for CG-PVA than for x4, which is unexpected as x4 has a higher crystallinity and forms bigger crystallites with larger stem length. The distribution of R_g^2 in the final semi-crystalline state exhibits several peaks for large values that explain the larger mean value of R_g^2 for CG-PVA.

tallite in the case of the CG-PVA model, whose size still increases after $t = \tau$. This results from the fact that the system is less crystallized than in the case of the x4 model, and thus it is still possible for a crystallite to grow, even if slowly, once the major structures are formed.

The characteristic time τ corresponds to the period during which the most important part of the crystalline regions arises. After this time, as shown in fig. 3.39, the fitting function stops reproducing the behavior shown by our simulation data. This could be explained by taking into account that the Avrami analysis considers several crystallites that grow until they impinge and cover the whole system. This is far from being possible either in the case of experimental systems (melts of high molecular mass polymers have been shown to follow an Avrami law until a certain crystallinity at which growth becomes much slower [135]) or for the growing crystallites in our simulation. We had to take into account the fact that only a partial crystallinity is attained by normalizing v_c with v_c^{\max} (as is also done for experiments); still, the simple Avrami equation makes no qualitative difference between growth of independent crystallites (in the early stages) and crystal growth of objects that are in contact with each other. This necessarily impeded growth should be taken into account, and that is the reason why the simple model fails at reproducing the behavior observed in our simulations at longer times.

It is interesting to note that even if crystallization appears similar for the models CG-PVA and x4 after having renormalized the evolution of crystallinity, there is still one difference so as how the system behaves after its most important part has crystallized. The evolution during cooling of the mean-square radius of gyration presented in fig. 3.43(a) shows that R_g^2 increases as the temperature is lowered,

which is expected since the chains tend to stretch while forming lamellae. However, while this increase is relatively small for the x2 model which is only weakly crystallized at low temperature, it is comparable for CG-PVA and x4. Furthermore, the final value of R_g^2 turns out to be larger in the case of CG-PVA, which seems to contradict the observation that the x4 model crystallizes more rapidly, forming longer stems (see fig. 3.44). Figure 3.43(b) brings an explanation by showing that there are peaks which developed at high R_g^2 in the distribution of the radius of gyration. These peaks are absent in the distribution measured for x4 (at least less peaks are observable, and at lower R_g^2), and the overall structure of the distributions for the two models are otherwise very similar (as is the case for the high temperature distribution, even though the values of P_{trans} are quite different). This is consistent with the observation that the x4 model is capable of a fast growth and achieves high crystallinity, but then ends up in a semi-crystalline state that cannot evolve anymore. This has been observed for very short chains which cannot organize in a satisfactory manner because they become rigid too early, and this hinders the *inter-chain* ordering (see fig. 3.24).

3.3.3 Volkenstein analysis of the influence of the angular potential

Changing the angular potential as described earlier allows to simulate different models that crystallize at different temperatures. Figure 3.45 recalls the phase diagrams obtained for three distinct models ($N = 100$): CG-PVA serves as a reference and the two “extreme” cases of models x2 and x4 are confronted. In the case of the x4 model, crystallization takes place at high temperature and leads to a better-ordered crystal (meaning that the final configuration is closer to a “perfect” crystal, as indicated by a measurement of crystallinity that yielded little less than 75%; see fig. 3.35). For x2 the transition occurs rather late, and gives rise to a frozen configuration with few ordered zones surrounded by lots of amorphous material (with crystallinity less than 5% as shown in fig. 3.35) which is characterized by a small drop in the volume per monomer.

The features of the three models can be compared by looking at the corresponding angular potentials, or equivalently at the angle probability distribution (fig. 3.46): It can be noticed that the *trans-trans* state is more favorable in the case of x4, and less in the case of x2. Conversely, the *trans-gauche* state is more populated for x2 than for x4. We have found a strong correlation between the probability P_{trans} of finding an angle $\theta > 150^\circ$ (*trans-trans* state) and the temperature of crystallization (or melting). This result is presented on fig. 3.47, where the temperature of melting for all the different models (18 models for $N = 10$ and $N = 50$, reduced to 7 for $N = 100$ because of higher computational-time requirements for longer chains) we used and for

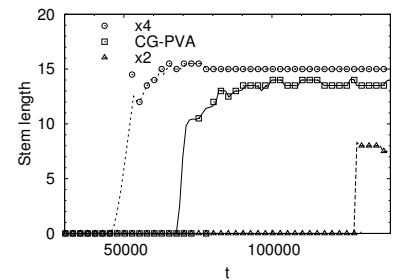


Figure 3.44: Increase of the stem length during the formation of the crystalline structure, measured from the minimum of the orientation correlation function (see sec. 1.3).

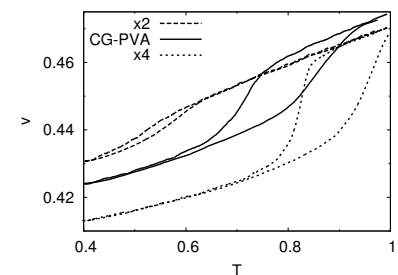


Figure 3.45: Phase diagrams for $N = 100$. Comparison of models with varying angular potential (CG-PVA, x2, x4).

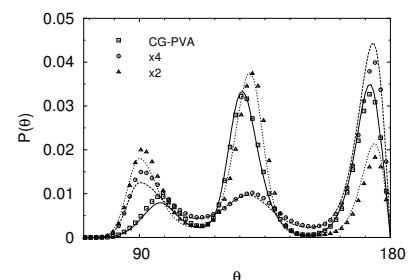


Figure 3.46: Comparison of the probability distributions of bond angle θ for CG-PVA and the x2 and x4 models. Points correspond to the distributions measured from the simulations at $T = 1.0$, while lines were obtained from direct inversion of the angular potential according to eq. (3.1).

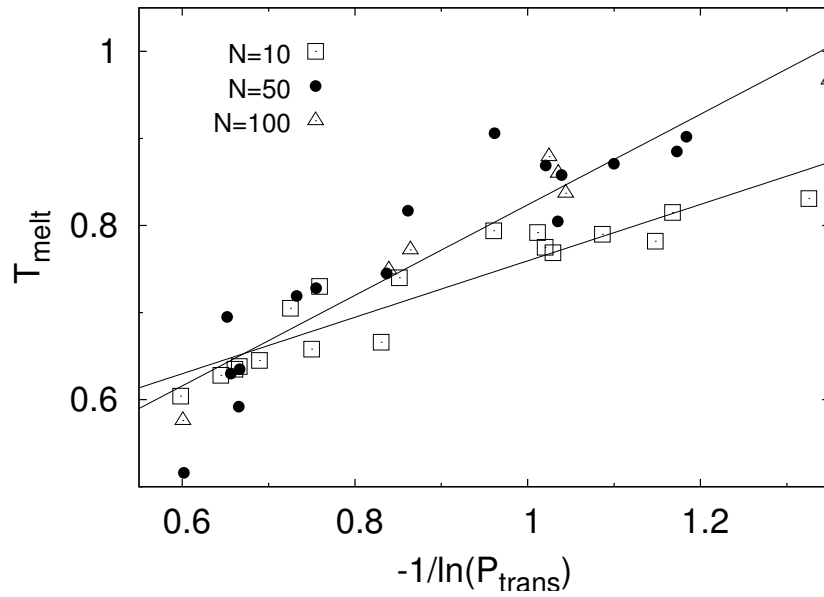


Figure 3.47: Influence of the angular potential on the melting temperature: Melting temperature T_{melt} as a function of $-1/\ln(P_{\text{trans}})$. Each point represents a different model, with a particular angular potential.

three different chain lengths are plotted as a function of $-1/\ln(P_{\text{trans}})$. A plot of T_{melt} vs. P_{trans} would show exactly the same trend, but this particular representation was preferred in order to allow for an easier comparison with the theoretical argument that follows. The solid lines show the results of a linear fit for these data; there is a shift in the slope when comparing $N = 10$ and $N = 50$, but for the two longest chain lengths, the fitting lines superimpose (the perfect superposition is only an accident here as there is not enough points nor statistical averages. Still, the tendency that results for short chains ($N = 10$) differ from findings for longer polymers seems natural).

It is possible to find a theoretical explanation for this relation between T_{melt} and P_{trans} in Volkenstein's work [130]; he describes crystallization as a first order phase transition,

$$\Delta G = 0 \quad (3.33)$$

$$\Delta H - T_{\text{melt}}\Delta S = 0 \quad (3.34)$$

and thus obtains this expression for the temperature of melting:

$$T_{\text{melt}} = \frac{\Delta H}{\Delta S} = \frac{\Delta E_{\text{inter}} + \Delta E_{\text{intra}} + p\Delta V}{\Delta S_{\text{inter}} + \Delta S_{\text{intra}}}, \quad (3.35)$$

having decomposed the energies and entropies of melting into *inter*- and *intra*-chain contributions. Volkenstein then neglects ΔS_{inter} , since most of the degrees of freedom in the system lie in the chain's internal conformations, for long chains. It is questionable whether this assumption is justified in the case of our simulation, for the chain lengths we were to probe are still rather small in comparison to the experimental standards; we will come back to this point later.

The following *intra*-chain entropy variation is obtained by modeling one chain as an ensemble of rotational isomers, possibly *trans* or

gauche[±] for a simple linear chain in the melt, and being all *trans* in the crystal. Volkenstein assumes the following partition function for a mixture of N uncorrelated units having the free energy F_i :

$$Q = N! \prod_{i=1}^N \frac{(e^{-\beta F_i})^{N_i}}{N_i!} . \quad (3.36)$$

N_i is the number of units in the state i , and $\beta = 1/T$. This partition function allows to calculate the free energy and entropy of one chain,

$$F_{\text{intra}} = -T \ln Q \quad (3.37)$$

$$= NT \sum_{i=1}^N x_i \ln \left(\frac{x_i}{w_i} \right) \quad (3.38)$$

for large N and N_i ; $x_i = N_i/N$ and $w_i = \exp(-\beta F_i)$;

$$S_{\text{intra}} = - \left(\frac{\partial F_{\text{intra}}}{\partial T} \right)_{N_i} \quad (3.39)$$

$$= -N \sum_{i=1}^N x_i \ln \left(\frac{x_i}{w_i} \right) - NT \sum_{i=1}^N x_i \frac{\partial}{\partial T} \ln \left(\frac{x_i}{w_i} \right) . \quad (3.40)$$

In equilibrium conditions, one has the following expression for the fraction of i states x_i :

$$x_i = \frac{\exp(-\beta F_i)}{\sum_k \exp(-\beta F_k)} = \frac{w_i}{\sum_k w_k} . \quad (3.41)$$

It is then possible to write the final expression for F_{intra} and S_{intra} :

$$F_{\text{intra}} = -NT \ln \sum_{k=1}^N w_k \quad (3.42)$$

and

$$S_{\text{intra}} = N \ln \sum_{k=1}^N w_k + NT \frac{\partial}{\partial T} \ln \left(\sum_{k=1}^N w_k \right) \quad (3.43)$$

$$= N \ln \sum_{k=1}^N w_k + \frac{1}{T} E_{\text{intra}} . \quad (3.44)$$

Considering in a first approximation that in the crystalline state the chains' isomers are exclusively *trans*, the change in free energy at the transition is

$$\Delta F_{\text{intra}} = F_{\text{intra}}^{\text{melt}} - F_{\text{intra}}^{\text{cryst}} \quad (3.45)$$

with $F_{\text{intra}}^{\text{cryst}} = NF_1$. Accordingly, the variation of *intra*-chain entropy becomes (at constant temperature T_{melt} , as we are considering a first-order phase transition)

$$S_{\text{intra}} = S_{\text{intra}}^{\text{melt}} - S_{\text{intra}}^{\text{cryst}} \quad (3.46)$$

$$= N \ln \sum_{k=1}^N \frac{w_k}{w_1} + \frac{1}{T_{\text{melt}}} \Delta E_{\text{intra}} . \quad (3.47)$$

The term $\sum_k w_k/w_1$ is just the inverse of the probability of finding a *trans* state in the melt, P_{trans} :

$$P_{\text{trans}} = \frac{\exp(-\beta F_{\text{trans}})}{Z} = \frac{\exp(-\beta F_1)}{\sum_k \exp(-\beta F_k)}. \quad (3.48)$$

Thus, Volkenstein arrives at the following expression for ΔS_{intra} :

$$\Delta S_{\text{intra}} = N \ln \frac{1}{P_{\text{trans}}} + \frac{\Delta E_{\text{intra}}}{T_{\text{melt}}}. \quad (3.49)$$

This leads to the next equation relating T_{melt} and the probability of finding an isomer in a *trans* state P_{trans} to the variations of volume and *inter*-chain energy:

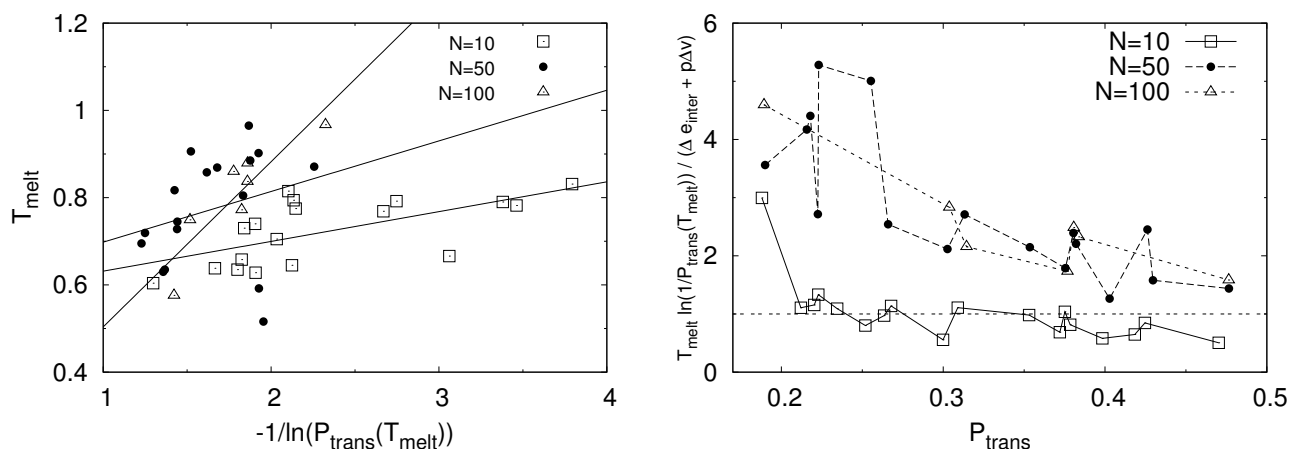
$$T_{\text{melt}} \ln \frac{1}{P_{\text{trans}}} = \Delta e_{\text{inter}} + p\Delta v, \quad (3.50)$$

where e and v are the energy and volume *per monomer*. Originally Volkenstein also neglected the last term over Δe_{inter} , but this turned out not to be justified in the case of our simulations.

This simple theoretical model suggests that the melting temperature is closely related to the probability of *trans* states, as we found out from our simulation data for several models with varying P_{trans} . We indeed found a linear variation of T_{melt} as a function of $-\ln \frac{1}{P_{\text{trans}}}$, as would be predicted by Volkenstein for the case of constant $\Delta e_{\text{inter}} + p\Delta v$, in eq. (3.50). However, the correlation we have determined involves the probability $P_{\text{trans}}(T = 1)$ measured *at high temperature*, and not at the equilibrium melting point. It is thus necessary to compare the melting temperature T_{melt} and $P_{\text{trans}}(T_{\text{melt}})$ in order to test Volkenstein's theory. This is what is presented in fig. 3.48(a); it is noticeable that for $N = 50$ the data seem too noisy to allow for a reliable fit, whereas this is possible for the other two chain lengths as there is an observable tendency. Still the resulting correlation between T_{melt} and $P_{\text{trans}}(T_{\text{melt}})$ does not appear as clearly as in fig. 3.47. A more demanding test of Volkenstein's equations consists in computing for every model the lhs of eq. (3.50) in order to check whether there is a good agreement between the different measured quantities. The result are presented in fig. 3.48(b), and it can be seen that for $N = 10$ the data agree quite well with eq. (3.50), as the ratio

$$R = \frac{T_{\text{melt}} \ln(1/P_{\text{trans}}(T_{\text{melt}}))}{\Delta e_{\text{inter}} + p\Delta v} \quad (3.51)$$

is close to unity. For longer chains, this is not the case anymore. The reason is that the assumption of an all-*trans* configuration in the crystalline state of polymer systems is obviously not valid, especially in the case of our simulations since the high cooling rates and small boxes do not permit the formation of such elongated structures with $N = 50$ or $N = 100$ chains. For $N = 10$ however, the mobility of the monomers is high enough so that fully stretched conformations occur. At both



(a) Melting temperature as a function of $-1/\ln(P_{\text{trans}}(T_{\text{melt}}))$. Each point represents a different model, with a particular angular potential.

(b) Improving agreement with Volkenstein's theory as P_{trans} increases.

Figure 3.48: Influence of the angular potential on melting temperature: Comparison of simulation data with Volkenstein analysis.

high and low P_{trans} , the agreement with Volkenstein's prediction is less satisfactory: For low P_{trans} , the x2 model has been observed to produce poorly crystalline configurations, which results in violating Volkenstein's hypothesis about stretched chains in the crystal. For high P_{trans} , crystallization of the x4 model for instance was shown to be hindered because the chains stretch too early, not leaving the monomers enough mobility to organize in a well-ordered crystal. In these respects deviations from the predicted behavior can be understood, and this also explains why longer chains failed to be quantitatively described by the simple model.

3.3.4 Isothermal relaxation

A very common way of studying the behavior of a crystallizing polymer melt consists in quenching it quickly under its melting temperature and let the crystal grow at constant temperature. The final state can then be characterized, and the consecutive melting occurs at a temperature that is related to that particular crystal morphology. We reproduced this experimental protocol with our simulations, again comparing our different models. The results are shown in fig. 3.49, and it can be seen that there is a linear relation between both the crystallization and melting temperatures and the corresponding lamellar thickness; this has been observed experimentally [42, 54, 55, 121]. More precisely, the smaller the supercooling, the thicker the lamellae; thus a system that is left to relax at a temperature close to its melting temperature will have enough thermal energy to allow the chains to arrange in long stems, whereas if the supercooling is too important, the chains' mobility will be low, so that only thin lamellae can form.

The relation between supercooling and lamellar thickness can be ob-

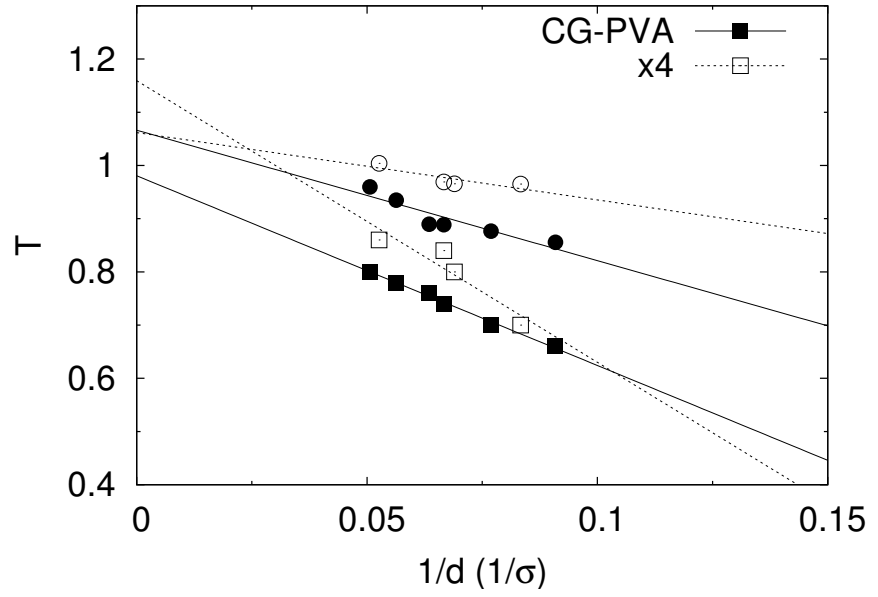


Figure 3.49: Crystallization and melting lines, comparison between x4 and CG-PVA (data for CG-PVA from Hendrik Meyer).

tained by calculating the free enthalpy of formation of a crystallite, taken as a volume of thickness l and surface A (this calculation is presented in refs. 5 and 87, for instance): This object is formed by stacked lamellae of folded chains with the folds lying in the surface of area A , separated by elongated stems of length l . In this case:

$$\Delta G = 2A\sigma - Al\Delta g_{\text{bulk}} \quad (3.52)$$

if one neglects the lateral surface effects; σ is the surface tension and Δg_{bulk} is the free energy variation of formation of a perfect crystal without boundaries, per unit volume. This leads to a restriction on the possible values of l , as a crystallite will only be stable if

$$l \geq \frac{2\sigma}{\Delta g_{\text{bulk}}} . \quad (3.53)$$

Under equilibrium conditions, the enthalpy variation associated with the melting of an infinitely large crystal is

$$\Delta g_{\text{bulk}}(T_{\text{melt}}^{\infty}) = \Delta h(T_{\text{melt}}^{\infty}) - T_{\text{melt}}^{\infty} \Delta s(T_{\text{melt}}^{\infty}) = 0 . \quad (3.54)$$

Assuming that the enthalpy and entropy do not vary too much for a temperature close to T_{melt}^{∞} , one could use the approximation

$$\begin{aligned} \Delta g_{\text{bulk}}(T) &= \Delta h(T_{\text{melt}}^{\infty}) - T \Delta s(T_{\text{melt}}^{\infty}) \\ &= \Delta h(T_{\text{melt}}^{\infty}) - T \frac{\Delta h(T_{\text{melt}}^{\infty})}{T_{\text{melt}}^{\infty}} \\ &= \Delta h(T_{\text{melt}}^{\infty}) \frac{\Delta T}{T_{\text{melt}}^{\infty}} . \end{aligned} \quad (3.55)$$

$\Delta T = T_{\text{melt}}^{\infty} - T$ is the supercooling. This allows one then to write, with eq. (3.53):

$$l \geq \frac{2\sigma T_{\text{melt}}^{\infty}}{\Delta h(T_{\text{melt}}^{\infty}) \Delta T} \quad \text{or:} \quad T \leq T_{\text{melt}}^{\infty} - \frac{2\sigma T_{\text{melt}}^{\infty}}{\Delta h(T_{\text{melt}}^{\infty}) l} . \quad (3.56)$$

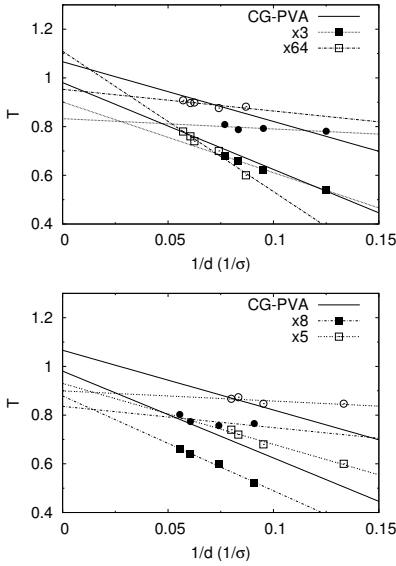


Figure 3.50: Crystallization and melting lines for other models. CG-PVA lines are shown for reference.

This last expression is the Gibbs-Thomson equation that can be used to account for the linear behavior observed in fig. 3.49 for the melting of crystals with different lamellar thickness. The temperature of melting for a completely elongated crystal T_{melt}^{∞} can be deduced from the figure by extrapolating the lines for $1/l \rightarrow 0$.

In the simulations, the lamella thickness is measured by determining the minimum of the orientation correlation function inside a chain; this provides the average distance between two consecutive folds along one chain that defines the stem length (see sec. 1.3).

3.3.5 Structure factors

The occurrence of a crystalline structure in a system can be conveniently displayed with structure factors [defined in eq. (1.74)], as there is a big qualitative difference between the smoothly-oscillating behavior of this quantity in the liquid and the Bragg peaks expected in the case of a solid. However, as polymer melts are supposed to become *semi-crystalline* only, the structure factor measured for our systems at low temperature still exhibit characteristics of both liquid and crystalline states.

For our coarse-grained models, we expect to find crystals with a hexagonal symmetry since the (elongated) chains have a cylindrical symmetry. The Bragg peaks should therefore correspond to the possible values of the length of vectors of the reciprocal lattice, which is also a hexagonal lattice [6]: If the original lattice has the following parameters,

$$\begin{aligned} \mathbf{a} &= a\mathbf{u}_x \\ \mathbf{b} &= \frac{1}{2}a\mathbf{u}_x + \frac{\sqrt{3}}{2}a\mathbf{u}_y \\ \mathbf{c} &= c\mathbf{u}_z, \end{aligned} \quad (3.57)$$

it can be shown that the reciprocal lattice is hexagonal with parameters

$$\tilde{a} = \frac{4\pi}{a\sqrt{3}} \quad (3.58)$$

$$\tilde{c} = \frac{2\pi}{c}. \quad (3.59)$$

The possible vectors of the reciprocal lattice are linear combinations of $\tilde{\mathbf{a}}$, $\tilde{\mathbf{b}}$ and $\tilde{\mathbf{c}}$, of length

$$d = \sqrt{|\alpha\tilde{\mathbf{a}} + \beta\tilde{\mathbf{b}} + \gamma\tilde{\mathbf{c}}|^2}; \quad (3.60)$$

in the case of polymer chains, the c -length is much larger than a , and the vectors with $\gamma \neq 0$ are not expected to contribute for small q vectors. Figure 3.51 sketches the hexagonal (reciprocal) lattice and the first few vectors $\mathbf{v} = \alpha\tilde{\mathbf{a}} + \beta\tilde{\mathbf{b}}$, with (α, β) equal $(1, 0)$, $(1, 1)$, $(2, 0)$. It can be seen in fig. 3.52 that the position of the first peaks appearing

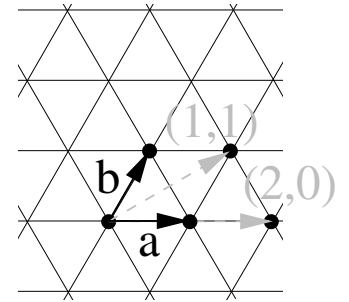
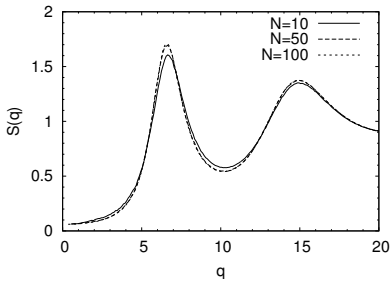


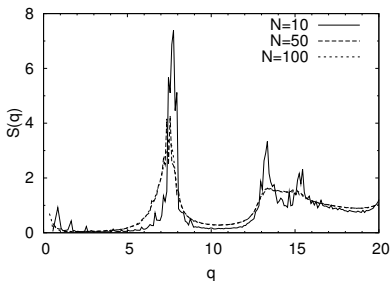
Figure 3.51: Schematic representation of the (two-dimensional) hexagonal lattice vectors. The length of the vectors is given by $d = \sqrt{|\alpha\tilde{\mathbf{a}} + \beta\tilde{\mathbf{b}}|^2}$, and the values for the first (α, β) -couples are:

α	β	d
1	0	1
1	1	$\sqrt{3}$
2	0	2
2	1	$\sqrt{7}$
\vdots	\vdots	\vdots

Figure 3.52: Structure factors for several models at low temperature ($T = 0.4$). CG-PVA and x4 have a semi-crystalline structure, as can be inferred from the presence of sharp peaks; x2 and w0 poorly or do not crystallize, and therefore have a structure that resembles the liquid structure at high temperature. For an easier comparison of the structure for one model, see fig. 3.54.

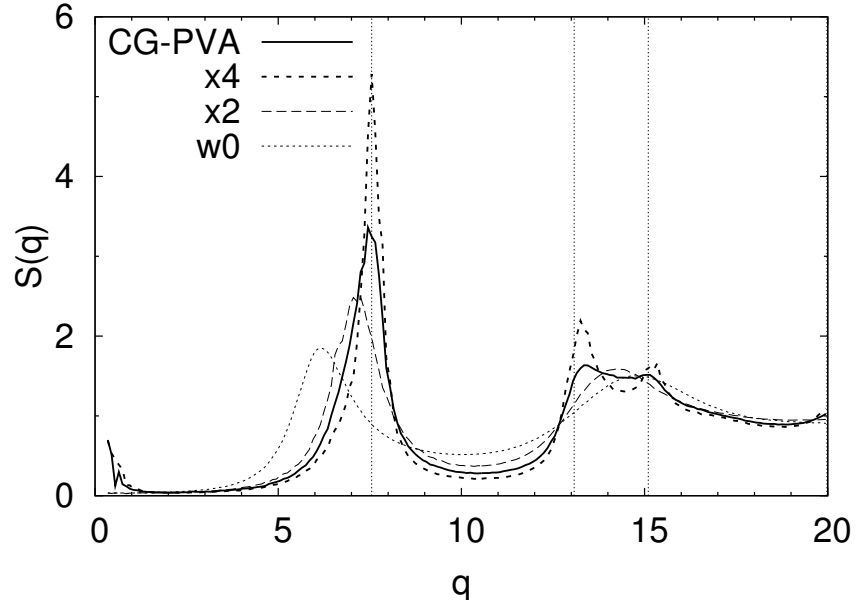


(a) $T = 1$



(b) $T = 0.4$

Figure 3.53: Structure factors for CG-PVA at $T = 1$ and $T = 0.4$, for different chain lengths. At high temperature there is a small difference between the results for $N = 10$ and $N = 50$, but the distinction between $N = 50$ and $N = 100$ is difficult to make (see chapter 4 for more details). At low temperature the data for short chains show much sharper peaks due to the fact that the system is almost perfectly ordered at this chain length; for longer chains the structure factors are almost identical and the peaks much attenuated because of the presence of amorphous media around the crystalline domains.



in the low-temperature structure factors for semi-crystalline are given by dq_{\max} , where q_{\max} corresponds to the position of the first peak. In the case of the x4 model, $q_{\max} \approx 7.55$, and the next peaks are about $q = 13.08$ and $q = 15.10$.

The dependence on the chain length is an interesting point about structure factors: At high temperature, it is observed that there is no important influence of the size of the chains on the structure of the melt (fig. 3.53(a)); we shall come back to high temperature structure factors in chapter 4.

The structure factors for several models at low temperature are presented in fig. 3.52. According to the likeliness of the model to crystallize, different structure are observed: The w0 model that has no explicit angular potential (fig. 3.5) cannot crystallize and therefore has the same features at $T = 0.4$ than in the melt. The x2 model gives rise to a poorly crystalline configuration after continuous cooling and its structure factor also shows almost no characteristics of an ordered system. Contrary to that, the models CG-PVA and x4 that have been shown to produce partially crystalline configurations upon cooling do exhibit crystal-specific features. These features are more pronounced in the case of x4, since this model has less amorphous regions in its low-temperature state than CG-PVA (fig. 3.35); this causes the average structure factor to display sharper peaks.

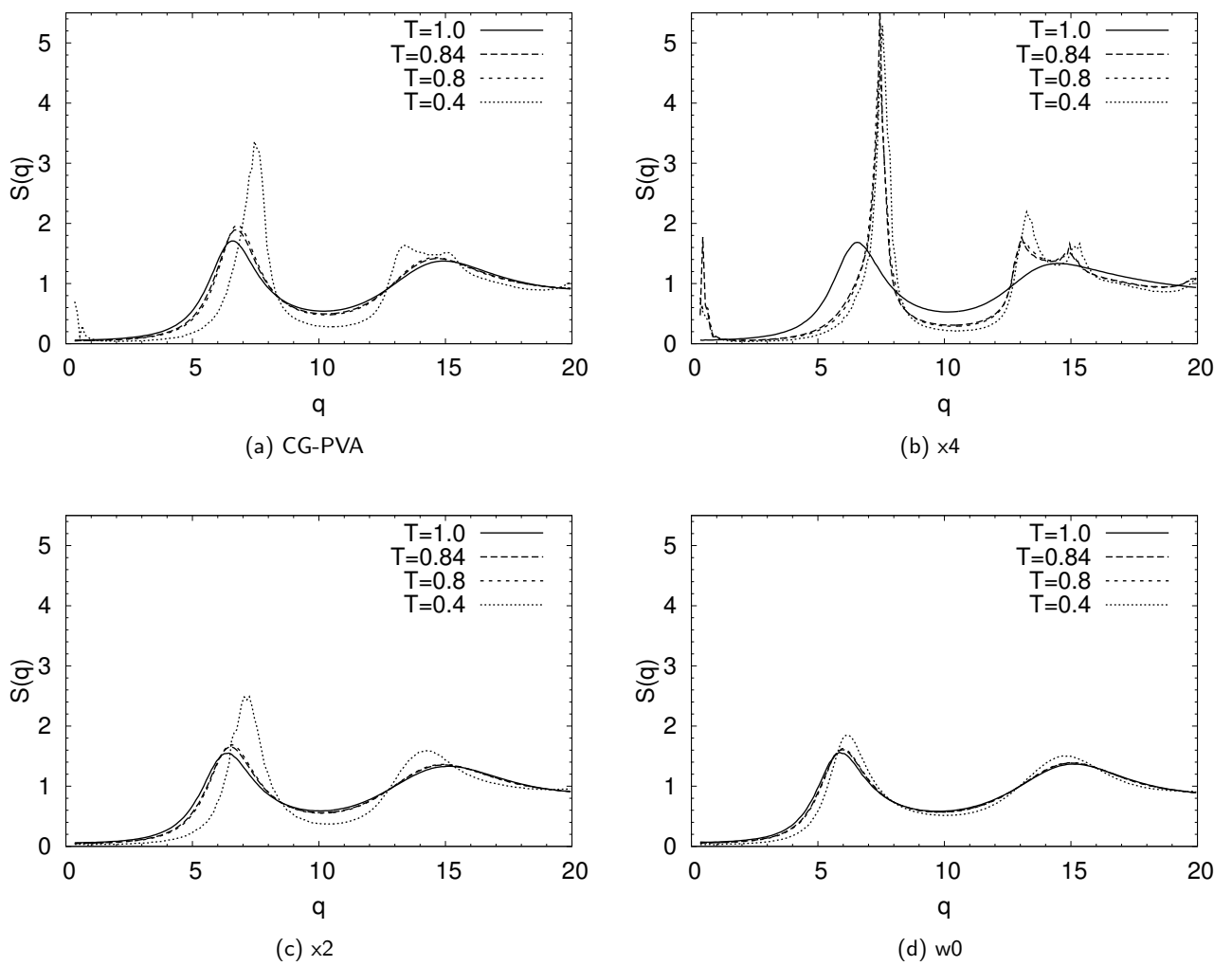


Figure 3.54: Comparison of the structure factors at high and low temperatures, for different models.

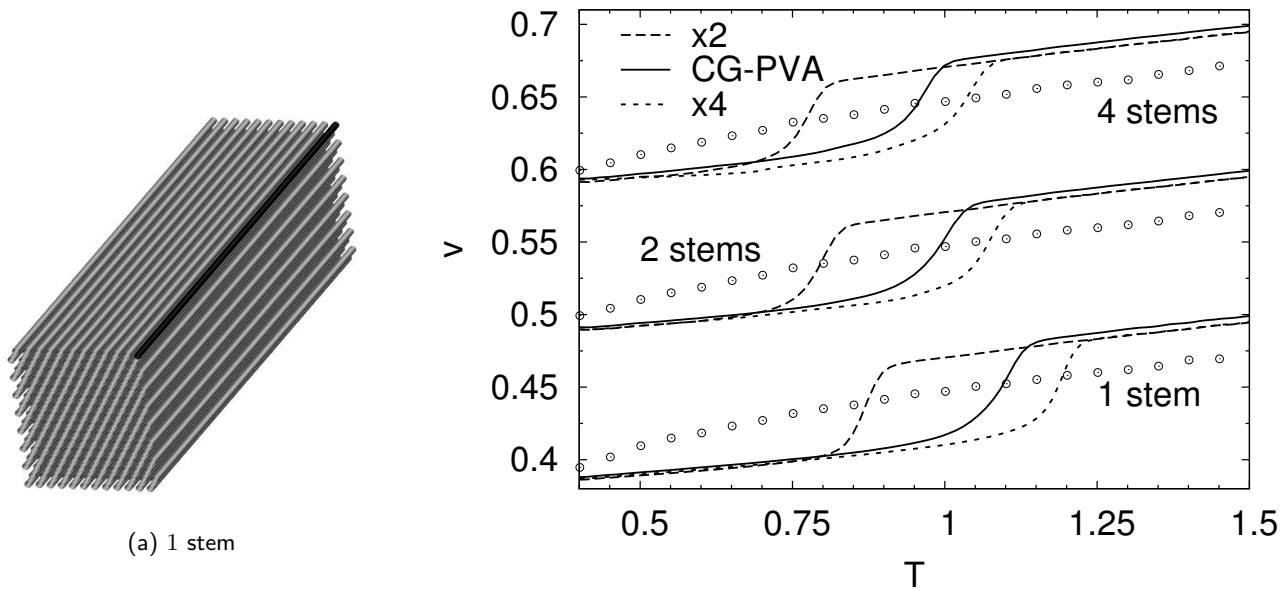


Figure 3.55: Phase diagrams for the melting of perfect crystals ($N = 100$), either fully stretched chains or folded into 2 or 4 stems. Results for four different models are presented, the symbols correspond to the model without angular potential w_0 (cf. fig. 3.5) for which no crystalline state is stable. The other models melt at lower temperatures when the number of stem is increased, indicating that the longer the stem, the more stable the crystal. Curves for the different stem lengths have been shifted by an amount of 0.1 for clarity.

3.3.6 Melting of perfect crystals

In order to compare our results from the preceding sections, we have also run simulations for some models starting with a “perfect crystal” configuration, that is a packing of fully stretched or regularly folded $N = 100$ chains (one system with two stacks of once-folded chains, and another with four layers of chains folded into four stems). The initial conditions are presented using simulation snapshots in fig. 3.56. The simulations were started at low temperature ($T = 0.4$) with a configuration generated by hand, and equilibrated at that temperature before heating up to $T = 2$ (at rate $2 \times 10^{-5} \tau^{-1}$).

Figure 3.55 shows the resulting phase diagrams for CG-PVA, x2 and x4, and also for a model without any angular potential that starts “melting” immediately at low temperature, since there is no rigidity to keep the chains in an elongated conformation; in this case, the artificial crystalline state is not stable at $T = 0.4$ and there is a smooth transition from low- to high-temperature melt. The other models exhibit a sharp phase transition, defining a melting temperature T_{melt}^{∞} much higher than the T_{melt} temperatures measured while heating up a crystalline configuration obtained via a continuous cooling, and also well above the temperature extrapolated from the melting lines from fig. 3.49. The melting temperature for the different models decrease with the number of folds, which is consistent with the observation made when considering the crystallization and melting lines in sec. 3.3.4. It

Figure 3.56: Simulation snapshots of the initial configuration used to study the melting of perfect crystals consisted of chains fully stretched or folded into 2 or 4 stems. One chain is colored in black in order to emphasize the folds.

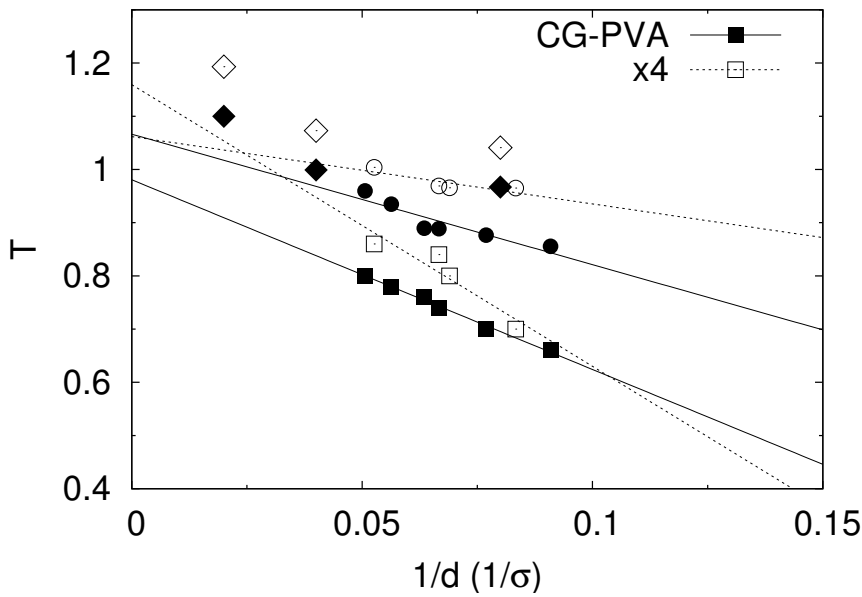


Figure 3.57: Melting and crystallization lines as shown in fig. 3.49, with added points corresponding to the melting temperature of perfect crystals with stem lengths $d = 12.5, 25$ and 50σ (1, 2 or 4 stems). As expected, the melting point is higher in the case of the perfect structures, since the occurrence of a phase transition is made easier at impurities or heterogeneities. Points for perfect crystals do not show the same tendency as the data obtained for the melting of crystals created during an isothermal relaxation below T_{cryst} .

can also be noticed that for x4 which has the more stable crystalline structure, the introduction of folds leads to a larger decrease in the melting temperature than for x2. This is presented in fig. 3.58.

For two different models the melting temperatures of perfect crystals for fully stretched chains and folded chains have been included (\diamond symbols) to the melting and crystallization lines plot for comparison (fig. 3.57). It can be seen on those examples that there is no linear relation anymore between the inverse stem length and the melting temperature. The reason why these new points do not fall on the lines which were found to extrapolate the melting temperatures to infinite stem lengths is that the crystalline structures cannot be compared directly. With artificial, perfectly crystalline configurations, one of the most important features of semi-crystalline polymers is lost, in that there are no amorphous regions anymore. The crystals obtained via isothermal relaxation after a quench discussed in sec. 3.3.4 contain a significant part of disordered material which plays a role during melting. The absence of such zones on the one hand makes the systems more stable, since the configurations are much more regular and in this respect resemble more a perfect crystal of simpler bodies (metal...). On the other hand, amorphous regions can play the role of large “defects” in the crystalline structure, and hence facilitate the transition to the liquid phase. This explains why the melting points determined for perfect crystals lie above the lines established for the melting of semi-crystalline system with the same models.

It is possible to compare the crystalline structures obtained through the different kinds of experiments using the measurement of the order parameter during melting: Figure 3.59 shows the renormalized P_2 for three different crystals during continuous heating (heating rate $2 \times 10^{-5} \tau^{-1}$, except for the configuration obtained after isothermal re-

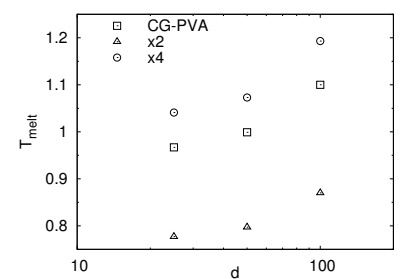
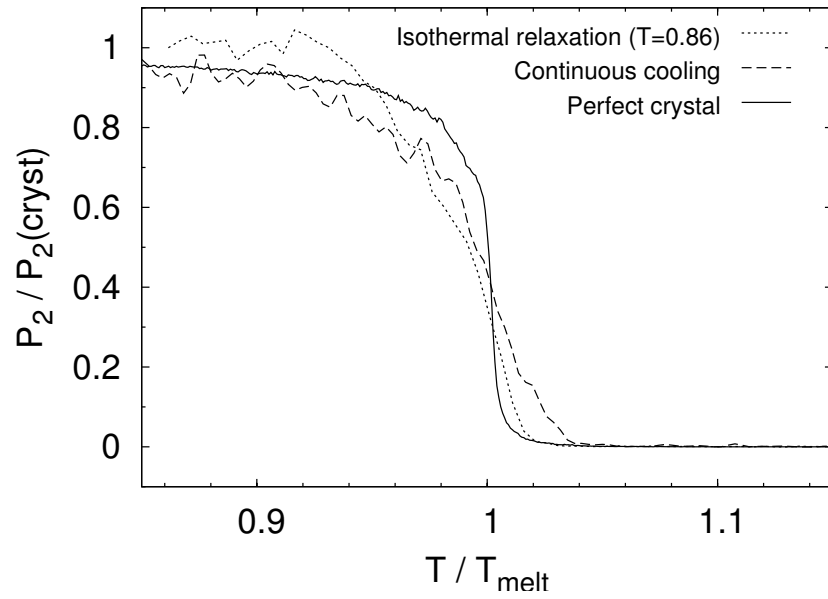


Figure 3.58: Melting temperature as a function of the stem length d for perfect crystals. T_{melt} increases faster with d for x4 than for x2.

Figure 3.59: Comparison of the evolution of the P_2 order parameter during melting of crystalline structure obtained with different methods (model $\times 4$, $N = 100$): Perfect crystal (hand-generated configuration) and crystals grown during continuous cooling (cooling rate $5 \times 10^{-6} \tau^{-1}$) or isothermal relaxation (at $T = 0.86$). The perfect crystal exhibit a much more abrupt transition. The values used to normalize the data are the melting temperature T_{melt} and the value of the order parameter in the crystalline phase (at $T = 0.4$ for the perfect crystal; at $T = 0.4$ after continuous cooling; or at $T = 0.86$ after isothermal relaxation).



laxation, heated at rate $10^{-5} \tau^{-1}$). The perfect crystal configuration melt very rapidly compared to the other two systems, which exhibit a more progressive transition. This is consistent with the expectation that a perfect crystal should undergo a first-order phase transition, while for more realistic semi-crystalline configurations, the large amount of amorphous material makes the transition less abrupt. The configuration obtained via continuous cooling is the least crystalline of the three, and appears to melt slightly more progressively than the crystal created during isothermal relaxation whose growth was not hindered by continuously decreasing thermal energy (the difference in heating rate probably has a small influence on the melting), because of its lower crystallinity.

The melting of perfect crystals can be described by looking at the distribution of angles in the system as a function of temperature. Figure 3.60 presents the variation of $P_{\text{trans}}(b)$ as a function of time during the continuous heating, for systems of perfect crystals, folded or not. $P_{\text{trans}}(b)$ corresponds to the probability of finding a *trans-trans* states at position b along the chain; this probability is uniformly 1 in the case of the perfectly stretched chain crystal at low temperature, and remains at a high value until the melting temperature is reached, and then the crystal melts. $P_{\text{trans}}(b)$ then decreases uniformly to its equilibrium value at high temperature, and for such a system one has $P_{\text{trans}}(b) = P_{\text{trans}}$ since there is no particular length scale b_0 appearing in the probability distribution in equilibrium. The situation is different for systems constituted of chains folded into 2 and 4 stems: In these cases, $P_{\text{trans}}(b)$ drops for b corresponding to the positions of the folds. At low temperatures there are sharp minima in the distribution for these values of b . As the temperature is increased, these minima tend to widen, and it can be inferred from the rounded shape of the distri-

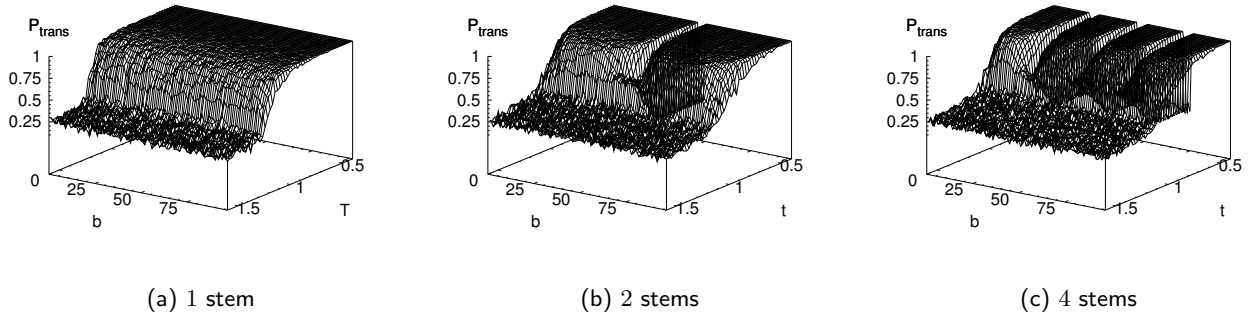


Figure 3.60: Probability of the *trans–trans* state along the chain during melting of perfectly crystalline structures with 1, 2 or 4 stems. It can be seen that all parts of the lamellae melt at the same time. b refers to the position of an angle along the chain, and as multi-lamellar systems consist of folded chains stacked together, holes occur in the distributions at the position of the folds.

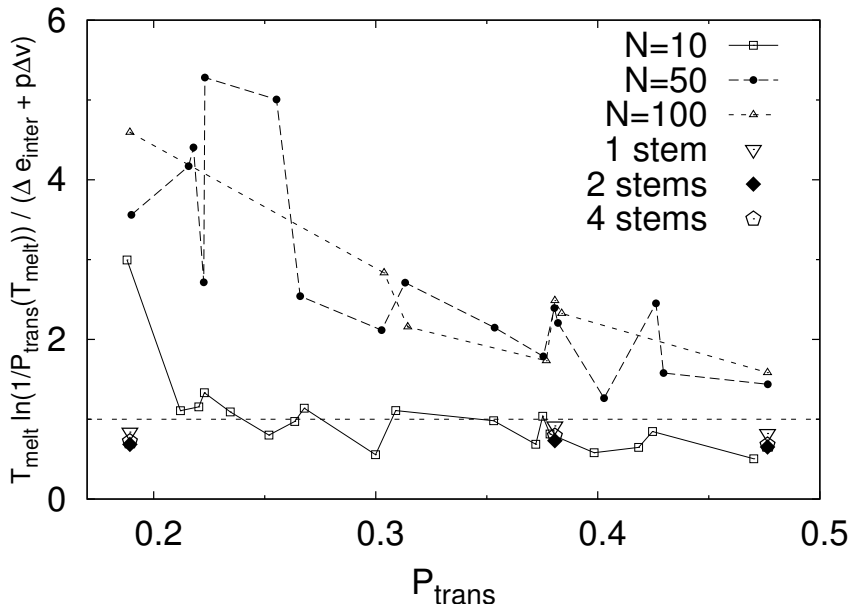


Figure 3.61: Test of Volkenstein's theory for the relation between the temperature of fusion T_{melt} and the probability of *trans–trans* states at T_{melt} , $P_{\text{trans}}(T_{\text{melt}})$ (three different models, $N = 100$). Besides the data already presented in fig. 3.48(b), the results obtained in the case of perfectly ordered structures have been added. It can be seen that these points match Volkenstein's prediction better than the data obtained from continuous cooling simulations. This indicates that the approximation of the crystalline state by an all-*trans* state is important. For perfect crystals, the data show that the quantity R of eq. (3.61) is very close to 1, meaning that Volkenstein's theory provides a good description of what is observed in the simulations. Points for folded configurations are slightly further away from 1 than for perfectly stretched configurations.

butions that “defects” (meaning non-*trans–trans* states) form preferentially around the original folds. At the transition, the site-dependent angular distribution becomes uniform as there is no correlation between angular states and the position along the chain in the molten state.

The simulations of the melting of perfectly ordered crystals provide another means of testing the theory by Volkenstein that was presented in sec. 3.3.3 in order to link the probability of *trans–trans* states and the temperature of melting. The theory establishes the following relation between T_{melt} , $P_{\text{trans}}(T_{\text{melt}})$, Δe_{inter} , p and Δv [eq. (3.51)]:

$$R = \frac{T_{\text{melt}} \ln(1/P_{\text{trans}}(T_{\text{melt}}))}{\Delta e_{\text{inter}} + p\Delta v} = 1. \quad (3.61)$$

This relation has been tested in fig. 3.48(b), and it was argued that the theory applies better to short than to long chains, since for small

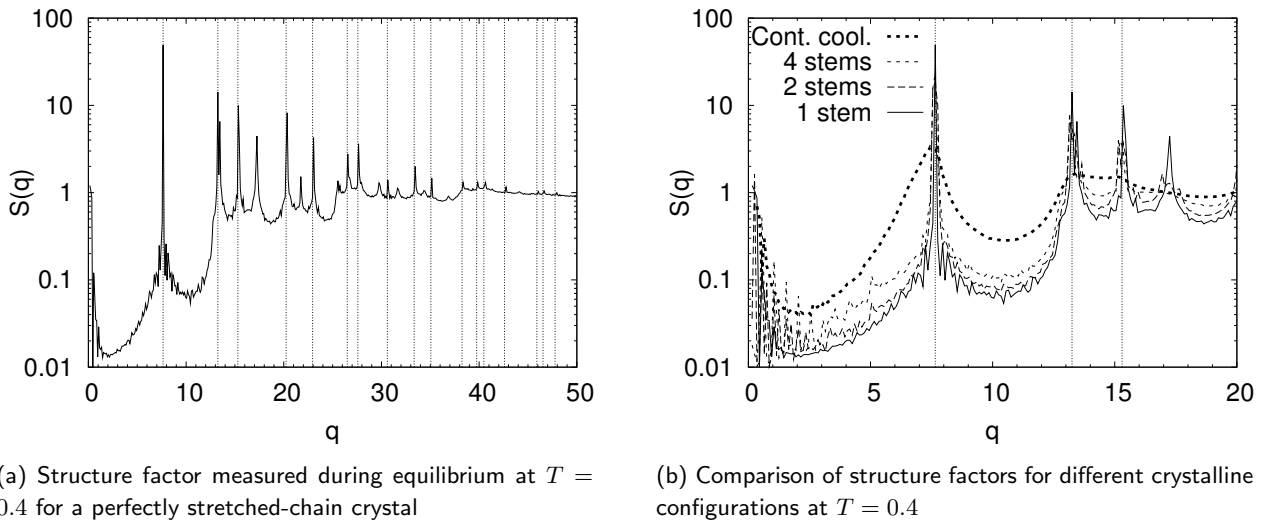


Figure 3.62: Structure factors at low temperature ($T = 0.4$), measured from simulation data for the CG-PVA model. The positions of the characteristic peaks corresponding to vectors of the hexagonal lattice are indicated. Figure 3.62(b) presents structure factors for semi-crystalline and perfectly crystalline systems (with chains folded differently).

enough chain lengths the low-temperature state is close to an all-*trans* state, which is used as an hypothesis in the theory. Figure 3.61 confirms this interpretation since for $N = 100$ it is shown that the data reproduce Volkenstein’s prediction very well *in the case of fully stretched chains*. For perfect crystals consisting of stretched chains, the ratio R is very close to unity ($R \lesssim 1$), and this is also the case for crystalline configurations in which the chains are folded into 2 or 4 stems. For the latter two cases, R is found to have a slightly lower value. This shows that the hypothesis of an all-*trans* crystal is predominant in Volkenstein’s theory, and this explains why the agreement with the theory is not better in the case of a crystalline configuration obtained via continuous cooling, in which the proportion of *trans-trans* states is by far smaller than in the crystals thus created by hand.

Simulations of fully stretched chain crystals allow us to study the structure of such “perfect” polymer crystals and provide a reference state to which the structure of the semi-crystalline configurations obtained via continuous cooling may be compared. Figure 3.62(a) shows the structure factor for a perfect crystal of fully stretched chains: Vertical lines indicate the position of the peaks corresponding to vectors of the two-dimensional reciprocal hexagonal lattice. The lattice parameter \tilde{a} is taken from the position of the first peak in the measured data, and corresponds to the characteristic length $d \simeq 0.95\sigma$ imposed by the packing of the chains. Most peaks are determined by the length of vectors of the 2- d lattice, and the peaks corresponding to vectors out of the $\tilde{\mathbf{a}}-\tilde{\mathbf{b}}$ plane (not shown) do not seem to have large contributions in the total structure factors. Extra peaks are found that do not correspond to vectors of the 2- d lattice. We will come back to that later. Figure 3.62(b) shows a comparison of structure factors for differ-

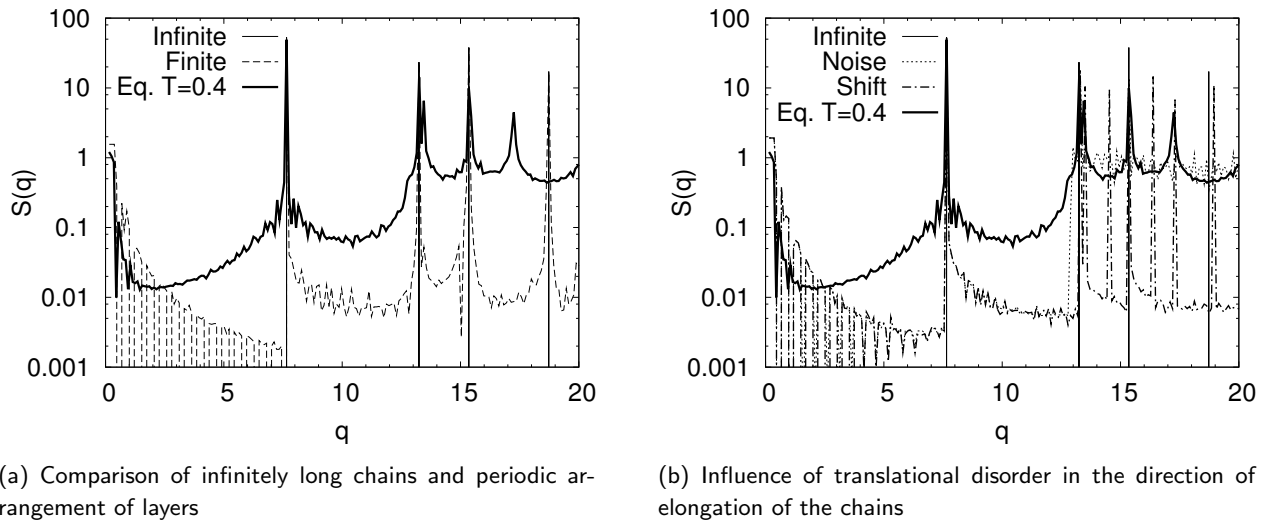


Figure 3.63: Comparison of the structure factor measured during an equilibrium simulation at $T = 0.4$ and structure factors obtained for fixed configurations generated by hand and not annealed in a simulation. Parameters of these configurations have been modified in order to find the origin of the extra peaks observed in the structure factor of perfectly stretched chain or regularly folded chain crystals (see text for details).

ent semi-crystalline configurations at $T = 0.4$. The structure factor for a semi-crystalline configuration obtained via continuous cooling of the melt contrasts with those measured for perfect crystal configurations generated by hand and simulated in equilibrium at low- T , which are closer to the Dirac-delta peak-like structure expected for a crystal of simpler particles. A greater number of folds is associated with higher noise and a more pronounced structure in the small- q region. One can also notice a fourth peak around $q = 17$ which does not correspond to a vector of the reciprocal lattice (see fig. 3.63).

In order to find the origin of the supplementary peaks, “artificial” configurations have been created with perfectly stretched chains on a regular hexagonal lattice. The translational order of chains in the layers and the inter-layer distance have been modified so that the influence of the different parameters on the overall structure can be determined. For the “Infinite” configuration, particles are set up on a perfectly regular lattice and the size of the periodic box is adjusted so that the distance between any two particles in the direction of elongation of the chains is always a multiple of the bond length. This is not the case for the “Finite” configuration, whose box size takes into account the inter-layer distance in the direction of the chains (the distance between two particles along the chain is $\sigma/2$, whereas the inter-layer distance is determined by the excluded volume interaction and is close to 0.95σ at $T = 0.4$). It can be seen in fig. 3.63(a) that the introduction of a new characteristic length (the chain length) causes the apparition of infinitely many peaks in between the Bragg peaks observable in the case of a perfect crystal. In fig. 3.63(b) the crystalline structure is compared to slightly distorted configurations: Adding “noise” to the

configuration (by displacing the chains by a small amount (uniform distribution between $\pm 0.2\sigma/2$) along the z -direction, their direction of elongation) is reflected in the occurrence of a signal closer to unity between the peaks after the second one, which is observed on the structure factor measured at $T = 0.4$. A periodic “shift” (chains in consecutive x - z planes are shifted along the z -axis by an amount of $\sigma/4$ so that their packing is more favorable) results in the occurrence in the structure factor of new peaks between those predicted by vectors of the two-dimensional hexagonal lattice, since this periodic displacement of the chains introduces a new characteristic length scale. This explains the presence of extra peaks in the structure factor measured for the “perfect” crystal of fully stretched chains at $T = 0.4$: This temperature is high enough to allow the chains to move in the z -direction and minimize their excluded-volume interaction by adopting new positions. The situation still cannot be exactly described by the structure factor for regularly displaced chains, since the hexagonal arrangement introduces frustration and does not induce regular displacements of the chains.

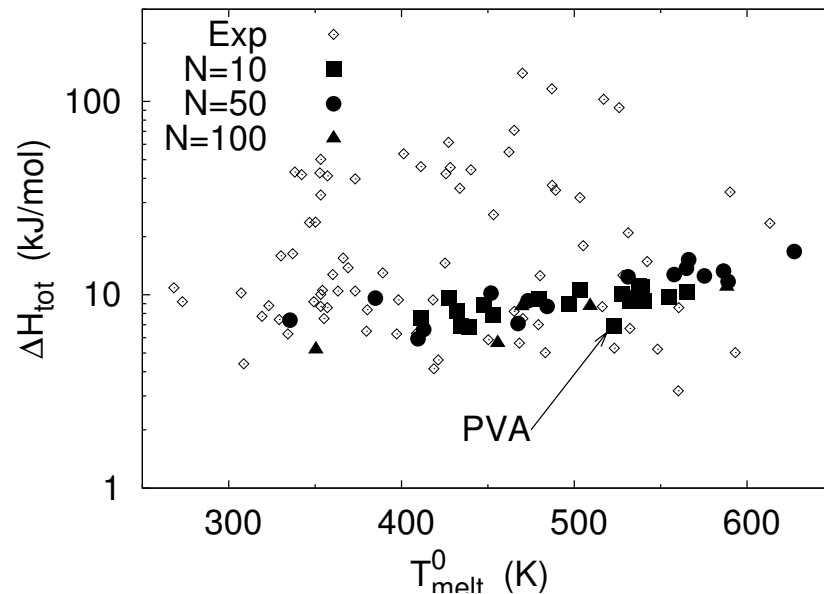


Figure 3.64: Comparison of simulation results with experimental values. The points corresponding to the simulation data are adjusted using the experimental values reported for poly(vinyl alcohol) [65]:

	T_{melt}^0	ΔH_{tot}
poly(vinyl alcohol)	523.2 K	6862 J/mol
CG-PVA ($N = 100$)	0.86	0.88

3.4 Summary

We used coarse-grained models derived from the CG-PVA model in order to study polymer crystallization with computer simulations. Such kind of models is suited to address this phenomenon, as it becomes possible to make the simulation algorithm very efficient in not taking into account the irrelevant degrees of freedom in the system. We have been focusing on the most important parameter in the CG-PVA model, the angular potential. The structure of this potential is reminiscent of details of the molecule on the atomistic level: Taking into account these specificities makes it possible to reproduce spontaneous crystallization from the melt, whereas a more generic model without an explicit angular potential yields an amorphous system at low temperature (fig. 3.65).

We created several models with the same parameters as the CG-PVA model, except for this angular potential, which has been varied (fig. 3.66); simulations of these different models allowed to test the influence of the angular potential on the properties of the models, especially on the transition to the semi-crystalline state at low temperature.

These new models are artificially designed and do not correspond to existing polymers; however, a very crude mapping shows that the set of created models covers to a large extent the range of crystallizable polymers: Figure 3.64 presents a comparison of the melting temperature and latent heat of fusion found experimentally for various polymers (from ref. 65) and data from our simulations. The experimental and simulation data should not be directly compared, since the experimental values are in fact extrapolations for infinitely thick crystalline lamellae; still, the graph provides an overview of the temperature scale over which real polymeric materials in a crystalline state are found and to what extent our coarse-grained models cover the range of existing crystalline polymers.

In particular, a correlation between the probability of finding *trans-trans* states in the melt at high temperature and the crystallization or melting temperature has been found (fig. 3.67); this means that the structure of the chains in the melt at high temperature is connected to the propensity of the system to crystallize.

This correlation can be described using a theory by Volkenstein which relates the probability of *trans* states to the melting point of the crystalline structures (see fig. 3.68); we could show that this theory for crystalline polymers accounts for the correlation we found between the angular states and the temperature of melting, provided that Volkenstein's hypothesis about the crystalline state is justified, i.e. that the chains are perfectly stretched. This is the case for small enough chains that can form nearly perfect crystals, and for longer chains arranged on perfect lattices whose simulated melting point also agrees with the theoretical predictions.

The structure of the semi-crystalline systems has been characterized by different order parameters and it was possible to provide a unified

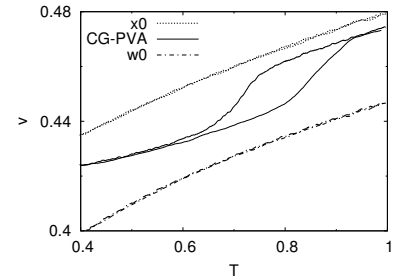


Figure 3.65: Comparison of the phase diagrams for CG-PVA and two other models **without** angular potential (fig. 3.5).

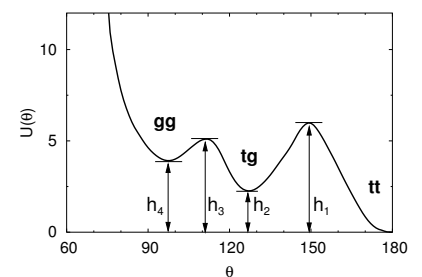


Figure 3.66: Parameterization of the coarse-grained angular potential (fig. 3.7).

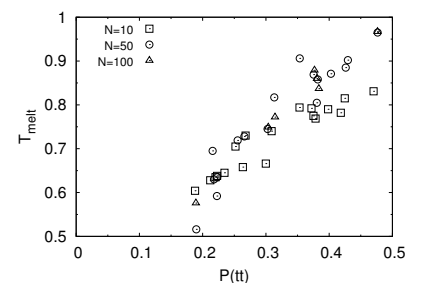


Figure 3.67: Correlation between the melting temperature and the probability of *trans-trans* states (fig. 3.16(d)).

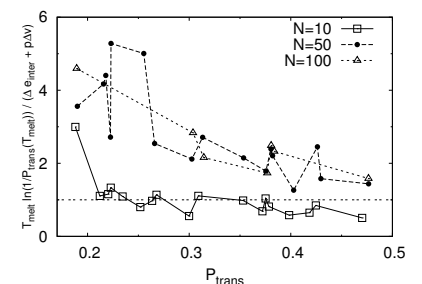


Figure 3.68: Improving agreement with Volkenstein's theory as P_{trans} increases (fig. 3.48(b)).

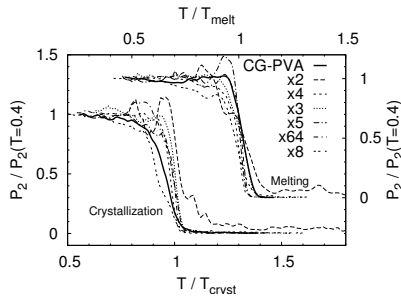


Figure 3.69: Superposition of the P_2 order parameters for different models during cooling and heating (fig. 3.28).

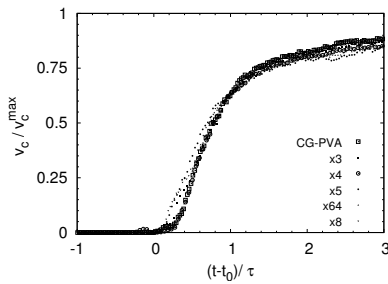


Figure 3.70: Master curve for the crystallinity during continuous cooling (fig. 3.40).

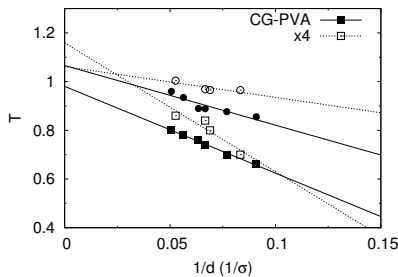


Figure 3.71: Crystallization and melting lines for the x4 and CG-PVA models (fig. 3.49).

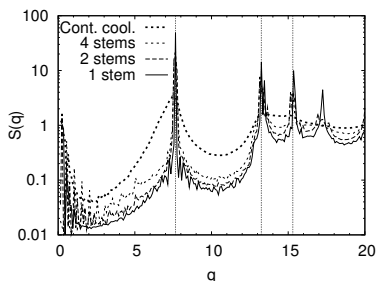


Figure 3.72: Comparison of structure factors for different crystalline configurations at $T = 0.4$ (fig. 3.62(b)).

description of the crystallization and melting processes: The order parameter P_2 can be used to account for the development of order in the melt during continuous cooling (fig. 3.69). The definition of another order parameter with a local criterion allows to distinguish the crystallites from the amorphous regions; together with a generic approach for the description of growing structures in a medium (Avrami analysis), it is possible to find the relevant parameters which yield a common picture for the development of crystallinity for the different models (fig. 3.70).

The coarse-grained models used reproduce the experimentally observed crystallization and fusion lines, relating the crystallization and melting temperatures to the thickness of the lamellae in the crystal (fig. 3.71). The structure of the semi-crystalline systems has been characterized and compared to perfect crystals of either stretched or folded chains simulated at low temperature (fig. 3.72).

The connection between simulations using an atomistic model presented in chapter 2 and the coarse-grained simulations can be established in deriving parameter for a coarse-grained model from the all-atom study: Taking in a first approximation the parameters for the excluded-volume and binding interactions from the CG-PVA model, it is possible to obtain a coarse-grained model for polyethylene using the data from alkane chains simulations. The angular potential is the predominant parameter of the coarse-grained models, and it contains most of the features corresponding to the specificity of one particular polymer. Moreover the distribution of angles has been found not to vary significantly with the chain length; thus our short n -alkane simulations may be used to determine an angular potential. Figure 3.73 shows the phase diagram obtained for this CG-PE model, and it can be seen that this model reproduces the crystallization and melting transitions whereas they were not observed using the original all-atom model.

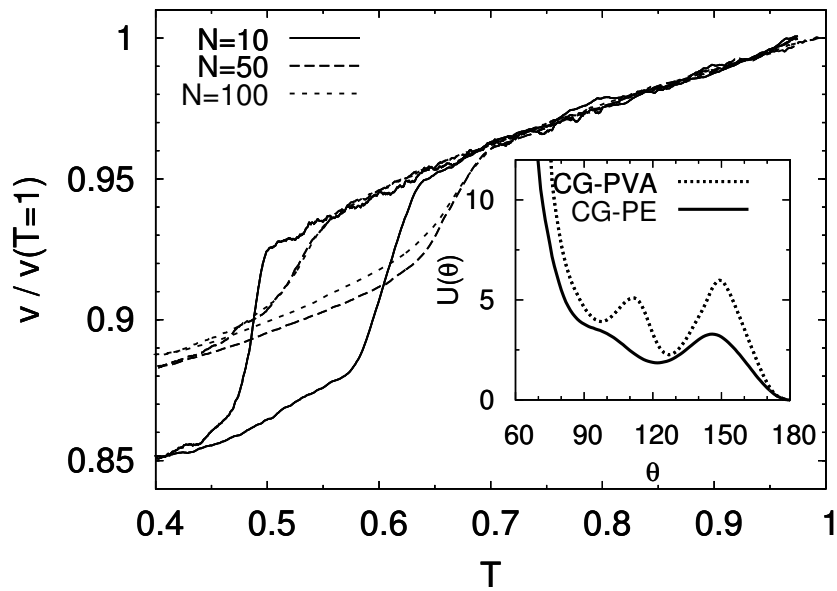


Figure 3.73: Phase diagram obtained for continuous cooling simulations of a coarse-grained model of polyethylene derived from the atomistic simulations presented in chapter 2. The parameters of the model are taken from the CG-PVA model, except for the angular potential that is inverted from the angular distribution measured at $T = 500$ K on a simulation of $C_{44}H_{90}$: A comparison of the two angular potential is shown in the inset. This coarse-grained model appears to form crystal upon cooling, whereas this could not be observed in the all-atom simulations.

4 Structure factors

The analysis of crystallizable models presented in the previous chapter suggests that it is relevant to make a distinction between *inter*- and *intra*-chain properties. Here, we want to complement this analysis by a detailed study of various static structure factors which provide insight into the spatial correlation of the monomers (or chains) on different length scales. As an extension to the structure factors we have already discussed (cf. sec. 3.3.5), *inter*- and *intra*-chain structure functions were calculated, as well as more detailed site-dependent quantities. Since these objects require to be averaged over a large amount of independent configurations in order to reduce statistical noise to an acceptable level, we focus here on four different models [CG-PVA and three of its variants: x2, x4 and w0 (see fig. 3.5 and sec. 3.2 for definitions)] simulated at high temperature ($T = 1$). At $T = 1$, no significant qualitative differences could be identified between the models most of the time, so the results presented in the following correspond mostly to CG-PVA, unless otherwise noted.

The temperature dependence of the quantities under consideration would certainly provide an interesting insight into the mechanisms responsible for the crystallization process. We did not pursue such a study here, mainly due to two reasons; a computational one and a physical one. An analysis at lower T would have been too demanding in computer time within the scope of this thesis. On the other hand, the results presented above for the variation of the melting or crystallization temperature with the probability of *trans* states suggested that crystallization is greatly influenced by the high temperature features (fig. 3.47).

The method employed consists in calculating various static structure functions as an extension of simple liquid theory [40], and confronting the findings to theoretical results originating e.g. from PRISM theory [108, 109]. Our presentation follows closely the discussion of Aichele et al. [1].

4.1 Definitions

We are considering polymer melts that consist of n chains containing N monomers each. For a system of total volume V , it is possible to define two different kinds of densities, either the monomer density ρ_m

Contents

4.1	Definitions	137
4.1.1	Density fluctuations	138
4.1.2	Static structure factors	138
4.1.3	Center-of-mass related structure factors	139
4.1.4	Technical details	140
4.2	Site-averaged structure factors	141
4.2.1	Intra-chain structure factors	141
4.2.2	Inter-chain structure factors	145
4.2.3	Comparison of different models	146
4.3	Site-resolved structure factors	148
4.3.1	Direct correlation functions	148
4.3.2	Intra-chain structure	153
4.3.3	Inter-chain structure	157
4.4	Structure factors involving the center of mass	159
4.5	Summary	164

or the chain density ρ_{ch} :

$$\rho_{\text{m}} = \frac{N}{V}, \quad (4.1)$$

$$\rho_{\text{ch}} = \frac{n}{V}. \quad (4.2)$$

4.1.1 Density fluctuations

The structure factor as defined in eq. (1.74) corresponds to a density fluctuation correlation function; thus we need to define the density fluctuations, which can be made dependent on the position of a particular monomer along the chain, so as to distinguish between chain ends and centers. With \mathbf{r}_i^a denoting the position of monomer a of chain i , the density fluctuations of monomer a for the wave vector \mathbf{q} in reciprocal space can be expressed as

$$\rho_a(\mathbf{q}) = \sum_{i=1}^n \exp(i\mathbf{q} \cdot \mathbf{r}_i^a) \quad (a = 1, \dots, N). \quad (4.3)$$

The density fluctuations created by all monomers of the melt are thus

$$\rho_{\text{tot}}(\mathbf{q}) = \sum_{i=1}^n \sum_{a=1}^N \exp(i\mathbf{q} \cdot \mathbf{r}_i^a), \quad (4.4)$$

and it is also useful to define the fluctuations associated with the centers of mass of the different polymer chains:

$$\rho_c(\mathbf{q}) = \sum_{i=1}^n \exp(i\mathbf{q} \cdot \mathbf{R}_i), \quad (4.5)$$

with \mathbf{R}_i being the position of the center of mass of chain i , i.e.:

$$\mathbf{R}_i = \frac{1}{N} \sum_{a=1}^N \mathbf{r}_i^a. \quad (4.6)$$

4.1.2 Static structure factors

A density-density correlation function that can be expressed using the preceding definitions depends on the position of two monomers a and b along the chain:

$$S_{ab}(\mathbf{q}) = \frac{1}{n} \langle \rho_a(\mathbf{q})^* \rho_b(\mathbf{q}) \rangle; \quad (4.7)$$

this quantity is called the site-site structure factor, and is the function we will compute from our simulation data in order to characterize the models we intend to study. The average here is to be taken over all configurations of the simulated melt. Since the polymer melts under consideration are spatially homogeneous and isotropic, the structure factors only depend on $q = |\mathbf{q}|$, and we have $S_{ab}(\mathbf{q}) = S_{ab}(q)$ in eq. (4.7). As we did for other quantities like the enthalpy of melting in sec. 3.3.1

for instance, it is possible to split the structure factor into *intra*- and *inter*-chain contributions:

$$S_{ab}(q) = \underbrace{w_{ab}(q)}_{\text{intra}} + \rho_{\text{ch}} \underbrace{h_{ab}(q)}_{\text{inter}} . \quad (4.8)$$

The intra-chain contribution is thus written

$$w_{ab}(q) = \frac{1}{n} \left\langle \sum_{i=1}^n \exp \left(-i\mathbf{q} \cdot (\mathbf{r}_i^a - \mathbf{r}_i^b) \right) \right\rangle , \quad (4.9)$$

and the corresponding inter-chain contribution reads

$$\rho_{\text{ch}} h_{ab}(q) = \frac{1}{n} \left\langle \sum_{i \neq j} \exp \left(-i\mathbf{q} \cdot (\mathbf{r}_i^a - \mathbf{r}_j^b) \right) \right\rangle . \quad (4.10)$$

Figure 4.1 presents a schematic illustration of the different inter- and intra-chain structure factors.

The static structure factor related to what is measured in scattering experiments is recovered by averaging over all pairs of monomers a and b :

$$S(q) = \frac{1}{N} \sum_{a,b=1}^N S_{ab}(q) \quad (4.11)$$

$$= \frac{1}{nN} \langle \rho_{\text{tot}}(\mathbf{q})^* \rho_{\text{tot}}(\mathbf{q}) \rangle , \quad (4.12)$$

which can also be decomposed into inter- and intra-chain contributions as follows:

$$S(q) = w(q) + \rho_{\text{m}} h(q) \quad (4.13)$$

[Notice that the *monomer* density now appears as a prefactor, instead of the chain density ρ_{ch} in the related expression of eq. (4.8)]. The function $w(q)$ is also called the form factor of one chain [22]. The definitions for these two functions are:

$$w(q) = \frac{1}{N} \sum_{a,b=1}^N w_{ab}(q) \quad (4.14)$$

and

$$h(q) = \frac{1}{N^2} \sum_{a,b=1}^N h_{ab}(q) . \quad (4.15)$$

4.1.3 Center-of-mass related structure factors

Another kind of structure factor that can be measured and analyzed in the simulation focuses on the centers of mass (CMs) of two distinct chains. Correlations between these can be studied as in the case of simple particles in a liquid; for that purpose one can define the CM–CM structure factor (see fig. 4.2)

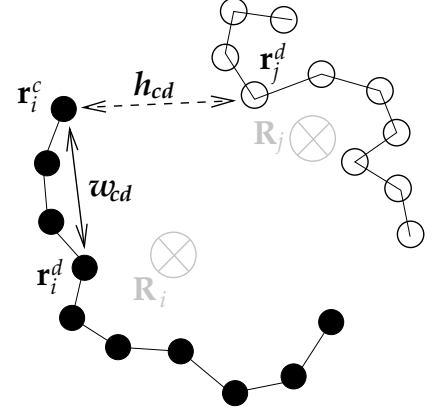


Figure 4.1: Definition of the *inter*- and *intra*-chain contributions to $S_{cd}(q)$, respectively $h_{cd}(q)$ and $w_{cd}(q)$. \mathbf{R}_i denotes the center of mass of chain i [defined in eq. (4.6)]. Other structure functions involving the centers of mass of the chains are presented in figs. 4.2 and 4.3.

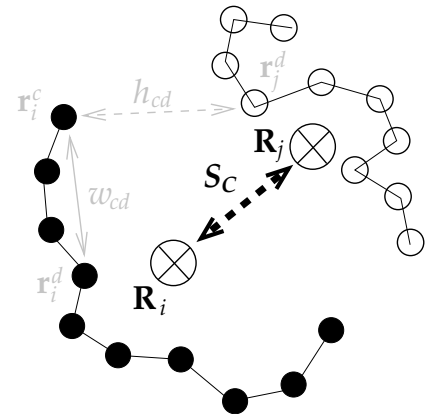


Figure 4.2: Definition of the center-of-mass structure factor.

$$S_C(q) = \frac{1}{n} \langle \rho_C(\mathbf{q})^* \rho_C(\mathbf{q}) \rangle \quad (4.16)$$

$$= \frac{1}{n} \left\langle \sum_{i,j=1}^n \exp \left(-i\mathbf{q} \cdot (\mathbf{R}_i - \mathbf{R}_j) \right) \right\rangle. \quad (4.17)$$

This is again split into inter- and intra-chain contributions this way:

$$S_C(q) = 1 + \rho_{\text{ch}} h_C(q), \quad (4.18)$$

the intra-chain contribution being simply unity since a simple particle has no “internal structure”.

It is also possible to calculate correlation functions describing the coupling between one monomer and the CM of a chain. Such monomer-polymer structure factors read (fig. 4.3):

$$S_{a,c}(q) = \frac{1}{n} \langle \rho_a(\mathbf{q})^* \rho_C(\mathbf{q}) \rangle \quad (4.19)$$

$$= \frac{1}{n} \left\langle \sum_{i,j=1}^n \exp \left(-i\mathbf{q} \cdot (\mathbf{r}_i^a - \mathbf{R}_j) \right) \right\rangle. \quad (4.20)$$

Another decomposition into inter-/intra-chain contributions yields:

$$w_{a,c}(q) = \frac{1}{n} \left\langle \sum_{i=1}^n \exp \left(-i\mathbf{q} \cdot (\mathbf{r}_i^a - \mathbf{R}_i) \right) \right\rangle, \quad (4.21)$$

and

$$\rho_{\text{ch}} h_{a,c}(q) = \frac{1}{n} \left\langle \sum_{i \neq j}^n \exp \left(-i\mathbf{q} \cdot (\mathbf{r}_i^a - \mathbf{R}_j) \right) \right\rangle. \quad (4.22)$$

The average packing of monomers around the CM of the chain they belong to or of other chains is described respectively by the following functions

$$w_{m,c}(q) = \sum_{a=1}^N w_{a,c}(q) \quad (4.23)$$

$$h_{m,c}(q) = \frac{1}{N} \sum_{a=1}^N h_{a,c}(q). \quad (4.24)$$

These equations allow us to define the average monomer-polymer structure factor:

$$S_{m,c}(q) = \sum_{a=1}^N S_{a,c}(q) \quad (4.25)$$

$$= w_{m,c}(q) + \rho_m h_{m,c}(q). \quad (4.26)$$

4.1.4 Technical details

The computation of structure factors from simulation data requires to average the considered functions over a great number of (independent) configurations, so that the statistical errors are minimal. This is particularly important in the case of site-resolved quantities [1], since for

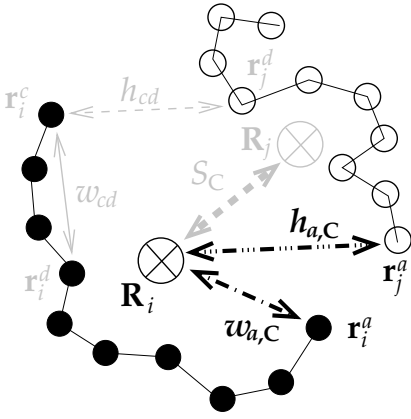


Figure 4.3: Definition of monomer-polymer structure factors.

quantities like $w_{ab}(q)$ and $h_{ab}(q)$ there are no averages over the positions of the monomers along the chain. In the case of our simulations, structure factors for $N = 10$ have been averaged over 360 *consecutive* configurations for CG-PVA (160 configurations for other models); 400 (200) configurations for $N = 50$ and 1000 (200) configurations for $N = 100$. The configurations used are consecutive, meaning that they belong to one equilibrium-run trajectory, and are separated by 50τ . This is not enough to ensure statistical independence of the configurations for the longer chains; it may be desirable to average over more remote configurations, but this would require much longer simulation runs. Table 4.1 shows a summary of the relevant quantities for the calculation of structure factors in the case of our coarse-grained models: The number of chains for each chain length is indicated, as well as the abovementioned number of configurations over which the structure factors are averaged; in the case of the CG-PVA model, the average box size $\langle L \rangle$ is given (in σ), and the corresponding minimum wave vector $q_{\min} = 2\pi/\langle L \rangle$ is indicated.

Table 4.1: Summary of parameters for the calculation of structure factors for the coarse-grained models.

N	10	50	100
chains	288	72	192
Nb. of confs. (CG-PVA)	360	400	1000
Nb. of confs. (other models)	160	200	200
$\langle L \rangle$ (CG-PVA)	11.31	11.98	20.89
q_{\min} (CG-PVA)	0.56	0.53	0.30

4.2 Site-averaged structure factors

A comparison of the total and intra-chain structure factors shows that the behavior of $S(q)$ at large q is entirely determined by the intra-chain contributions. Figure 4.4 presents $S(q)$ and $w(q)$ for different chain lengths, and points out the similarity between these two functions after the second peak. This effect does not appear to depend on the chain length. According to the model used, the intra-chain function may or may not reproduce the total structure factor $S(q)$: For a simple bead-spring model it is not the case [8, 60], whereas for an atomistic model of 1,4-polybutadiene, it has been shown that $S(q)$ and $w(q)$ also superimpose [1, 8]; it seems that realistic models like atomistic models and CG-PVA, by introducing explicit stiffness imply strong intra-molecular correlations, which tend to determine almost completely the structure factor at large q vectors.

On the other hand, the first and second peaks of $S(q)$ show that inter-chain contributions are important. The comparison of fig. 4.4 suggests to analyze $w(q)$ and $h(q)$ in more detail.

4.2.1 Intra-chain structure factors

The structure of the intra-chain function $w(q)$ can be interpreted by looking at different length scales separately.

Debye function. For the small q regime, it is very common to consider a polymer as an ensemble of segments, the distance between which is given by a gaussian distribution [22]; this approach is relevant if the excluded volume interactions between the monomers have been sufficiently “averaged out” so that one chain can be considered as a random

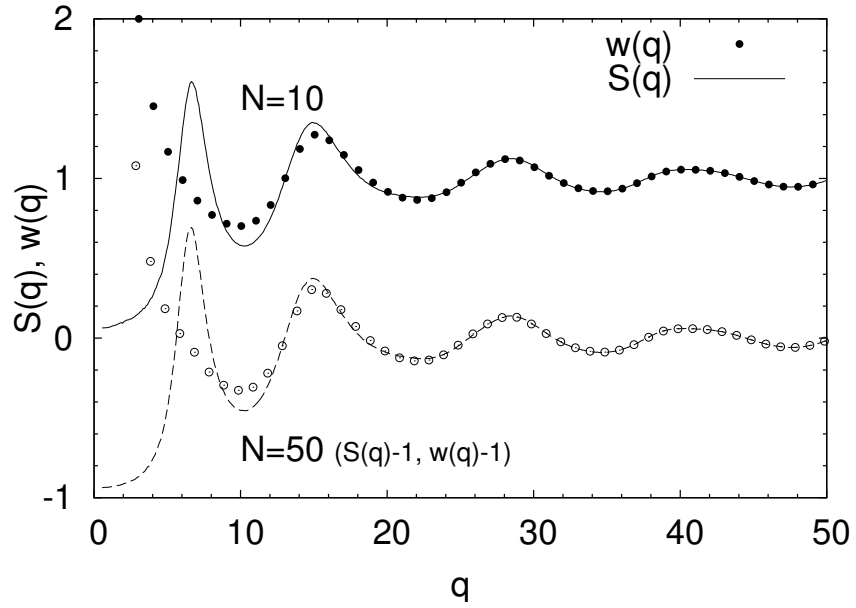


Figure 4.4: Comparison of the total structure factor $S(q)$ and the intra-chain only contribution, $w(q)$. For two chain lengths ($N = 10$ and $N = 50$), $S(q)$ is completely determined by the value of $w(q)$ from the third peak onward. For $q \rightarrow 0$, the intra-chain structure factors tend to the number of monomers per chain, N . Data for $N = 50$ have been shifted for clarity. The data obtained for longer chains ($N = 100$) superimpose almost perfectly with the data presented here for $N = 50$.

walk. This comes from the “ideality” of the polymer chains in the melt [33]: Whereas in dilute solutions the chains can be either swollen or collapsed depending on the solvent and temperature (with only one particular temperature T_θ at which the chains are “ideal”), it can be shown that in a melt the intra-chain interactions are screened by the presence of the surrounding polymers [19, 22, 30]. This leads to chains behaving ideally, i.e. in a random-walk-like manner on large length scales; in particular, this implies $R_g \sim N^{1/2}$. On large scales, the gaussian model which reproduces the random-walk structure of the chains implies the following probability distribution for the distance between monomer a and b (for a 3-dimensional melt):

$$G(\mathbf{r}^a, \mathbf{r}^b) = G(\mathbf{r}) = \left(\frac{3}{2\pi\langle \mathbf{r}^2 \rangle} \right)^{3/2} \exp\left(-\frac{3\mathbf{r}^2}{2\langle \mathbf{r}^2 \rangle} \right); \quad (4.27)$$

the mean square distance between two monomers a and b being given by

$$\langle (\mathbf{r}^a - \mathbf{r}^b)^2 \rangle = \langle \mathbf{r}^2 \rangle = |a - b| \ell^2, \quad (4.28)$$

where ℓ is the statistical segment length, which is defined by

$$\ell = \sqrt{\frac{6R_g^2}{N}}. \quad (4.29)$$

[R_g is the radius of gyration defined in eq. (1.65)]. The expression of the static structure factor can be derived analytically: Equation (4.14) can be written

$$w(q) = \frac{1}{N} \sum_{a,b=1}^N \langle \exp(i\mathbf{q} \cdot [\mathbf{r}^a - \mathbf{r}^b]) \rangle, \quad (4.30)$$

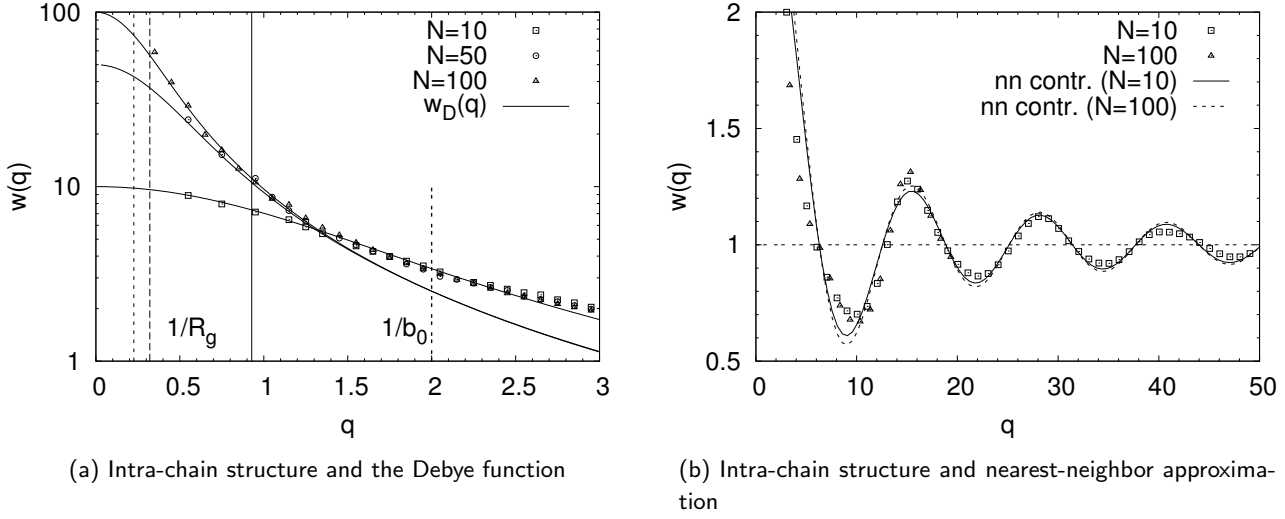


Figure 4.5: Intra-chain structure factor compared to approximations in different regimes: The Debye function at small q [eq. (4.33) and (4.34)] and nearest neighbors for large q [eq. (4.40)]. In fig. 4.5(a), inverse characteristic lengths $1/R_g$ and $1/b_0$ have been indicated by vertical lines (see footnote 1 on page 143); it can be observed that the small- q approximation reproduces faithfully the behavior of $w(q)$ for $q < 1/R_g$ but fails as $1/b_0$ is approached. The large- q expression retaining only nearest-neighbor contribution is a good approximation to $w(q)$ and reproduces qualitatively the observed oscillating structure (fig. 4.5(b)).

We used the symmetry of the site-site structure factors that arises from the fact that the two ends of one chain are indistinguishable, i.e. $w_{ab}(q) = w_{ba}(q)$. In eq. (4.9) the average over all orientations of the vector $\mathbf{r}_i^a - \mathbf{r}_i^b$ can be carried out, so that we obtain

$$w_{a\ a+1}(q) = \left\langle \frac{\sin(q|\mathbf{r}_i^a - \mathbf{r}_i^{a+1}|)}{q|\mathbf{r}_i^a - \mathbf{r}_i^{a+1}|} \right\rangle, \quad (4.38)$$

where the average is to be taken over the length of vector $\mathbf{r}_i^a - \mathbf{r}_i^{a+1}$. To do so, we can argue that the bond potential used in our simulation as defined in eq. (3.5) is very stiff, and therefore yields a sharp distribution of the bond length around the mean value b_0 . This results in $|\mathbf{r}_i^a - \mathbf{r}_i^{a+1}| \approx b_0$, and thus

$$w_{a\ a+1}(q) \approx \frac{\sin(qb_0)}{qb_0}. \quad (4.39)$$

Inserting this into eq. (4.37) finally gives

$$w_{\text{nn}}(q) \approx 1 + \frac{2}{N}(N-1) \frac{\sin(qb_0)}{qb_0} \quad (4.40)$$

for large q .

Figure 4.5 presents a comparison of the data from the simulations and the approximations given above; it can be seen that the large- q approximation based on the nearest-neighbor contributions given by eq. (4.40) yields the correct qualitative structure, reproducing the characteristic oscillations of $w(q)$. For small q vectors, the Debye function provides a good description of the behavior of the intra-chain structure, as the chains exhibit a random-walk-like behavior for $q \ll 1/b_0$

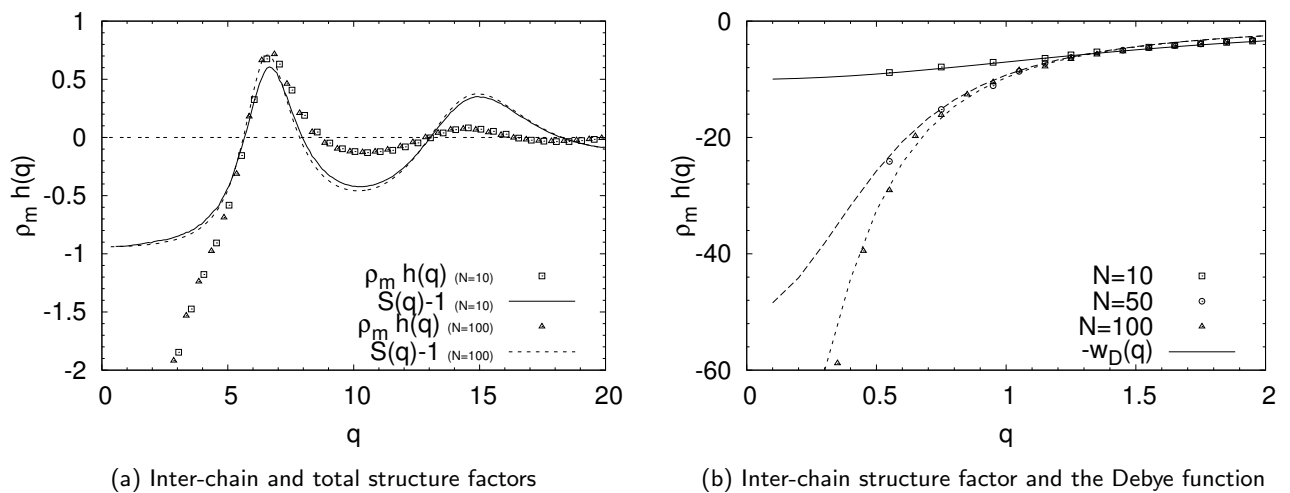


Figure 4.6: Inter-chain structure factor compared to the total structure factor and the Debye function, for CG-PVA and for several chain lengths. The inter-chain structure strongly determines the first peak of the collective structure factor $S(q)$. The small- q regime is well described by the negative of the form factor of an ideal chain, $-w_D(q)$.

(b_0 corresponds to the length of one bond; see eq. (3.5). See footnote 1 on page 143).

4.2.2 Inter-chain structure factors

The inter-chain structure of the polymer melts we have simulated can be understood by considering the case of a simple liquid: Simple liquids do not have internal structure, and thus $w(q) = 1$. Therefore, the inter-particle structure factor is just $\rho_m h(q) = S(q) - 1$.

Figure 4.6(a) compares $\rho_m h(q)$ to $S(q) - 1$ and stresses the similarity between these two functions around the first peak: The first peak of $S(q)$ characterizes the packing of monomers in the melt, and hence is dominated by the inter-chain contribution, with a small contribution arising from the intra-chain structure (cf. fig. 4.4). This agreement between $\rho_m h(q)$ and $S(q) - 1$ appears to improve as the chain length increases.

For large q vectors, the inter-chain structure factor tends to 0 with small oscillations. Here the structure factor becomes mostly determined by intra-chain effects (see fig. 4.4) and so the simple-liquid approximation $\rho_m h(q) = S(q) - 1$ must considerably deviate from the simulation data.

For small q , there are also deviations between $\rho_m h(q)$ and $S(q) - 1$ which may be explained by the polymer-specific “correlation hole” effect: The probability of finding a monomer from another chain is lowered in the typical volume occupied by a particular chain. Thus the correlation between particles of distinct chains drops with increasing distance, and this compensates the increase in intra-chain correlations. Figure 4.6(b) shows that $\rho_m h(q)$ indeed varies like $-w_D(q)$, which explains why the sum of the inter- and intra-chain structure factors yields

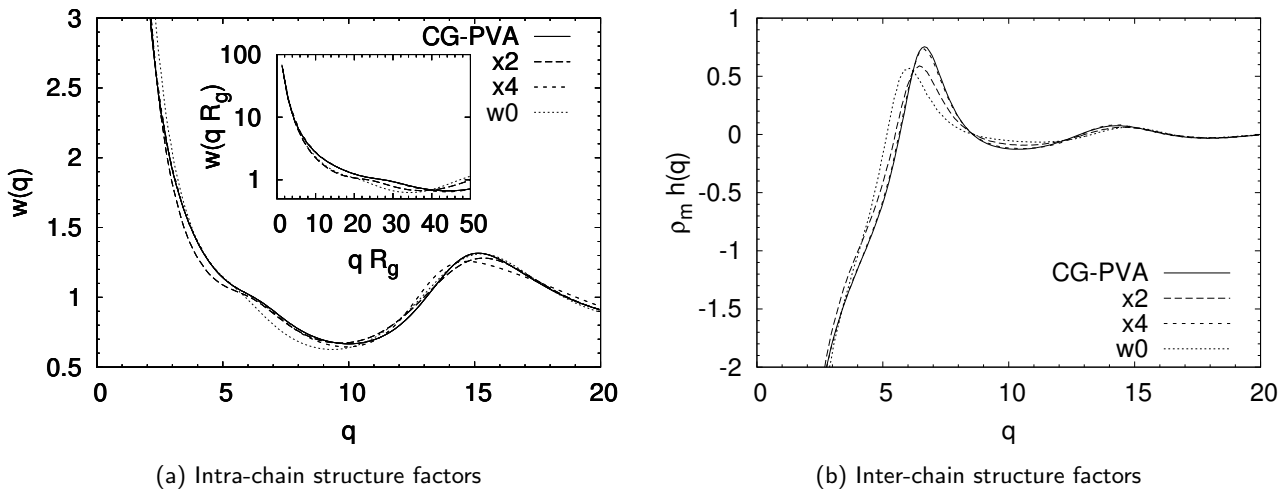


Figure 4.7: Comparison of the structure factors for four different models ($N = 100$). There are slight differences in the intra-chain structure factors that tend to disappear as q increases (fig. 4.9(a)); for smaller q , the differences arise from the flexibility of the chain that is specific to every model. This requires a description taking into account the intra-chain properties (Koyama distributions, see fig. 4.18(b)). For small q vectors, an inset shows $w(qR_g)$ as a function of qR_g . For inter-chain functions, a mismatch in the values of q^* for which $h(q)$ is maximal can be noticed. This corresponds to different specific lengths for the packing of monomers of distinct chains (fig. 4.9(b)).

a finite value for $S(q)$ as $q \rightarrow 0$, corresponding to the melt's (weak) compressibility.

4.2.3 Comparison of different models

Figure 4.7 presents a comparison of different models for the inter- and intra-chain structure factors; the total structure factor $S(q)$ that was already presented in fig. 3.54 for the different models at $T = 1$ is shown in fig. 4.8. The difference in the models with which the influence of the flexibility of the chains on crystallization was studied. The models x2 and x4 have respectively very low and very high crystallization/melting temperatures (fig. 3.45), whereas w0 has no explicit angular potential and does not crystallize (fig. 3.5).

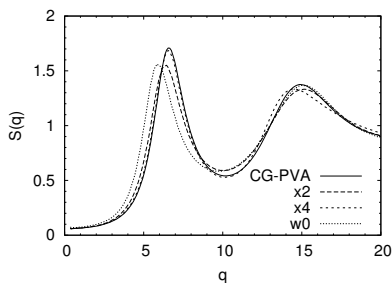


Figure 4.8: Structure factors at high temperature ($T = 1$) for four different models: CG-PVA, x2, x4, w0. These structure factors were already presented in fig. 3.54, together with data for lower temperatures.

The intra-chain structure of the different models exhibits slight variations of the positions of the peaks and minima. Nevertheless it can be observed that these differences seem to be washed out as the wave vector increases (cf. fig 4.9(a)). For small q , the flexibility of the model also influences the intra-chain structure, as can be seen on the inset of fig. 4.7(a): When rescaled by the radius of gyration, all functions $w(qR_g)$ for the different models superimpose as $qR_g \rightarrow 0$. The nearest-neighbor approximation presented in eq. (4.37) can be tested against the data obtained for the different models at several chain lengths; it appears that the description is only qualitative at large q vectors, as can be seen on fig. 4.10. The agreement is good around the third peak but does not hold for smaller or larger wave vectors. Still the oscillations are well reproduced; the different models exhibit the same deviations from the behavior predicted by the nearest-neighbor approx-

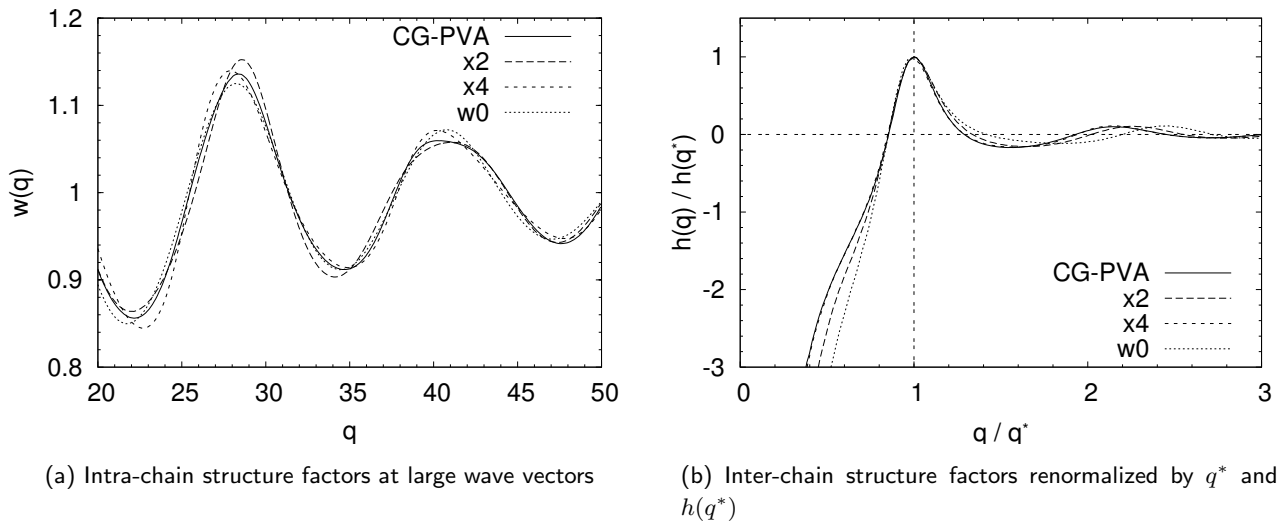


Figure 4.9: Inter- and intra-chain structure factors for different models. Figure 4.9(a) shows the evolution of $w(q)$ at large q vectors, showing that the differences between the structures of the different models seem to vanish as $q \rightarrow \infty$. Figure 4.9(b) presents a rescaled plot of the inter-chain structure factors for the different models.

imation. One would then need to take into account the contributions arising from next neighbors, which are determined by the interactions between monomers inside the chains; this would imply more complicated calculations in which the flexibility of the chains plays a role.

These observations suggest that a more accurate description of the intra-chain structure factors is needed, which would account for the flexibility of the different models; this can be done through the use of Koyama distributions as we shall see in sec. 4.3.2.

Figure 4.9(b) shows the inter-chain structure factors for the different models already presented in fig. 4.7(b), but rescaled using the wave vector q^* corresponding to the maximum h_{\max} of $h(q)$; it can be seen that the data do not superimpose for other q vectors, indicating that there is no general behavior for $h(q)$. One can try to relate the position of the main peak to a typical length in the system, so as to give a physical meaning to q^* ; it could be naively expected that there is a relation between q^* and the density of the system, as q^* corresponds to the inverse distance between two monomers of two distinct chains, and one could assume that the larger this distance, the lower the density. Figure 4.11 shows that this assumption is wrong in the case of our simulation data, since the inverse density decreases with the distance $1/q^*$. Hence the shift in the main peak's position observed in fig. 4.7(b) cannot be explained by the change in density at high temperature for our models. It is also presented on fig. 4.11 that the radius of gyration decreases with increasing distance $1/q^*$, and thus R_g neither is the relevant length scale that could allow to superimpose the structure factors for the different models.

The change in the first peak's position is most important in the case of the w0 model which has no angular potential; in this case, the

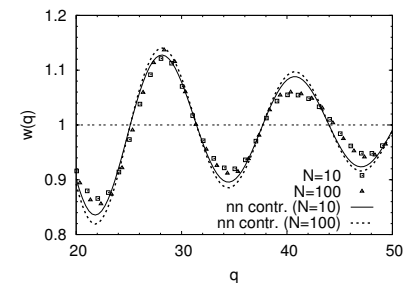


Figure 4.10: Comparison of the intra-chain structure factors measured for CG-PVA, with chain length $N = 10$ and $N = 100$, and the nearest-neighbor approximation [eq. (4.37)]: This is a magnification of the large- q region of fig. 4.5(b). Data and approximation for $N = 50$ match closely the results obtained for $N = 100$. It is seen that the nearest-neighbor approximation only yields a qualitative description of the simulation data, since the contribution of other neighbors become important as well.

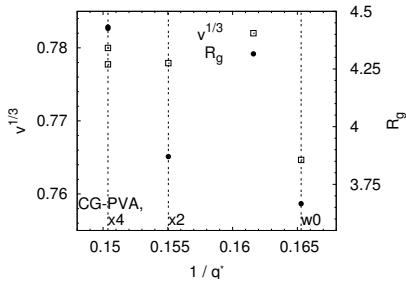


Figure 4.11: Characteristic lengths for the melts (four different models): $v^{1/3}$ (v is the volume per monomer) and the radius of gyration R_g ($N = 100$). Both lengths decrease with $1/q^*$, showing that they are not suited to describe the shift of the inter-chain structure factor toward the small wave vectors.

chains are more flexible, and stiffness is only introduced by the non-bonded potential. This makes it possible for parts of the chains to fold back on themselves, leading to a greater distance on average between monomers of distinct chains. This can explain why the inter-chain structure factors exhibit a peak at lower q for a more flexible model that leads to a denser melt.

4.3 Site-resolved structure factors

In liquid-state theories the structure of fluids is commonly discussed in terms of different correlation functions; in the case of simple liquids, the Ornstein-Zernike equation provides an insight into the behavior of the particles through the introduction of the direct correlation function [40]. The direct correlation function is an important concept and may be interpreted as the effective potential by which two particles interact in the presence of all other particles. It is natural to attempt to extend this approach to more complex molecules; in this case the molecules can be seen as an ensemble of sites, and this leads to the introduction of site-site correlations.

4.3.1 Direct correlation functions

Introductory example: Simple liquids. In order to accurately describe the structure of a liquid of density ρ , the Ornstein-Zernike approach introduces a self-consistent relation between the function h and the direct correlation function c . In direct space, $h(r)$ is simply related to the pair-distribution function $g(r)$ via

$$h(r) = g(r) - 1, \quad (4.41)$$

and the static structure factor $S(q)$ is related to the Fourier transform of $h(r)$:

$$S(q) = 1 + \rho h(q). \quad (4.42)$$

The Ornstein-Zernike equation states that

$$h(r) = c(r) + \rho c * h(r) \quad (4.43)$$

$$= c(r) + \rho \int d\mathbf{r}' c(|\mathbf{r} - \mathbf{r}'|) h(r'), \quad (4.44)$$

which simplifies in Fourier space, as the convolution becomes a simple product:

$$h(q) = c(q) + \rho c(q) h(q). \quad (4.45)$$

Equation (4.44) means that the correlation between two particles separated by a distance r can be decomposed into a *direct* correlation c involving the two particles under consideration only, and the correlations mediated by all the other particles (see fig. 4.12). Equation (4.45) allows one to determine $h(q)$, while eq. (4.44) does not; still it may be

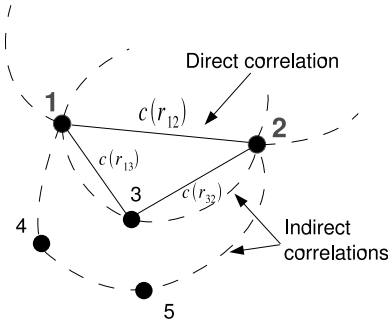


Figure 4.12: Schematic representation of the Ornstein-Zernike approach that implies a decomposition into *direct* correlations between particles 1 and 2 [$c(r_{12})$] and *indirect* correlations mediated by all other particles (particle 3 [$c(r_{13})$] and $c(r_{32})$], particle 4 and 5...).

used to provide a more intuitive presentation of the decomposition into direct and indirect correlations, when put into its iterative form:

$$h(r) = c(r) + \rho c * c(r) + \rho^2 c * c * c(r) + \dots , \quad (4.46)$$

where the first term corresponds to direct correlations by definition, and all other terms describe indirect correlations mediated by 1,2,3... other particles. The reciprocal-space form of the Ornstein-Zernike equation allows us to give a simple definition of the direct correlation function c : Using eqs. (4.45) and (4.42), we obtain

$$\rho c(q) = 1 - \frac{1}{S(q)} . \quad (4.47)$$

Taking a crude approximation allows to give $c(q)$ a more intuitive physical meaning: In the limit of a very dilute system, one can neglect the indirect correlations in the Ornstein-Zernike picture [eq. (4.44)]. Then

$$h(r) = g(r) - 1 \simeq c(r) . \quad (4.48)$$

The pair distribution function $g(r)$ can be expanded in powers of ρ (this assumes that the density is a small parameter):

$$g(r) = \sum_{n=0}^{\infty} \rho^n g^{(n)}(r) , \quad (4.49)$$

and the $g^{(n)}(r)$ enter the fluid's equation of state which can be expressed as [40]:

$$P = \rho k_B T - \sum_{n=0}^{\infty} \rho^{n+2} \left(\frac{2\pi}{3} \int_0^{\infty} dr r^3 \frac{dU(r)}{dr} g^{(n)}(r) \right) \quad (4.50)$$

$$= \rho k_B T + \sum_{n=0}^{\infty} \rho^{n+2} k_B T B_{n+2} . \quad (4.51)$$

$U(r)$ is the inter-particle potential and the first term corresponds to the ideal gas limit; the virial coefficients are defined as

$$B_n = -\frac{2\pi}{3k_B T} \int_0^{\infty} dr r^3 \frac{dU(r)}{dr} g^{(n-2)}(r) \quad (n \geq 2) . \quad (4.52)$$

In the $\rho \rightarrow 0$ limit, the first coefficient B_2 is the predominant term in the series, and is written as [15]:

$$B_2 = -2\pi \int_0^{\infty} dr r^2 \left(e^{-\beta U(r)} - 1 \right) ; \quad (4.53)$$

this can be identified with the definition eq. (4.52) to yield

$$g(r) \simeq \exp(-\beta U(r)) \simeq 1 - \beta U(r) , \quad (4.54)$$

which approximates $g(r)$ to first order, in the case of weak interactions in a dilute system. Hence we can identify $c(r)$ with a pair potential in combining eqs. (4.48) and (4.54):

$$c(r) \sim -\beta U(r) . \quad (4.55)$$

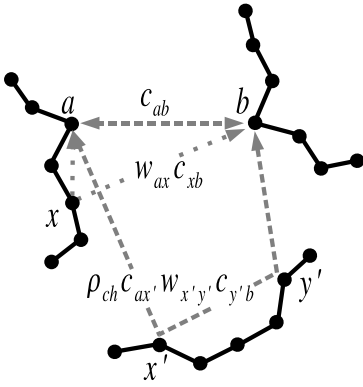


Figure 4.13: Schematic representation of a few examples of direct and indirect correlation functions entering the development of eq. (4.58). The direct correlation function $c_{ab}(q)$ relates sites a and b of two distinct chains i and j , as $w_{ax}c_{xb}$ also does via another site of the first chain. $\rho_{\text{ch}}c_{ax'}w_{x'y'}c_{y'b}$ corresponds to the indirect correlation function linking a and b of chain i and j via two sites x' and y' of a third chain k .

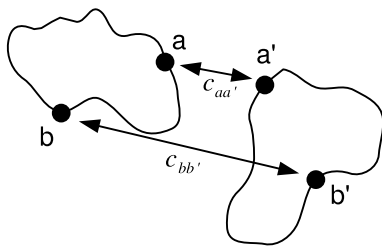


Figure 4.14: Schematic representation of the direct correlation functions in the case of ring polymers, showing that the different sites are equivalent, thus making the PRISM approximation exact:

$$c_{aa'} = c_{bb'} = c.$$

Extension to polymers: PRISM theory. For the description of polymers, as pointed out in sec. 4.1, the basic constituents of the system are more complex and one has to consider a generalization of eq. (4.42) which becomes eq. (4.7):

$$S_{ab}(q) = w_{ab}(q) + \rho_{\text{ch}}h_{ab}(q) \quad (4.56)$$

It is still possible to introduce direct correlation functions in this formalism, which will then take a tensorial character. These functions will be denoted by the matrix $\mathbf{c}(q)$, and their elements $c_{ab}(q)$. The generalized Ornstein-Zernike equation [40] introducing $\mathbf{c}(q)$ has been derived in the framework of Reference Interaction Site Model (RISM) [13, 14, 16], and reads:

$$\mathbf{h}(q) = \mathbf{w}(q)\mathbf{c}(q)\mathbf{w}(q) + \rho_{\text{ch}}\mathbf{w}(q)\mathbf{c}(q)\mathbf{h}(q) \quad (4.57)$$

This equation can be understood by an iterative development as in eq. (4.46):

$$\mathbf{h}(q) = \mathbf{w}\mathbf{c}\mathbf{w}(q) + \rho_{\text{ch}}\mathbf{w}\mathbf{c}\mathbf{w}\mathbf{c}\mathbf{w}(q) + \rho_{\text{ch}}^2\mathbf{w}\mathbf{c}\mathbf{w}\mathbf{c}\mathbf{w}\mathbf{c}\mathbf{w}(q) \dots \quad (4.58)$$

($\mathbf{w}\mathbf{c}\mathbf{w}(q)$ is simply a short-hand notation for $\mathbf{w}(q)\mathbf{c}(q)\mathbf{w}(q)$). An expansion of the first term yields

$$\mathbf{w}\mathbf{c}\mathbf{w}(q) = \sum_{x,y=1}^N w_{ax}(q)c_{xy}(q)w_{yb}(q) \quad (4.59)$$

$$= c_{ab}(q) + \sum_{\substack{x=1 \\ x \neq a}}^N w_{ax}c_{xb} + \sum_{\substack{y=1 \\ y \neq b}}^N c_{ay}w_{yb} \quad (4.60)$$

$$+ \sum_{\substack{x=1 \\ x \neq a}}^N \sum_{\substack{y=1 \\ y \neq b}}^N w_{ax}(q)c_{xy}(q)w_{yb}(q) \quad (4.61)$$

The first term of the last expression corresponds to the direct correlation between site a of a chain i and site b of a chain $j \neq i$ ($w_{aa}(q) = 1$ has been used). The second and third terms account for correlation between the same sites but mediated respectively via all possible sites x on the first chain or sites y on the second. The last term takes into account all other correlations mediated by both the sites x and y of the two chains. The other terms in the development of eq. (4.58) can be analyzed on the same basis, the factor ρ_{ch}^n corresponding to the number n of chains through which the a - b correlation is relayed. This is illustrated on fig. 4.13.

Combining this equation to the definition of eq. (4.56) gives an expression for $\mathbf{c}(q)$:

$$\rho_{\text{ch}}c_{ab}(q) = [w_{ab}^{-1}(q) - S_{ab}^{-1}(q)] \quad (4.62)$$

In order to simplify this general expression that implies to solve a system of N^2 equations, the adaptation of RISM to polymers (PRISM)

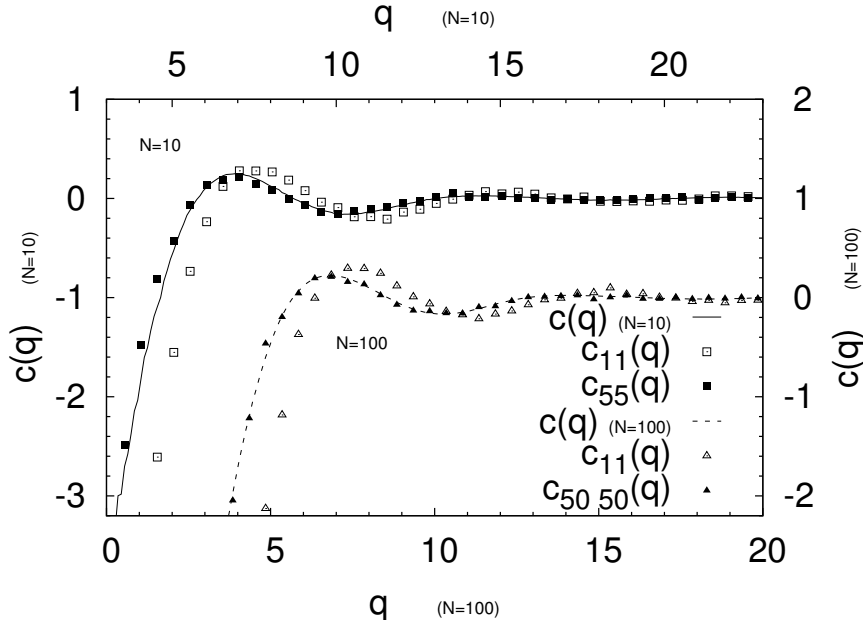


Figure 4.15: Comparison of the site-resolved direct correlation functions $c_{ab}(q)$ and the equivalent-site approximation $c(q)$ for CG-PVA ($N = 10$ and $N = 100$). End-end correlation functions [$c_{11}(q)$] show a large deviation from $c(q)$, whereas correlations for monomers lying at the center of chains are very well described by the PRISM approximation. The agreement with this approximation ameliorates with increasing chain length.

postulates that all sites of a polymer chain are equivalent—which is true for ring-polymers (see fig. 4.14) and a good approximation for very long chains in the case of which end effects tend to be negligible [108, 109]. This equivalent-site approximation can be formulated as

$$c_{ab}(q) = c(q) . \quad (4.63)$$

Using this approximation, eq. (4.57) becomes

$$h(q) = w(q)c(q)[w(q) + \rho_m h(q)] , \quad (4.64)$$

and the expression for the direct correlation functions reduces to [see eq. (4.47)]

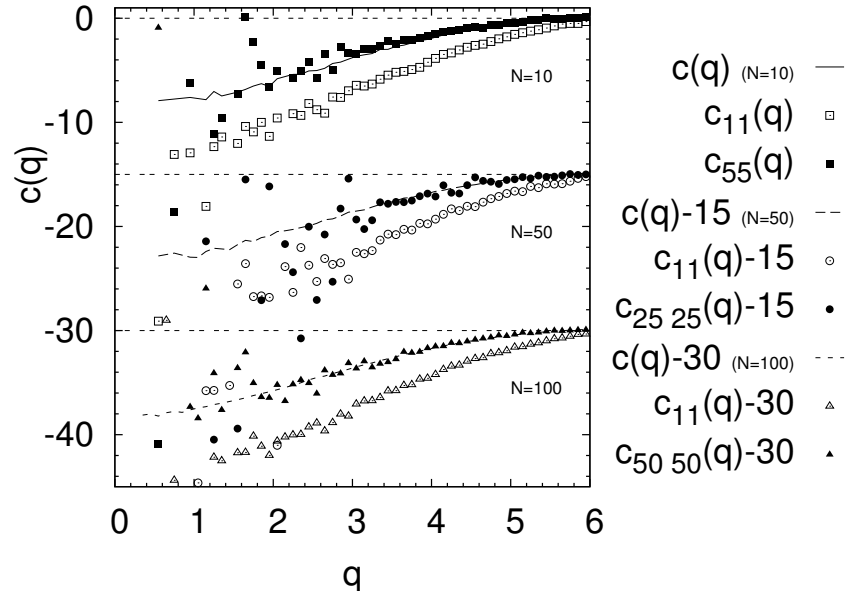
$$\rho_m c(q) = \frac{1}{w(q)} - \frac{1}{S(q)} . \quad (4.65)$$

Comparison with the simulation. The direct correlation functions were calculated from the simulation data, both in the framework of the PRISM approximation and with site-resolved details. Figures 4.15 and 4.16 show a comparison of the results which reveals a mismatch between $c_{ab}(q)$ and $c(q)$ when the chain ends are involved. Correlation functions for inner monomers on the contrary appear to have a behavior very close to what is predicted using the PRISM approximation of eq. (4.63). It is observed from the graphs that the agreement between $c_{N/2 N/2}(q)$ and $c(q)$ is better for longer chains, since the chain-end effects are much weaker.

Another interesting point is that the end-end correlation does not seem to be strongly influenced by the chain length; this indicates that the behavior of chain ends is independent of N .

This very crude estimate of eq. (4.55) is certainly not valid in the case of our dense melts, but it still provides an interpretation for the direct

Figure 4.16: Same comparison as presented in fig. 4.15, with a focus on the small- q regime. Results for $N = 50$ and $N = 100$ have been shifted for clarity; data for $N = 50$ are more affected by noise because of a too small box size which restricts the statistics. The deviation from the PRISM prediction $c(q)$ is seen clearly, and it is noticeable that there is no increase for longer chains. Center-center correlation functions [$c_{55}(q)$, $c_{25\ 25}(q)$ and $c_{50\ 50}(q)$] show a very good agreement with $c(q)$, which improves with increasing N since in a longer chain the center segments are not influenced by the chain ends anymore.



correlation function, whether for the simple-liquid or site-averaged $c(q)$ or for the site-dependent functions; in particular $c_{ab}(r)$ corresponds to an effective interaction potential between two monomers a and b . From our measurements of the Fourier transforms of $c_{ab}(r)$, we can observe that the extrapolated values of $c_{ab}(q)$ as $q \rightarrow 0$ are different for chain ends and centers:

$$c_{N/2\ N/2}(0) > c_{11}(0) . \quad (4.66)$$

Considering that the limit of $c_{ab}(q)$ for $q \rightarrow 0$ corresponds to the average value of the effective potential $c_{ab}(r)$ in direct space

$$\lim_{q \rightarrow 0} \frac{1}{V} c_{ab}(q) = \frac{1}{V} \int \mathbf{dr} c_{ab}(r) = \overline{c_{ab}} , \quad (4.67)$$

we arrive at the conclusion that

$$\overline{U_{N/2\ N/2}} < \overline{U_{11}} \quad (4.68)$$

i.e. the average (repulsive) potential describing the effective interaction between two particles is stronger for chain ends.

Another interpretation of the direct correlation function can be proposed from eq. (4.65), taking the $q \rightarrow 0$ limit:

$$\rho_m c(q) \xrightarrow{q \rightarrow 0} \frac{1}{N} - \frac{1}{k_B T \rho_m \kappa_T} , \quad (4.69)$$

since the form factor $w(q)$ approaches N at small wave vectors, and the limit value of the structure factor is related to the isothermal compressibility κ_T :

$$S(q \rightarrow 0) = \frac{\langle N^2 \rangle - \langle N \rangle^2}{\langle N \rangle} = k_B T \rho_m \kappa_T . \quad (4.70)$$

In the limit of long chains, the second term in eq. (4.69) becomes dominant over the first one, and therefore $c(q) \approx -1/(k_B T \rho_m^2 \kappa_T)$. As an

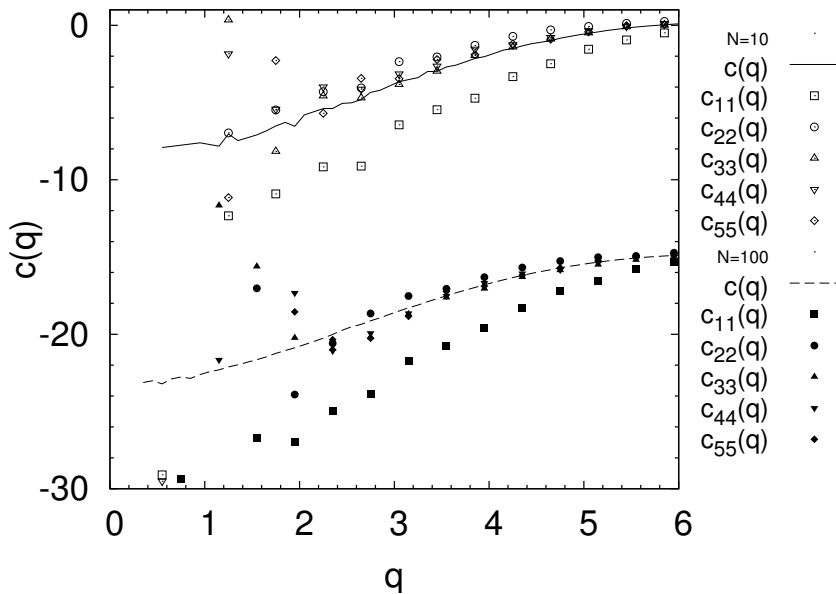


Figure 4.17: Comparison of the first $c_{aa}(q)$ elements of the direct correlation function tensor with the PRISM approximation $c(q)$. For both short and longer chains ($N = 10$ and $N = 100$, in the case of which data have been shifted by an amount of -15 for clarity), it is observed that end-end correlation strongly differ from $c(q)$. While $c_{11}(q)$ is lower than $c(q)$, $c_{22}(q)$ appears to have large values. For $c_{33}(q)$ already the asymptotic behavior is reached and $c_{aa}(q)$ is very close to $c(q)$, at least until the statistics is not sufficient (for $q \lesssim 2$). For longer chains, the collapse of the data on $c(q)$ is better since the end-effects are weaker.

extension of this approximation, the site-site direct correlation function can be expressed as:

$$c_{ab}(q) \sim -\frac{1}{\kappa_T^{ab}}, \quad (4.71)$$

as $q \rightarrow 0$, where κ_T^{ab} can be interpreted as a “site-dependent compressibility”. This yields the following expression for the direct correlation functions:

$$c_{N/2 N/2}(0) \sim -\frac{1}{\kappa_T^{N/2 N/2}} > c_{11}(0) \sim -\frac{1}{\kappa_T^{11}}, \quad (4.72)$$

which gives

$$\kappa_T^{N/2 N/2} > \kappa_T^{11}. \quad (4.73)$$

This corresponds to a larger “compressibility” of the monomers buried in the middle of the chains than those sitting at the ends, which is understandable since the end segments are less constrained by the binding potential than those in the center of the chains.

The validity of the PRISM approximation can be tested for the different elements $c_{ab}(q)$ of the direct correlation function tensor. It can be observed more precisely that all elements involving a chain end do not reproduce the PRISM prediction, whereas the convergence to $c(q)$ is quite fast for other elements; fig. 4.17 shows that $c_{aa}(q) \approx c(q)$ for $a \gtrsim 3$, and this effect appears to be independent of the chain length. The graph shows the small- q regime only, in which the variations of the functions appear more clearly. It could also be shown that the elements $c_{1a}(q)$ that involve one chain end do not converge to $c(q)$; even for $c_{1 N/2}(q)$, there is a large deviation between these two functions.

4.3.2 Intra-chain structure

The site-resolved intra-chain structure can be calculated for several models. We have already encountered a simple estimate of $w_{ab}(q)$,

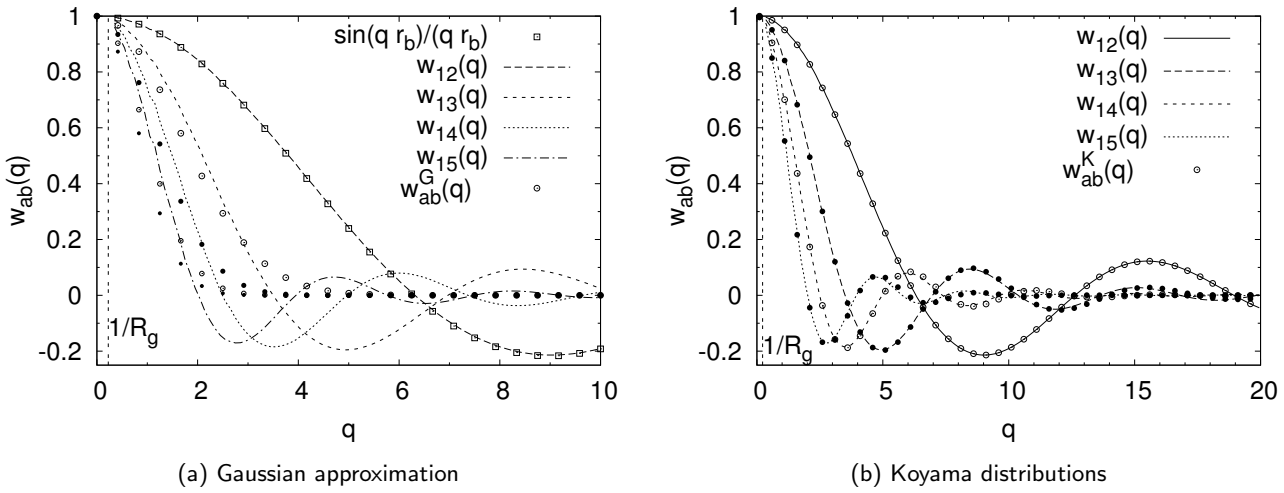


Figure 4.18: Comparison of the site-resolved structure factors to different approximations ($N = 100$). The gaussian approximation given in eq. (4.74) gives a description of the $q \rightarrow 0$ limit but breaks down very close to $q = 1/R_g$. The first element $w_{a, a+1}(q)$ is very well reproduced by the approximation of eq. (4.39). The Koyama distributions are used to describe the data for $w_{ab}(q)$ (fig. 4.18(b)); it appears that eq. (4.75) yields a very good approximation for all a and b .

provided by the gaussian approximation. It consists in assuming the distribution given by eq. (4.27) for the distance between two monomers a and b along the chain; the use of this distribution in eq. (4.9) yields the following expression:

$$w_{ab}^G(q) = \exp(-q^2|a-b|\ell^2/6), \quad (4.74)$$

As we mentioned it before, the squared statistical segment length ℓ^2 corresponds to $6R_g^2/N$. As suggested by fig. 4.5(a), this description of $w_{ab}(q)$ can only be valid for small q values, and thus only provides insight into the asymptotic behavior of the site-resolved structure factor. On the other hand our simulation data do not allow to accurately check the $q \rightarrow 0$ limit since the simulation box size defines a lower limit q_{\min} which is too high, as shown on fig. 4.18(a): The measured $w_{ab}(q)$ appear to depart from the gaussian approximation at very low q . However, the intra-chain structure factors $w_{ab}(q)$ appear to depend only on the difference $|a-b|$, as suggested by the gaussian expression; the data show only negligible differences for two functions $w_{ab}(q)$ and $w_{a'b'}(q)$ with $|a-b| = |a'-b'|$ (see fig. 4.19). The nearest-neighbor approximation of eq. (4.39) gives another expression that can be used to compare to the data obtained for $w_{a, a+1}(q)$: Fig. 4.18(a) also shows this approximation which describes the simulation data very well.

Another description of the detailed intra-chain structure can be obtained by using the Koyama distribution that was proposed as an approximation for the end-to-end distance distribution of a wormlike chain [57, 66]; this approach takes into account the deviations from the gaussian behavior by a non-gaussian parameter C_{ab}^2 (This coefficient is defined in ref. 40, for dynamical quantities). This parameter in turn determines A_{ab}^2 and B_{ab}^2 that enter the definition of $w_{ab}(q)$ in the

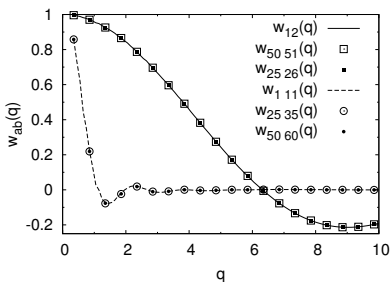


Figure 4.19: Independence of the site-resolved intra-chain structure factors $w_{a, a+n}(q)$ on a (CG-PVA, $N = 100$). The graph shows three different examples for $n = 1$ and $n = 10$, for pairs of monomers $(a, a+n)$ located in the chain end, chain center and in between. In both cases the data superimpose very well.

Koyama theory:

$$w_{ab}^K(q) = \frac{\sin B_{ab}q}{B_{ab}q} \exp(-A_{ab}^2 q^2) , \quad (4.75)$$

the coefficients are expressed as

$$C_{ab}^2 = \frac{1}{2} \left(5 - 3 \frac{\langle [\mathbf{r}^a - \mathbf{r}^b]^4 \rangle}{\langle [\mathbf{r}^a - \mathbf{r}^b]^2 \rangle^2} \right) \quad (4.76)$$

$$A_{ab}^2 = \frac{1 - C_{ab}}{6} \langle [\mathbf{r}^a - \mathbf{r}^b]^2 \rangle \quad (4.77)$$

$$B_{ab}^2 = C_{ab} \langle [\mathbf{r}^a - \mathbf{r}^b]^2 \rangle . \quad (4.78)$$

This approximation seems reasonable since it allows one to recover the two limit behaviors that can be derived for $w_{ab}(q)$: In the small- q regime, the gaussian approximation is reproduced, as for $q \rightarrow 0$ the sine prefactor tends to unity and $w_{ab}^K(q)$ reduces to the exponential:

$$w_{ab}^K(q) \xrightarrow{q \rightarrow 0} \exp(-A_{ab}^2 q^2) . \quad (4.79)$$

Equation (4.74) is recovered in this limit because the chains are gaussian on large length scales; $C_{ab} = 0$, $A_{ab}^2 = |a - b|\ell^2/6$ [cf. eq. (4.28)].

In the large- q limit, we already used the hypothesis according to which the nearest-neighbor contribution is predominant [eq. (4.37)]; for the Koyama approximation this implies that $\langle [\mathbf{r}^a - \mathbf{r}^b]^2 \rangle \approx b_0^2$, and thus the C_{ab} coefficient reduces to unity. In this case A_{ab} is zero, and the behavior of $w_{ab}^K(q)$ is dominated by the oscillations imposed by the sinusoidal part of eq. (4.75):

$$w_{ab}^K(q) \underset{q \rightarrow \infty}{\sim} \frac{\sin B_{ab}q}{B_{ab}q} . \quad (4.80)$$

These coefficients were computed from the simulations at $T = 1$ and characterize the static conformation of the chains. A comparison of $w_{ab}(q)$ and $w_{ab}^K(q)$ is presented in fig. 4.18(b); it can be observed that the intra-chain structure is very well reproduced by eq. (4.75), for all a and b pairs. Small deviations are observed for the shortest chains, in the case of the most remote monomers, i.e. as $|a - b| \rightarrow N - 1$. This means that the intra-chain structure of the polymers in the melt can be very accurately predicted using only the two moments $\langle [\mathbf{r}^a - \mathbf{r}^b]^2 \rangle$ and $\langle [\mathbf{r}^a - \mathbf{r}^b]^4 \rangle$.

As the Koyama approximation works fine to describe the site-resolved structure factors, it is expected that it also yields a satisfactory description of the site-averaged quantity $w(q)$, since the latter is only the sum of all the site-resolved $w_{ab}(q)$:

$$w^K(q) = \sum_{a,b=1}^N w_{ab}^K(q) . \quad (4.81)$$

Figures 4.81 and 4.21 show that this expectation is well borne out for the small- and large- q limits.

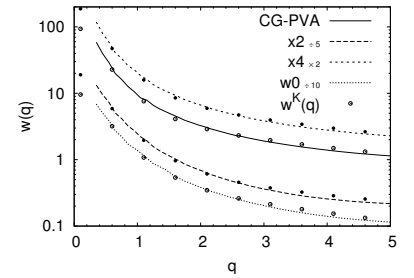


Figure 4.20: Large q limit of the comparison of $w(q)$ and $w^K(q)$; using the Koyama approximation, the gaussian description is recovered for $q \rightarrow 0$ [eq. (4.79)] and thus $w^K(q)$ yields a good approximation of the intra-chain structure factor in the small q regime. The curves for the different models have been shifted for clarity (the respective factors used are displayed next to the model names).

Figure 4.21: Comparison of the intra-chain structure factors for different models and the corresponding site-averaged Koyama approximations. For the models other than CG-PVA, the $w(q)$ and $w^k(q)$ have been offset by an amount indicated in parenthesis next to the model name. For intermediate q vectors there are deviations from the behavior predicted by the Koyama approximation [eq. (4.81)], but for small (see fig. 4.20) and large wave vectors (cf. inset where data are presented for $0 < q < 50$ in the case of CG-PVA), the agreement is good.

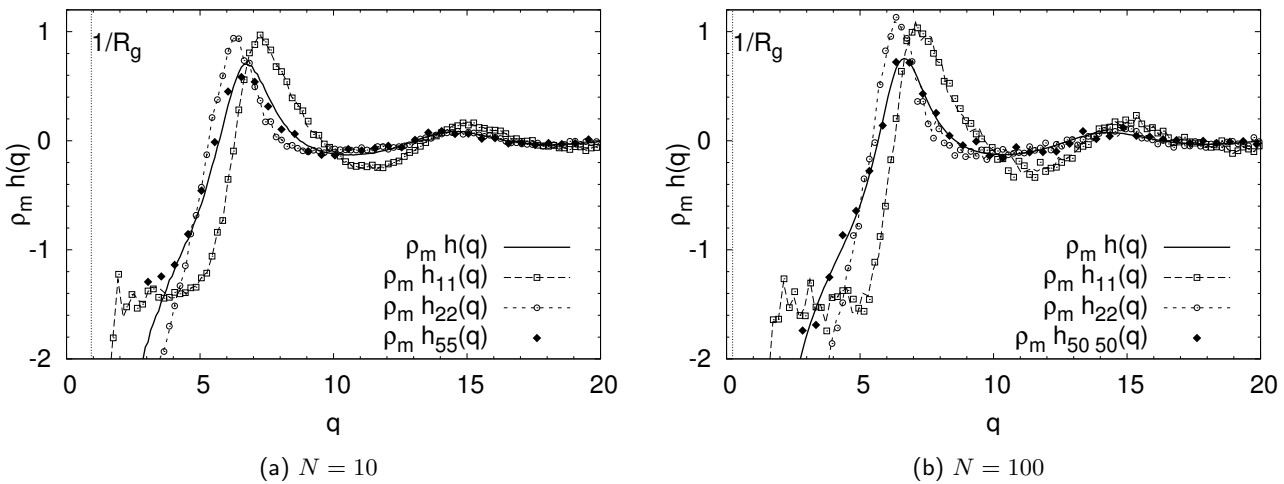
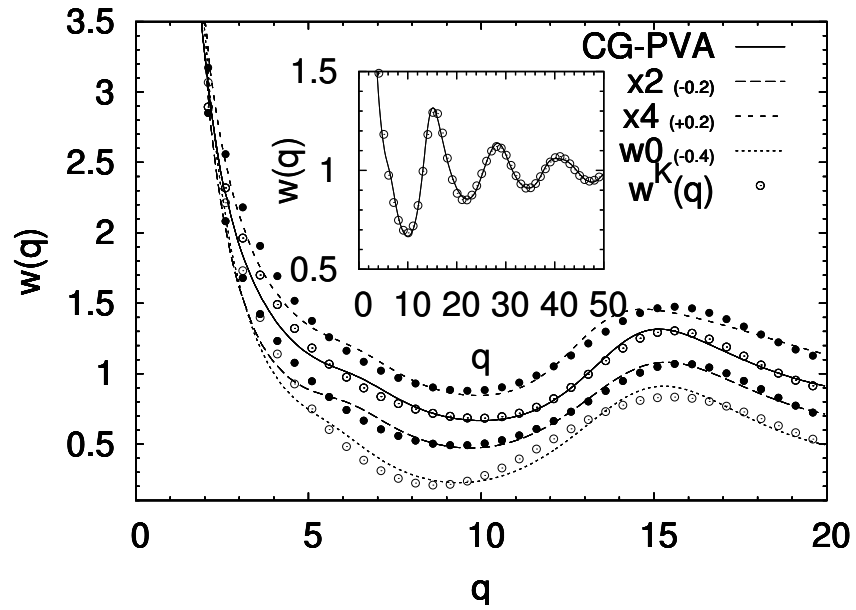


Figure 4.22: Averaged and site-resolved inter-chain structure factors for CG-PVA; two different chain lengths are considered. The first elements of the $h_{ab}(q)$ tensor (corresponding to chain ends) exhibit strong deviations from the behavior indicated by $h(q)$; from $a = 3$ on, the data for $h_{aa}(q)$ collapse on the average $h(q)$ as the chain-end effects vanish. For middle segments ($c_{11}(q)$ for $N = 10$ and $c_{50\ 50}(q)$ for $N = 100$), one can observe a good agreement with $c(q)$. This agreement is better for longer chains though.

4.3.3 Inter-chain structure

The site-resolved inter-chain structure factors have features similar to what is obtained for the site-averaged $h(q)$, with a few differences showing up around the first peaks (cf. fig. 4.22). Again the chain-end effects are responsible for these deviations, and for two monomers a and b that are far enough from the chain ends they are negligible, i.e. $h_{ab}(q) \approx h(q)$. For a and b close to the chain ends, the peaks are slightly shifted horizontally. Figure 4.22 presents a comparison of $h_{aa}(q)$ and $h(q)$; it is observed that for end-end correlations $[h_{11}(q)]$, the main peak is shifted to higher q -values and a prominent shoulder is visible before the correlation hole as $q \rightarrow 0$; this corresponds to a stronger repulsive interaction between end monomers. For $h_{22}(q)$, the peak is shifted in the opposite direction and the shoulder vanishes; these opposite trends for $h_{11}(q)$ and $h_{22}(q)$ correspond to what was already pointed out from the study of direct correlation functions in fig. 4.17.

We may attempt to interpret these observations more quantitatively within the framework of the PRISM theory. An expression for $h_{ab}(q)$ involving only intra-chain correlations and site-average quantities can be found from the Ornstein-Zernike equation (4.57), using the PRISM approximation of eq. (4.63):

$$h_{ab}(q) = \sum_{x,y=1}^N w_{ax}(q) c_{xy}(q) [w_{yb}(q) + \rho_{\text{ch}} h_{yb}(q)] \quad (4.82)$$

$$= c(q) \left(\sum_{x=1}^N w_{ax}(q) \right) \left[\sum_{y=1}^N w_{yb}(q) + \rho_{\text{ch}} \sum_{y=1}^N h_{yb}(q) \right]. \quad (4.83)$$

Using the fact that $h_{ab}(q) = h_{ba}(q)$ (all the tensors used here are symmetric), it is possible to express the last term [eq. (4.57) is used again]:

$$\sum_{y=1}^N h_{yb}(q) = \sum_{b=1}^N h_{yb}(q) \quad (4.84)$$

$$= \sum_{b=1}^N \left\{ \sum_{u,v=1}^N w_{yu}(q) c_{uv}(q) [w_{vb}(q) + \rho_{\text{ch}} h_{vb}(q)] \right\} \quad (4.85)$$

$$= c(q) \left(\sum_{u=1}^N w_{yu}(q) \right) \left\{ \sum_{b,v=1}^N [w_{vb}(q) + \rho_{\text{ch}} h_{vb}(q)] \right\} \quad (4.86)$$

$$= c(q) \left(\sum_{u=1}^N w_{yu}(q) \right) NS(q) \quad (4.87)$$

$$= Nc(q)S(q) \left(\sum_{y=1}^N w_{yb}(q) \right). \quad (4.88)$$

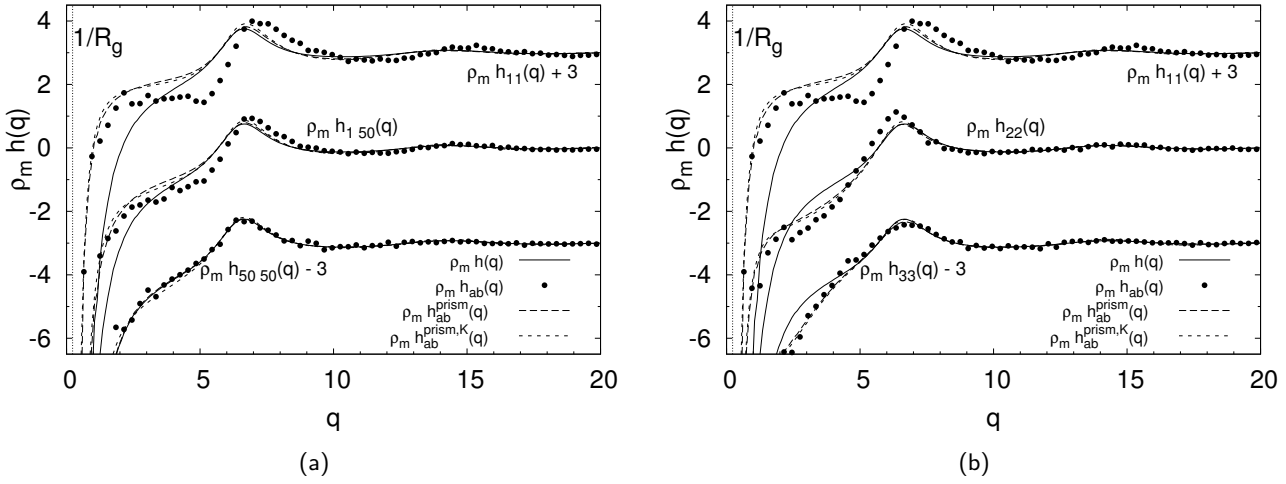


Figure 4.23: Comparison of the site-site inter-molecular pair-correlation functions $h_{ab}(q)$ determined from the simulation data (CG-PVA, $N = 100$) and from the PRISM theory. Some curves are shifted vertically for clarity. It can be seen that the behavior of $h_{ab}(q)$ is only approximately reproduced by the prism estimate $h_{ab}^{\text{prism}}(q)$, but this rapidly improves as a and b increase: For $a = b = 3$, the approximation is already accurate.

From eq. (4.64) one has $c(q)S(q) = h(q)/w(q)$; then, with $\rho_m = N\rho_{\text{ch}}$:

$$h_{ab}(q) = c(q) \left(\sum_{x=1}^N w_{ax}(q) \right) \left(\sum_{y=1}^N w_{yb}(q) \right) [1 + N\rho_{\text{ch}}S(q)c(q)] \quad (4.89)$$

$$= c(q) \left(\sum_{x=1}^N w_{ax}(q) \right) \left(\sum_{y=1}^N w_{yb}(q) \right) \left[1 + \rho_m \frac{h(q)}{w(q)} \right], \quad (4.90)$$

which leads to the final results

$$h_{ab}(q) = \frac{h(q)}{w(q)^2} \left[\sum_{x=1}^N w_{ax}(q) \right] \left[\sum_{y=1}^N w_{yb}(q) \right]. \quad (4.91)$$

Figure 4.23(a) presents a comparison of this approximation and the measured $h_{ab}(q)$, showing a good agreement, with still some deviations for chain ends. As was observed in the case of the direct correlation functions (fig. 4.17), the functions $h_{ab}(q)$ which involve a chain end (a and/or b equals 1) always deviate from the PRISM behavior, whereas other correlation functions are well described; here again the structure factors $h_{aa}(q)$ converge quickly to the PRISM approximation $h_{aa}^{\text{prism}}(q)$ (from $a = 3$ on, see fig. 4.23(b)).

Since the Koyama distribution [eq. (4.75)] used in fig. 4.18(b) proved to be a very good approximation for $w_{ab}(q)$, it is interesting to try and compute the inter-chain structure factor by inserting $w_{ab}^{\text{K}}(q)$ into the PRISM expression for $h_{ab}(q)$; the function $h_{ab}^{\text{prism,K}}(q)$ thus obtained is shown in fig. 4.23(a) and exhibits only very small deviations from $h_{ab}^{\text{prism}}(q)$. This indicates that the site-resolved information about a polymer melt can be approximated with good accuracy using both the PRISM approximation and the Koyama distribution; doing so, it is possible to reproduce from the site-averaged quantities $w(q)$ and $h(q)$ the

more detailed $w_{ab}^K(q)$ using eq. (4.75) and $h_{ab}^{\text{prism},K}(q)$ using eq. (4.91). The complete site-resolved data are then obtained from the inter- and intra-chain decomposition of the site-averaged structure factor $S(q)$ and the first two moments of the distributions of distances between monomers, $|\mathbf{r}^a - \mathbf{r}^b|$. These quantities are much easier to compute than the site-resolved structure factors that require to be averaged over many uncorrelated configurations.

Using either the Koyama distribution approximation from eq. (4.75) or the simulation data for site-resolved intra-chain structure factors, it is then possible to predict the site-resolved inter-chain structure using the PRISM theory [eq. (4.91)]; this works well except for the correlations between monomers including the chain ends, and improves rapidly as the considered monomers are taken deeper inside the chain.

4.4 Structure factors involving the center of mass

It is interesting to consider the correlations between the centers of mass of the different chains, since the interactions between the monomers could mediate an effective force that would influence the overall relative motion of the polymers coils. In order to probe these effective interactions in the melt, we computed the structure factor of the centers of mass (CM) as defined in eq. (4.17); the results can be analyzed in comparison with a theoretical estimate using the PRISM approximation. Here, we will first briefly sketch the theory developed by Krakoviak and then compare to the simulation results [59].

PRISM theory for the CM. The PRISM approximation is obtained by considering the center of mass of one chain as a new site whose interactions with the monomers and itself are described by a generalization of the quantities we used to account for the structure of the melt: The structure factor and related functions are now 2×2 matrices whose elements correspond to monomer-monomer, CM-CM and monomer-CM correlations. They are defined as follows:

$$\tilde{S} = \begin{pmatrix} \tilde{S}_{m,m} & \frac{1}{\sqrt{N}}\tilde{S}_{m,\text{CM}} \\ \frac{1}{\sqrt{N}}\tilde{S}_{m,\text{CM}} & \tilde{S}_{\text{CM},\text{CM}} \end{pmatrix}, \quad \tilde{w} = \begin{pmatrix} \tilde{w}_{m,m} & \frac{1}{\sqrt{N}}\tilde{w}_{m,\text{CM}} \\ \frac{1}{\sqrt{N}}\tilde{w}_{m,\text{CM}} & \tilde{w}_{\text{CM},\text{CM}} \end{pmatrix}, \quad (4.92)$$

$$\tilde{h} = \begin{pmatrix} N\tilde{h}_{m,m} & \sqrt{N}\tilde{h}_{m,\text{CM}} \\ \sqrt{N}\tilde{h}_{m,\text{CM}} & \tilde{h}_{\text{CM},\text{CM}} \end{pmatrix}, \quad \tilde{c} = \begin{pmatrix} N\tilde{c}_{m,m} & \sqrt{N}\tilde{c}_{m,\text{CM}} \\ \sqrt{N}\tilde{c}_{m,\text{CM}} & \tilde{c}_{\text{CM},\text{CM}} \end{pmatrix}. \quad (4.93)$$

The correspondence between the above matrix elements and the previously defined structure functions is given by the following relations

(see sec. 4.1):

$$\begin{aligned} \tilde{S}_{m,m} &= S, & \tilde{w}_{m,m} &= w, & \tilde{h}_{m,m} &= h, \\ \tilde{S}_{m,CM} &= S_{m,C}, & \tilde{w}_{m,CM} &= w_{m,C}, & \tilde{h}_{m,CM} &= h_{m,C}, \\ \tilde{S}_{CM,CM} &= S_C, & \tilde{w}_{CM,CM} &= 1, & \tilde{h}_{CM,CM} &= h_C. \end{aligned} \quad (4.94)$$

The correlation function matrices obey the two relations generalized from eqs. (4.45) and (4.57):

$$\rho_{\text{ch}}\tilde{c}(q) = \tilde{w}^{-1}(q) - \tilde{S}^{-1}(q), \text{ and} \quad (4.95)$$

$$\tilde{h}(q) = \tilde{w}(q)\tilde{c}(q) \left[\tilde{w}(q) + \rho_{\text{ch}}\tilde{h}(q) \right]. \quad (4.96)$$

Using the definitions of eq. (4.92) to compute eq. (4.95), the elements of the direct correlation function read

$$\rho_{\text{ch}}\tilde{c}_{m,m} = \frac{1}{w - \frac{w_{m,C}^2}{N}} - \frac{1}{S - \frac{S_{m,C}^2}{NS_C}}; \quad (4.97)$$

$$\rho_{\text{ch}}\tilde{c}_{m,CM} = -\frac{1}{\sqrt{N}} \frac{w_{m,C}}{w - \frac{w_{m,C}^2}{N}} + \frac{1}{\sqrt{N}} \frac{S_{m,C}}{SS_C - \frac{S_{m,C}^2}{N}}; \quad (4.98)$$

$$\rho_{\text{ch}}\tilde{c}_{CM,CM} = \frac{1}{1 - \frac{w_{m,C}^2}{Nw}} - \frac{1}{S_C - \frac{S_{m,C}^2}{NS}}. \quad (4.99)$$

It can be assumed that the centers of mass of the chains neither interact with each other nor with the monomers, meaning that the only non-zero element of $\tilde{c}(q)$ is $\tilde{c}_{m,m}$. This simplification allows to find a simple relation between the center-of-mass related quantities: The lhs of eqs. (4.98) and (4.99) are zero, which leads to:

$$S_{m,C} = \frac{S}{w} w_{m,C}; \quad (4.100)$$

this relation inserted into eq. (4.97) in turn yield an expression for the center-of-mass structure factor:

$$S_C(q) = 1 + \frac{1}{N} \frac{w_{m,C}^2}{w^2} \rho_m h(q), \quad (4.101)$$

where eq. (4.13) has been used.

Comparison with the simulation. Figure 4.24 shows the CM structure factor $S_C(q)$ for different chain lengths; it can be seen that the approximation of eq. (4.101) reproduces the simulation data quite well; there seems to be a small deviation for the shortest chains $N = 10$ for $2 \lesssim q \lesssim 3$, but on the other hand the data for longer chains exhibit more noise; so, it is hard to decide whether the shoulder vanishes for large N . The data show a smooth increase of the structure factor, from a low value that corresponds to the isothermal compressibility (since $\lim_{q \rightarrow 0} S_C(q) = \frac{\langle n^2 \rangle - \langle n \rangle^2}{\langle n \rangle} \sim \kappa_T/N$) to 1 which is the ideal gas value.

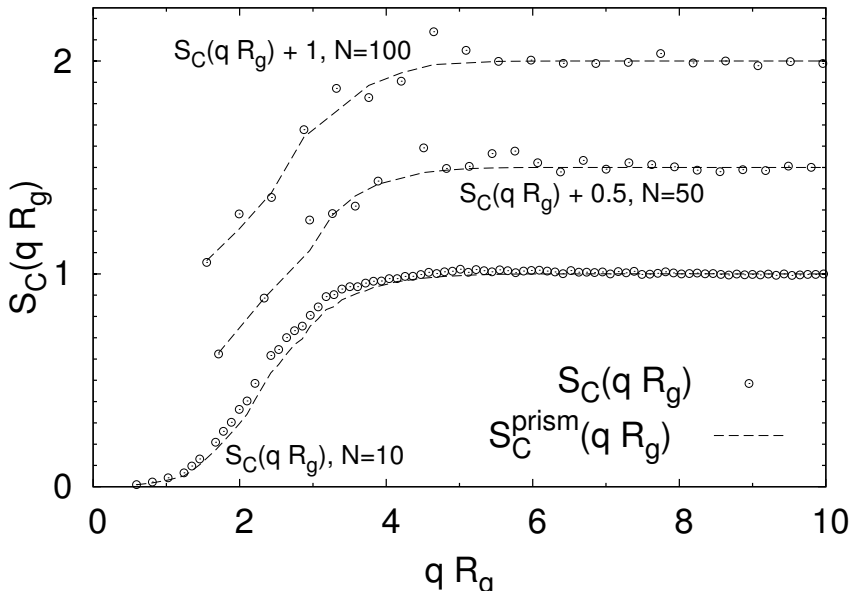


Figure 4.24: S_C as a function of qR_g for $N = 10$, $N = 50$ and $N = 100$ (CG-PVA). Data for the longer chains have been shifted vertically. Lines correspond to S_C^{prism} , the approximation given in eq. (4.101); except for a small deviation at intermediate q for $N = 10$ and noise in the case of $N = 50$ and $N = 100$, the simulation data show a good agreement with this estimate.

The factor $\frac{w_{m,c}}{w}$ that appears in eq. (4.101) depends on intra-chain correlations only, and can be compared to a gaussian approximation; to do so we use the following expression for the monomer a -CM structure factor [106, 137]:

$$w_{a,c}^G(q) = \exp\left(-\frac{q^2 R_g^2}{3} \left[1 - 3\frac{a}{N} + 3\left(\frac{a}{N}\right)^2\right]\right) \quad (4.102)$$

This approximation allows to calculate the average monomer density about the center of mass:

$$w_{m,c}^G(q) = \sum_{a=1}^N w_{a,c}^G(q) \quad (4.103)$$

$$= N \int_0^1 dx w_C^G(x, q) \quad (4.104)$$

$$= \frac{N\sqrt{\pi}}{qR_g} e^{-q^2 R_g^2/12} \text{erf}(qR_g/2), \quad (4.105)$$

with

$$w_C^G(x, q) = \exp\left(-\frac{q^2 R_g^2}{3} [1 - 3x + 3x^2]\right) \quad (4.106)$$

and $\text{erf}(x)$ denoting the error function $(2/\sqrt{\pi}) \int_0^x dt \exp(-t^2)$. The gaussian estimate for the ratio $w_{m,c}(q)/w(q)$ is obtained by dividing eq. (4.106) by the Debye function $w_D(q)$ from eq. (4.33).

Figure 4.25 presents the simulation results for the ratio $w_{m,c}(q)/w(q)$ along with the gaussian approximation $w_{m,c}^G(q)/w_D(q)$. The latter reproduces qualitatively the features of the data measured from the simulations, the agreement becoming better as the chain length increases.

The expression given in eq. (4.102) can also be tested directly with measurements of $w_{a,c}^G(q)$; this is what is shown in fig. 4.26 for chains consisting of 100 monomers; the two extreme cases ($a = 1$ and $a = 50$)

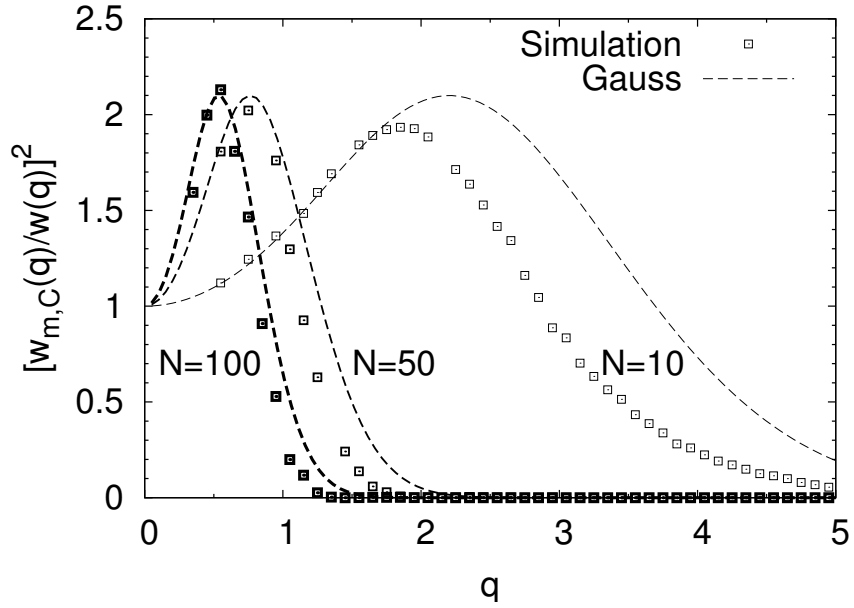


Figure 4.25: Comparison of measured value and gaussian estimate for the ratio $(w_{m,c}(q)/w(q))^2$, for different chain lengths. It can be seen that the agreement gets better as N increases from 10 to 100: As expected, the gaussian description becomes valid in the limit of long chains.

are well reproduced by the gaussian approximation, as well as the intermediate $a = 25$. Figure 4.26 also presents the total correlation function $S_{a,c}(q)$ and the inter-chain contribution $h_{a,c}(q)$; the latter has a low value at $q \rightarrow 0$, so as to compensate $w_{a,c}(q)$ and yield an almost zero value of $S_{a,c}(q)$. This is expected since $S_{a,c}(q)$ corresponds to the probability of finding a monomer of one chain at a distance of its center of mass, which must tend to 0 as the distance increases (or $q \rightarrow 0$). Accordingly, the correlation between a monomer of chain i and the center of mass of the same chain is high ($w_{a,c}(q) \xrightarrow{q \rightarrow 0} 1$), while the correlation with the center of mass of chain $j \neq i$ is small ($\rho_{ch} h_{a,c}(q) \xrightarrow{q \rightarrow 0} 0$). This explains the tendency exhibited by $S_{a,c}(q)$ for low q values, but this function shows a more complicated behavior for intermediate q values (for $q \gtrsim 2$, all monomer-CM correlation functions tend to 0): There is a dependence on the position of monomer a inside the chain. If a is an end monomer, $S_{a,c}(q)$ exhibits a minimum at $q \approx 0.6$ whereas for middle segments a maximum is observed. This means that there is an intermediate distance at which the intramolecular correlations are either overcompensated by the inter-chain correlations in the case of middle monomers, or undercompensated for chain ends.

It is possible to find an expression which approximates the monomer-CM inter-chain correlation function $h_{a,c}(q)$ in the framework of the PRISM theory and the decomposition into monomer and CM elements of the structure factors that was used to find an estimate of $S_c(q)$ [eq. (4.101)]. This is done by taking $a = c$ in eq. (4.91) and applying the PRISM approximation $c_{ab}(q) = c(q)$:

$$h_{ab}(q) = \sum_{x,y=1}^N w_{ax}(q) c_{xy}(q) [w_{yb}(q) + \rho_{ch} h_{yb}(q)] \quad (4.107)$$

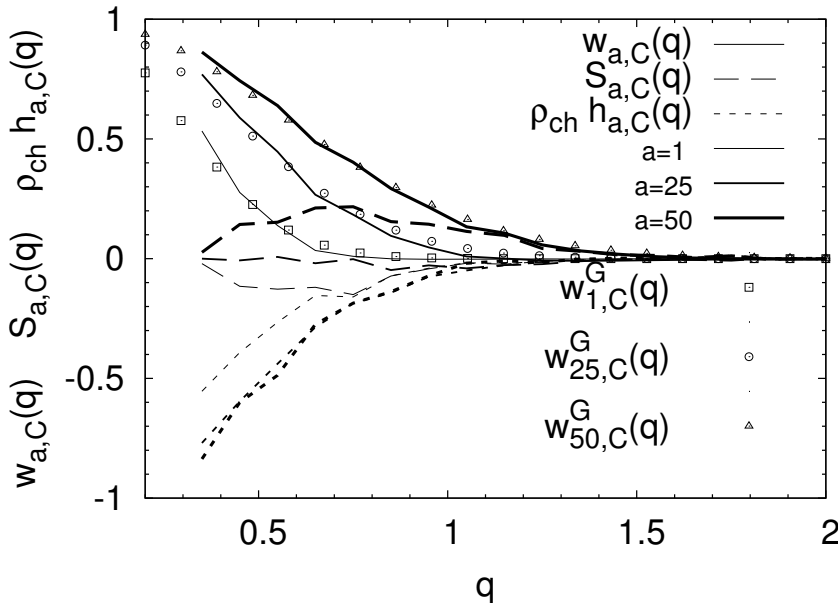


Figure 4.26: Monomer-CM correlation functions measured for the CG-PVA model, chain length $N = 100$. Results are presented for three different positions along the backbone of the chain, $a = 1$ (chain end), $a = 50$ (middle segment) and $a = 25$ (intermediate). The gaussian approximation given in eq. (4.102) provides a good estimate for the intra-chain function $w_{a,c}(q)$, for all values of a . The total structure factors $S_{a,c}(q)$ exhibit much different behaviors according to the position of the monomer: In both the small- and large- q limits the function tends to zero, meaning there is no correlation between monomers and centers of mass; on the other hand for chain ends there is a minimum at intermediate q vectors ($q \approx 0.6$) and a maximum in the case of middle segments. For intermediate monomers ($a = 25$), there is no significant structure.

becomes

$$h_{a,c}(q) = c(q) \left(\sum_{x=1}^N w_{ax}(q) \right) \left[\underbrace{\sum_{y=1}^N w_{y,c}(q)}_{w_{m,c}(q)} + \rho_{ch} \underbrace{\sum_{y=1}^N h_{y,c}(q)}_{Nh_{m,c}(q)} \right] \quad (4.108)$$

$$= \frac{h(q)}{w(q)S(q)} \left(\sum_{x=1}^N w_{ax}(q) \right) [w_{m,c}(q) + \rho_m h_{m,c}(q)] \quad (4.109)$$

$$= \frac{h(q)S_{m,c}(q)}{w(q)S(q)} \left(\sum_{x=1}^N w_{ax}(q) \right), \quad (4.110)$$

where eq. (4.64) has been used to express $c(q)$. Using eq. (4.100) for $S_{m,c}$, we obtain

$$h_{a,c}(q) = \frac{w_{m,c}(q)}{w(q)^2} \left(\sum_{x=1}^N w_{ax}(q) \right) h(q). \quad (4.111)$$

It can be checked in fig. 4.27 that this estimate yields a very good approximation to the measured $h_{a,c}(q)$; the agreement does not appear to depend strongly on the chain length, nor on the position along the chain, a . This shows again that the inter-chain correlations are well described by site-independent approximations.

Figure 4.27: Monomer-CM inter-chain structure factor, for several sites and two chain lengths (CG-PVA). Lines correspond to the estimate of PRISM theory presented in eq. (4.111); a very good agreement is found with the simulation data independently of the position along the chain ($a = 1$: chain end; $a = N/2$: middle segment; and an intermediate value: $a = 3$ for $N = 10$, $a = 25$ for $N = 100$). There is still a slight deviation of the simulation data from the predicted behavior in the case of short chains, that seems to vanish for $N = 100$.

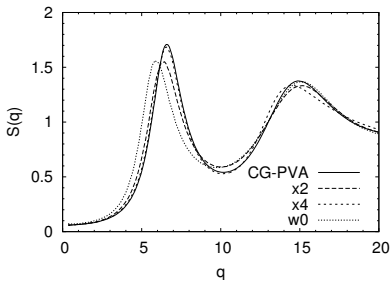
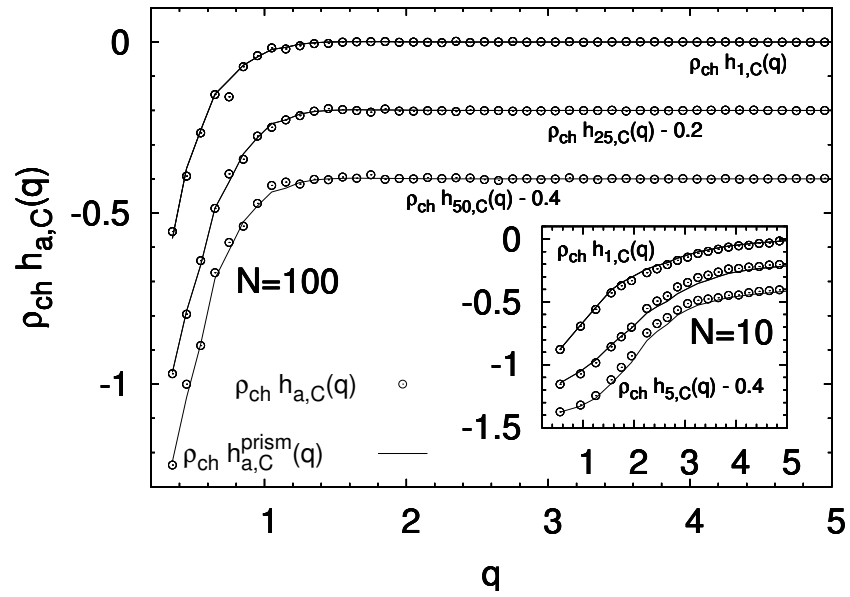


Figure 4.28: Structure factors at high temperature ($T = 1$) for four different models (fig. 4.8)

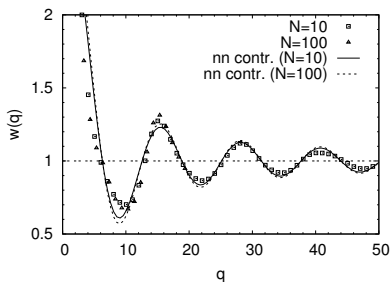


Figure 4.29: Intra-chain structure and nearest-neighbor approximation (fig. 4.5(b)).

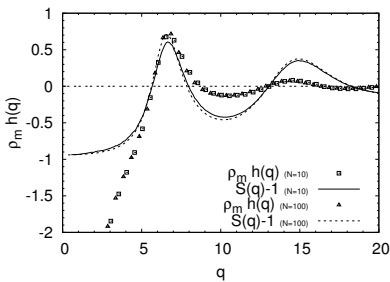


Figure 4.30: Inter-chain and total structure factors (fig. 4.6(a)).

4.5 Summary

Detailed structure factors for different models have been computed at high temperature (fig. 4.28). It would have been also very interesting to investigate low-temperature structure factors with this detailed approach, but this is more difficult as a result of the great number of configurations needed to yield satisfactory statistics. And still, this study of the detailed structure of the melts at high temperature was triggered by the observation that high- T properties seem to influence the low- T phase (fig. 3.47).

As was suggested by the analysis of the crystallization observed for the different models, a distinction was made between *intra*- and *inter*-chain quantities, which were calculated in addition to the total structure factors. However, no clear evidence for a high propensity to crystallize could be isolated from the data computed at high temperature; all models showed qualitatively identical features.

The observed structure can be rationalized by comparing the simulation data with limiting behaviors: The intra-chain structure $w(q)$ is well-described by the gaussian approximation at small q , and by a nearest-neighbor approximation at large q (fig. 4.29). The inter-chain structure $h(q)$ determines the first peak in the total structure factor $S(q)$ as the packing in the melt is controlled by chain-chain interactions, and only slightly influences the global structure at higher wave vectors (fig. 4.30).

The more detailed structure of the simulated polymer melts can be accessed by the computation of site-resolved quantities $S_{ab}(q)$, $w_{ab}(q)$ and $h_{ab}(q)$ depending on the positions of monomers a and b . The correlations between these monomers are conveniently studied by the introduction of direct correlation function $c_{ab}(q)$ from the Ornstein-Zernike formalism; the Polymer-RISM approximation suggests that for

long chains the correlations between monomers a and b do not depend on their position, and thus $c_{ab}(q) = c(q)$. This is verified in the case of our simulations, even though the investigated systems only involve relatively short chains ($N \leq 100$), except in the case of chain ends for which there is a clear difference. These differences do not depend on the chain length (fig. 4.31).

Again the intra- and inter-chain structures can be studied separately; it is shown that for our CG models with an explicit angular potential constraining the flexibility of the chains, the Koyama approximation taking into account the chains' non-gaussianity provides a very good description of the site-resolved intra-chain structure (fig. 4.32). The inter-chain structure can be predicted in a good approximation (except for chain ends as expected) in the framework of the PRISM theory (fig. 4.33).

Quantities involving the center of mass (CM) of the chains have also been calculated, showing a good agreement with the PRISM theory for the CM-CM structure factors (fig. 4.34) and the inter-chain monomer-CM structure, whereas the gaussian approximation is shown to yield a good description of the intra-chain monomer-CM structure which improves with longer chain lengths (fig. 4.35).

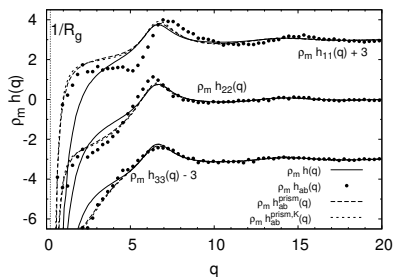


Figure 4.33: Comparison of the site-resolved inter-chain structure factors to the PRISM approximation (fig. 4.23(b)).

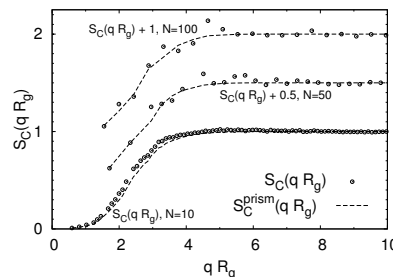


Figure 4.34: Center-of-mass structure factor for different chain lengths (fig. 4.24)

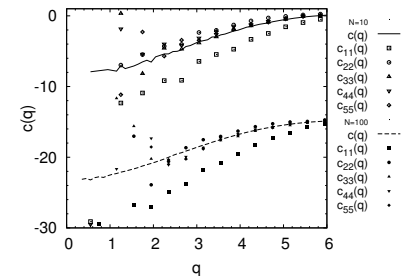


Figure 4.31: Comparison of the first $c_{aa}(q)$ elements with the PRISM approximation $c(q)$ (fig. 4.17).

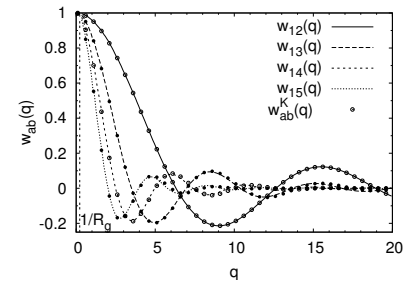


Figure 4.32: Comparison of the site-resolved structure to the Koyama approximation (fig. 4.18(b)).

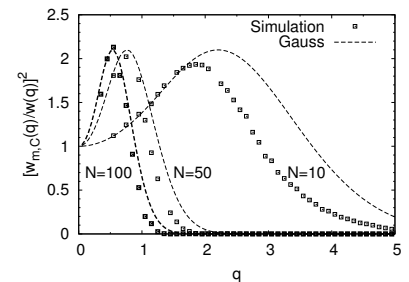


Figure 4.35: Comparison of the monomer-CM structure factor with the gaussian approximation (fig. 4.25).

Conclusion

Summary

In this thesis, we examined the crystallization and melting of a variety of polymer models. We summarize here the most important results obtained, and finally give ideas about how to benefit from this insight to address open questions in future studies.

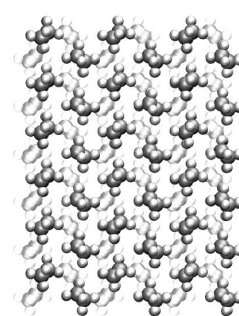
Simulation methods

We want to get insight into the crystallization *process* in polymer melts and thus used molecular dynamics simulations to follow the time evolution during heating of crystalline states, during cooling of the melt, or during isothermal relaxation after a quench of the melt.

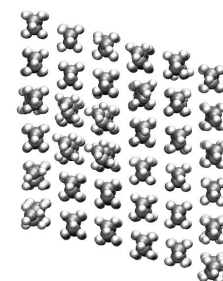
n-alkanes

Atomistically detailed models are needed to reproduce realistic chain packing in crystalline structures with computer simulations as they can be observed in experiments. The use of a simulation model that describes all the atoms of the considered molecules *explicitly* seems necessary to yield the precise characteristics of polymer crystals. In order to test this kind of method, we created configurations that mimic the structure of short *n*-alkane chains and simulated their melting process from the low temperatures up to the occurrence of the liquid state. These simulations allowed us to probe the validity of the all-atom model, showing that even a “simple” model aimed at reproducing the features of a liquid may be suited to describe the solid state of a polymeric system to a reasonable extent.

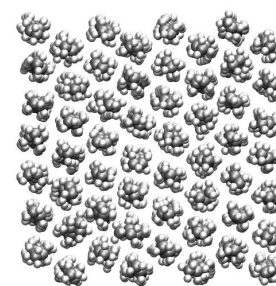
We used this model to simulate several phases that have been observed experimentally in the case of *n*-alkanes (C_nH_{2n+2}), since these systems are known to produce a great wealth of different structures at low temperature; we were particularly interested in a transitory phase that exists between the (low-temperature) solid and liquid states, which has been extensively studied experimentally and that was reproduced in our simulations (fig. c.1). This “rotator” phase occurs after a solid–solid phase transition in the course of melting, in the case both the orthorhombic and the triclinic crystals that we have been studying (fig. c.2); it is observed that continuous heating and isothermal



(a) Orthorhombic



(b) Triclinic



(c) Rotator

Figure c.1: Snapshots from simulations of the different crystal structures of *n*-alkanes.

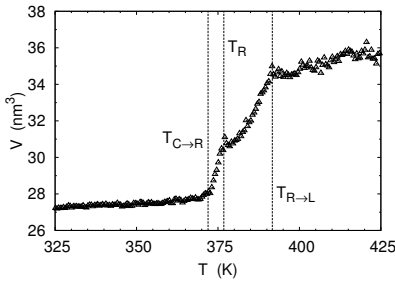


Figure c.2: Phase diagram (volume as a function of temperature) for $C_{15}H_{32}$ showing the different phase transitions observable during melting of the orthorhombic structure: crystal–rotator and rotator–liquid.

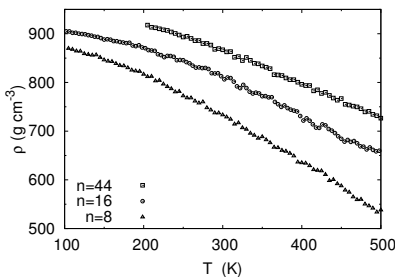


Figure c.3: Density as a function of temperature for n -alkanes with different chainlength. No jump characteristic of the crystallization is observed, as systems rather freeze.

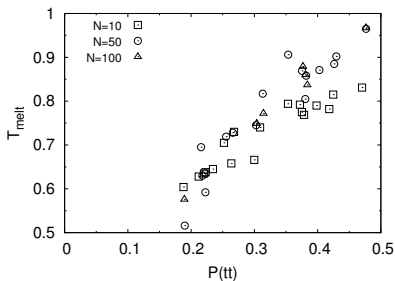


Figure c.4: Correlation between the melting temperature and the probability of *trans*–*trans* states.

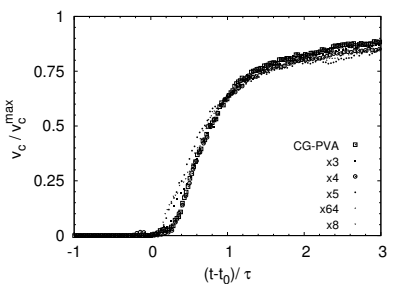


Figure c.5: Master curve presenting a unified description of the evolution of crystallinity (v_c represents the volume fraction of the crystal) during continuous cooling for several coarse-grained models.

relaxation above the melting temperature of the perfect crystals we simulated gave rise to a change in the symmetry of the system. The orthorhombic or triclinic packing turn into a hexagonal arrangement of the chains which remain stretched along their main axis but whose orientations in the perpendicular plane are not constrained anymore. These features could be attested by calculation of several order parameters that help characterizing the decay to the liquid state through this transitory phase.

Another approach of the n -alkane crystals consisted in simulating the cooling process leading to the formation of the crystal via homogeneous nucleation in the melt, starting from the liquid state at high temperature. As expected, in this case the detailed model proves too time-consuming for a realistic cooling rate to be applied, and the configurations we could obtain showed a glassy structure rather than crystalline order (fig. c.3). Still, it was possible to observe signs of the ordering of the molecules after annealing at low temperature: An order parameter calculated during isothermal relaxations of the system at different temperatures showed no particular features in the cases of the liquid or glassy systems but could be observed to increase at intermediate temperature, indicating the occurrence of a change in the system. Whether this is the sign of a true phase transition would require longer simulations to be checked.

This study of short polymer chains demonstrates that it is possible to accurately describe the behavior of the melt at the interface between the liquid and solid states, at least when starting from the crystalline configuration, since even for such small chains as n -alkanes, simulations of the cooling process is already prohibitive as far as computational time is concerned. Thus a more appropriate method is needed to address the problem of crystallization via homogeneous nucleation in the melt, and that is the reason why we used *coarse-grained* models to complete this task.

Coarse-grained models

As it is important to consider large enough length and time scales to address polymer crystallization (since this phenomenon involves various structures of different sizes which develop over a long time), the use of a model taking into account the details of the polymers in a more appropriate manner is needed. The CG-PVA model we used as the basis of this study of polymer crystallization represents the monomers of the polymer chains as single particles, and thus allows us not to consider the fast motion of all the atoms constituting the molecules as we did with all-atom models; this way we can focus on larger scales on which the semi-crystalline structures form. This coarse-grained model simplifies the all-atom description and makes the simulation more efficient since larger systems are accessible over longer times, but it remains a low-level model in which the underlying chemistry of the chain is still visible

via the structure of the angular potential. This parameter of the model is determined by the interactions between the particles of the original model on the atomistic scale, and constrains the flexibility so as to reproduce realistic conformations of the chains.

We created several models derived from CG-PVA in order to understand the influence of the angular potential, since this parameter is responsible for the crystallization of the CG-PVA model (a similar model *without* angular potential cannot crystallize); indeed, a comparison of the properties calculated for the different models showed that the probability of finding *trans-trans* states at high temperature (which is directly related to the shape of the angular potential) conditions the propensity of the chains to crystallize (fig. c.4). We could also show that the persistence length is not the most appropriate quantity to account for the flexibility of the chain in the case of our models, as it is largely influenced by the probability of folded states rather than stretched states, which is not as clearly correlated to the temperature of crystallization/melting measured during continuous cooling/heating (fig. c.6).

The correlation between the probability of *trans-trans* states and the melting temperature can be rationalized by means of a theoretical description by Volkenstein. The importance of the amount of fully stretched states in the crystalline configuration has been shown since the theory provides an accurate description in the case of short chains and perfect structures generated by hand; such systems were used to characterize the different models we simulated, yielding a reference state.

Simulations were performed to study the development of crystalline structures during isothermal relaxation after a quench, and this led to the evidence of a linear relation between the inverse lamellar thickness of the crystals and the supercooling under which they formed, as is observed experimentally.

The different models we have been simulating exhibited different behaviors at low temperature, depending on the probability of stretched states: Semi-crystalline structure with either a large or small amount of amorphous material can form as a result of cooling, leading to final configurations that resemble more a perfect crystal or a glass. Studying the evolution of a global order parameter during the cooling experiments, we could however establish that the development of the semi-crystalline structure is similar for the different models, even though the systems' properties are different. This observation is confirmed when using a different order parameter that allows one to distinguish the different crystallites forming in the melt and to follow their evolutions; the analysis of these domains makes it possible to identify parameters allowing for a unified description of the crystallization process for the different models (fig. c.5) having otherwise very different crystallinities (fig. c.7).

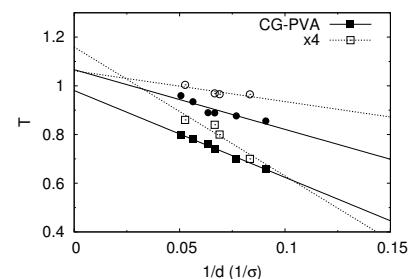
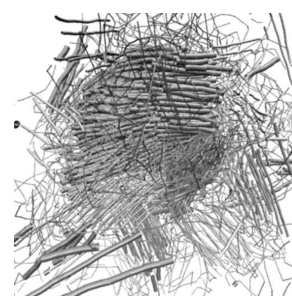
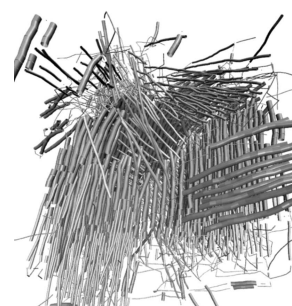


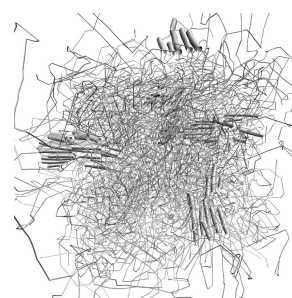
Figure c.6: Crystallization and melting lines for the x4 and CG-PVA models.



(a) CG-PVA



(b) x4



(c) x2

Figure c.7: Snapshots showing the final configurations obtained after continuous cooling simulations of the CG-PVA model and two of its variations: x4 has a high crystallization temperature and forms thick lamellae whereas x2 crystallizes at very low temperature, forming only a small amount of crystalline material.

Structure factors

The existence of a correlation between the melting temperature and the probability of *trans-trans* states at *high temperature* also prompted us to study the structure of the polymer melts corresponding to our models in more details, using concepts from simple-liquid theory extended to more complex molecules.

In order to probe the intimate structure of polymer melts and get a precise comparison of different models, the theory of simple liquids suggests the computation of structure factors. In the spirit of the Ornstein-Zernike description of such systems, an extension to the case of more complex molecules has been proposed and allows one to characterize more accurately the behavior of the different parts of the constituents of a fluid. We have used this RISM approach and tested the associated PRISM approximation that is aimed at describing long polymer chains.

We calculated the detailed structure factors for the CG-PVA model and three of its variants, showing that the PRISM approximation which states the equivalence of the different monomers of a chain is justified in the case of our models, even for relatively short chains, except for the chain ends for which significant differences are noticed as expected (PRISM is exact for ring polymers, and we could show that the deviations to this limit behavior are only important for the last few monomers at the chain ends, independently of the chain length).

The correlation functions defined in the framework of the RISM theory are well suited to study the structure of polymer melts, and offer a convenient approach to their characterization; nevertheless, no significant qualitative difference between the different models we analyzed with such methods could be isolated, and we were unable to determine from the detailed structure of the polymer melts at high temperature what causes them to crystallize or not (fig. c.8). The correlation observed between a high temperature property (probability of finding stretched states) and the stability of the crystalline structure (temperature of crystallization/melting) cannot be rationalized by the analysis of the detailed structure of the melt with density correlation functions at high temperature.

The study of these correlation functions still provides many interesting results which allow for a better understanding of the structure of the melts, through the comparison with several approximations and limiting behaviors: Gaussian approximations and expressions derived from the PRISM theory could be used to account for the characteristics of the measured quantities including inter- and intra-chain detailed structure factors as well as center-of-mass related correlation functions.

Outlook

Our studies of polymer melts and the crystalline structures they form at low temperature give some insight into the phenomenon of crystal-

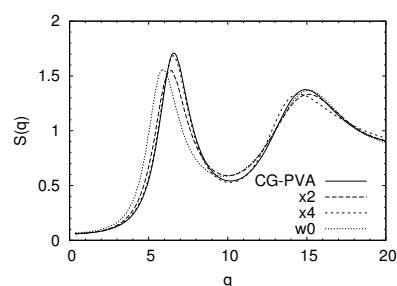


Figure c.8: Structure factors measured at high temperature for four different models: CG-PVA, x2, x4 and the w0 variant that has no explicit angular potential and therefore does not crystallize.

lization that is still not well understood. In this context, our work and the results obtained suggest directions for further studies. The coarse-grained models we used have been shown to successfully reproduce the experimentally observed behavior of linear polymer chains; polymers like PE and PVA with a simple chemical structure are well described by these models with cylindrical symmetry. It would be necessary to address polymers with a more complex geometry using a refined coarse-grained model that could be built on the basis of CG-PVA: One could, for instance, think of a model for PP which would take into account the chirality of the monomers. To this end, side-groups may be introduced along the coarse-grained backbone (fig. c.9), and the use of explicit torsional potentials on the coarse-grained level would allow one to reproduce the characteristic helices of such a chiral polymer (a similar approach has been presented in ref. 139). This could be used in order to probe the behavior of chiral semi-crystalline polymers and check whether in this case the crystallization scenario requires the “test phase” during which one chain probes the preexisting growth front: This selection mechanism has been put forward as a contradicting evidence that rules out the description of crystallization involving the occurrence of a large-scale mesomorphic phase [63].

The development of such a simulation study would involve the use of an all-atom model of polypropylene, similarly to what we have been attempting to do from our experience with alkanes (cf. sec. 2.5); using an appropriate model to simulate polypropylene chains with full details, one could measure the relevant probability distributions and infer from them the effective coarse-grained potentials that are needed to reproduce the overall structure of the melt and be able to simulate the crystallization process [97, 125].

The interplay between the different length and time scales and the availability of simulation schemes on both the atomistic and the mesoscopic levels suggest that these two techniques could be combined so as to take advantage of both the efficiency and the accuracy accessible to the different methods: Once the all-atom simulation has been used to parametrize its coarse-grained counterpart, one could imagine to benefit from the coarse-grained method to simulate the long-time process of crystallization and then reintroduce the atomistic details into the so-generated configuration in order to access the precise structure of polymer crystals in the end [125, 126]. We could verify that the coarse-grained model is very efficient and fully succeeds at reproducing the characteristic features of polymer crystals at intermediate and large scale, but cannot yield anything else than a hexagonal packing of the chains, due to its intrinsic symmetry. This model is therefore not accurate enough to provide a precise description of the arrangement of PE chains in the crystal, whereas we showed with all-atom simulations of *n*-alkanes that the orthorhombic phase—that is a common feature of odd-*n* alkanes and PE—is stable in an atomistic simulation. How-

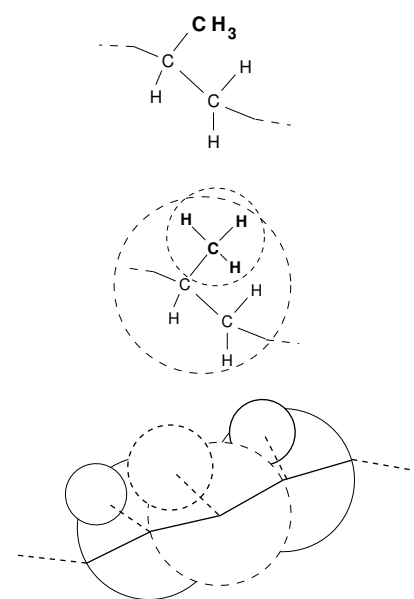


Figure c.9: Illustration of the coarse-graining procedure allowing to take the side-groups into account for polypropylene. A second bead per monomer is introduced, in order to keep track of the chirality of the molecule; this way, the typical helical structure of the stereoregular isomers of PP may be recovered.

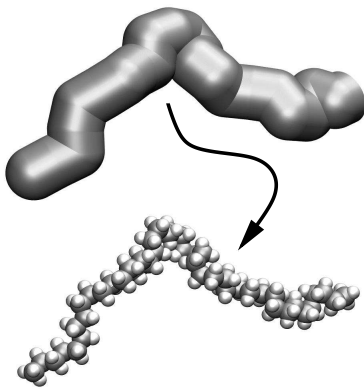


Figure c.10: Reintroduction of the atomistic details into a coarse-grained configuration.

ever, the reintroduction of atomistic details into the output of a coarse-grained method is far from being straight-forward, and there are many unsolved questions so as how to map the atomistic conformations onto the structure of the simplified molecules (since this inverse mapping is no longer unique as the simplification procedure of the coarse-graining was). Still, this study appears a very stimulating opportunity to improve the comprehension of the processes that lead to the formation of semi-crystalline systems; it would be especially attractive to investigate the influence of the moment at which the details are reintroduced during the formation of the lamellae, so that a characteristic time scale can be identified; moreover, it is not clear that simply inputting all-atom chains into a hexagonally symmetric configuration would be sufficient to recover the expected orthorhombic pattern when simulating PE, as our simulations of alkanes showed that it is not possible—at least with a simple force-field, and in a restricted amount of time—to obtain the orthorhombic order from the hexagonal phase via cooling (the crystal-rotator phase transition discussed in chapter 2 could not be reversed).

Parts of our work would deserve some complementary studies in order to improve the understanding of the observed phenomena; the crystallization and melting lines that could be reproduced in the simulation as they are observed experimentally need a more precise treatment in order to give an insight into the properties of the crystallization (and fusion) mechanisms [54, 55, 121]. In particular, it is desirable to compare more closely the simulation results to the existing theories; this requires the determination of the surface tension of the crystalline domains, which needs a complete study on its own, as different simulation techniques are necessary to determine free energies. It would be particularly interesting to address the question of the significance of the crossing of crystallization and melting lines: Unlike in the case of CG-PVA, the other coarse-grained models exhibit intersecting crystallization and melting lines in the $T_{\text{melt/cryst}}-1/d$ diagram; the existence of an intersection of the two lines (which is also found in experiments [42, 121]) would imply an upper limit for the lamellar thickness above which the crystals become unstable [55]. Observation of the results obtained with perfect crystal simulations show that the crystallization and melting lines might actually be *bent* in the limit of large thickness d ; this should be investigated in more details.

The characterization of the crystalline domains using an order parameter taking into account the distance between two bonds and their relative orientation allowed us to give a definition of a crystallite, and we could then measure the crystallinity in the samples in order to describe crystal growth during continuous cooling or isothermal relaxation of the coarse-grained models; it would be interesting to refine this approach and in particular to monitor the dynamic evolution of these crystallites during the development of the crystalline phase; one could then use this more precise characterization of the shape of the

crystalline domains to compare the different models and different conditions for the growth of the crystals.

Along with these perspectives for the more detailed study of crystal growth in the polymer melt, it appears very important to focus on the early stages of the crystallization process: This is probably the regime in which computer simulation is more likely to provide decisive results, owing to the detailed information available from the possibility to locate the particles at all times, which is not accessible to experiments, and to the restrictions on the simulation length and box size. In order to take advantage of the simulations being appropriate to study in detail the beginning of the crystallization process, it appears crucial to extend our studies of the structure of polymer melts to the lower temperature where the detailed correlation functions we have been using to characterize the melt at high temperature might be suited to grasp the precursors of the phase transition; the site-resolved quantities in particular provide an accurate description of the structure of the melt and may offer the opportunity to detect signals associated with the formation of ordered patterns during the very first steps.

Another approach of the crystallization phenomenon could consist in using the simulation to test the development of the hypothetical mesomorphic phase [121]; this requires massive computer time resources that could be used to simulate the polymer melt at very weak supercooling in order not to perturb the formation of the semi-crystalline phase. Under these conditions, and provided long times and large simulation boxes are accessible, the process of homogeneous nucleation could be precisely investigated and the numerical experiment could yield very interesting results on the possibly large-scale process responsible for the development of realistic crystals unaffected by the interactions between simultaneously growing crystallites and the too large supercooling that hinders crystal growth as is the case in our current simulations.

The results of the present thesis which clarified the influence of many simulation parameters on atomic and mesoscopic scales lay the basis to address the outlined perspectives in the future.

List of Tables

2.1	Units used in all-atom simulations (YASP package)	36
2.2	Values of the coefficients used in the definition of the total torsional potential .	39
2.3	Comparison of P_{trans} for different models and at different temperatures	40
2.4	Summary of equilibrium simulations of n -alkanes at $T = 500$ K	40
2.5	Summary of n -alkane cooling simulations	59
3.1	Units used in the coarse-grained simulations	80
3.2	Comparison of angular potentials: Group 1, $N = 10$	86
3.3	Comparison of angular potentials: Group 1, $N = 50$	86
3.4	Comparison of angular potentials: Group 2, $N = 10$	87
3.5	Comparison of angular potentials: Group 2, $N = 50$	87
3.6	Comparison of angular potentials: Group 3, $N = 10$	88
3.7	Comparison of angular potentials: Group 3, $N = 50$	88
3.8	Comparison of angular potentials: Group 4, $N = 10$	89
3.9	Comparison of angular potentials: Group 4, $N = 50$	89
3.10	Comparison of angular potentials: Group 5, $N = 10$	90
3.11	Comparison of angular potentials: Group 5, $N = 50$	90
3.12	Comparison of angular potentials: Group 6 — Parameters	91
3.13	Comparison of angular potentials: Group 6, $N = 10$	92
3.14	Comparison of angular potentials: Group 6, $N = 50$	92
3.15	Comparison of angular potentials: Group 1–2, $N = 10$	94
3.16	Comparison of angular potentials: Group 4–2, $N = 10$	94
3.17	Comparison of angular potentials: Group 1–2, $N = 50$	94
3.18	Comparison of angular potentials: Group 4–2, $N = 50$	94
3.19	Reference values for chain length $N = 100$	97
3.20	Reference values for chain length $N = 100$ — Parameters	97
4.1	Summary of parameters for the calculation of structure factors for the coarse-grained models	141

List of Figures

i.1	Chemical formulae of three polymers with simple structure	1
i.2	Sketch of a chain folded to form a lamella	2
i.3	The different length scales involved in semi-crystalline polymers	2
i.4	Sketch of the formation of a lamella from the amorphous melt	3
i.5	Comparative summary of different simulation schemes and the associated length scales	4
i.6	Schematic representation of different coarse-graining level of a short alkane chain	5
1.1	Lennard-Jones potential	18
1.2	Binding potential	19
1.3	Angular potential	20
1.4	Torsional potential	21
1.5	Protocol for continuous cooling and heating	23
1.6	Protocol for a quench	23
1.7	Determination of the crystallization temperature	26
1.8	Determination of enthalpy variation during melting	26
2.1	Comparison of the expected torsional angular distributions and the simulation data for $C_{44}H_{100}$	38
2.2	Illustration of the three different contributions to the torsional energy	38
2.3	Comparison of theoretical expectation and the measured variance for C–C–C bond angle distributions ($C_{16}H_{34}$)	41
2.4	Evolution of radial distribution functions with temperature ($C_{16}H_{34}$)	41
2.5	Bond length distributions as a function of temperature	42
2.6	Evolution of temperature fluctuations as a function of the total number of particles	42
2.7	Comparison of Berendsen and Langevin thermostats for temperature and enthalpy	43
2.8	Comparison of Berendsen and Langevin thermostats for the volume and squared radius of gyration	44
2.9	Sketches of the packing of n -alkanes in different crystal structures	46
2.10	Snapshots of orthorhombic $C_{15}H_{32}$	47
2.11	Schematic drawing of the triclinic lattice's base vectors	47
2.12	Snapshots of triclinic $C_{20}H_{42}$	48
2.13	Evolution of lattice parameters during startup simulation for orthorhombic and triclinic crystals	48
2.14	Lattice parameters measured for orthorhombic and triclinic crystals as a function of temperature	49

2.15	Definition of vectors used to characterize the order in the solid phases	50
2.16	Schematic representation of the computation method of the P_2 order parameter	50
2.17	Orientation correlation of vectors perpendicular to the elongated chains' planes	51
2.18	Snapshot of the rotator phase ($C_{20}H_{42}$)	51
2.19	Comparison of phase diagrams for the heating of an orthorhombic structure at different rates ($C_{15}H_{32}$)	52
2.20	Comparison of phase diagrams for orthorhombic and triclinic crystals	52
2.21	Different order parameters indicating the transition from the orthorhombic crystal to the melt	53
2.22	Evolution of P_{gauche} with temperature close to the transition ($C_{15}H_{32}$)	53
2.23	Definition of the temperatures associated with the observed phase transitions	53
2.24	Ratio of the cell parameters a and b for orthorhombic $C_{15}H_{32}$ during continuous heating	54
2.25	Melting temperature as a function of n for even- and odd- n chains	55
2.26	Instability of the triclinic phase	55
2.27	Schematic drawing of temperature protocols used in the simulations	56
2.28	Evolution of the lattice parameters a and b with temperature during continuous heating	57
2.29	Evolution of the volume during isothermal relaxations at various temperatures ($C_{15}H_{32}$)	57
2.30	Order parameters during the melting transition at $T = 360$ K ($C_{15}H_{32}$)	58
2.31	Inverse of the density as a function of $1/n$ at $T = 500$ K	58
2.32	Evolution of the density as a function of temperature during cooling	59
2.33	Relaxation of the end-to-end vector during the initialization part of the simulation	59
2.34	Volume and order parameter as a function of temperature during cooling	60
2.35	Variation of the mean-square radius of gyration with temperature ($n = 10$ and $n = 44$)	60
2.36	Comparison of the original and modified OPLS-AA torsional potential with the ST potential	61
2.37	Snapshot of the final structure after cooling the ST model	61
2.38	Volume and R_g^2 as functions of temperature for the OPLS-mod and ST models ($C_{16}H_{34}$)	62
2.39	Experimental melting temperature as a function of n for n -alkanes	62
2.40	Schematic drawing of the temperature protocol for simulations of n -alkanes	62
2.41	Characteristics of the liquid at different temperatures around and below the experimental melting point (C_8H_{18})	63
2.42	Volume and mean-square radius of gyration as functions of time and temperature ($C_{16}H_{34}$)	64
2.43	Order parameter P_2 as a function of time and temperature ($C_{16}H_{34}$)	65
2.44	Chemical formula of propylene	66
2.45	Chemical formula of polypropylene	66
2.46	Chemical formulae of isotactic and syndiotactic polypropylene	67
2.47	Snapshot of a short chain of isotactic polypropylene (iPP)	69
2.48	Snapshot of a short chain of syndiotactic polypropylene (sPP)	69
2.49	Probability distributions of torsion angles for iPP and sPP chains at $T = 450$ K	70
2.50	Schematic representation of the <i>intra</i> - and <i>inter</i> -monomer torsions	70

2.51	Evolution of the probabilities P_{trans} , P_{gauche^+} and P_{gauche^-} for iPP and sPP . . .	71
2.52	Density as a function of temperature for iPP and sPP fir cooling at two different rates	71
3.1	Coarse-grained model: Bonded interaction potential	79
3.2	Coarse-grained model: Intermolecular interaction potential	79
3.3	Coarse-grained model: Angular potential	80
3.4	Determination of the glass transition temperature for w0	81
3.5	Influence of the angular potential on the crystallization of coarse-grained models	82
3.6	Correspondence between atomistic backbone angles and coarse-grained angles .	83
3.7	Parameterization of the coarse-grained angular potential	85
3.8	Influence of the angular potential: Depth of the tg well	86
3.9	Influence of the angular potential: Another study of the tg well	87
3.10	Influence of the angular potential: Height of the tt - gg barrier	88
3.11	Influence of the angular potential: Depth of the gg well	89
3.12	Influence of the angular potential: Height of the tg - gg barrier	90
3.13	Influence of the angular potential: Models close to CG-PVA	91
3.14	Influence of the angular potential: Depth of the gg well	93
3.15	Influence of the angular potential: Depth of the gg well	93
3.16	Correlations observed for different models and different chain lengths	96
3.17	Dynamical quantities measured from data for the coarse-grained models	98
3.18	Characteristic lengths R_e , R_g and l_p as functions of $\langle \cos \theta \rangle$	100
3.19	Influence of the angular states on the torsional angle distributions for several models	101
3.20	Influence of the cooling rate on the phase diagram of short chains ($N = 10$) . .	102
3.21	Evolution of P_{trans} during continuous cooling for various chain lengths	103
3.22	Dependence of the phase diagram on the chain length (CG-PVA)	104
3.23	Evolution of the crystallization temperature as a function of the chain length .	104
3.24	Evolution of the P_2 order parameter during continuous cooling ($N = 10$ and $N = 100$)	105
3.25	Evolution of the <i>intra</i> -chain order parameter P_2^{intra} during continuous cooling ($N = 10$ and $N = 100$)	105
3.26	Superposition of the P_2 order parameters for different models during cooling ($N = 10$ and $N = 50$)	106
3.27	Snapshots of conrinuous cooling, CG-PVA, $N = 10$	106
3.28	Superposition of the P_2 order parameters for different models during cooling and heating ($N = 100$)	107
3.29	Snapshots of conrinuous cooling, x4 model, $N = 10$	107
3.30	Low-temperature value of the order parameter $P_2(T = 0.4)$ as a function of the crystallization temperature of different models	108
3.31	Comparison of the two order parameters P_2 and S	109
3.32	Definition of the local order parameter used to determine the crystallinity . . .	109
3.33	Snapshots of semi-crystalline configurations	110
3.34	Extrapolation giving the limit value of crystallinity v_c	110
3.35	Crystal fraction as a function of temperature for three different models ($N = 100$)	111

3.36	Evolution of the crystal volume fraction during crystallization and melting . . .	111
3.37	Sketch presenting the analogy between growing crystal and expanding waves (Avrami approach)	112
3.38	Avrami plots for the CG-PVA and x4 models	113
3.39	Comparison of the simulation data and the fitted Avrami expression for the crystallinity	113
3.40	Master curve for the crystallinity during continuous cooling	114
3.41	Evolution of the number of crystallites during continuous cooling	115
3.42	Evolution of the number of bonds and sizes of the three biggest crystallites . .	115
3.43	Evolution of the radius of gyration during continuous cooling, for three models	116
3.44	Increase of the stem length during crystal growth	117
3.45	Phase diagrams for $N = 100$	117
3.46	Probability distributions of the bond angle θ for three models	117
3.47	Influence of probability P_{trans} on the melting temperature	118
3.48	Influence of the angular potential on melting temperature: Volkenstein analysis	121
3.49	Crystallization and melting lines (CG-PVA and x4)	122
3.50	Crystallization and melting lines (x3, x64, x5, x8)	122
3.51	Representation of the two-dimensional hexagonal lattice	123
3.52	Structure factors at $T = 0.4$ for several models	124
3.53	Structure factors at $T = 1$ and $T = 0.4$ for CG-PVA, for different chain lengths	124
3.54	Comparison of the structure factors for different models at different temperatures	125
3.55	Phase diagrams for the melting of perfect crystals ($N = 100$)	126
3.56	Simulation snapshots of configurations of perfect crystals	126
3.57	Melting and crystallization lines from fig. 3.49 compared to the data obtained for the melting of perfect crystals	127
3.58	Melting temperature as a function of the stem length for perfect crystals	127
3.59	Evolution of the P_2 order parameter during melting of systems having varying crystallinities	128
3.60	Probability of the <i>trans-trans</i> state along the chain during melting of perfectly crystalline structures	129
3.61	Comparison of data for the melting of perfect crystals and Volkenstein's theory	129
3.62	Structure factors at low temperature for different semi-crystalline configurations	130
3.63	Comparison of structure factors for crystalline configurations of fully stretched chains	131
3.64	Comparison of simulation results with experimental values.	132
3.73	Phase diagram for continuous cooling simulations of a coarse-grained model of polyethylene	135
4.1	Definition of the <i>inter-</i> and <i>intra-</i> chain structure factors	139
4.2	Definition of the center-of-mass structure factor	139
4.3	Definition of monomer-polymer structure factors	140
4.4	Comparison of the total and intra-chain structure factors	142
4.5	Approximations to the intra-chain structure factor in different regimes	144
4.6	Approximations to the inter-chain structure factor in different regimes	145
4.7	Comparison of the intra- and inter-chain structure factors for four different models	146

4.8	Comparison of total structure factors for four different models	146
4.9	Comparison of different models: Intra-chain structure at large q and rescaled inter-chain structure factors using the position of the first peak q^*	147
4.10	Comparison of the intra-chain and total structure factors for large q	147
4.11	Variation of characteristic lengths with q^* for different models	148
4.12	Schematic representation of the Ornstein-Zernike approach	148
4.13	Schematic representation of a few correlation functions for molecular systems .	150
4.14	Schematic representation of the direct correlation functions in the case of ring polymers (PRISM approximation)	150
4.15	Comparison of the site-resolved and site averaged direct correlation functions .	151
4.16	Comparison of the site-resolved and site averaged direct correlation functions in the small- q regime	152
4.17	Improvement of the PRISM approximation with the distance from the chain ends	153
4.18	Comparison of the site-resolved intra-chain structure factors to the gaussian and Koyama approximations	154
4.19	Symmetry of the site-resolved intra-chain structure factors	154
4.20	Large q limit of the comparison of the intra-chain structure and the Koyama approximation	155
4.21	Comparison of the site-averaged intra-chain structure factors to the Koyama approximation	156
4.22	Averaged and site-resolved inter-chain structure factors	156
4.23	Comparison of the site-resolved inter-chain structure factors to the PRISM approximation	158
4.24	Center-of-mass (CM) structure factor for different chain lengths	161
4.25	Comparison of the monomer-CM structure factor with the gaussian approximation for different chain lengths	162
4.26	Monomer-CM correlation functions for different positions of the monomers along the chain	163
4.27	Monomer-CM inter-chain structure factor for different sites and chain lengths .	164
c.1	Snapshots of the different crystal structures of n -alkanes	167
c.2	Phase diagram for $C_{15}H_{32}$ during melting	168
c.3	Density vs. temperature for n -alkanes	168
c.4	Correlation between the melting temperature and the probability of <i>trans-trans</i> states	168
c.5	Master curve showing the evolution of crystallinity	168
c.6	Crystallization and melting lines for the x4 and CG-PVA models	169
c.7	Snapshots of crystalline configurations obtained with coarse-grained models . .	169
c.8	Structure factors at high temperature for different coarse-grained models	170
c.9	Illustration of the coarse-graining procedure for polypropylene	171
c.10	Reintroduction of the atomistic details	172

Bibliography

- [1] M. Aichele, S.-H. Chong, J. Baschnagel, and M. Fuchs, *Static properties of a simulated supercooled polymer melt: Structure factors, monomer distributions relative to the center of mass, and triple correlation functions*, Phys. Rev. E. **69** (2004), 61801.
- [2] M.P. Allen and D.J. Tildesley, *Computer Simulation of Liquids*, Oxford Science, Oxford, 1987.
- [3] H. C. Andersen, *Molecular dynamics simulations at constant pressure and/or temperature*, J. Chem. Phys. **72** (1980), 2384.
- [4] K. L. Anderson and G. Goldbeck-Wood, *Simulation of thickening growth in polymer crystallisation*, Polymer **41** (2000), 8849.
- [5] K. A. Armistead and G. Goldbeck-Wood, *Theories of polymer crystallization*, Adv. Polym. Sci. **100** (1992), 221.
- [6] N. W. Ashcroft and N. D. Mermin, *Solid state physics*, Saunders College, Philadelphia, 1976.
- [7] R. Auhl, R. Everaers, G. R. Grest, K. Kremer, and S. J. Plimpton, *Equilibration of long chain polymer melts in computer simulations*, J. Chem. Phys. **119** (2003), 12718.
- [8] J. Baschnagel and F. Varnik, *Computer simulation of supercooled polymer melts in the bulk and in confined geometry*, J. Phys.: Condens. Matter, in preparation.
- [9] J. Baschnagel, J. P. Wittmer, and H. Meyer, *Monte-Carlo simulation of polymers: Coarse-grained models*, Computational Soft Matter: From Synthetic Polymers to Proteins (Jülich) (N. Attig, K. Binder, H. Grubmüller, and K. Kremer, eds.), vol. 23, NIC Series, Jülich, 2004, (available from <http://www.fz-juelich.de/nic-series>), p. 83.
- [10] H. J. C. Berendsen, J. P. M. Postma, W. F. van Gunsteren, A. DiNola, and J. R. Haak, *Molecular simulation with coupling to an external bath*, J. Chem. Phys. **81** (1984), 368.
- [11] K. Binder, J. Horbach, W. Kob, W. Paul, and F. Varnik, *Molecular dynamics simulations*, J. Phys.: Condens. Matter **16** (2004), S429.
- [12] B. R. Brooks, R. E. Bruccoleri, B. D. Olafson, D. J. States, S. Swaminathan, and M. Karplus, *CHARMM: A program for macromolecular energy, minimization, and dynamics calculations*, J. Comp. Chem. **4** (1983), 187.
- [13] D. Chandler, *Derivation of an integral equation for pair correlation functions in molecular fluids*, J. Chem. Phys. **59** (1973), 2742.
- [14] D. Chandler, *Equilibrium theory of polyatomic fluids*, Studies in Statistical Mechanics VIII (Amsterdam) (E. W. Montroll and J. L. Lebowitz, eds.), North-Holland, Amsterdam, 1982, p. 275.
- [15] D. Chandler, *Introduction to modern statistical mechanics*, Oxford University Press, New York, 1987.
- [16] D. Chandler and H. C. Andersen, *Optimized cluster expansions for classical fluids. II. theory of molecular liquids*, J. Chem. Phys. **57** (1972), 1930.

-
- [17] S. Z. D. Cheng, C. Y. Li, and L. Zhu, *Commentary on polymer crystallization: Selection rules in different length scales of a nucleation process*, Eur. Phys. J. E **3** (2000), 195.
- [18] C. Das and D. Frenkel, *Numerical calculation of the melting phase diagram of low molecular-weight polyethylene*, J. Chem. Phys. **118** (2003), 9433.
- [19] P. G. de Gennes, *Scaling concepts in polymer physics*, Cornell University Press, Ithaca, 1996.
- [20] I. Denicolò, J. Doucet, and A. Craievich, *X-ray study of the rotator phase of paraffins (III): Even-numbered paraffins $C_{18}H_{38}$, $C_{20}H_{42}$, $C_{22}H_{46}$, $C_{24}H_{50}$ and $C_{26}H_{54}$* , J. Chem. Phys. **78** (1983), 1465.
- [21] B. Diu, C. Guthmann, D. Lederer, and B. Roulet, *Physique statistique*, Hermann, 1989, Complément V.F, p. 745.
- [22] M. Doi and S. F. Edwards, *The theory of polymer dynamics*, Oxford University Press, Oxford, 1986.
- [23] E. Donth, *The glass transition*, Springer, Berlin–Heidelberg, 2001.
- [24] D. L. Dorset, *Crystallography of the polymethylene chain. an inquiry into the structure of waxes*, Oxford University Press, Oxford, 2004.
- [25] J. Doucet, I. Denicolò, and A. Craievich, *X-ray study of the rotator phase of the odd-numbered paraffins $C_{17}H_{36}$, $C_{19}H_{40}$ and $C_{21}H_{44}$* , J. Chem. Phys. **75** (1981), 1523.
- [26] J. Doucet, I. Denicolò, A. Craievich, and A. Collet, *Evidence of a phase transition in the rotator phase of the odd-numbered paraffins $C_{23}H_{48}$ and $C_{25}H_{52}$* , J. Chem. Phys. **75** (1981), 5125.
- [27] J. P. K. Doye, *Computer simulations of the mechanism of thickness selection in polymer crystals*, Polymer **41** (2000), 8857.
- [28] J. P. K. Doye and D. Frenkel, *Crystallization of a polymer on a surface*, J. Chem. Phys. **109** (1998), 10033.
- [29] J. P. K. Doye and D. Frenkel, *Mechanism of thickness determination in polymer crystals*, Phys. Rev. Lett. **81** (1998), 2160.
- [30] S. F. Edwards, *The size of a polymer molecule in a strong solution*, J. Phys. A: Math. Gen. **8** (1975), 1670.
- [31] K. Esselink, A. J. Hilbers, and B. W. H. van Beest, *Molecular dynamics study of nucleation and melting of n-alkanes*, J. Chem. Phys. **101** (1994), 9033.
- [32] E. W. Fischer, *Stufen- und spiralförmiges Kristallwachstum bei Hochpolymeren*, Z. Naturforsch. A **12** (1957), 753.
- [33] P. J. Flory, *Statistical mechanics of chain molecules*, Wiley, 1969.
- [34] D. Frenkel and B. Smit, *Understanding molecular simulations*, 2nd ed., Academic Press, San Diego, 2002.
- [35] S. Fujiwara and T. Sato, *Molecular dynamics simulation of structural formation of short polymer chains*, Phys. Rev. Lett. **80** (1998), 991.
- [36] S. Fujiwara and T. Sato, *Structure formation of a single polymer chain. I. Growth of trans domains*, J. Chem. Phys. **114** (2001), 6455.
- [37] C. W. Gear, *The numerical integration of ordinary differential equations of various order*, Tech. Report ANL 7126, Argonne National Laboratory, 1966.
- [38] C. W. Gear, *Numerical initial value problems in ordinary differential equations*, Prentice-Hall, 1971.

- [39] G. S. Grest and K. Kremer, *Molecular dynamics simulation for polymers in the presence of a heat bath*, Phys. Rev. A **33** (1986), 3628.
- [40] J. P. Hansen and I. R. McDonald, *Theory of simple liquids*, Academic Press, London, 1986.
- [41] T. Hayashida, J. Phys. Soc. Japan (1962), 306.
- [42] B. Heck, T. Hugel, M. Iijima, E. Sadiku, and G. Strobl, *Steps in the transition of an entangled polymer melt to the partially crystalline state*, New Journal of Physics **1** (1999), 17.1.
- [43] A. B. Herhold, H. E. King Jr, and E. B Sirota, *A vanishing nucleation barrier for the n-alkane rotator-to-crystal transformation*, J. Chem. Phys. **116** (2002), 9036.
- [44] R. W. Hockney, *The potential calculation and some applications*, Methods Comput. Phys. **9** (1970), 136.
- [45] J. D. Hoffman, G. T. Davis, and J. I. Lauritzen, *The rate of crystallization of linear polymers with chain folding*, Treatise in solid state chemistry (N. B. Hannay, ed.), vol. 3, Plenum Press, 1976.
- [46] J. D. Hoffman and R. L. Miller, *Kinetics of crystallization from the melt and chain folding in polyethylene fractions revisited: Theory and experiment*, Polymer **38** (1997), 3151.
- [47] B. L. Holian, A. F. Voter, and R. Ravelo, *Thermostatted molecular dynamics: How to avoid the Toda demon hidden in Nosé-Hoover dynamics*, Phys. Rev. E **52** (1995), 2338.
- [48] W. G. Hoover, *Canonical dynamics: Equilibrium phase-space distributions*, Phys. Rev. A **31** (1985), 1695.
- [49] M. Imai, K. Kajii, and T. Kanaya, *Orientation fluctuations of poly(ethylene terephthalate) during the induction period of crystallization*, Phys. Rev. Lett. **71** (1993), 4162.
- [50] V. A. Ivanov, M. R. Stukan, M. Müller, W. Paul, and K. Binder, *Phase diagram of solutions of stiff-chain macromolecules: A Monte-Carlo simulation*, J. Chem. Phys. **118** (2003), 10333.
- [51] W. L. Jorgensen, D. S. Maxwell, and Tirado-Rives J., *Developpement and testing of the OPLS all-atom force field on conformational energetics and properties of organic liquids*, J. Am. Chem. Soc. **118** (1996), 11225.
- [52] N. Karasawa, S. Dasgupta, and W. A. Goddard III, *Mechanical properties and force field parameters for polyethylene crystal*, J. Phys. Chem. **95** (1991), 2260.
- [53] A. Keller, *A note on single crystals in polymers: Evidenc for a folded chain configuration*, Philos. Mag. **2** (1957), 1171.
- [54] A. Keller and S. Z. D. Cheng, *The role of metastability in polymer phase transitions*, Polymer **39** (1998), 4461.
- [55] A. Keller, G. Goldbeck-Wood, and M. Hikosaka, *Polymer crystallization: Survey and new trends with wider implications for phase transformations*, Faraday Discuss. **95** (1993), 109.
- [56] Y. Kim, H. L. Strauss, and R. G. Snyder, *Conformational disorder in crystalline n-alkanes prior to melting*, J. Phys. Chem. **93** (1989), 7520.
- [57] R. Koyama, J. Phys. Soc. Jpn. **34** (1973), 1029.
- [58] H. Kraack, M. Deutsch, and E. B. Sirota, *n-alkane homogeneous nucleation: Crossover to polymer behavior*, Macromolecules **33** (2000), 6174.

- [59] V. Krakoviack, J. P. Hansen, and A. A. Louis, *Relating monomer to centre-of-mass distribution functions in polymer solutions*, Europhys. Lett. **58** (2002), 53.
- [60] S. Krushev and W. Paul, *Intramolecular caging in polybutadiene due to rotational barriers*, Phys. Rev. E **67** (2003), 021806.
- [61] C. Liu and M. Muthukumar, *Langevin dynamics simulations of early-stage polymer nucleation and crystallization*, J. Chem. Phys. **109** (1998), 2536.
- [62] T. P. Lodge and M. M. Muthukumar, *Physical chemistry of polymers: Entropy, interactions, and dynamics*, J. Phys. Chem. **100** (1996), 13275.
- [63] B. Lotz, *What can polymer crystal structure tell about polymer crystallization processes?*, Eur. Phys. J. E **3** (2000), 185.
- [64] B. Lotz, J.-C. Wittmann, and A. J. Lovinger, *Structure and morphology of poly(propylenes): A molecular analysis*, Polymer **37** (1996), 4979.
- [65] L. Mandelkern and R. G. Alamo, *Thermodynamic quantities governing melting*, Physical properties of polymers handbook (New York) (J. E. Mark, ed.), AIP Press, New York, 1996, p. 119.
- [66] M. L. Mansfield, *Broken wormlike chain model of semiflexible polymers*, Macromolecules **19** (1986), 854.
- [67] M. Maroncelli, S. Ping Qi, H. L. Strauss, and R. G. Snyder, *Nonplanar conformers and the phase behavior of solid n-alkanes*, J. Am. Chem. Soc. **104** (1982), 6237.
- [68] R. Martoňák, W. Paul, and K. Binder, *Orthorhombic phase of crystalline polyethylene: A constant pressure path-integral Monte-Carlo study*, Phys. Rev. E **57** (1997), 2425.
- [69] R. Martoňák, W. Paul, and K. Binder, *Orthorhombic phase of crystalline polyethylene: A Monte-Carlo study*, J. Chem. Phys. **106** (1997), 8918.
- [70] G. Matsuba, T. Kanaya, M. Saito, K. Kaji, and K. Nishida, *Further evidence of spinodal decomposition during the induction period of polymer crystallization: Time-resolved small-angle x-ray scattering prior to crystallization of poly(ethylene naphthalate)*, Phys. Rev. E **62** (2000), R1497.
- [71] I.-E. Mavrantza, D. Prentzas, V. G. Mavrantzas, and C. Galiotis, *Detailed atomistic molecular dynamics simulation of the orthorhombic phase of crystalline polyethylene and alkane crystals*, J. Chem. Phys. **115** (2001), 3937.
- [72] M. R. McGann and D. J. Lacks, *Molecular simulations of shear instabilities in polyethylene and n-alkane crystals under axial compression*, Macromolecules **31** (1998), 6356.
- [73] H. Meyer, *Structure formation and chain-folding in supercooled polymer melts. Some ideas from MD simulations with a coarse-grained model*, Polymer Crystallization: Observations, Concepts and Interpretations (Berlin) (J.-U. Sommer and G. Reiter, eds.), Lecture Notes in Physics, vol. 606, Springer, Berlin, 2003, p. 177.
- [74] H. Meyer and F. Müller-Plathe, *Formation of chain-folded structures in supercooled polymer melts*, J. Chem. Phys. **115** (2001), 7807.
- [75] H. Meyer and F. Müller-Plathe, *Formation of chain-folded structures in supercooled polymer melts examined by MD simulations*, Macromolecules **35** (2002), 1241.
- [76] J. Mnyukh, J. Phys. Chem. Solid **24** (1963), 631.
- [77] M. Mondello, G. Grest, E. B. Webb III, and P. Peczak, *Dynamics of n-alkanes: Comparison to Rouse model*, J. Chem. Phys. **109** (1998), 798.
- [78] A. Müller, Proc. Roy. Soc. (London) **120** (1928), 455.

- [79] A. Müller, Proc. Roy. Soc. (London) **138** (1932), 514.
- [80] A. Müller and K. Lonsdale, Acta Cryst. **1** (1948).
- [81] A. Müller and W. B. Saville, J. Chem. Soc. **127** (1925), 599.
- [82] F. Müller-Plathe, *YASP: A molecular simulation package*, Comp. Phys. Comm. **78** (1993), 77.
- [83] F. Müller-Plathe, *Computational chemistry I: Molecular simulation*, Lecture Notes, 1998.
- [84] F. Müller-Plathe, *Coarse-graining in polymer simulation: From the atomistic to the mesoscopic scale and back*, ChemPhysChem **3** (2002), 754.
- [85] M. Muthukumar, *Localized structures of polymers with long-range interactions*, J. Chem. Phys. **104** (1996), 691.
- [86] M. Muthukumar, *Commentary on theories of polymer crystallization*, Eur. Phys. J. E **3** (2000), 199.
- [87] M. Muthukumar, *Nucleation in polymer crystallization*, Adv. Chem. Phys. **128** (2004).
- [88] M. Muthukumar and P. Welch, *Modeling polymer crystallization from solutions*, Polymer **41** (2000), 8833.
- [89] J. Naghizadeh, *Quasi-two-dimensional phase transitions in paraffins*, Adv. Chem. Phys. **65** (1986), 44.
- [90] N.-Q. Nguyen, M. R. McGann, and D. J. Lacks, *Elastic stability limits of polyethylene and n-alkane crystals from molecular simulation*, J. Phys. Chem. B **103** (1999), 10679.
- [91] S. C. Nyburg and H. Lüth, Acta Cryst. B **28** (1972).
- [92] G. Odian, *Principles of polymerization*, 2nd ed., John Wiley & Sons, 1993.
- [93] P. D. Olmsted, W. C. K. Poon, T. C. B. McLeish, N. J. Terrill, and A. J. Ryan, *Spinodal-assisted crystallization in polymer melts*, Phys. Rev. Lett. **81** (1998), 373.
- [94] W. Paul, D. Y. Yoon, and G. D. Smith, *Optimized united atom model for simulations of polymethylene melts*, J. Chem. Phys. **103** (1995), 1702.
- [95] D. A. Pearlman, D. A. Case, J. W. Caldwell, W. R. Ross, T. E. Cheatham III, S. DeBolt, D. Ferguson, G. Seibel, and P. Kollman, *AMBER, a computer program for applying molecular mechanics, normal mode analysis, molecular dynamics and free energy calculations to elucidate the structures and energies of molecules*, Comp. Phys. Commun. **91** (1995), 1.
- [96] J. M. Polson and D. Frenkel, *Numerical prediction of the melting curve of n-octane*, J. Chem. Phys. **111** (1999), 1501.
- [97] D. Reith, H. Meyer, and F. Müller-Plathe, *Mapping atomistic to coarse-grained polymer models using automatic simplex optimization to fit structural properties*, Macromolecules **34** (2001), 2335.
- [98] D. Rigby and R.-J. Roe, *Molecular dynamics simulation of polymer liquid and glass. I. Glass transition*, J. Chem. Phys. **87** (1987), 7285.
- [99] D. Rigby and R.-J. Roe, *Molecular dynamics simulation of polymer liquid and glass. II. Short range order and orientation correlation*, J. Chem. Phys. **89** (1988), 5280.
- [100] M. Rubinstein and R. H. Colby, *Polymer physics*, Oxford University Press, Oxford, 2003.
- [101] G. C. Rutledge, D. J. Lacks, R. Martoňák, and K. Binder, *A comparison of quasi-harmonic lattice dynamics and monte-carlo simulation of polymeric crystals using orthorhombic polyethylene*, J. Chem. Phys. **108** (1998), 10274.

- [102] J. P. Ryckaert, G. Ciccotti, and H. J. C. Berendsen, *Numerical integration of the cartesian equations of motion of a system with constraints: Molecular dynamics of n-alkanes*, J. Comp. Phys. **23** (1977), 327.
- [103] J.-P. Ryckaert and M. L. Klein, *Translational and rotational disorder in solid n-alkanes: Constant temperature-constant pressure molecular dynamics calculations using infinitely long flexible chains*, J. Chem. Phys. **85** (1986), 1613.
- [104] J.-P. Ryckaert, M. L. Klein, and I. R. McDonald, *Disorder at the bilayer interface in the pseudo-hexagonal rotator phase of solid n-alkanes*, Phys. Rev. Lett. **58** (1987), 698.
- [105] D. M. Sadler and G. H. Gilmer, *Rate-theory model of polymer crystallization*, Phys. Rev. Lett. **56** (1986), 2708.
- [106] L. Schäfer and B. Krüger, J. Phys. France **49** (1988), 749.
- [107] T. Schneider and E. Stoll, *Molecular dynamics study of a three-dimensional one-component model for distortive phase transitions*, Phys. Rev. B **17** (1978), 1302.
- [108] K. S. Schweizer and J. G. Curro, *Integral equation theory of the structure of polymer melts*, Phys. Rev. Lett. **58** (1987), 246.
- [109] K. S. Schweizer and J. G. Curro, Adv. Chem. Phys. **98** (1997), 1.
- [110] H. M. M. Shearer and V. Vand, Acta Cryst. **9** (1956), 379.
- [111] T. Shimizu and T. Yamamoto, *Melting and crystallization in thin film of n-alkanes: A molecular dynamics simulation*, J. Chem. Phys. **113** (2000), 3351.
- [112] E. B. Sirota, *Supercooling, nucleation, rotator phases and surface crystallization of n-alkane melts*, Langmuir **14** (1998), 3133.
- [113] E. B. Sirota and A. B. Herhold, *Transient rotator phase induced nucleation in n-alkane melts*, Polymer **41** (2000), 8781.
- [114] A. E. Smith, *The crystal structure of the normal paraffin hydrocarbons*, J. Chem. Phys. **21** (1953), 2229.
- [115] R. G. Snyder, M. Maroncelli, S. Ping Qi, and H. L. Strauss, *Phase transitions and nonplanar conformers in crystalline n-alkanes*, Science **214** (1981), 188.
- [116] R. G. Snyder, M. Maroncelli, and H. L. Strauss, *Distribution of gauche bonds in crystalline n-C₂₁H₄₄*, J. Am. Chem. Soc. **105** (1983), 133.
- [117] T. Soddemann, B. Dünweg, and K. Kremer, *Dissipative particle dynamics: A useful thermostat for equilibrium and nonequilibrium molecular dynamics simulations*, Phys. Rev. E **68** (2003), 046702.
- [118] G. T. W. Solomons and C. B. Fryhle, *Organic chemistry*, 8th ed., Wiley, 2003.
- [119] J.-U. Sommer and G. Reiter (eds.), *Polymer crystallization: Observations, concepts and interpretations*, Lecture Notes in Physics, vol. 606, Springer, Berlin, 2003.
- [120] G. Strobl, *The physics of polymers: Concepts for understanding their structures and behavior*, Springer, Berlin–Heidelberg, 1997.
- [121] G. Strobl, *From the melt via mesomorphic and granular crystalline layers to lamellar crystallites: A major route followed in polymer crystallization?*, Eur. Phys. J. E **3** (2000), 165.
- [122] W. C. Swope, H. C. Andersen, P. H. Berens, and K. R. Wilson, *A computer simulation method for the calculation of equilibrium constants for the formation of physical clusters of molecules: Application to small water clusters*, J. Chem. Phys. **76** (1982), 637.

- [123] H. Takeuchi, *Structure formation during the crystallization induction period of a short chain-molecule system: A molecular dynamics study*, J. Chem. Phys. **109** (1998), 5614.
- [124] J. M. Thijssen, *Computational physics*, Cambridge, 1999.
- [125] W. Tschöp, K. Kremer, J. Batoulis, T. Bürger, and O. Hahn, *Simulation of polymer melts. I. Coarse-graining procedure for polycarbonates*, Acta Polymer **49** (1998), 61.
- [126] W. Tschöp, K. Kremer, O. Hahn, J. Batoulis, and T. Bürger, *Simulation of polymer melts. II. From coarse-grained models back to atomistic description*, Acta Polymer **49** (1998), 75.
- [127] G. Ungar, *Structure of rotator phases in n-alkanes*, J. Phys. Chem. **87** (1983), 689.
- [128] F. Varnik, *Molekulardynamik Simulationen zum Glasübergang in Makromolekularen Filmen*, Ph.D. thesis, Johannes Gutenberg-Universität Mainz, 2000.
- [129] L. Verlet, *Computer "experiments" on classical fluids. I. Thermodynamical properties of Lennard-Jones molecules*, Phys. Rev. **159** (1967), 98.
- [130] M. V. Volkenstein, *Configurational statistics of polymer chains*, Interscience Wiley, 1963, chapter 5.
- [131] N. Waheed, M. S. Lavine, and G. C. Rutledge, *Molecular simulation of crystal growth in n-eicosane*, J. Chem. Phys. **116** (2002), 2301.
- [132] P. Welch and M. Muthukumar, *Molecular mechanisms of polymer crystallization from solution*, Phys. Rev. Lett. **87** (2001), 218302.
- [133] J.-P. Wittmer, H. Meyer, J. Baschnagel, A. Johner, S. Obukhov, L. Mattioni, M. Müller, and A. Semenov, *Long range bond-bond correlations in dense polymer solutions*, Phys. Rev. Lett. **93** (2004), 147801.
- [134] B. Wunderlich, *Macromolecular physics*, vol. 1, Academic, New York, 1973, Crystal Structure, Morphology, Defects.
- [135] B. Wunderlich, *Macromolecular physics*, vol. 2, Academic, New York, 1976, Crystal Nucleation, Growth, Annealing.
- [136] B. Wunderlich, *Macromolecular physics*, vol. 3, Academic, New York, 1980, Crystal Melting.
- [137] Hiromi Yamakawa, *Modern theory of polymer solutions*, Harper & Row, New York, 1971.
- [138] T. Yamamoto, *Molecular dynamics modeling of polymer crystallization from the melt*, Polymer **45** (2004), 1357.
- [139] T. Yamamoto, N. Orimi, N. Urakami, and K. Sawada, *Molecular dynamics modeling of polymer crystallization; from simple polymers to helical ones*, Faraday Discuss. **128** (2005), 75.
- [140] D. Y. Yoon, G. D. Smith, and T. Matsuda, *A comparison of a united atom and an explicit atom model in simulations of polymethylene*, J. Chem. Phys. **98** (1993), 10037.